Three-dimensional and multicolour approaches in super-resolution fluorescence microscopy for biology

Clément Cabriel

université PARIS-SACLAY

NNT : 2019SACLS220

Thèse de doctorat

UNIVERSITÉ PARIS SUD
Comprendre le monde, construire l'avenir

Three-dimensional and multicolour approaches in super-resolution fluorescence microscopy for biology

Thèse de doctorat de l'Université Paris-Saclay
préparée à Université Paris-Sud

Ecole doctorale n°572 Ondes et matière (EDOM)
Spécialité de doctorat : Optique et photonique

Thèse présentée et soutenue à Orsay, le 12 juillet 2019, par

CLÉMENT CABRIEL

Composition du Jury :

Nathalie Westbrook Professeur, Institut d'Optique Graduate School (Laboratoire Charles Fabry)	Présidente
Sophie Brasselet Directrice de recherche, Institut Fresnel	Rapporteure
Christophe Zimmer Directeur de recherche, Institut Pasteur (Unité Imagerie et Modélisation)	Rapporteur
Bassam Hajj Chargé de recherche, Institut Curie (Laboratoire Physico Chimie Curie)	Examinateur
Sandrine Lévêque-Fort Directrice de recherche, Institut des Sciences Moléculaires d'Orsay	Directrice de thèse
Guillaume Dupuis Maître de conférences, Université Paris-Sud (Centre de Photonique BioMédicale)	Co-directeur de thèse

université
PARIS-SACLAY

Thèse de doctorat de l'université Paris Sud / Paris Saclay

Spécialité: optique et photonique

présentée par

Clément CABRIEL

pour obtenir le grade de:

Docteur de l'université Paris Sud / Paris Saclay

Three-dimensional and multicolour approaches in super-resolution fluorescence microscopy for biology

---

Soutenue le: **12 juillet 2019**

devant le jury composé de:

Directrice de thèse	Dr. Sandrine Lévêque-Fort	*ISMO, Orsay*
Co-directeur de thèse	Dr. Guillaume Dupuis	*CPBM, Orsay*
Présidente	Pr. Nathalie Westbrook	*IOGS, Palaiseau*
Rapporteurs	Dr. Sophie Brasselet	*Institut Fresnel, Marseille*
	Dr. Christophe Zimmer	*Institut Pasteur, Paris*
Examinateur	Dr. Bassam Hajj	*Institut Curie, Paris*

Contents

Abstract

Cell biology relies on imaging tools to provide structural and dynamic information about samples. Among them, fluorescence microscopy offers a compromise between high specificity and low toxicity. Recently, super-resolution methods overcame the diffraction barrier to unlock new fields of investigation. Single molecule approaches prove especially useful for three-dimensional nanoscale imaging, and allow couplings between different detection modalities. Still, their use is hindered by the complexity of the methods as well as the lack of reproducibility between experiments.

We propose new methods to render super-localisation microscopy more easily applicable to relevant studies in cell biology, chemistry and material science. First, we introduce dedicated protocols and samples to eliminate sources of error in calibration and performance measurement acquisitions. We also provide examples of uses of three-dimensional super-localisation for state-of-the-art studies in the frameworks of cell adhesion and bacterial resistance to drugs.

Then, we focus on the development of a novel optical method that provides unbiased results in three-dimensional single molecule localisation microscopy. This is achieved through the combination of two complementary axial detection strategies: point spread function shaping on the one hand, and supercritical angle fluorescence detection on the other hand. By cross-correlating and merging the lateral and axial positions provided by the different sources, we achieve quasi-isotropic localisation precisions down to 15 nanometres over a 1-micrometre capture range. We demonstrate the insensibility of the method to imaging non-idealities such as axial drift, chromatic aberration and sample tilt, and we propose applications in neurobiology and bacteria labelling.

Finally, we introduce two new post-processing approaches for the demixing of simultaneous multi-species acquisitions. They are based respectively on the measurement of the spot sizes, and on the assessment of the dynamic blinking behaviour of molecules. After demonstrating a proof of principle, we assess the impact of the different parameters likely to influence the results. Eventually, we discuss leads to improve the demixing performances, and we discuss the coupling possibilities with complementary single molecule localisation techniques.

Keywords: Optics, Microscopy, Fluorescence, Super-resolution, Biology

Résumé

Pour analyser la structure et la dynamique des échantillons, la biologie cellulaire repose sur l'utilisation d'outils d'imagerie. En particulier, la microscopie de fluorescence offre une grande spécificité et une toxicité réduite. L'émergence récente des méthodes de super-résolution a permis d'outrepasser la limite de diffraction et ouvert de nouvelles perspectives d'études. Les stratégies de molécule unique sont particulièrement adaptées à l'imagerie nanométrique tridimensionnelle, et permettent de nombreux couplages avec des modalités complémentaires ; toutefois, leur manque de reproductibilité entrave leur généralisation.

Nous proposons ici de nouvelles méthodes dans le but de remédier à ces problèmes en facilitant leur application en biologie cellulaire, en chimie et en science des matériaux. Tout d'abord, nous présentons des protocoles et échantillons dédiés aux acquisitions de calibration et de mesure de performances. Nous décrivons également plusieurs exemples d'utilisation de super-localisation tridimensionnelle dans le cadre d'études d'adhésion cellulaire et de résistance bactérienne.

Ensuite, nous nous concentrons au développement d'une nouvelle méthode de microscopie de localisation de molécules uniques tri-dimensionnelle permettant l'élimination de biais de détection. Ceci est permis par le couplage entre deux stratégies complémentaires: la mise en forme de fonction d'étalement de point, et la détection de la fluorescence d'angle super-critique. L'intercorrélation et la recombinaison des informations latérales et axiales permet l'obtention d'une résolution quasi-isotrope, avec des précisions jusqu'à 15 nanomètres sur une plage de capture d'un micron. Nous mettons en évidence l'insensibilité de la méthode aux biais d'imagerie comme la dérive axiale, l'aberration chromatique et l'inclinaison de l'échantillon, et nous l'illustrons à travers des applications à la neurobiologie et au marquage de bactéries.

Pour finir, nous présentons deux nouvelles approches pour le découplage d'acquisitions multi-espèces simultanées. Toutes deux basées entièrement sur le post-traitement des données acquises, elles exploitent respectivement la mesure des tailles des taches et le comportement dynamique du clignotement. Après une preuve de principe, nous évaluons l'impact des différents paramètres susceptibles d'influencer les résultats. Nous concluons en proposant des pistes d'amélioration des performances de découplage, et en suggérant de possibles couplages avec des méthodes complémentaires en imagerie de molécules uniques.

Mots-clefs : Optique, Microscopie, Fluorescence, Super-résolution, Biologie

« Aime la vérité mais pardonne à l'erreur. »
— Voltaire

« *If you are going through hell, keep going.* »
— Winston Churchill

Remerciements

Ce manuscrit est le fruit de plusieurs années de travail, durant lesquelles j'ai pu compter sur de nombreuses personnes pour m'aider. Je tiens tout d'abord à remercier mes encadrants, Sandrine Lévêque-Fort et Guillaume Dupuis pour avoir supervisé mes travaux en étant présents pour me guider sur tous les sujets que je ne maîtrisais pas en commençant ma thèse, et en me laissant par la suite la latitude d'orienter mes travaux. Merci à eux d'avoir mis à disposition les moyens techniques nécessaires à la réalisation de ce projet, et de m'avoir toujours incité à valoriser et communiquer autour de mes avancées.

Un grand merci également à Nicolas Bourg pour avoir pris le temps (même pendant la phase de rédaction de son manuscrit) de me transmettre les nombreuses connaissances qu'il avait constituées en défrichant les domaines de la SMLM, du SAF et du marquage fluorescent, et pour avoir continué par la suite à échanger régulièrement, souvent par simple curiosité scientifique.

Je remercie également Nathalie Westbrook et Bassam Hajj pour avoir accepté de faire partie de mon jury. Tout particulièrement je remercie les rapporteurs de ma thèse Sophie Brasselet et Christophe Zimmer pour avoir relu mes travaux dans des délais courts et pour avoir proposé des avis constructifs.

Tout au long de mes travaux, j'ai eu la chance de travailler avec de nombreux collaborateurs qui ont fait preuve de bonne volonté et ont pris la peine de chercher à comprendre le langage des physiciens qui ne leur était pas forcément familier de manière à ce que nous puissions travailler ensemble malgré les contraintes. Merci donc à Rym Boudjemaa, Gianluca Cattinari, Karine Steenkeste, Marie-Pierre Fontaine-Aupart, de même qu'à Aurélie Baron et à Boris Vauzeilles, à Christophe Leterrier, à Thomas Orré, Olivier Rossier et Grégory Giannone, à Anaïs Bouissou et Renaud Poincloux.

Merci également à Emmanuel Fort pour avoir proposé son avis sur mes travaux, et pour les discussions toujours intéressantes sur la SMLM, le SAF et la physique ondulatoire.

Grâce à leur zèle et à leur enthousiasme, j'ai également pu interagir avec Abbelight pour que chacun puisse bénéficier des travaux et de l'expertise des autres (sans compter leur bonne humeur, ni les quelques verres que nous avons pris ensemble). Je remercie

tous les membres, notamment Nicolas et Jean-Baptiste, ainsi que l'équipe logiciel, en particulier Caroline et Yann, l'équipe applications, notamment Cyndelia et Cataldo, et Marion de l'équipe développement optique.

Je n'oublie pas le CPBM, bien sûr, qui a été d'une aide précieuse. Merci à Sandrine Lécart et à Ludivine Houel-Renault pour leur disponibilité et leur bonne volonté.

Je suis également reconnaissant envers l'EDOM pour sa contribution au bon déroulement de ma thèse, ainsi que l'ENS Cachan (qui portait encore ce nom-là *de mon temps*) pour le financement dont j'ai eu la chance de bénéficier. Merci également aux nombreuses sources de financement qui m'ont permis de bénéficier des moyens techniques pour réaliser mes travaux et de participer à des conférences.

Bien évidemment, je tiens à remercier l'ensemble de l'ISMO pour avoir rendu possibles ces travaux et avoir apporté leur aide. Merci à la direction, aux équipes techniques, aux services administratifs, mais également aux collègues des autres équipes. Merci notamment aux doctorants, post-doctorants et stagiaires pour leur bonne humeur. Merci à ceux que j'ai côtoyés et avec qui j'ai discuté tous les jours, notamment Rym, Gianluca et Alan. Pour finir, j'aimerais remercier les autres membres de l'équipe avec qui j'ai eu la chance de travailler : Pierre, Marion, Thomas, Nicolas, Adrien, Abigail et Jean. Merci à eux pour leur inestimable contribution, des discussions scientifiques à leur aide pour la préparation d'échantillons, de la bonne humeur qu'ils mettaient dans le bureau aux pauses café !

Au-delà de la science, j'aimerais remercier tous ceux qui m'ont soutenu pendant ces années de travail parfois intense. Merci donc à mes amis de la JEABSCHM pour les randonnées en terres exotiques et les excursions culinaires non moins exotiques. Merci en particulier à Aurélien, Jean, Hadrien et Pauline avec qui j'ai partagé des découvertes cinématographiques et des petits godets. Merci également aux collègues qui ont été plus que des collègues : Pierre, Marion (plus Charles et Kevin), Thomas, Gianluca, Adrien et Abigail. Sans eux, le quotidien aurait été plus terne. Merci bien sûr à ceux que je ne cite pas nommément mais qui ont été présents aussi.

Pour finir, je remercie ma famille, et plus particulièrement mes parents et mes frères pour leur compréhension, leur soutien et leur indéfectible humour.

Introduction

Scientific advances rely on both inductive and deductive reasonings. From the observation of our environment, general laws are inferred to describe phenomena; and these principles are then applied to explore unknown domains by trial and error. This constant feedback requires the capacity to gather knowledge about the subject of study and assess the effect of experiments carried out. Imaging finds its place in this framework, hence the development of various strategies, from telescopes to describe astronomical objects to X-ray diffraction to understand atomic structures.

Biological research has long been of particular interest, as the comprehension of organism and cell behaviour enables the development of drugs and treatments. To image and understand processes of interest, it heavily relies on the use of electron, phase and fluorescence microscopy. The latter offers the advantages of high specificity, high contrast and low toxicity. It has been used for decades in cell biology to record images of samples up to a hundred micrometres deep. Although resolutions long remained limited by the diffraction, the recent development of so-called super-resolution techniques unlocked a whole new field of applications.

In particular, single-molecule strategies allow the measurement at the molecular scale of a considerable amount of information, from the three-dimensional position to the spectrum, the polarisation or the lifetime. This generally requires dedicated optical setups, as well as labelling and acquisition strategies, not to mention data analysis workflows. Powerful yet perfectible methods yield promising results, with many potential applications in cell biology. Nevertheless, several fields still need improvement before super-localisation methods can be routinely used for bioimaging. In particular, there exists a need for standardisation of the calibration and performance measurement protocols. Also, due to unavoidable experimental biases, single-molecule approaches suffer from a certain lack of reproducibility. Finally, simplification of the setups and processing workflows leaves plenty of scope for improvement.

This thesis finds its place in this framework. We aim at addressing some of the current limitations of super-localisation by proposing reliable calibration and measurement protocols, as well as to develop unbiased and straightforward methods for three-

dimensional and multicolour super-resolution imaging. These improvements will be illustrated on samples of particular relevance for biological and chemical studies. This work was carried out at the Institut des Sciences Moléculaires d'Orsay, and was made possible by the interdisciplinary and collaborative environment between the optics and data processing team and colleagues from biology or chemistry teams, as well as the technical platforms and the startup companies.

Outline and description of the chapters

This manuscript comprises an introduction chapter to set the frame of the methods and protocols that we developed. They will then be detailed in three separate chapters, even though the advances demonstrated in the three chapters are closely intertwined.

In the first chapter, we will describe the background of fluorescence microscopy. The diffraction limit will be explained, and we will introduce Single Molecule Localisation Microscopy (SMLM) strategies to overcome this limitation through blinking chemical processes. Then, we will provide an overview of the state of the art in three-dimensional super-localisation: we will describe in detail their implementations and performances, as well as their current shortcomings. In particular, Point Spread Function (PSF) shaping methods will be introduced. Similarly, we will explain the Supercritical Angle Fluorescence (SAF) detection method, alongside its implementation in single molecule regime, Direct Optical Nanoscopy with Axially Localised Detection (DONALD).

Chapter 2 will be devoted to the presentation of experimental considerations related to 3D SMLM methods. More precisely, we will tackle the questions of calibration, performance measurement and biological applications. First, we will concentrate on issues linked to the calibration of the axial detection in 3D SMLM. This step is necessary in many cases (especially PSF shaping methods), but it appears that most protocols reported in the literature exhibit significant biases that are bound to alter the results of acquisitions. Consequently, we will propose an alternative calibration protocol that relies on the use of a sample of known three-dimensional geometry imaged in nominal conditions. Having dealt with this question, we will take a closer look at performance measurements. The performance of a technique defines its ability to image a sample with sufficient precision. We will present and discuss the different approaches and samples available, and propose solutions to decouple the different factors contributing to the performance, from the information actually contained in the PSFs to the stability of the setup and the size of the labels. Eventually, applications of DONALD imaging to relevant studies in biology and chemistry will be given. We will focus on three particular collaborations, the first about resistance of bacteria to drugs, and the latter two in the framework of cell adhesion and motility. The particular challenges linked to each of these projects will be explained, and the developments carried out to overcome them through sample preparation and data analysis will be highlighted.

Then, in the third chapter, we will focus on the development of a new 3D SMLM technique that aims at improving the reproducibility and the reliability of the results.

This method, called Dual-view Astigmatic Imaging with SAF Yield (DAISY), combines the complementary DONALD and astigmatic imaging approaches. More precisely, it intends to make up for both the reduced capture range of DONALD and the experimental biases hampering PSF shaping-based methods. With this end in view, we will describe how it is possible to measure, for each molecule, two axial positions thanks to SAF and astigmatism. In this detection scheme, each molecule provides an absolute reference thanks to the SAF measurement. We will detail how we use these references to build a correction algorithm that makes up for the non-idealities of the PSF shaping-based detection, i.e. the axial drift, the chromatic aberration and the sample tilt. Thorough characterisation of the performances of DAISY will be carried out in connection with the protocols proposed in chapter 2. Finally, applications will be provided in the framework of collaboration with colleagues from biology and chemistry teams to investigate state-of-the-art questions.

The fourth and final chapter will tackle the issue of multi-species imaging in SMLM. After an overview of currently available methods, we will highlight the need for simplification of the optical setups. Then we will present two post-processing-based methods that enable demixing of simultaneous multi-species acquisitions without requiring modifications of the optical setups. The first, called Spot width Evaluation for Spectral Assignment in Multicolour Experiments (SESAME), is based on the measurement of spot size, which is intrinsically related to the fluorescence wavelength. The second relies on the assessment of the photophysical behaviour of the fluorophores: by measuring the fluorescence photon flux and the ON state duration for each molecule, we will show how they can be used to identify the corresponding species—we call this method PHotophysics-based Allocation for Nanoscopy through inTensity and On time Measurement (PHANTOM). For each technique, the principle, the acquisition protocol and the data processing workflow will be explained. Then, we will evaluate the performances in terms of specificity and localisation loss. Finally, we will discuss how the simplicity of these methods make them suited for combination with other approaches in 2D or 3D SMLM.

Chapter 1

Single Molecule Localisation Microscopy

1.1 Introduction to fluorescence microscopy

Fluorescence microscopy is a widespread tool for biological imaging due to its versatility, its relatively low toxicity and thus its suitability for live cell imaging. Unlike phase microscopy, it is able to produce highly contrasted images of specific proteins. In fluorescence microscopy, the observation relies on the use of fluorescent labels that are attached to the targets. The labelling is typically obtained either through transfection—a deliberate modification of the genes of the organism so that it produces fluorescent proteins in addition to the proteins of interest—or through immunolabelling, which relies on the use of primary antibodies that target the species of interest, and secondary antibodies labelled with organic dyes that bind to the primary antibodies. Other labelling strategies might be available, depending on each specific case: the common principle is to use a fluorescent label that presents a specific chemical affinity to its target.

Once the sample is labelled, it can be imaged through the use of fluorescence: the molecules are excited with a light source (such as a thermal lamp or a laser), absorb photons to reach an excited electronic state and spontaneously reemit a fluorescence photon. The excitation light should be bright enough for the molecules to emit a signal that can be detected on a camera or a photodetector. Each molecule has its own photochemical properties, which define the lifetime of its excited state, its absorption cross-section and quantum yield, as well as its absorption and fluorescence spectra. Unless non-linear processes are involved, the fluorescence spectrum is always higher in wavelength compared to the absorption spectrum—this energy loss is due to the relaxation through vibrational states (see Fig. 1.1). In order to image a specific fluorophore, the wavelength of the excitation has to match its absorption peak. This can be used in practise to image different targets in the same field of view: each protein of interest is labelled with a different fluorophore, and their positions are then obtained thanks to sequential acquisitions with different excitation wavelengths.

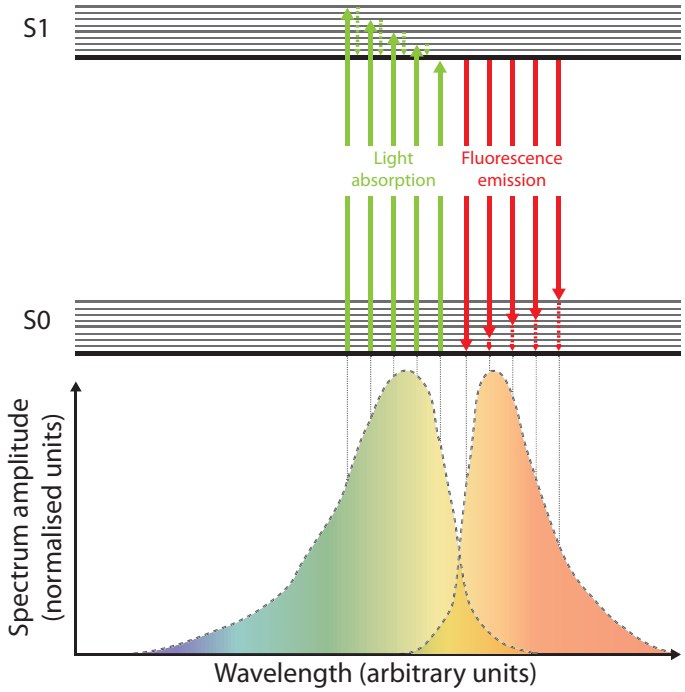

Figure 1.1 – Principle of the fluorescence. Molecules in the ground state S0 absorb incoming photons from the excitation beam to reach the excited state S1. They then undergo a relaxation through vibrational states, thus dissipating energy, before returning to the ground state through spontaneous emission. Source: adapted from the PhD manuscript of Nicolas Bourg [1].

Both fluorescent proteins and organic dyes generally exhibit relatively broad excitation and emission spectra (typically 50 nm Full Width at Half Maximum), however. Considering that most fluorophores are in the visible range of the electromagnetic spectrum, this represents a major hindrance in fluorescence microscopy. Indeed, spectrally separated probes have to be used in order to preserve the specificity of the imaging. In practise, it is rarely possible to image more than four targets on the same field. Still, this is sufficient in many cases, as biological studies often target only a few proteins of interest. Besides, it is generally possible to label one protein which stand for a common known reference through all the acquisitions, and different proteins of interest on different samples.

Naturally, it is necessary to use a dedicated optical setup to record an image of a sample. Every fluorescence setup is composed of two distinct parts: an excitation setup that aims at creating a suitable illumination pattern, and a detection setup that recovers the fluorescence light and shapes it before sending it on a detector. Two main strategies are available (see Fig. 1.2): the most simple is the wide field microscope. It relies on the use of a broad excitation beam—typically a white lamp or an expanded laser beam—to shine a whole field of view. The fluorescence is collected by the objective and sent on a camera, which records the image of the sample. Although it is very straightforward to implement and easy to use, the wide field microscope suffers from a major drawback: the

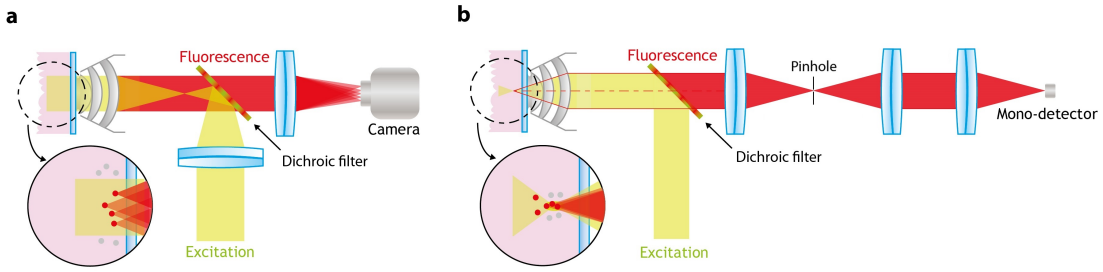

Figure 1.2 – Optical setups used in fluorescence microscopy. **(a)** Wide field microscope. The excitation beam is sent through the objective lens to create a wide homogeneous excitation. The fluorescence is collected by the same objective and separated from the excitation beam thanks to a dichroic beam splitter. Finally, the image is formed on the camera. **(b)** Point scanning microscope. The excitation beam is focused through the objective on a tiny region of the sample, and the fluorescence is collected by the same objective, separated from the excitation thanks to a dichroic beam splitter, and sent on a monodetector (such as a photodiode). In the confocal microscope, a pinhole is added in the detection path to get rid of the out-of-focus signal. Source: adapted from the PhD manuscript of Nicolas Bourg [1].

sample is imaged only over a depth of field (1 µm to a few µm) in the axial direction, and the light emitted by out-of-focus molecules creates a roughly uniform background that causes the contrast to deteriorate.

The second setup category relies on a point scanning excitation: an excitation laser beam is focused on a tiny region of the sample, and the fluorescence light is acquired by a fast photodetector. Then the beam is scanned across the field of view to record the image of the whole sample. In the confocal microscope configuration, a pinhole is added in the detection plane near the focusing point of the fluorescence beam. The aperture is optimised so that only the in-focus light is transmitted, while the out-of-focus signal is rejected—thus, the contrast is enhanced compared to a wide field microscope configuration.

Both strategies only allow to record lateral information about the organisation of the proteins of interest in the imaged plane. In order to obtain 3D images, complementary axial information is necessary. It can be accessed thanks to axial scanning of the focus plane in the wide field configuration, or a displacement of both the excitation beam and the pinhole (or simply the stage on which the sample is placed) in the confocal configuration.

Even though they are able to produce highly specific images of the spatial organisation of different proteins in a sample, these methods are fundamentally limited by the effect of the diffraction. Indeed, a source, whether coherent or not, cannot be focused below a certain threshold that is defined by the laws of diffraction. In other words, it creates a spot that has a size dependent on the wavelength of the source and on the numerical aperture of the system. For a circular aperture, the size of the spot is called the Airy radius:

$$r_{\text{Airy}} = 0.61 \frac{\lambda_{\text{fluo}}}{\text{NA}} \tag{1.1}$$

where λ_{fluo} is the fluorescence wavelength, and NA is the numerical aperture of the system—generally limited by the numerical aperture of the objective lens itself.

This has different effects depending on the optical setup used: in confocal microscopy, the excitation laser beam cannot be narrowed below the Airy radius (200 to 300 nm typically), and the excited area is thus not a point strictly speaking, but a narrow spot. In other words, it is not possible to optically resolve the organisation of the proteins below that scale. In the wide field configuration, the excitation is not focused, but the focal plane of the objective is conjugated with the camera, which records the image of the fluorescent probes. However, due to the effect of the diffraction, two sources that are closer to each other than the Airy radius cannot be distinguished, which again limits the resolution of the optical system.

In the rest of this work, we will focus on the wide field implementation rather than on the confocal microscope. It is worth noticing that the resolution limit is directly related to the transfer function of the optical system: the image of a point source[1] through the detection path of the wide field microscope is an Airy function. This response of the optical system is called Point Spread Function (PSF). In the presence of aberrations or wavefront shaping in the detection setup, the PSF can exhibit a more complex shape than an Airy function. Mathematically, the image obtained from a spatial distribution of fluorescence emission $O(x, y)$ through the microscope can be written as its convolution with the PSF:

$$I(x, y) = (\text{PSF} * O)(x, y) \tag{1.2}$$

Consequently, the transmission through the detection setup induces a blurring of the imaged structures at the scale of a 200–300 nm, and the fine structure of the sample is lost (see Fig. 1.3a). It should be noted that the PSF is defined as a 3D object, as the diffraction also limits the resolution in the axial direction. The axial extension of the PSF (defined by the depth of field) is generally significantly larger than its lateral (see Fig. 1.3b).

1.2 Principle of the localisation

Even though the wide field microscope is not able to distinguish two sources closer than the Airy radius, the fluorescence signal emitted by a single isolated source can be recorded on the camera and sampled over several pixels. Then, the centre of the spot can be localised precisely through software processing. Several methods are available here: the detection of the centre of mass is probably the most straightforward, although the

[1] Fluorophores can be considered point sources, as their size is well below the Airy radius.

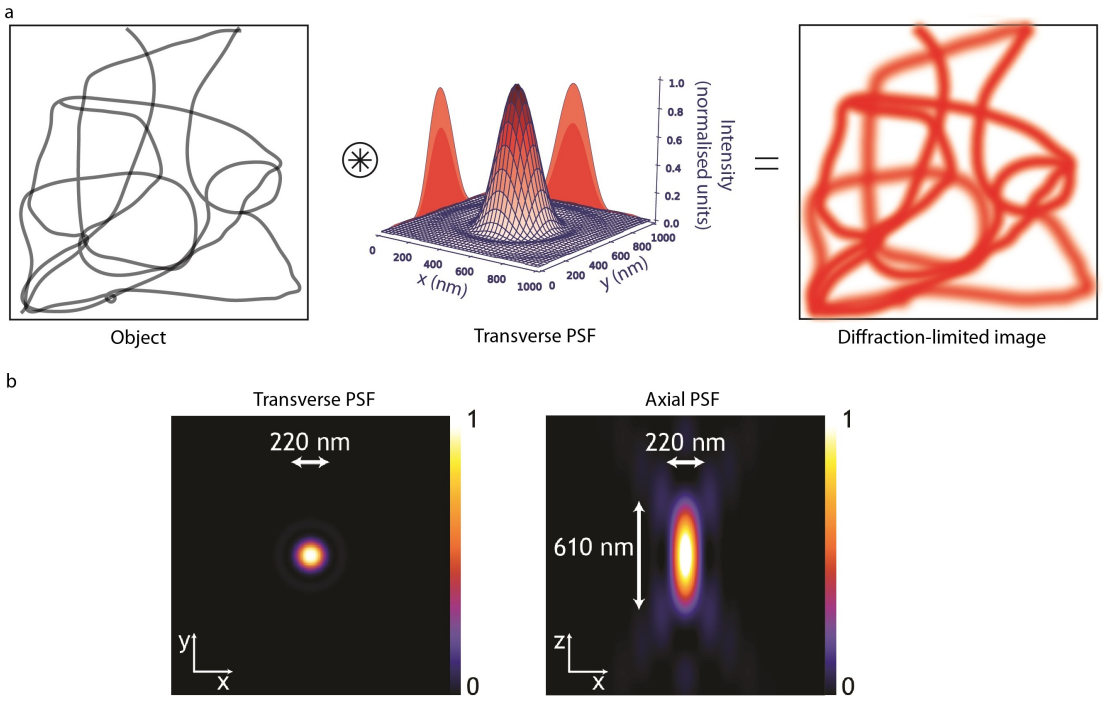

Figure 1.3 – Point Spread Function and diffraction limit. **(a)** Formation of an image through a microscope. As the imaged structure is convolved by a 250-nm wide PSF, fine details of the sample are lost. **(b)** Simulated lateral and axial PSFs for a 1.49-numerical-aperture objective. Source: adapted from the PhD manuscript of Nicolas Bourg [1].

precision is not optimal. Another solution is to assume a model for the spatial distribution and fit the corresponding 2D function on the experimental data. In particular, Gaussian fitting yields satisfactory results[2], even if other models are possible, such as cubic spline interpolation. Independently of the method, the localisation yields the position with a precision much lower than the Airy radius (see Fig. 1.4).

The best attainable precision for the localisation of the centre of a PSF (the so-called Cramér-Rao Lower Bound, or CRLB) can be determined from the Fisher information matrix. Even if it is based on strong assumptions that are not fully satisfied in realistic experimental conditions, the CRLB is a rather practical tool to predict the expected localisation precision of an experiment. It is especially useful to assess the importance of the different parameters that influence the precision. In the case of Gaussian fitting, the CRLB is equal to [3]:

$$\sigma_{x,y} = \frac{\sqrt{w^2 + a^2/12}}{N} \sqrt{1 + 4\tau + \sqrt{\frac{2\tau}{1+4\tau}}} \tag{1.3}$$

where $\sigma_{x,y}$ is the error (defined as the standard deviation of the statistical distribu-

[2] In theory, the image of a point source is expected to be an Airy function, but in practise, due to optical aberrations and polarisation effects, the Gaussian model is more suited to the experimental data.

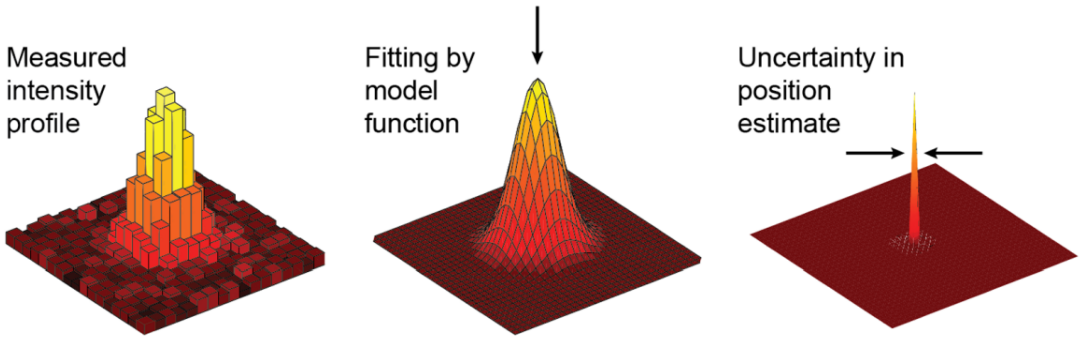

Figure 1.4 – Localisation of a single emitter. **(a)** PSF recorded on the camera (note the sampling and the noise). **(b)** Fitting by a model function (for instance a 2D Gaussian), that yields the position of the centre. **(c)** Uncertainty associated with the localisation, i.e. spatial distribution of the detected centre position due to the noise. This spatial distribution of the localised position can be understood as the effective localised PSF. Source: Diezmann *et al.*, *Chemical Reviews* (2017) [2].

tion) on the lateral position of the centre (x,y). N is the number of photons detected in the whole PSF, and w is its width (defined as the standard deviation of the spatial distribution). a is the pixel size—indeed, the sampling on the camera induces a slight loss of precision. Finally, τ is a term that contains information about the signal to background ratio (the higher τ, the lower the signal to background ratio):

$$\tau = \frac{2\pi b(w^2 + a^2/12)}{Na^2} \tag{1.4}$$

One can notice that the localisation precision is mostly determined by the number of photons in the PSF and the brightness of the background. As a consequence, bright probes such as metal nanobeads, quantum dots or organic dyes are expected to yield a good (i.e. low) localisation precision (below 10 nm), while fluorescent proteins, that emit a dimmer fluorescence signal, produce mediocre localisation precisions (around 15 nm). The background fluorescence signal coming from out-of-focus molecules is also likely to induce a deterioration of the performances, hence the development of optical sectioning methods (this will be described more exhaustively in section 1.4.)

The possibility to localise individual molecules enables the tracking (Single Particle Tracking, or SPT) of individual proteins in living samples for instance. It can find applications in the framework of time-resolved studies of endocytosis and drug internalisation for instance [4]. Nevertheless, it does not directly enhances the resolution of the microscope, as it is still not possible to distinguish two sources that are closer than the Airy radius.

In order to unlock imaging of dense structures below the diffraction limit, it is necessary to resort to photochemical processes to switch some of the fluorescent molecules in a dark state while a small fraction of them emit signal and can be localised. Then other molecules can be switched to a fluorescent state to be imaged. In other words, the fluorescence emission of the labels is spread over time so that a series of frames can be acquired

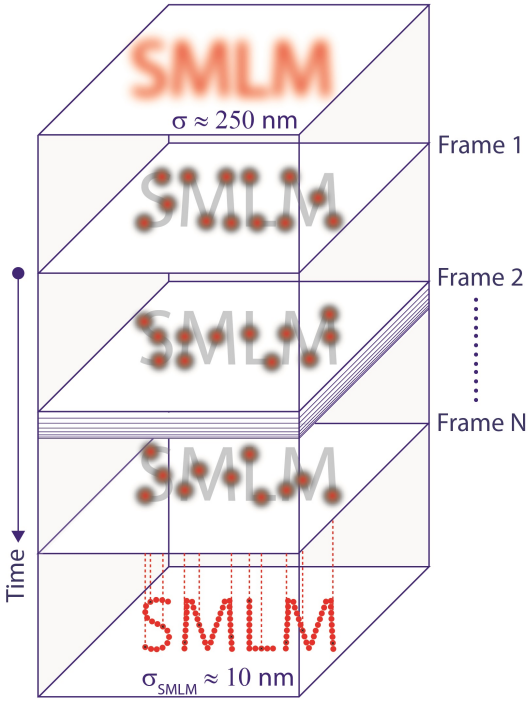

Figure 1.5 – Principle of SMLM. The resolution of the wide-field image is limited by the diffraction to 200–300 nm approximately. By chemically inducing the blinking of the fluorescent probes, individual spots can be acquired and localised with extreme precision. The emission of the fluorophores is spread over time, and the accumulation of the results yields the image of the sample with a precision down to 5–15 nm. Source: adapted from the PhD manuscript of Nicolas Bourg [1].

with isolated PSFs on each—this is called single molecule regime. The molecules thus have to exhibit a blinking behaviour to be localised individually on each frame, and the structure of the whole sample is reconstructed by accumulation of all the localisations. The principle of this Single Molecule Localisation Microscopy modality is presented in Fig. 1.5.

1.3 Blinking processes

For the purpose of inducing the blinking behaviour, several chemical processes are possible. The first is called Photo-Activated Localisation Microscopy (PALM). It relies on the use of photoactivable fluorescent proteins (see Fig. 1.6a). Initially, the fluorescent proteins are in a non fluorescent state. Through the absorption of near-UV light (typically a 405-nm laser beam), their conformation can change in such a way that they become fluorescent. In this state, they are likely to absorb excitation photons (typically in the 450–600 nm range of the spectrum) to reach the excited state and reemit fluorescence light, as described in Fig. 1.1. At each excitation-deexcitation cycle, the protein has a certain probability to change conformation again to reach a non fluorescent state, from

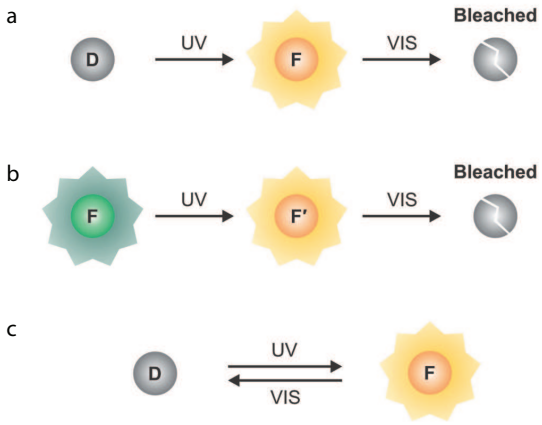

Figure 1.6 – Illustration of SMLM blinking processes. **(a)** Photoactivation: a fluorophore initially in the dark state (D) is converted to a fluorescent state (F) thanks to UV light and is imaged before photobleaching. **(b)** Photoconversion: a fluorophore initially in a fluorescent state (F) is converted to a different fluorescent state (F') thanks to UV light and is imaged before photobleaching. **(c)** dSTORM reversible switching of a fluorophore between a dark state (D) and a fluorescent state (F): visible light sometimes triggers a transition to the dark state, and UV light can be used to bring fluorophores back from the dark state to the fluorescent state. Source: adapted from Van de Linde and Sauer, *Chemical Society Reviews* (2014) [5].

which it cannot be recovered, even through the near-UV excitation. This process is called photobleaching, and it limits the number of photons that a fluorescent protein can emit before being lost (typically, they can emit around 1000 photons before photobleaching).

While it is in the fluorescent state, the protein can be imaged and tracked, until it photobleaches. This also unlocks quantitative imaging aspects: under certain conditions, each protein can be active only once, it is possible to count the fluorophores to obtain information about the number of proteins of interest[3]. PALM microscopy is especially suited for time-resolved imaging on living samples, as the proteins are typically expressed by the transfected cells themselves, and thus do not require fixation or permeabilisation. Besides, they require relatively low illumination power. Nevertheless, they are rather poor fluorophores in terms of quantum yield and number of cycles before photobleaching—consequently, they are rather dim emitters.

Several variants of PALM exist: for instance, photo-convertible proteins differ from photo-activable proteins in the sense that they are initially fluorescent, but the near-UV excitation induces a change of their absorption and emission spectra (see Fig. 1.6b).

Another strategy, called direct Stochastic Optical Reconstruction Microscopy (abbreviated to dSTORM), makes use of organic dyes that can reversibly switch from the fluorescent state (ON state) to a dark state (OFF state). This is illustrated in Fig. 1.6c. The transition from the ON state to the OFF state is stochastic: the molecule has a small

[3] It is worth noticing that PALM fluorescent proteins may exhibit a slight blinking behaviour in some cases [6], not to mention that two emitters closer than the Airy radius may be detected as a single spot. These non-idealities may induce biases in the quantitative analysis.

probability to reach the OFF state from the excited state. Other processes can also be involved, such as collision-induced transitions. The transition from the OFF state to the fundamental (ON) state can occur randomly after a certain time (typically a few hundred milliseconds to a few seconds), but it can also be triggered thanks to a near-UV light source that reexcites the molecules. Finally, organic dyes can also randomly photobleach just like fluorescent proteins. The probabilities of the ON to OFF transition and photobleaching are highly dependent on the chemical composition of the medium surrounding the molecules; thus it is possible to optimise these transition rates through the engineering of dedicated imaging buffers.

Unlike fluorescent proteins, dSTORM fluorophores repeatedly blink before photobleaching. This makes them rather unsuited for quantitative imaging, as each is localised a random number of times before photobleaching. Besides, organic dyes have to be attached to the proteins of interest, which is often done by fixing and permeabilising the cells before using immunolabelling to attach the dyes. This is incompatible with live cell imaging—not to mention that the chemical imaging buffer is also toxic to cells. Still, dSTORM is widely used for its vastly superior brightness compared to PALM. As the localisation precision depends on the number of photons, dSTORM images typically exhibit a much better resolution than PALM. It should be noted that most efficient dSTORM fluorophores are excited in the 530–680 nm domain, and fluoresce around 560–750 nm. Finally, the optical power densities required to induce most molecules in the OFF state and achieve single molecule regime are much higher than in PALM (around 4 $kW.cm^{-2}$).

The last category of blinking probes is PAINT, which stands for Point Accumulation for Imaging in Nanoscale Topography. In this regime, fluorescent probes are directly present in the immersion buffer. As long as they remain diffusive, they contribute to creating a roughly uniform fluorescence background, since their diffusion length over one exposure time is considerable. However, thanks to chemical affinities, they can also transiently bind to their targets, in which case their fluorescence localisation becomes localised at their docking site. This creates a PSF that can be imaged until the molecule undocks from its binding site or photobleaches.

Several variants of this method are available: some probes are non fluorescent as they are not bound to their target, which has the advantage of greatly reducing the background fluorescence. One notorious subcategory of PAINT is DNA-PAINT, which makes use of DNA strands for both the docking sites and the imagers. More precisely, DNA-conjugated antibodies are attached to the proteins of interest through immunolabelling. The imagers contained in the buffer are composed of fluorophores functionalised with the complementary DNA strand, which ensures the specific binding to their target.

PAINT exhibits relatively similar photophysical performances than dSTORM in terms of photon yield. The docked times are typically higher than the ON times of dSTORM organic dyes (a few hundred milliseconds versus a few ten milliseconds). Except in the case of imagers that are non fluorescent as long as they are not docked, PAINT produces rather high amounts of background fluorescence light, which sometimes require the use of complementary optical sectioning methods (see part 1.4). A major ad-

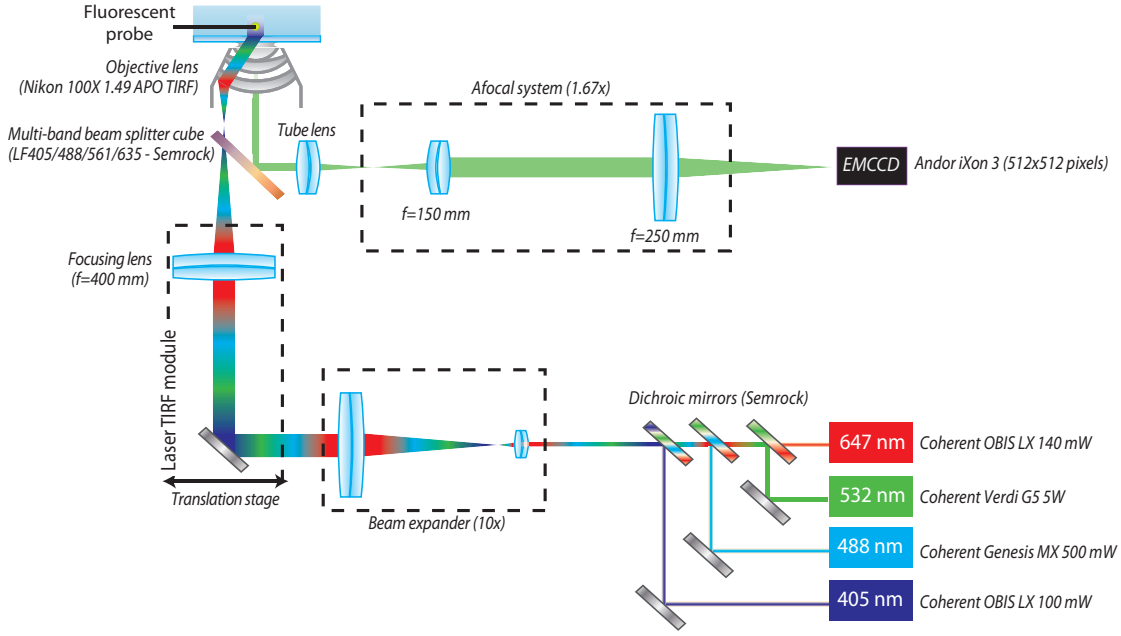

Figure 1.7 – Optical setup used for 2D SMLM. Source: adapted from the PhD manuscript of Nicolas Bourg [1].

vantage of PAINT is that the imagers are provided in large excess in the immersion buffer, and photobleaching is thus not a problem since the docking site remains accessible to unbleached molecules, enabling longer experiments. Generally, optical power densities used in PAINT experiments are somewhat lower than in dSTORM (1–2 kW.cm^{-2} typically).

1.4 Experimental implementation

Typical 2D SMLM setups are very similar to wide-field microscopes insofar as the resolution increase is mostly brought by the chemical blinking processes. Fig. 1.7 presents the optical system that we use for 2D SMLM. The excitation setup consists in either a white lamp associated to spectral filters (mostly for PALM) or one to several laser beams (for dSTORM and PAINT, as well as for PALM in many cases)—in our case, as we will focus on dSTORM and DNA-PAINT, the excitation path only features lasers as light sources. In the latter case, the beams are superimposed thanks to laser dichroic mirrors. They are also expanded thanks to a beam expander (i.e. a couple of lenses) to match the desired excitation field size. The lasers typically require relatively high power outputs (100 mW to 1 W, depending on the field area) to induce blinking. Then the excitation light is sent through the objective lens by a laser dichroic mirror. The beam is generally focused in the back focal plane of the objective to produce a collimated beam in the sample.

The fluorescence light is collected by the objective lens. For super-localisation experiments, the numerical apertures used are generally high (between 1.33 and 1.49) to collect most of the photons and reduce the PSF width, and the magnifications range be-

tween 60x and 100x in order to sample the PSF on the camera (for typical PSFs, the optimal pixel size is around 100 nm in the object plane [7]). The fluorescence light is transmitted by the dichroic mirror and sent to the detection setup, which contains the tube lens and the camera. Depending on the objective lens and the camera pixel size, an afocal system composed of two lenses is sometimes necessary between the tube lens and the camera to match the total magnification. The camera needs to be sensitive to very low signals and enable frame rates from 10 to 200 typically. The most widely used technologies are cooled EMCCD (Electron-multiplying Charged-Coupled Device) and SCMOS (Scientific Complementary Metal-Oxide-Semiconductor). The first perform better with very low photon counts, but the latter have recently come to be less noisy with dSTORM and DNA-PAINT signal levels, and offer better frame rates.

In many cases, the background noise generated by out-of-focus molecules is problematic, as it is likely to cause a degradation of the localisation precision (see equation (1.3)). Therefore, it is often relevant to restrict the excitation to the very imaging plane. This process is called optical sectioning, and it can be performed through various methods[4]. A simple optical sectioning method is TIRF (Total Internal Reflection Fluorescence microscopy) [8]: it is presented in Fig. 1.8. It requires the use of a high-numerical-aperture objective (above 1.33): by focusing the excitation laser beam in the outer region of its back focal plane, the light is sent to the objective with a high angle, beyond the critical angle corresponding to the glass coverslip/biological medium index mismatch[5]. Consequently, the excitation is totally reflected at the interface, and it only creates an evanescent wave close to the coverslip. This evanescent wave has a penetration depth around half the excitation wavelength. In other words, the excitation is confined in a region of a few hundred nanometres above the coverslip. Figure 1.9 presents a comparison between standard (also called epifluorescence) illumination and TIRF configurations.

Another approach is light sheet microscopy (also called Selective Plane IMaging, or SPIM) [9]: thanks to a cylindrical lens placed in the excitation path, the excitation laser beam is shaped into a sheet perpendicular to the optical axis. As the sheet is limited by the diffraction, it has a width equal to 1 µm, which matches the depth of field of SMLM imaging. Although light sheet microscopy often requires a dedicated excitation setup with an objective lens placed perpendicular to the imaging objective, it effectively reduces the fluorescence background, as well as photobleaching outside of the imaging plane—this can be useful for 3D imaging of the samples through axial scanning.

The last possibility to perform optical sectioning is structured illumination microscopy (SIM). It relies on the principle of modulation/demodulation and makes use of the transfer function of the microscope to suppress the out-of-focus components [10]. More precisely, a sine excitation pattern is created on the sample thanks to either two

[4]Optical sectioning can be performed in standard (i.e. diffraction-limited) widefield imaging to enhance the contrast and in SMLM to improve the localisation precision. The experimental implementations are the same in both cases.

[5]Typical index values are $n_g = 1.51$ for the glass coverslip and $n_s = 1.33$ for the biological medium or the imaging buffer. This results in a critical angle value equal to: $\theta_c = \arcsin\left(n_s/n_g\right) \approx 62°$.

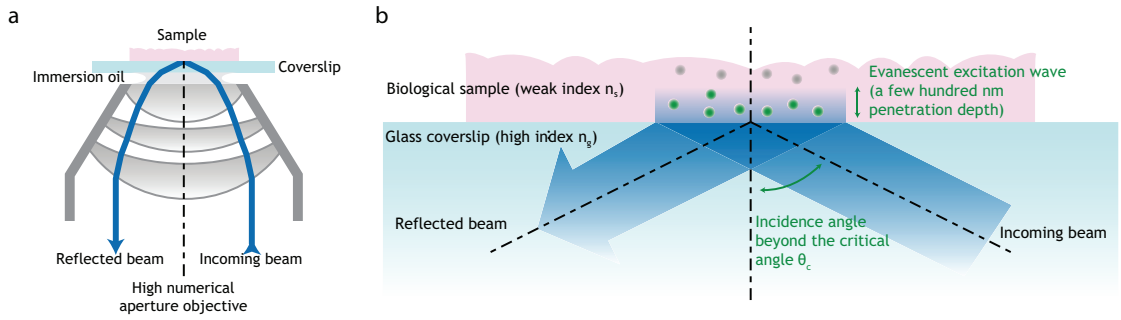

Figure 1.8 – Principle of Total Internal Reflection Fluorescence microscopy. **(a)** Excitation configuration. **(b)** Creation of the evanescent excitation in the sample. Source: adapted from the PhD manuscript of Nicolas Bourg [1].

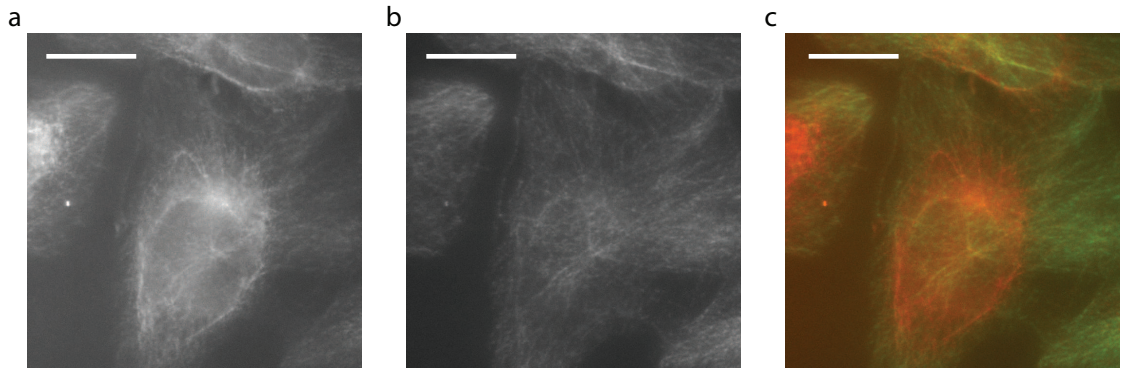

Figure 1.9 – Illustration of the optical sectioning obtained in TIRF on fixed COS-7 cells with the α-tubulin labelled with Alexa Fluor 647. The epifluorescence **(a)** and TIRF **(b)** images of the same field are displayed, as well as the merging (red: epifluorescence, green: TIRF) of the two **(c)**. Note that the TIRF sectioning results in a background suppression. Besides, the nuclei, which are located a few µm in the volume, are not visible on the TIRF image. Scale bars: 20 µm.

interfering beams or a grid placed in the excitation path. This allows a transposition of the spatial spectrum of the object: the spatial frequencies are translated to the edges of the spectrum. On the camera, the image observed is the convolution of the modified object pattern and the transfer function of the microscope. This transfer function is axially dependent: in the focus plane, its spectrum is wide enough to transmit the translated object spectrum, but far from the focus plane, it is not sufficient, and most of the out-of-focus signal is thus lost. In other words, only the light coming from the focus plane is not discarded. Nevertheless, even if they are not fundamentally incompatible, SIM is rather seldom used in combination with SMLM.

1.5 Experimental challenges

Although super-localisation microscopy is able to produce high resolution to observe the structure of samples well below the diffraction limit (see Fig. 1.10), it suffers from several sources of errors and biases that are likely to induce a degradation of the results if left

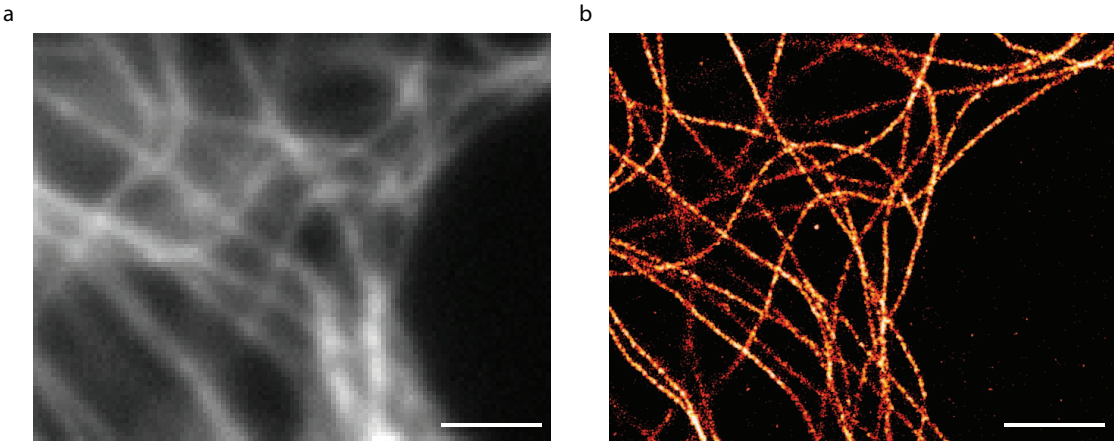

Figure 1.10 – Experimental results obtained with 2D SMLM. Fixed COS-7 cells were immunolabelled with AF647 on the α-tubulin and imaged in dSTORM conditions. The comparison between the wide-field diffraction-limed image **(a)** and the dSTORM reconstructed image **(b)** is illustrated.

uncorrected. The first source of error is the drift: as SMLM acquisitions are generally long (between 10 minutes and a few hours), they are subject to motions of the sample, even on fixed samples. They can be produced either by a poor mechanical stability of the stage on which the sample holder is placed, or by thermal fluctuations. Super-resolution experiments are extremely sensitive to these motions, which produce a blurring of the final image. If these motions cannot be eliminated by careful optical and mechanical design, they have to be tracked over time to enable their correction. This can be done using fluorescent markers, such as nanobeads or nanorods. These so-called fiducial markers are distributed in the sample and illuminated with either the same source as the sample itself or a different. Their positions are localised over time, which provides the drift curve that has to be subtracted from the localisation list. However, this method is not very practical, as these marker are subject to photobleaching in long experiments, not to mention that they require a modification of the sample preparation protocol, which is not always possible. Another solution is to track the motion of the reconstructed sample itself: the acquisition is divided in temporal slices and the shifts between the super-localised intermediary images are measured thanks to a cross-correlation algorithm [11]. The interpolation of these measurements yields the drift curve, as illustrated in Fig. 1.11.

Aside from lateral motions, axial drifts may also occur. In 2D SMLM, no axial information is retrieved, so fine tracking of axial drift is not necessary. Still, the position of the imaging plane should be roughly maintained, with a stability below the depth of field. If the mechanical stability is not sufficient, an active locking system may be necessary. Some microscopes are equipped with such a system, that uses the reflection of an infrared beam on the coverslip to track the axial motion and correct it thanks to the piezoelectric actuator on which the objective lens is mounted.

Another potential source of error is the polarisation of the fluorophores. Indeed,

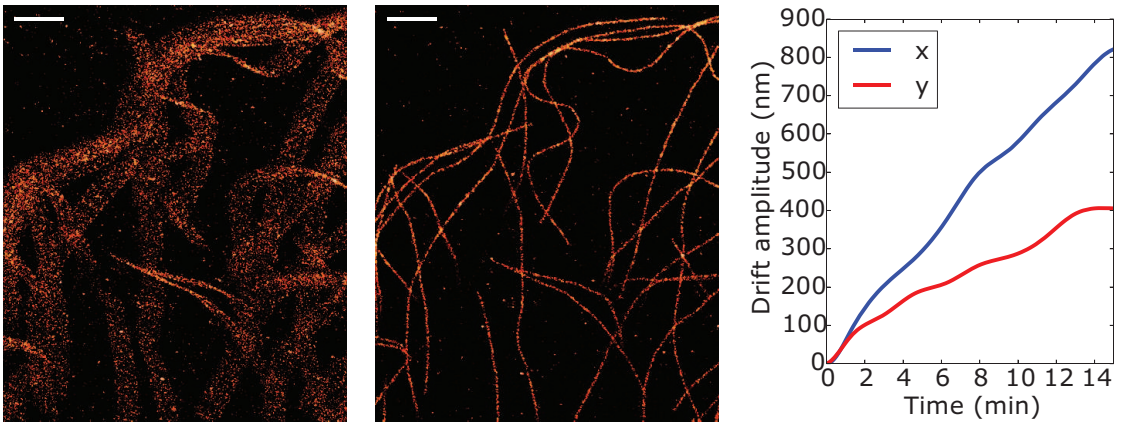

Figure 1.11 – Effect of the lateral drift in a dSTORM experiment (COS-7 cells, α-tubulin labelled with AF647) The uncorrected 2D super-localisation image (left) displays a clear drift over the acquisition, associated to a large resolution loss, whereas the corrected (centre) maintains an optimal resolution. The right panel shows the drift curves measured for this acquisition. Note that the curve seems rather smooth, and that, as the stage is not motorised, only low frequencies are present. Scale bars: 2 µm.

the fluorescent molecules behave like dipoles, which emit light directionally rather than isotropically. This induces translation of the apparent PSF relative to the centre of the emitter, which results in a bias of the localised position. The value of this bias can be huge, up to 150 nm for defocused PSFs, and cannot be corrected easily as it requires knowledge of the polarisation of each molecule. Fortunately, most labels have a certain degree of freedom in translation and rotation around their binding point and diffuse locally over a time scale far below the integration time of the camera. This results in an averaging of the polarisation for each recorded PSF, with errors below 10 nm for a rotation cone half angle inferior to 60° [12].

It should be noted that in some cases, fluorescent labels exhibit a low rotational degree of freedom, which results in polarised PSFs. The polarisation angle can thus carry useful information about the local structure of the imaged sample. This was reported in [13], where the local polarisation of the membrane labels is used to probe the membrane topography thanks to a dedicated detection setup. This can be used in SMLM to obtain polarisation information at the single molecule scale, for instance to determine the orientation of actin in stress fibres, as well as microtubules and DNA [14].

Errors and biases can further stem from issues related to the labelling itself. First, the recorded image corresponds to the spatial distribution of the fluorescent labels rather than that of the targets themselves. In the case of fluorescent proteins, this is rarely problematic since the distance to their targets is of the order of a few nm, i.e. well below the localisation precision. However, in the case of immunolabelling (which is very common in dSTORM or DNA-PAINT), the size of the label (i.e. the construction with the primary antibody, the secondary antibody and the fluorescent probe itself) is typically around 10–15 nm. Such a size can be noticeable given the levels of precision accessible in dSTORM

and DNA-PAINT. For example, on a microtubule, this creates a broadening of the apparent cylinder, with diameters above the expected values [15]. This is not necessarily a major problem if the size of the label is roughly known, but it has to be taken into account in order to relevantly analyse the localisation results. Several alternative labelling methods are being developed to tackle this problem by using shorter linkers: one can cite in particular click chemistry reactions [16], HaloTags, SNAP-tags and nanobodies [17–19].

Similarly, the labelling density plays an important role in SMLM experiments: if it is not regular and dense enough, it may not faithfully reflect the structure that is to be imaged, which can appear patchy for instance. This problem is generally tackled through optimisation of the labelling protocol. For instance, in the framework of immunolabelling, the choice of the antibodies plays an important role, as some are not as specific as others. The concentration of antibodies and the incubation conditions are also crucial parameters.

Finally, independently of the labelling itself, the single molecule regime is defined by the density of PSFs per frame. All localisation-based super-resolution approaches intrinsically rely on the hypothesis that isolated spots can be distinguished and characterised individually to extract specific information about each emitter. If too many molecules are active simultaneously, PSFs may overlap, which is bound to induce mislocalisations. While overlapping PSFs can sometimes be identified and discarded via software analysis of the localisations: for instance, a spot might display too large a width, or an unusual aspect ratio between the x and y widths, or even too bright an intensity[6]. Still, this obviously induces a detrimental loss of localisations. Besides, not all mislocalisations can be detected, and the final localisation list is bound to be altered if the single molecule regime is imperfect[7]. On the contrary, too low a density of fluorophores increases the required acquisition time, thus making experiments more sensitive to drifts. In PALM, the density of active molecules per frame is controlled through the photoactivation rate, which is defined by the near-UV light power sent to the sample. In dSTORM, controlling the density of molecules is more difficult; still, it can be changed to some extent by optimising the excitation power, as well as the composition of the chemical buffer. Finally, in DNA-PAINT, it can be changed thanks to a simple modification of the density of imagers in the imaging buffer, or an optimisation of the excitation power. The impact of the density of molecules per frame is highly dependent on the technique used, and will be assessed in part 3.3 for a particular case.

[6] If the frame rate is high enough to sample the emission over several frames, temporal fluctuations may also be distinguishable.

[7] Alternative super-resolution methods have been developed to circumvent the problems of density of active molecules per frame. Non-localisation-based approaches perform especially well here: one can mention Super-Resolution Radial Fluctuations (SRRF) [20], which is based on a sub-pixel calculation of the 2D intensity gradient to produce a radiality map. The radiality is a measurement of the gradient convergence, and contains significant information about the spatial distribution of emitters. Super-resolution Optical Fluctuation Imaging (SOFI) [21] is another possibility: it is based on the analysis of the higher order temporal fluctuations of the fluorescence emission. As neither SRRF nor SOFI rely on the single molecule regime hypothesis, they are particularly suited for dense labels imaging. Both achieve better resolutions than PSF fitting methods in high density regime [20, 22].

1.6 Three-dimensional Single Molecule Localisation Microscopy

Even though SMLM proves a very powerful tool in many cases, it lacks axial information to efficiently assess the structure of the colocalisation of different species inside biological or material samples. Indeed, lateral information is a priori insufficient, as axially separated species can appear superimposed on 2D images for example. Hence there is a need for complementary axial information. In some cases, it can be obtained through software-based analysis, but most of the time it requires dedicated excitation and/or detection optical setups. Unlike optical sectioning, 3D super-localisation methods are generally intrinsically based on single molecule analysis, and cannot be used in diffraction-limited wide field microscopy. Three major categories can be distinguished: PSF shape measurement, interferometric and phase measurement strategies, and near-field and interface effects.

1.6.1 PSF shape measurement

The lack of axial information stems from the fact that the PSF is not sampled in the axial direction as it is in the observation plane; on the contrary, the recorded PSF is a slice of the 3D PSF. Nevertheless, each spot contains axial information encoded in its shape (see Fig. 1.3b), simply due to the defocus: the wider the spot, the farther the molecule from the focus plane. However, the axial dependence of the width is almost symmetric relative to the focus plane, which does not allow effective axial measurement—positive defoci cannot be distinguished from negative, and the localisation precision is extremely degraded close to the focus[8]. The first approach is thus to sample the PSF axially thanks to measurements performed in different observation planes at different axial positions: this is called multifocal plane microscopy, or multifocus microscopy. Although the number of imaging planes can be arbitrary, only two are necessary to effectively break the axial symmetry of the detection. A schematic of the biplane implementation [24] is shown in Fig. 1.12a: the fluorescence collected by the objective is simply separated in two parts thanks to a 50/50 beam splitter, and the tube lenses form the images on two different cameras. One of the cameras is slightly shifted (by a distance typically around the depth of field, i.e. 400 nm approximately) in order to image a different focus plane than the other. As a consequence, each spot has different sizes on the two recorded frames depending on the axial position of the emitter (see Fig. 1.12b). Thanks to software analysis, it is possible to measure the size of each PSF on each frame and to calculate the corresponding depth thanks to previously acquired calibration data obtained using objects placed at known heights (the axial calibration will be more thoroughly discussed in part 2.1). Eventually, this method allows 3D imaging over an axial capture range around 500 nm–1 µm with axial precisions down to 15–20 nm for dSTORM organic dyes. It

[8] Some information can still be extracted from the PSF, for instance using the TRABI (Temporal, Radial-Aperture-Based Intensity estimation) software-based method [23]. Although it does not make up for the axial symmetry of the PSF, it allows the extraction of free information, insofar as no modification of the optical setup is necessary and the lateral performances are not degraded.

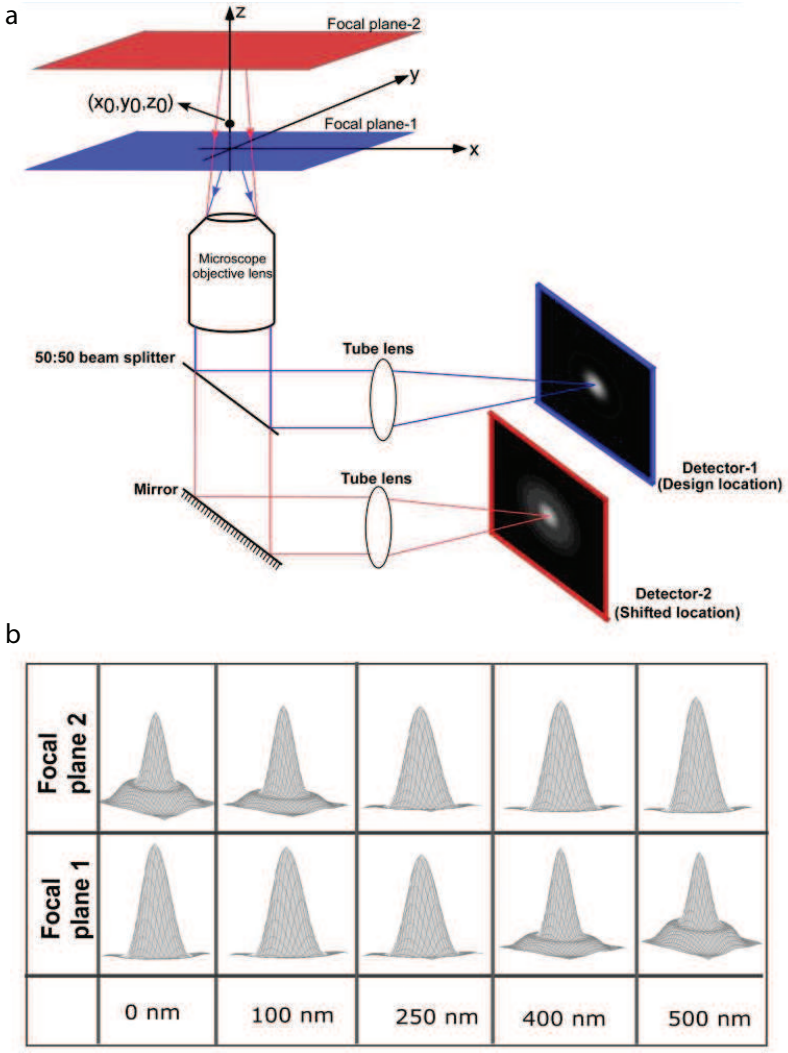

Figure 1.12 – Principle of biplane microscopy. **(a)** Optical setup used for the detection. **(b)** PSF shapes recorded on each camera for different axial positions. Source: adapted from Ram *et al.*, *Biophysical Journal* (2008) [24].

should be noted that the 3D localisation exhibits a noticeable anisotropy, as the lateral precision is typically around 5 nm for such fluorophores.

This principle can be generalised for any number of simultaneous imaging planes, the only limitations being the complexity of the setup and the splitting of the fluorescence signal, which causes a degradation of the localisation precision. In order to image multiple planes, the signal must be divided in different optical paths, either thanks to simple beam splitters [25] or with a custom fabricated diffractive element [26–28]. Even if multifocus microscopy can be somewhat cumbersome in terms of optical implementation, it offers uncommon imaging possibilities. In particular, it allows single acquisition 3D SMLM reconstruction of dense labels through whole cells. An example is presented in Fig. 1.13 with nine imaging planes: capture ranges around 4 µm and lateral and axial

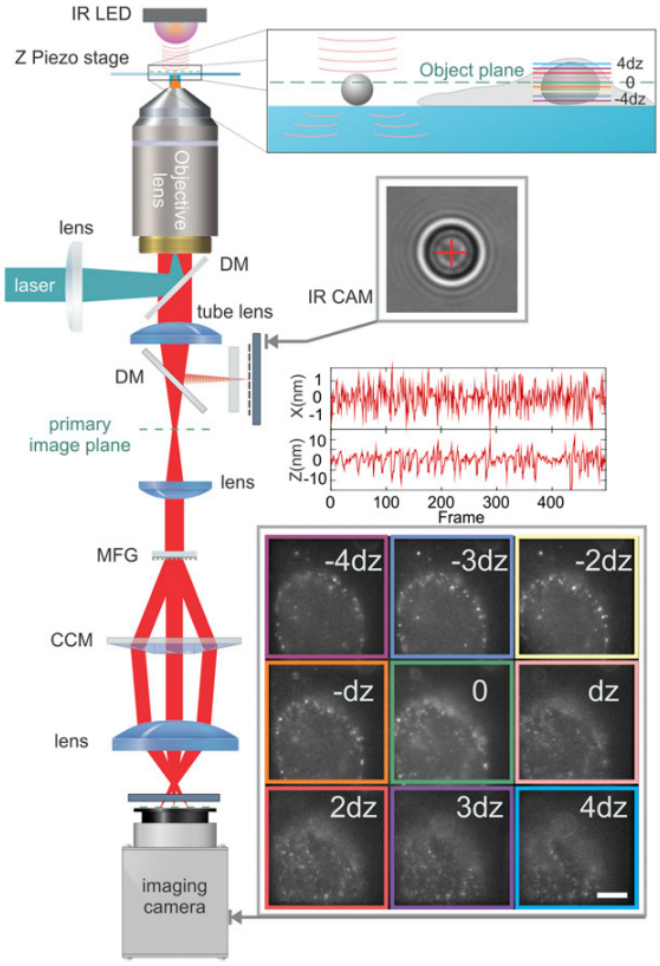

Figure 1.13 – Principle of multifocus microscopy. The sample is shone with a laser beam, and the fluorescence light is collected by the objective and sent to the detection setup. A diffraction grating (MFG) splits the fluorescence in nine focus-shifted paths arranged in a 3 × 3 array (only 3 beams are represented). Another phase grating (CCM) is used to correct chromatic aberrations. The bottom right inset displays the frame recorded by the camera, with the nine shifted planes. A drift tracking system is also implemented: it consists of in infrared LED, a dichroic mirror to separate the infrared light from the fluorescence, and a dedicated camera. The drift curves are displayed in the right inset. Source: Hajj *et al.*, *PNAS* (2014) [27].

precisions down to 20 nm and 50 nm are reported [27].

The axial sampling of the PSFs is not necessary, however, if they are not symmetric—i.e. if the shape of the spot recorded in an arbitrary imaging plane provides unambiguous information about the axial position of the source. This is not the case of the standard PSF, but it can be obtained through phase engineering of the fluorescence wavefront to shape the spots. This process is called PSF shaping, and it has various experimental implementations.

The first and most simple example is astigmatic imaging [29], which is obtained by

placing a cylindrical lens in the detection setup in order to create an astigmatism. This induces an elongation of the spots according to the position of the emitter relative to the focus plane. For example, molecules below the focus may produce horizontal spots while emitters above may generate vertical, and isotropic spots correspond to molecules near the focus. It is then necessary to analyse the recorded data and assess the shape of each spot. This can be done either thanks to a fitting with a model function (2D Gaussian, cubic spline, etc.) or to an evaluation of the best match with a PSF database, although it requires more advanced software methods. Muck like in the case of biplane imaging, the axial position is retrieved by comparing the measured PSF shape with the results obtained in previously recorded axial calibration data.

Other experimental implementations of PSF shaping include double helix PSF [30], corkscrew PSF [31], phase ramp PSF [32], self-bending PSF [33], and saddle-point and tetrapod PSFs of various kinds [34,35]. A common feature between these methods is their optical implementation, which is more demanding and more expensive than astigmatic imaging, as it requires the use of either a specifically designed phase mask, or a Spatial Light Modulator (SLM) placed in the Fourier plane to obtain the desired shaping of the fluorescence wavefront[9]. Still, they allow the optimisation of the performances for a specific purpose: they can provide optimal localisation precision or capture range for instance. Figure 1.14 presents a summary of these methods as well as a comparison of their capture ranges: axial precisions below 10 nm and capture ranges up to several µm can be obtained. It should be noted, however, that most of these shapes were theoretically designed to optimise the localisation precision and the capture range without taking into account the effective PSF size. As a result, some produce particularly large PSFs that makes them ideal for single particle tracking but unsuited for imaging of dense samples due to the risk of overlap between the different spots[10]. Finally, most are also multi-spot PSFs, which feature at least two spots per emitter, which brings challenges related to software analysis, as the processing code has to be capable of efficiently extracting all the information contained in the PSFs and identifying the clusters in order not to induce degradation of the lateral information.

A feature shared by all these PSF shape measurement methods (both multifocus and PSF shaping-based) is that the axial position is always measured relative to the focal plane. This raises different issues: first, the absolute position of the molecules is not known unless the position of the focus plane itself is precisely measured. This is generally not very problematic, as most biological studies only require colocalisation between different proteins. Still, it can be limiting in some cases where the position to the cover-

[9] A phase mask or an SLM can also be used to produce an astigmatic aberration. It generally creates a cleaner wavefront; still, it should be noticed that phase masks and SLMs generally provide strongly wavelength-dependent responses. This implies that the applied wavefront is optimised only for one particular wavelength, and that the deformation must be calibrated for each wavelength of interest.

[10] A relevant way to alleviate this problem is to use adaptive optics to generate a rather compact PSF at the beginning of the acquisition, and, as photobleaching induces a decrease of the active molecule density during the acquisition, switch to a wider PSF featuring a better capture range or localisation precision. Such a scheme was used by Aristov *et al.* in [36]: the shaping pattern was initially set to astigmatism, and then changed to saddle point PSF during the course of the acquisition.

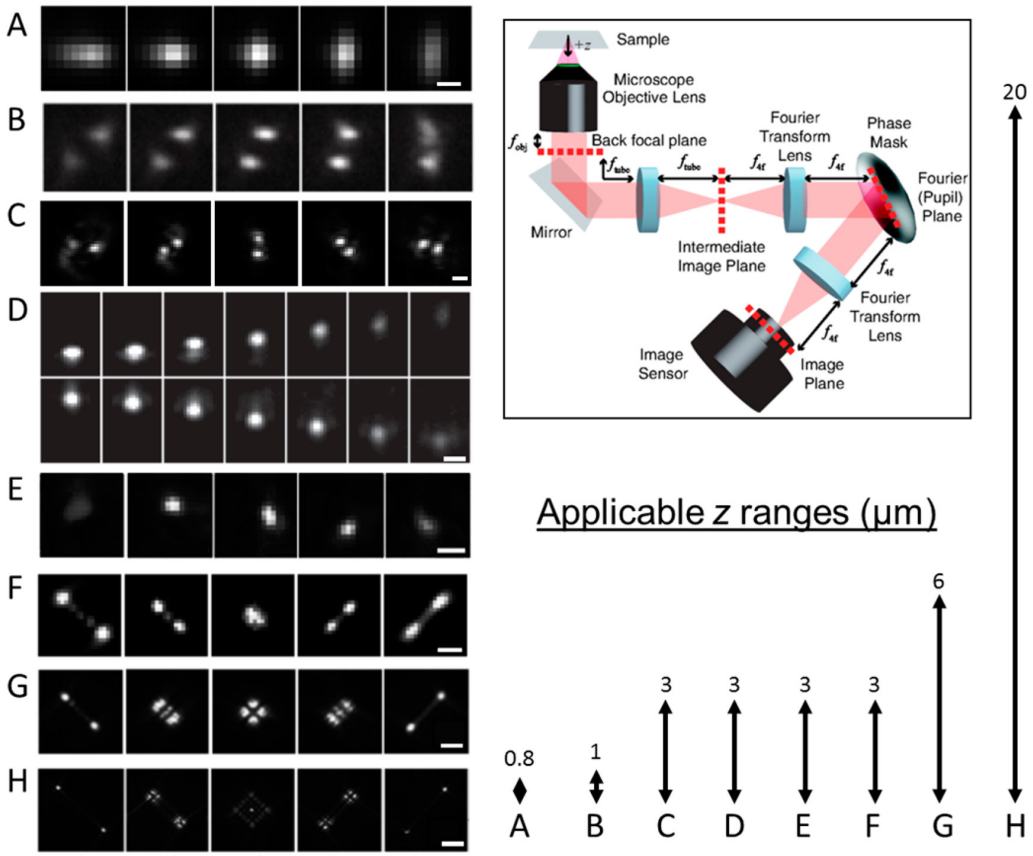

Figure 1.14 – Principle and implementations of PSF shaping methods. The typical phase mask- or SLM-based detection setup is displayed in the top right corner. The left panel shows the PSF shapes recorded for different axial positions of the emitter for the following methods: astigmatism **(A)**, phase ramp **(B)**, double helix **(C)**, self-bending PSF **(D)**, corkscrew PSF **(E)**, saddle-point **(F)**, 6-µm **(G)** and 30-µm **(H)** tetrapods. The axial capture ranges of the various methods are shown in the bottom right corner. Scale bars: 0.5 µm **(A)**, 2 µm **(C)**, 1 µm **(D–F)**, 2 µ **(G)**, 5 µm **(H)**. Source: Diezmann *et al.*, *Chemical Reviews* (2017) [2].

slip is especially relevant, such as in adhesion or motility studies (examples will be given in section 2.3): in these cases, one needs to precisely and accurately assess the position of the coverslip, for instance using fluorescent beads deposited on the surface.

Other problems stem from the fact that distances are only measured relative to the focal plane. For example, any axial drift of the objective lens or the stage on which the sample is placed, or any thermal fluctuation are likely to induce axial displacements of the focus plane, which results in a blurring of the structures, much like in the case of lateral drift illustrated in Fig. 1.11. If different fluorescence wavelengths are used, axial chromatic aberration may also be involved, simply due to the dispersion of the optical elements in the detection path (especially the objective lens). The chromatic aberration induces a wavelength-dependent axial bias, highly detrimental in colocalisation experiments. Finally, if the sample is not placed perfectly perpendicular to the imaging plane, a tilt may be visible on the reconstructed 3D data—such a detection bias can be difficult

to decorrelate from the structure of the sample itself. Even though issues can be tackled using fiducial markers deposited on the surface coverslip, such a method can prove problematic in some cases. Indeed, fiducial markers are subject to photobleaching as well as chromatic aberration, not to mention that they impose constraints on the preparation that are not compatible with all samples[11]. In chapter 3, we will illustrate and measure the effect of these non-idealities in typical dSTORM experiments, and propose an alternative correction method that uses the very fluorescent labels as references, and thus does not require fiducial markers.

One last limitation of PSF shape-based methods is linked to unwanted optical aberrations. They can stem from poor optical alignment of the detection setup or non-idealities of the optical elements. They can further be caused by the index mismatch between the glass coverslip and the sample medium, which results in spherical aberration. Finally, they can be due to inhomogeneities of the sample. This is all the more problematic as the sample is imaged deep in volume, which eventually limits the imaging range of PSF shaping to a few µm[12]. Aberrations can also vary through the field of view, or through the axial direction. In any case, unwanted aberrations induce deformations of the PSF that result in axial detection biases if unaccounted for. A part of these aberrations can be taken into account in the calibration (this will be more thoroughly explained in section 2.1), but field-varying and axially-varying aberrations are especially difficult to make up for.

1.6.2 Interferometric methods and phase-encoding

The second category of axial single molecule detection methods relies on phase encoding of the axial position through interferometric detection. The first demonstrated experimental implementation was the so-called interferometric PALM (iPALM) [38]. Fig. 1.15 displays the principle of the technique: the fluorescence is collected by two opposed objective lenses and superimposed thanks to a dedicated beam splitter. This creates interference between the two beams over a short range (due to the short coherence length of the fluorescence light), which results in an axially modulated fluorescence intensity for each spot. For the purpose of measuring the phase associated to each PSF, it is necessary to perform a demodulation step that requires at least three measurement points. In other words, three images of the same field are necessary. This is provided by the beam splitter, which separates the fluorescence in three 33 % intensity output paths imaged on separate cameras. Due to the optical path difference undergone by the three paths inside the beam splitter the phase is shifted by a $2\pi/3$ between the different images. This sampling of the axial interference pattern allows the measurement of the axial positions of fluorophores

[11] In the particular case of axial drift, the correction can be corrected without resorting to fiducial markers. Indeed, the motion can be tracked very much like the lateral drift, as described in section 1.5 and Fig. 1.11. This is done by dividing the localisation list in temporal slices and cross-correlating the reconstructed partial images allowing 3D displacements. This sample-based 3D drift correction algorithm reported by Aristov *et al.* [36] does not require addition of fiducial markers to the sample.

[12] The imaging range can be enhanced through the use of adaptive optics to make up for sample-induced aberrations [37]

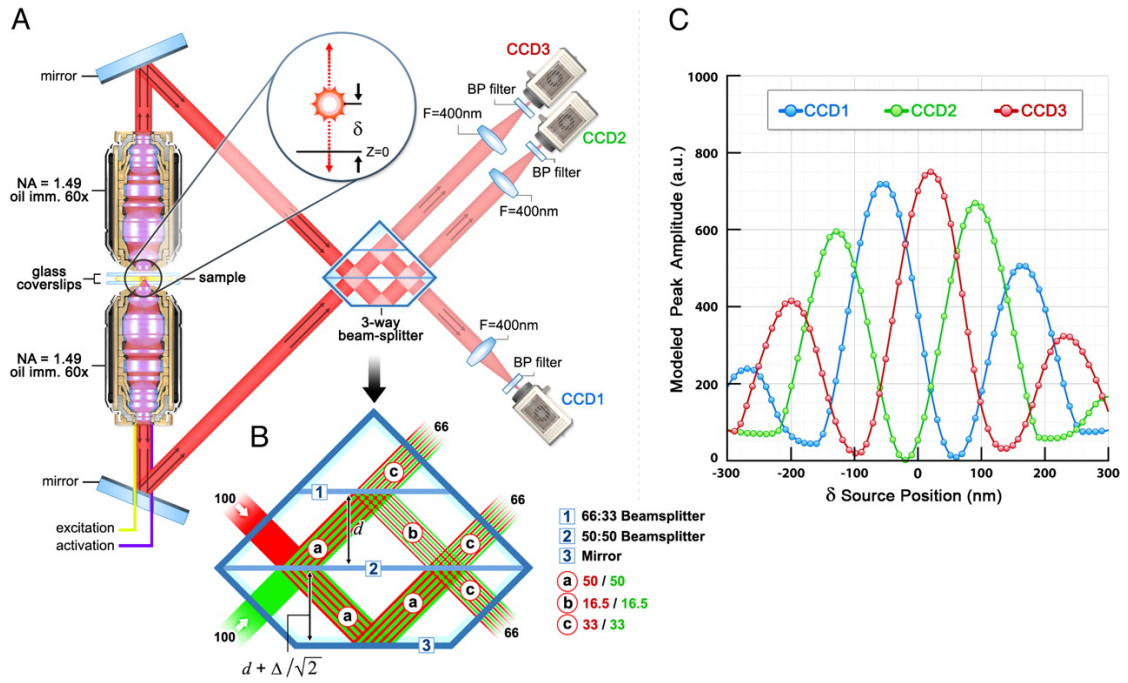

Figure 1.15 – Principle and implementations of iPALM. **(A)** Optical setup used for the excitation and the detection. **(B)** Schematic of the beam splitter used to recombine the two incoming fluorescence beams and create three phase-shifted outputs. **(C)** Intensities measured on each camera versus the axial position of the emitter. Source: Shtengel *et al.*, *PNAS* (2009) [38].

over a 250-nm capture range with axial precisions down to 10 nm with fluorescent proteins. Even if the axial sensitivity remains unrivalled, the method is strongly limited by its capture range, which stems from the wrapping of the phase. Besides, the optical setup is one of the most complicated reported in 3D SMLM. It relies on the use of a custom-made beam splitter, and requires extremely careful alignment in order to match both the path lengths of the beams collected by the two objectives, and to adjust the angles of incidence at the entrance of the beam splitter. Even with a careful alignment of the optical paths, the system remains very sensitive to any source of error, especially thermal fluctuations or mechanical axial drifts. Active feedback systems may be required to correct these unwanted motions in real time during the acquisition. Finally, the response is fluorescence spectrum-dependent, and requires characterisation for each wavelength that is to be used.

Although interferometric intensity-based measurement is a very powerful tool to evaluate the position of fluorophores, the fabrication and alignment constraints imposed by iPALM are so demanding that alternative schemes have been developed. In particular, our group recently proposed an interferometric method called ModLoc (Modulated Localisation) [39–41]. It uses a tilted structured single-objective excitation to encode the axial position of fluorophores at the excitation rather than at the detection. This approach presents two major advantages: first, it does not require an expensive and alignment-sensitive dual-objective detection setup nor a custom fabricated splitting prism. Besides,

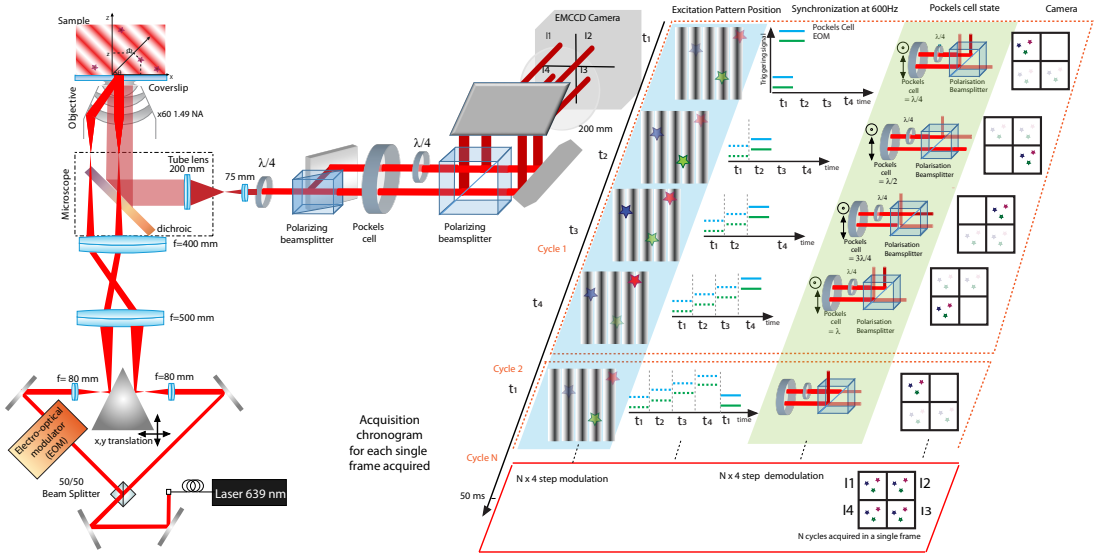

Figure 1.16 – Principle and implementation of ModLoc. The excitation relies on two coherent beams phase-shifted thanks to an electro-optic modulator. This results in a tilted illumination fringe pattern in the sample. The detection setup uses four pre-aligned channels with a variable transmission created by a system composed of a Pockels cell, a quarter waveplate and a polarising beam splitter. The transmission function is synchronised with the excitation modulation. Source: adapted from Jouchet *et al.*, (2019, submitted) [41].

the coherence of the fluorescence light is not a limiting factor, which unlocks the possibility to image in thick samples. The excitation is performed thanks to two beams displaying a phase shift $\Delta\phi$ created by an electro-optic modulator (see Fig. 1.16). In the sample plane, this creates a fringe pattern directed in the x-z plane with a known angle. The intensity of each molecule is thus modulated according to its position in the x-z direction. To obtain the position, the phase has to be retrieved through a demodulation, which requires intensity values for four different values[13] of $\Delta\phi$ spaced by $\pi/2$. The z position is finally calculated from the x position measured through Gaussian fitting on the one hand, and the position along the modulation direction. In order to account for the limited ON time of the emitters, the modulation is performed at high frequency (600 Hz), and the images corresponding to the different $\Delta\phi$ values are formed on four sub-arrays of the camera (with an exposure time equal to 50 ms). The detection setup is synchronised with the excitation frequency to distribute the signal on the four sub-arrays using a variable transmission produced by a Pockels cell. ModLoc achieves a weakly anisotropic 3D resolution, with axial localisation precisions down to 12 nm for AF647 fluorophores. More importantly, as the detection relies on intensity measurement rather than on centroid detection, it exhibits little sensitivity to optical aberrations. Thus, it is especially suited for deep and aberrating samples—imaging was demonstrated up to 30 µm depth.

Another approach consists in reading the phase of the fluorescence in the shape of the PSFs rather than in its brightness—indeed, the phase of the fluorescence beam

[13] The demodulation only requires three measurements, but four provides a better precision.

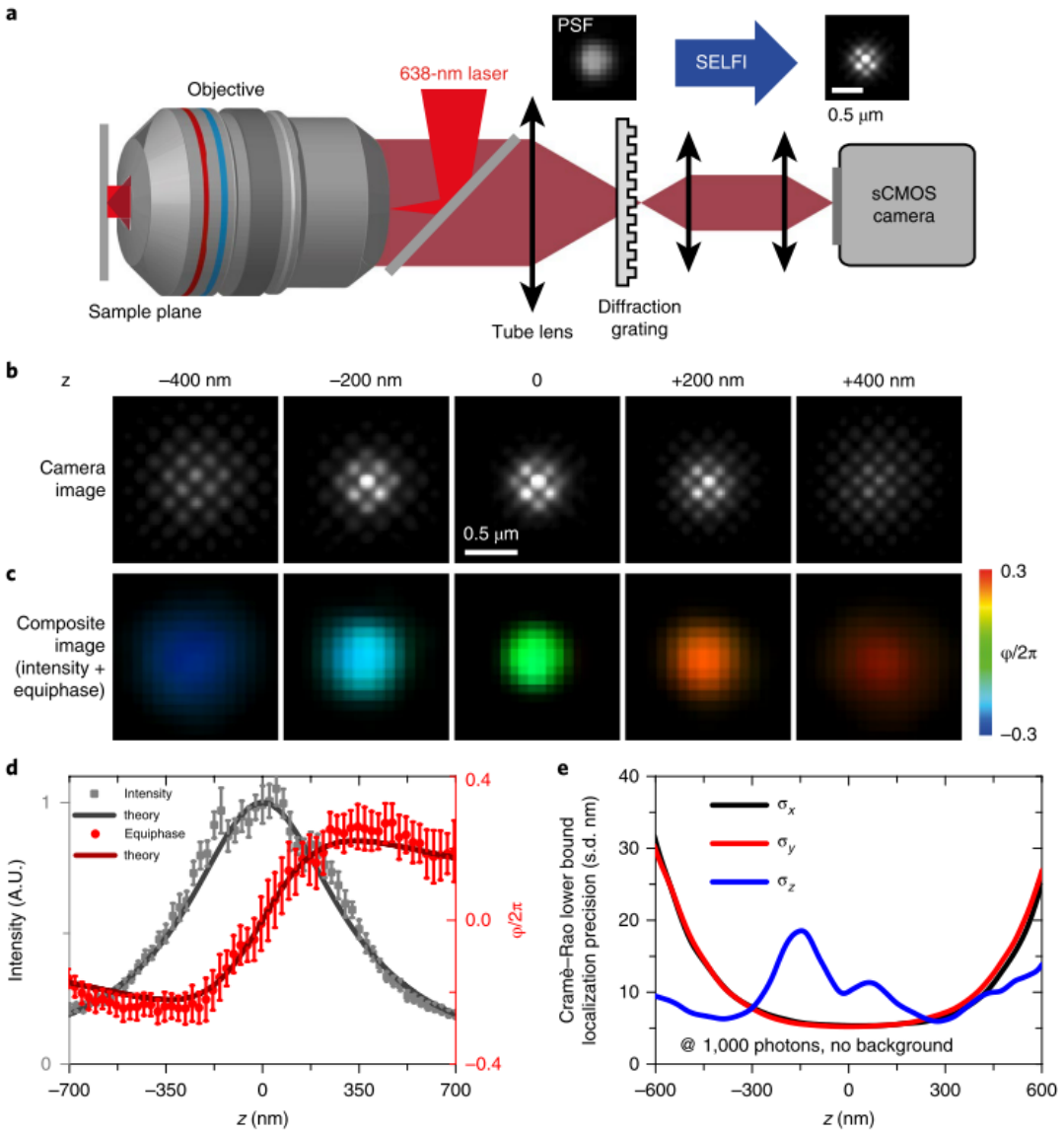

Figure 1.17 – Principle and implementations of SELFI. **(a)** Optical setup used for the excitation and the detection. **(b)** Interference patterns obtained for emitters at various depths. **(c)** Images of the phase and intensity distribution corresponding to the different positions of the emitter. **(d)** Intensity and phase versus the axial position of the emitter (note the symmetry of the intensity and the strong asymmetry of the phase). **(e)** Theoretical 3D localisation precision expected. Source: Bon *et al.*, *Nature Methods* (2018) [42].

exhibits a π phase shift around the focus due to the Gouy phase. This requires self-interference of the fluorescence, hence the name of the method (SELFI) [42]. It relies on the use of a custom-made diffraction grating placed in the detection system (see Fig. 1.17). The grating induces an interference pattern inside each spot, with a spatial frequency that depends on the axial position of the source. For each PSF, the spatial frequency is retrieved via Fourier analysis and compared to calibration data, which eventually provides precise depth measurements even in thick samples (axial precisions below

25 nm and 30 nm are reported on adherent cells and 40 µm in volume respectively).

In spite of their extreme precisions, all these methods remain subject to similar limitations as PSF measurement methods. In particular, the axial drift needs to be monitored and corrected in a post-processing step in order to avoid resolution loss. Sample tilts also have to be measured using fiducial markers. Besides, as the response of interferometric systems is intrinsically wavelength-dependent, chromatic aberrations are bound to occur, inducing axial biases. It should be noted, however, that unlike PSF shaping, interferometric approaches are not subject to sample-induced and field-dependent aberrations, which makes them especially suited for imaging deep in samples (except for iPALM, which remains limited by the coherence length of the fluorescence).

1.6.3 Supercritical Angle Fluorescence

The last 3D imaging method is based on the detection of a near-field effect occurring at the interface between two media of different refractive indices. This is very similar to the generation of an axially-varying evanescent wave in TIRF excitation due to the glass coverslip/biological medium interface. A very similar effect can arise at the detection rather than at the excitation: independently of the illumination pattern, fluorophores located in a biological medium emit both a far-field (i.e. propagative) and a near-field (i.e. evanescent) fluorescence components[14]. The intensity of the evanescent component quickly decays before it reaches the interface. Due to the higher refractive of the glass coverslip, the propagation conditions change at the interface: in particular, the complex wave vector associated to certain components becomes purely real. In other words, a part of the evanescent field becomes coupled into propagative waves when it reaches the interface. It then propagates beyond the critical angle—hence the name of this phenomenon, called Supercritical Angle Fluorescence (SAF). The supercritical angle light can be collected thanks to a high-numerical-aperture objective lens (see Fig. 1.18a). Due to the decay of the evanescent waves before they reach the interface, the SAF intensity exhibits a sharp axial dependence, while the far-field emission (also called Undercritical Angle Fluorescence, or UAF) does not depend on the axial position (see Fig. 1.18b–c). The axial dependence of the SAF intensity can thus be used to perform either optical sectioning or axial position measurement, depending on the experimental implementation (see sections 1.6.3.1 and 1.6.3.2). This, however, requires an optical separation of the UAF and SAF parts in order to extract and isolate the axially varying component of the fluorescence.

In order to discriminate between the two components, one can perform a filtering in the Fourier plane (in other words, a relay plane of the Back Focal Plane, or BFP): the UAF region corresponds to the central disk, while the SAF region is the outer ring[15]. This is illustrated in Fig. 1.18d. Due to the sharp decay of the SAF signal with the depth, this

[14] Fluorescent molecules can be modelled as dipoles to evidence this understand this effect.

[15] The diameter of the UAF disk is determined by the critical angle (which depend on the indices of the sample n_s and the glass coverslip n_g, whereas the diameter of the SAF ring is limited by the numerical aperture of the objective.

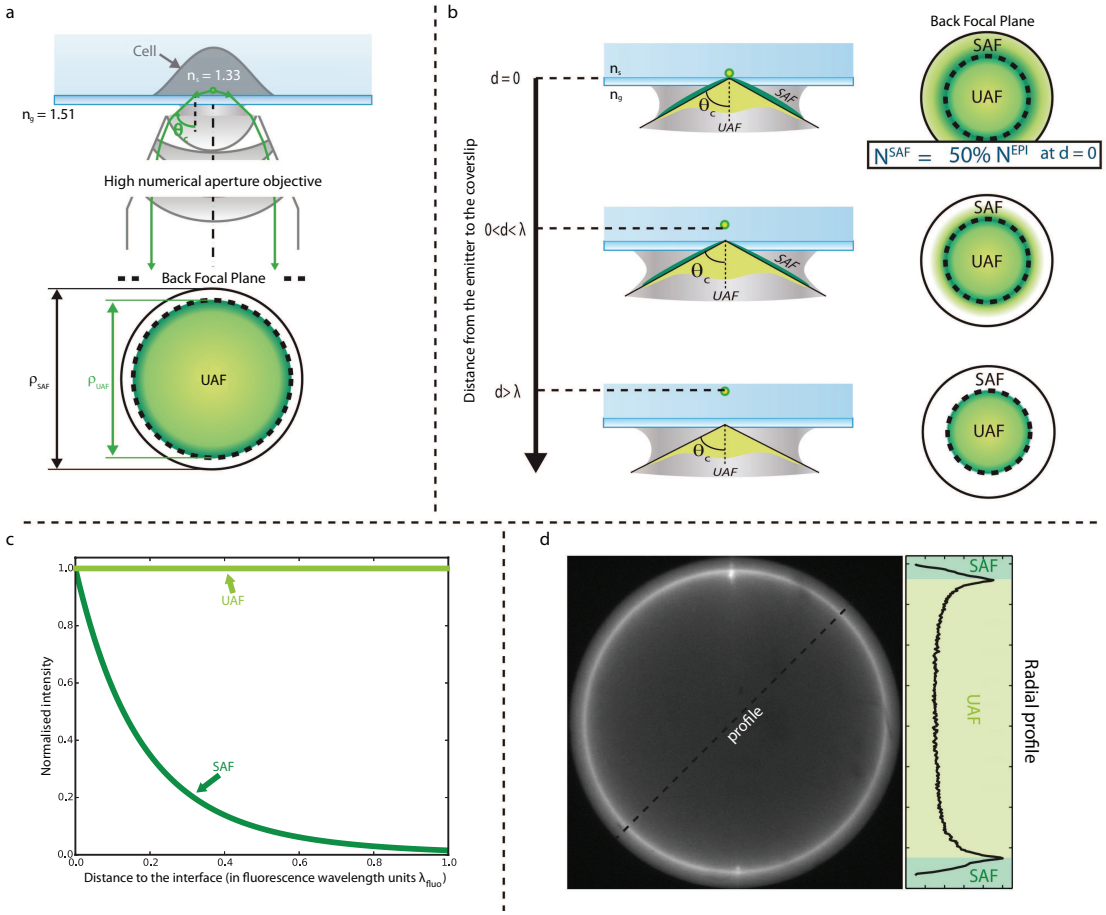

Figure 1.18 – Principle of SAF. **(a)** Optical setup used for the collection of the Supercritical Angle Fluorescence. In the Back Focal Plane of the objective, two regions are distinguishable: the central disk is the UAF region, while the outer ring is the SAF **(b)** Axial dependence of the SAF signal: the farther the emitter from the coverslip, the higher the dampening of the evanescent waves before they reach the interface. **(c)** Normalised intensities of the UAF and SAF signals versus the distance from the emitter to the interface (normalised as a fraction of the fluorescence wavelength). **(d)** Experimental intensity distribution in the BFP for a 1.49-numerical-aperture and refractive indices equal to 1.33 and 1.51. Note that the limit between the UAF and SAF regions is clearly visible on the radial profile. Source: adapted from the PhD manuscript of Nicolas Bourg [1].

detection is especially effective very close to the interface, but it is not suited for imaging beyond a few hundred nanometres.

1.6.3.1 Experimental implementations of Supercritical Angle Fluorescence microscopy

Unlike most axial detection methods presented in sections 1.6.1 and 1.6.2, SAF is not intrinsically limited to the single molecule regime. It was successfully applied to standard wide field microscopy for live cell imaging: it allows to simultaneously image processes occurring in the cytoplasm and at the membrane for instance [43]. This relies on the Di-

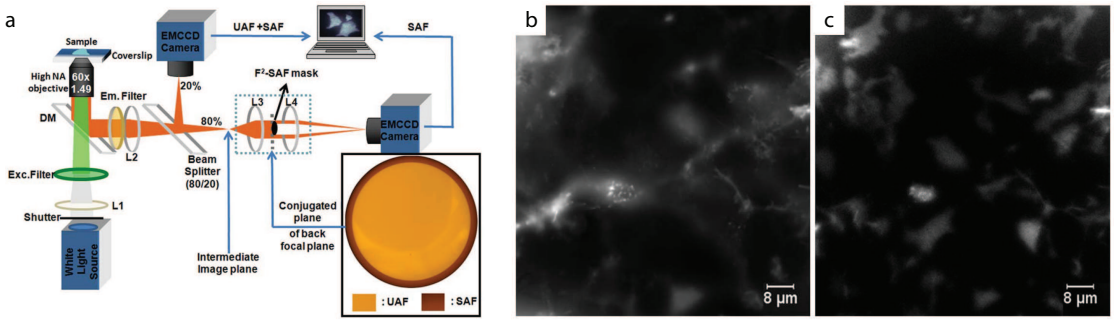

Figure 1.19 – Experimental implementation of the Direct SAF detection. **(a)** Setup used for the excitation and the detection. **(b)** and **(c)**: respectively EPI and SAF images of living HEK cells (HEK 293 cells transfected with type I cannabinoid receptors tagged with green fluorescent protein. Note the optical sectioning on the SAF image. Source: adapted from Barroca *et al.*, *Optics Letters* (2011) [43].

rect SAF (dSAF) implementation, which is probably the simplest way to perform the SAF detection experimentally (see Fig. 1.19a): the fluorescence light is separated in two parts thanks to a beam splitter, and one part is directly imaged on a camera. The other part is filtered thanks to a physical mask placed in a relay plane of the BFP[16] to remove the UAF component and finally imaged on a second camera. Two images are thus obtained: the first contains both the UAF and SAF components[17], which provides information emitted from all the volume of the sample (Fig. 1.19b). The second contains only the SAF information—i.e. fluorescence emitted only by fluorophores close to the coverslip. In other words, the filtering effectively produces an optical sectioning by removing fluorescence components emitted by fluorophores located in the volume of the sample (beyond a few hundred nanometres). This optical sectioning is clearly visible in Fig. 1.19c, where only the part of the membrane attached to the coverslip is visible, whereas deeper parts of the cells are also visible on the UAF image.

The dSAF strategy was also used in combination with a STED (STimulated Emission Depletion microscopy [44]) setup [45]: the illumination setup is a standard STED, and the detection uses a beam splitter to separate the fluorescence in two paths—one of them is directly imaged whereas the other is filtered with an amplitude mask placed in a relay plane of the BFP to remove the UAF component before being imaged. Muck like in the wide field dSAF implementation, the EPI and SAF are eventually imaged on the two separated detection channels; the only difference is that photodetectors are used instead of cameras to record the signals. In the STED implementation, the SAF detection brings a complementary sub-diffraction confinement of the detection. This results in an effective

[16] Experimentally, it is necessary to precisely align the mask in the relay plane of the BFP. This is done thanks to a Bertrand lens that is inserted in the detection setup to conjugate the BFP with the camera plane. Then, the position of the mask can be precisely adjusted both laterally and axially. Finally, the Bertrand lens can be removed to image the object plane on the camera. It is worth noticing that the diameter of the mask should match the position of the UAF/SAF boundary as accurately as possible in order to avoid any axial performance loss.

[17] The whole fluorescence, i.e. the UAF and the SAF, is also called epifluorescence (abbreviated EPI).

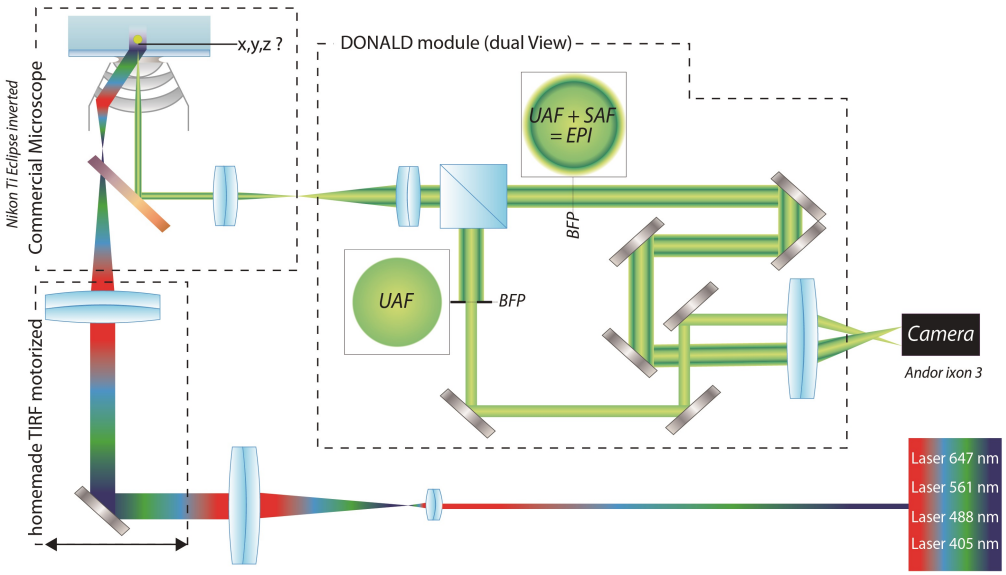

Figure 1.20 – Experimental vSAF setup. Source: adapted from the PhD manuscript of Nicolas Bourg [1].

optical sectioning, and thus an improvement of the 3D detection.

The dSAF detection scheme is not adapted in all cases, however: indeed, it can be counterproductive insofar as the SAF signal can be quite weak if the emitters are far from the coverslip. This is not problematic for optical sectioning, but it proves inefficient to calculate the axial position of the molecules in SMLM (see part 1.6.3.2), where the detection of the PSFs is crucial. Besides, the effective numerical aperture of the SAF signal alone is very low, and the associated PSF is broad, which results in a degradation of the lateral resolution—both in wide field imaging and SMLM. To circumvent these issues, an alternative approach was proposed by Barroca *et al.* [46]. It relies on an indirect measurement of the SAF signal, hence the name of the method virtual SAF (or vSAF). More precisely, instead of filtering out the UAF components to obtain the SAF signal, the opposite detection scheme is used: the SAF signal is removed thanks to a filtering in the BFP with a ring-shaped mask. As the epifluorescence image is also recorded (the optical setup used is presented in Fig. 1.20, and will be described more precisely in part 1.6.3.2 for the SMLM implementation of the vSAF approach), two fluorescence components are acquired: the EPI on the one hand, and the UAF on the other hand. Then, the SAF can be extracted by subtraction between the two images. Still, it should be noted that this is not strictly equivalent to a dSAF measurement. This can be understood by writing the epifluorescence emission as the sum of the UAF and SAF electromagnetic fields:

$$E_{\mathrm{EPI}} = E_{\mathrm{UAF}} + E_{\mathrm{SAF}} \tag{1.5}$$

where E_i is the complex amplitude of the i component of the fluorescence electromagnetic field.

The images recorded are the EPI and UAF intensities:

$$\begin{aligned} I_{\mathrm{EPI}} &= |E_{\mathrm{UAF}} + E_{\mathrm{SAF}}|^2 \\ &= |E_{\mathrm{UAF}}|^2 + |E_{\mathrm{SAF}}|^2 + 2\mathcal{R}\left(E_{\mathrm{UAF}} + E^*_{\mathrm{SAF}}\right) \end{aligned} \tag{1.6}$$

$$I_{\mathrm{UAF}} = |E_{\mathrm{UAF}}|^2 \tag{1.7}$$

where $\mathcal{R}$ stands for the real part.

Consequently, the difference between the EPI and UAF images reads:

$$I_{\mathrm{EPI}} - I_{\mathrm{UAF}} = |E_{\mathrm{SAF}}|^2 + 2\mathcal{R}\left(E_{\mathrm{UAF}} + E^*_{\mathrm{SAF}}\right) \tag{1.8}$$

whereas the SAF image recorded in the dSAF implementation reads:

$$I_{\mathrm{SAF}} = |E_{\mathrm{SAF}}|^2 \tag{1.9}$$

Compared to the dSAF, the vSAF image comprises an additional term $2\mathcal{R}(E_{\mathrm{UAF}} + E^*_{\mathrm{SAF}})$, which represents the interference between the SAF and the UAF parts of the fluorescence emission. This brings a major improvement, first in terms of effective numerical aperture—the vSAF PSF is thus much narrower compared to the SAF PSF[18]. Besides, it is also much brighter due to the contribution of E_{UAF}. As a result, the vSAF image is much less noisy compared to the SAF obtained in wide field microscopy, and it exhibits a much better lateral resolution. The principle of the vSAF detection and the improvement brought compared to the dSAF implementation are illustrated in Figure 1.21.

1.6.3.2 DONALD

The vSAF configuration greatly improves the performances in wide field imaging by providing superior image intensity and lateral resolution while maintaining the optical sectioning. These enhanced capabilities also prove useful to perform 3D SMLM through SAF detection. Here, both the goal and the requirements are slightly different from the wide field implementation. Indeed, the axial dependence of the SAF signal is not to be used for optical sectioning, but rather for axial localisation: by measuring the SAF signal recorded for each molecule, it is possible to determine its axial position. Obviously, this requires the ability to detect the SAF PSFs. As mentioned in section 1.6.3.1, the dSAF configuration is ill suited for this purpose, as the SAF PSFs are especially difficult to detect due to their low intensities and broad sizes. This would result in either vastly degraded lateral and axial localisation precisions, or simply localisation losses (dim PSFs are bound not to be detected by the localisation algorithm). For the purpose of 3D SMLM, the vSAF configuration is much more relevant, as both the EPI and UAF PSFs are expected to be

[18] The vSAF PSF is very similar to the EPI PSF in terms of effective numerical aperture (i.e. in terms of PSF width).

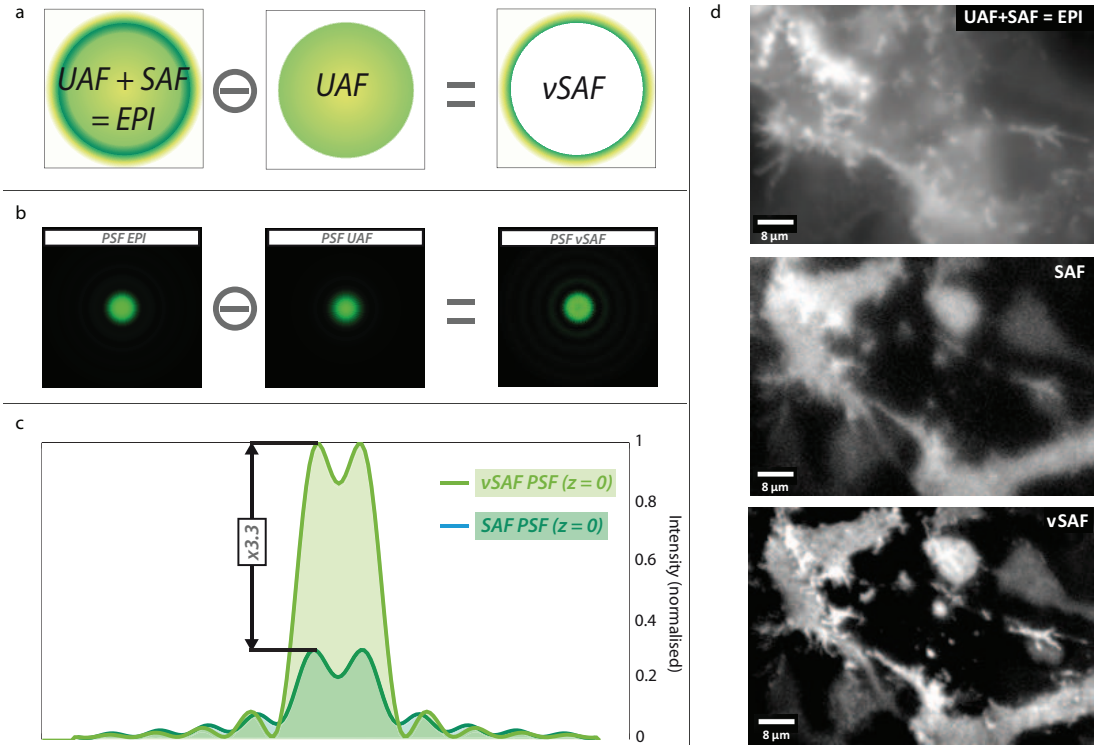

Figure 1.21 – Principle of the vSAF detection. **(a)** Fluorescence components used (in the BFP) for the EPI, the UAF and the vSAF images. **(b)** Corresponding lateral PSFs. **(c)** Comparison between the dSAF and the vSAF PSFs. Note the improvement brought by the vSAF in terms of PSF brightness and width (the tails of the vSAF PSF are much dimmer than those of the SAF PSF). **(d)** Comparison between the EPI, dSAF and vSAF images obtained on the same field (HEK cells with GFP-labelled membrane). Much like the dSAF, the vSAF image shows a clear optical sectioning, but its lateral resolution is vastly enhanced. Source: adapted from the PhD manuscript of Nicolas Bourg [1].

bright and narrow enough to be detected, even for molecules located relatively far from the coverslip and thus featuring low SAF signals. This was done by Bourg *et al.* [47], as well as by Deschamps *et al.* [48]. In this manuscript, we will take the work of Bourg *et al.* as a reference—the technique was called Direct Optical Nanoscopy with Axially Localised Detection (DONALD).

The typical experimental setup used was presented in Fig. 1.20: the excitation setup is a standard wide field illumination comprising four laser lines for dSTORM imaging and a TIRF stage[19], very much like the 2D SMLM setup presented in Fig. 1.7. The detection setup comprises a 50/50 beam splitter to separate the fluorescence light in two parts: one of them is directly imaged on one half of the camera—it thus produces the EPI image. The other is filtered thanks to a physical mask placed in the relay plane of the

[19]The TIRF optical sectioning can appear somewhat redundant with the SAF detection, but the two modalities are perfectly compatible. As the SAF signal dwindles to almost zero for molecules far from the coverslip, their fluorescence signal is unwanted. Therefore, TIRF sectioning at the excitation is expected to improve the performances by reducing the background produced by out-of-focus molecules.

BFP to block the SAF component, and imaged on the other half of the camera to form the UAF image according to the principle of the vSAF configuration.

As mentioned previously, the purpose of the SAF detection in DONALD is not to perform optical sectioning, but to measure the axial position of each molecule to achieve SMLM. In order to calculate the axial position of a fluorophore, it is necessary first to measure the numbers of SAF and UAF photons for each molecule, and second to have knowledge of the dependence of the SAF signal on the axial position to the coverslip. The measurement of the SAF and UAF photons is performed by running a dedicated localisation algorithm on the recorded data. In our case, we use a home made Python script to run the processing workflow described in part A.3.1. First, the spots are localised using an intensity lower threshold. Then each PSF is localised thanks to a Gaussian fitting to assess its lateral position (x,y). The correspondence between the EPI and UAF PSFs is found by searching for the nearest neighbour, and the lateral positions detected on the EPI and UAF frames are recombined to improve the lateral localisation precision. Then, the numbers of EPI and UAF photons are measured through an intensity integration: this provides the EPI and UAF numbers of photons N^{EPI} and N^{UAF}. These steps are sequentially performed for each acquired frame of the series, which provides a localisation list containing the values of x, y, N^{EPI} and N^{UAF} for each PSF on each frame. Finally, the lateral drift is corrected (see section 1.5, Fig. 1.11).

The last step is to use the measured values of N^{EPI} and N^{UAF} to calculate the axial position of the molecule. The axial dependence of the fluorescence intensity is contained in the so-called SAF ratio:

$$\rho^{\mathrm{SAF}} = \frac{N^{\mathrm{EPI}} - N^{\mathrm{UAF}}}{N^{\mathrm{UAF}}} \tag{1.10}$$

As the number of EPI photons reads $N^{\mathrm{EPI}} = N^{\mathrm{UAF}} + N^{\mathrm{SAF}}$, the SAF ratio also corresponds to:

$$\rho^{\mathrm{SAF}} = \frac{N^{\mathrm{SAF}}}{N^{\mathrm{UAF}}} \tag{1.11}$$

Both N^{SAF} and N^{UAF} are dependent on the brightness of the molecule, but the ρ^{SAF} is not, as it is a normalised quantity. On the contrary, the SAF ratio is determined only by the axial position of the emitter and the fluorescence wavelength[20]—more precisely, it follows an almost exponential decay with the distance to the coverslip (see Fig. 1.22). Once ρ^{SAF} is known, it is matched to the theoretical curve[21] (black dash-dotted line in Fig. 1.22) to retrieve the corresponding axial position.

[20] The SAF ratio also depends on the numerical aperture of the objective and the refractive indices of the sample and the glass coverslip, but these are constant values.

[21] The theory predicts an almost exponential decay with the axial distance to the coverslip. This is closely linked to the exponential decay of evanescent waves—the sharpness being defined by the imaginary part of the wave vector. Still, it should be noted that, in the case of DONALD, several angle components (each associated to a different characteristic decay distance) are summed over the SAF angle domain, hence the slight deviation to the purely exponential decay.

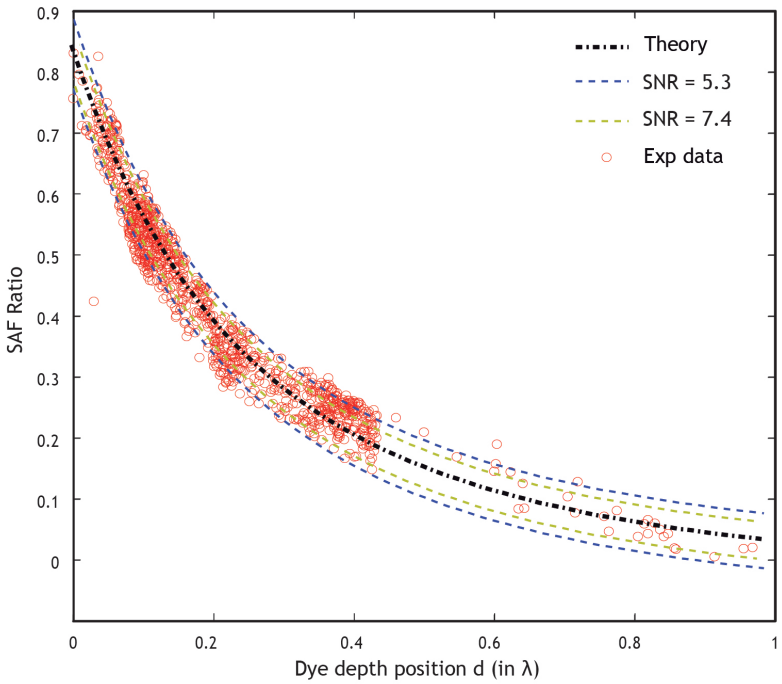

Figure 1.22 – Evolution of the SAF ratio with the depth. Both the theoretical expectation and the experimental verification are displayed. Source: PhD manuscript of Nicolas Bourg [1].

Several experimental factors have to be taken into account when calculating the axial position, though. First, the decay is spectrally dependent, and thus the fluorescence wavelength has to be known. Second, the theoretical curve displayed in Fig. 1.22 is valid for a given objective numerical aperture, and for given coverslip and sample indices. If these values are not measured accurately enough, or if the mask size aperture does not perfectly match the UAF part in the back focal plane, axial biases are bound to occur, as described in Fig. 1.23. Although the biases remain moderate for the relatively large inaccuracies considered in Fig. 1.23, they have to be taken into account. Therefore, it is necessary either to measure them precisely, or to apply correction factors to make up for slight discrepancies of these values (this will be described more thoroughly in section 3.1.2). It should be mentioned here that the index of the sample is not homogeneous a priori: indeed, although fixed samples are immersed in imaging buffer, biological structures themselves can be expected to have very different indices. This results in a complex series of transitions between evanescent and propagative behaviours through the light path. In practise, however, the SAF detection seems to behave as in a homogeneous medium of fixed mean index, which is bound to be very close to that of the immersion buffer.

Another potential source of error is the vectorial behaviour of electromagnetic waves. More specifically, if the fluorescence light is polarised, lateral detections may be inaccurate, as reported in [12], with biases as large as 150 nm over one capture range. Similar biases are bound to arise in PSF-shape-measurement-based axial detections since

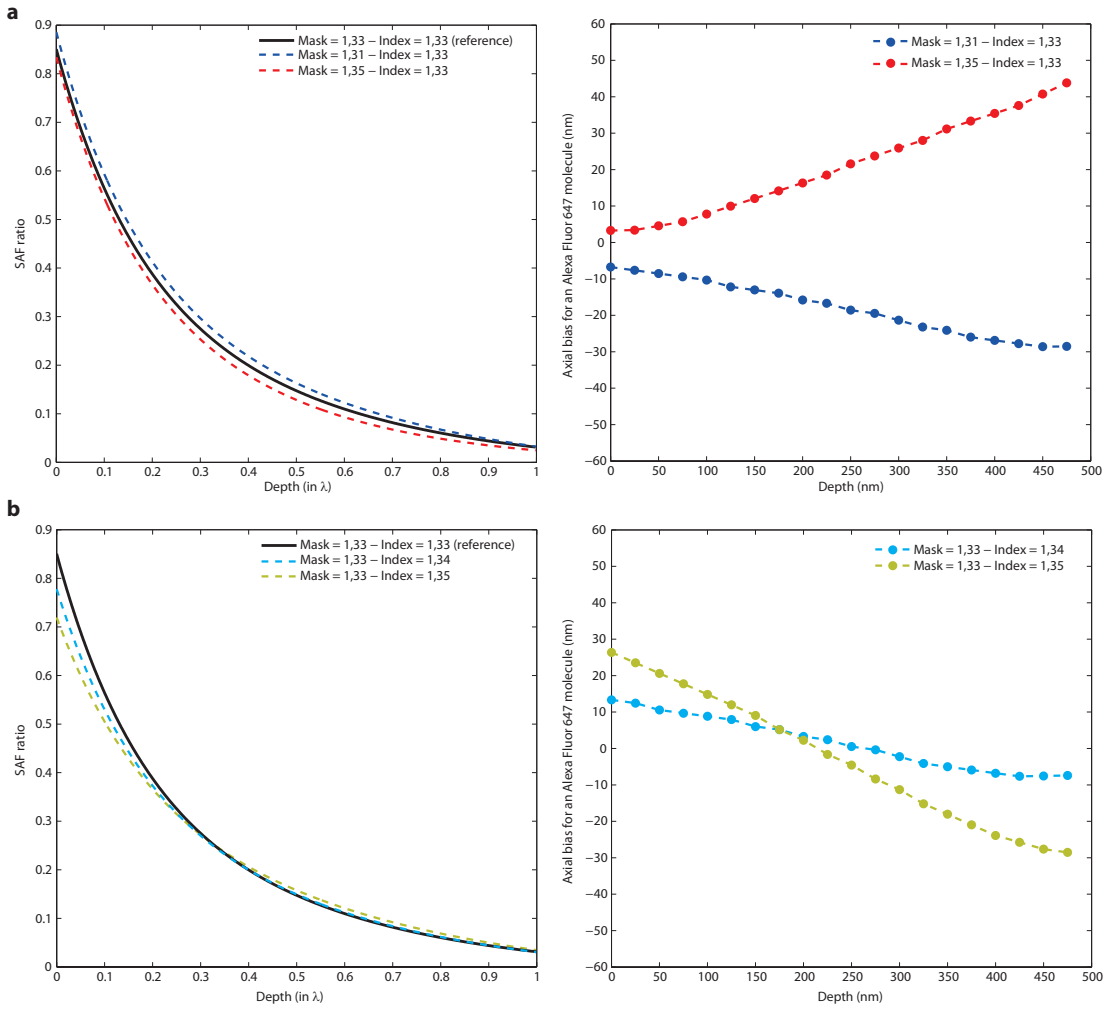

Figure 1.23 – Axial biases induced by mask size **(a)** or index **(b)** inaccuracies. The left panel shows the dependence of the SAF ratio with the depth for different indices and mask apertures, while the right panel displays the subsequent axial bias. Source: adapted from the PhD manuscript of Nicolas Bourg [1].

the PSF shape is highly dependent on the polarisation of the fluorescence—although this problem is seldom reported in the literature. Intensity-based axial measurements are also affected by polarisation effects. Indeed, the intensity distribution in the back focal plane is dependent on the angle of the emitter and the rotational degree of freedom of the fluorophore, as explained in [49]. Still, given the large amplitude of the biases expected from the results published in [12], one can reasonably assume that the rotational degree of freedom of the vast majority of the fluorophores is high, at least with dSTORM labelling—otherwise, 2D SMLM would not be possible. Therefore, axial biases can similarly be expected to be almost negligible in DONALD.

Provided these experimental non-idealities are adequately dealt with, DONALD thus produces 3D SMLM results thanks to the intensity-based SAF axial detection. Pre-

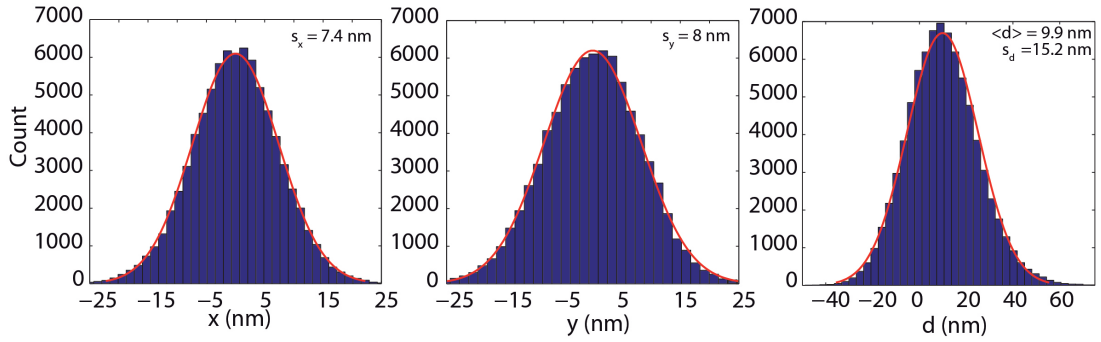

Figure 1.24 – DONALD experimental localisation precisions measured on 20-nm diameter fluorescent beads deposited on a coverslip. The excitation power was adjusted so that the number of fluorescence photons per bead matched that obtained for Alexa Fluor 647 molecules in a standard dSTORM imaging buffer. Source: PhD manuscript of Nicolas Bourg [1].

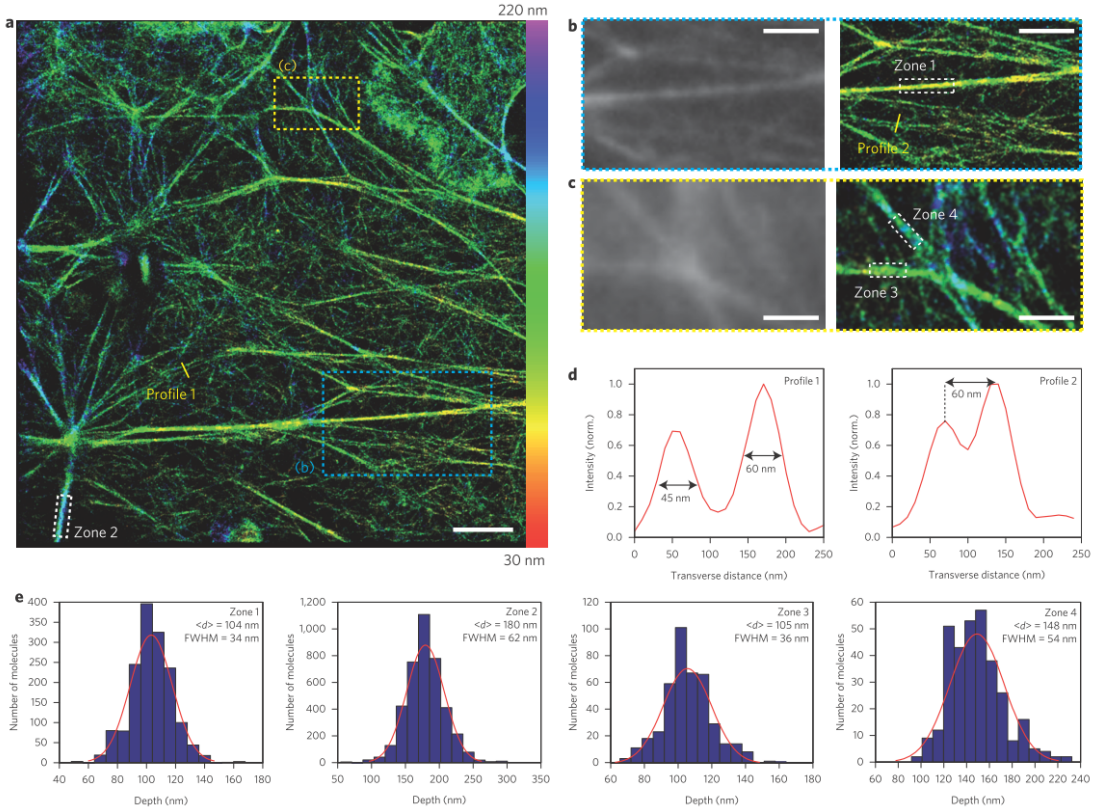

Figure 1.25 – DONALD imaging of the actin network in fixed cells (CHO cells labelled with phalloidin-Alexa Fluor 488) and measurement of the precision. **(a)** 3D DONALD image of a region of interest (the depth is colour-coded). **(b–c)** Diffraction-limited (2D wide field imaging) of the boxed regions in **(a)** and corresponding 3D DONALD sub-images. **(d)** Transverse profiles plotted along the lines labelled "Profile 1" and " Profile 2" in **(a)** and **(b)**. **(e)** Axial profiles plotted in the regions labelled "Zone 1" to "Zone 4" in **(a–c)**. The average depth and the full width at half maximum of the histograms are displayed for each zone. Scale bars: 3 µm **(a)**, 2 µm **(b)**, 1 µm **(c)**. Source: Bourg **et al.**, *Nature Photonics* (2015) [47].

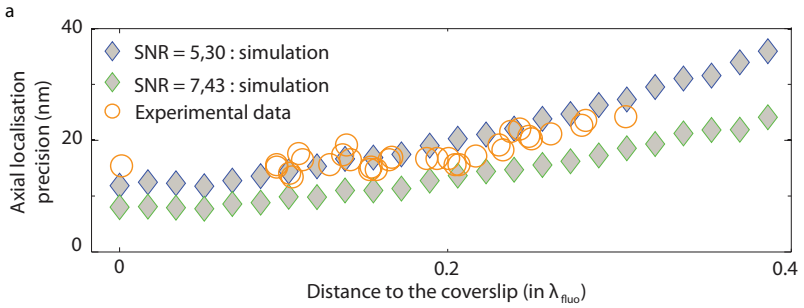

Figure 1.26 – Evolution of the axial precision with the depth of the emitter. Experimental results (obtained on 20-nm diameter fluorescent beads embedded in an agarose gel) are displayed, as well as simulated data for different Signal to Noise Ratios (SNR). Source: adapted from the PhD manuscript of Nicolas Bourg [1].

cisions down to 8 nm in the lateral direction and 15 nm in the axial direction were reported, both on fluorescent beads and on dSTORM-labelled biological samples, as illustrated in Figures 1.24 and 1.25. While the lateral precision slowly varies over the capture range as in standard 2D SMLM, the axial precision is optimal at the coverslip, where the SAF signal is the strongest, and then quickly deteriorates away from the coverslip (see Fig. 1.26)—thereby, DONALD is effective mostly below half the fluorescence wavelength, i.e. in the first 300 nm above the coverslip.

A particular feature makes DONALD somewhat unique among other 3D SMLM techniques: the axial information retrieved by the SAF detection is absolute, as it is intrinsically referenced to the coverslip. This is due to the decay of the near-field intensity before it reaches the glass coverslip/biological sample interface, where the index mismatch arises. In other words, the axial positions measured are independent on the position of the focus plane. Unlike PSF shape measurement and phase-encoding methods (iPALM, ModLoc, SELFI), DONALD is thus insensitive to experimental non-idealities such as axial drift, axial chromatic aberration and sample tilt (this was mentioned in section 1.6.1, and will be more thoroughly characterised in section 3.3). Consequently, DONALD proves more straightforward to use, as it requires fewer post-processing correction steps. This is highly advantageous, as some of those correction steps might require fiducial markers placed in the sample to be carried out, or might induce slight accuracy or precision losses if not perfectly corrected[22].

1.7 Conclusion

After an introduction to the principle and the advantages of fluorescence microscopy, we have stressed the fundamental resolution barrier raised by the effect of the diffraction.

[22]Note that DONALD might also present axial detection biases if either the size of the mask does not perfectly match the limit between the SAF and UAF regions, or the index of the sample is not accurately known. Nevertheless, these biases remain quite low, with values typically below 15 nm over a 300-nm imaging range (see [1], Figure 3.13). Besides, these sources of error only induce systematic biases without altering the localisation precision or the stability over time for instance.

We have then presented super-resolution methods as a means to circumvent this limitation. In particular, single molecule localisation strategies have been identified as powerful tools, not only to reconstruct high resolution images, but also to extract strongly specific complementary information about each detected molecule. We have exposed the photochemical processes available to achieve single molecule regime. Experimental issues linked to super-localisation acquisitions have been highlighted, from drifts to polarisation phenomena, as well as labelling and blinking questions, and solutions have been proposed to tackle or even exploit them. We have then introduced axial detection strategies to unlock three-dimensional single molecule localisation microscopy. This state of the art has allowed us to emphasise both the versatility of PSF shaping and multiplane methods, and the high performances of phase measurement approaches, especially in thick samples due to their resistance to sample-induced aberrations. Still, we have come to the conclusion that the two approaches suffer the same bottlenecks—experimental axial detection biases such as axial drift, chromatic aberration and sample tilt. Due to its insensitivity to these error sources, the absolute SAF detection has proven a sound alternative in this regard.

Because of its short capture range and its limitation to imaging near the coverslip, the SAF approach seems less general than PSF-measurement- and phase-based methods. Still, it appears especially suited in SMLM to provide an absolute reference that can be used to correct the axial detection biases inherent in relative methods. Such a coupling will be developed in chapter 3, which will be devoted to the combination of astigmatic and SAF detections for the purpose of making 3D super-localisation experiments more reliable and reproducible.

Chapter 2

Characterisation and applications in 3D SMLM

Having presented the framework in which this work finds its place, we will now present much more experimental considerations related to 3D SMLM. These points are nonetheless capital, all the more as they are rather scarcely documented in the literature available in the domain of super-localisation imaging. We will illustrate the description of the methods and protocols that we propose with experimental results, and discuss their relevance in 3D SMLM characterisations and applications.

More precisely, we will first tackle the question of axial calibrations: indeed, most 3D SMLM methods rely on the use of theoretical or experimental axial calibrations to provide the depth of each molecule from its measured characteristics. Obtaining such calibration curves is challenging, as it requires dedicated samples in order to avoid detrimental biases. We will propose a fully experimental sample-based method to perform such a calibration in a simple manner. Note that samples of known 3D geometry can also be used on already calibrated setups to verify the absence of biases.

Once the question of biases is addressed, we will deal with performance measurements. The performances of a method take into account the lateral and axial precisions, as well as its robustness to the previously mentioned error sources (see section 1.6.1). This is also an important step, as it defines the ability of a technique to produce reliable results with a sufficient 3D spatial resolution—in other words, it allows to a priori foresee if a specific application study can be performed, not to mention that it provides clues to interpret the localisation results obtained.

Eventually, we will present several studies that we carried out with the DONALD method in collaboration with colleagues from biology and chemistry teams. We will explain the interest of these applications and the experimental approaches used to perform the sample preparations and acquisitions. Finally, we will detail the processing codes developed to analyse the 3D SMLM data in these specific cases in connection with the previously mentioned non-ideality sources, and we will interpret the results obtained.

2.1 Axial calibration and biases

In all 3D SMLM approaches, the axial detection relies on the measurement of certain parameters of the PSFs that exhibit an axial dependence. In other words, information is extracted from the spots and the axial positions are calculated using the expected variation of this information with the depth. This requires knowledge of the axial dependence of the measured parameters, which can be provided by a theoretical model if the phenomenon producing the axial specificity is simple enough to be modelled reliably—this is the approach used for the iPALM method for instance [38]. In other cases, the model might be more complex and require realistic simulations to assess the impact of axially dependent processes on the PSFs characteristics. The DONALD curve used to convert the measured SAF ratio into axial distances was obtained following this scheme [47]. Nevertheless, the processes involved in the axial dependence of the PSFs are often too complex to be modelled: in these cases, the remaining solution is to perform axial calibrations using samples of known geometry or controlled motions of the optical system to produce the required axial shifts. This is the case in PSF shaping methods for example [29].

This calibration scheme is a very powerful approach insofar as it allows to account for non-idealities of the detection setup[1]. Still, such a calibration has to be performed and analysed carefully since experimental sources of error might alter the localisation results—for instance, axial drifts may induce biases in the final calibration characteristics if left uncorrected (see section 1.6.1). However, even if these non-idealities are accounted for within the data processing workflow, axial calibrations require the use of suited samples.

2.1.1 State of the art

Most of the time, axial calibrations are performed by using fluorescent beads or molecules deposited on a coverslip and scanning the objective with a piezoelectric stage to introduce defocus in the system [29]. While inexpensive and simple to perform, this method exhibits several drawbacks arising from the refractive index mismatch between the sample and the glass coverslip.

First, the distance over which the focus plane is moved is not equal to the displacement of the objective. In practice, this so-called focal shift effect produces a stretching of the apparent distances. Although theoretical formulae [50] and experimental protocols [51, 52] of various complexities are available to determine the value of the correction factor for different depth ranges, these methods are not sufficient to provide readily usable calibration data suitable for SMLM experiments.

Indeed, they do not account for the effect of spherical aberration on the PSFs. Such an aberration alters the shape of the spots and thus induces a bias in the axial positions detected through PSF shaping methods. Calibrations performed by scanning the objec-

[1] For instance, a cylindrical lens may not induce exactly the expected astigmatism amount, not to mention that it is bound to add to the wavefront other slight aberrations, which have an influence on the shape of the PSF.

tive do not allow to record the PSFs corresponding to a realistic experimental situation where the focus plane is fixed. Several techniques have been proposed to circumvent this issue, notably by numerical computation [53]. While it does not require a cumbersome experimental procedure, it does not fully correct the effect of spherical aberration. Deng and Shaevitz proposed a reliable experimental method using optical tweezers to axially move fluorescent beads relative to the object plane [54], at the cost of a major modification of the setup. Similarly, adaptive optics can be used to correct spherical aberration [55], but this requires expensive devices and induces a loss of photons.

Other effects may also alter the results of these calibration acquisitions. The size of the fluorescent probes imaged on the coverslip can contribute in some cases if they cannot be considered strictly point sources (see equation (1.2)). Organic dyes or fluorescent proteins display sizes below a few nanometres, which is obviously well below the Airy radius. Still, fluorescent beads are often used as well. As their diameter is typically between 20 nm and 100 nm, their image may be slightly different from a PSF—this is bound to induce biases in the calibration results obtained. Another factor that should be considered is the contribution of the SAF component to the PSF (see section 1.6.3): if the numerical aperture of the objective lens used for the detection is higher than the refractive index of the sample (which is the most common case in SMLM, as objective lenses commonly feature NA values around 1.49), a part of the SAF fluorescence is collected. This adds components in the Fourier plane and thus changes the shape of the PSF. However, this change is dependent on the axial position of the emitter relative to the coverslip: those located far deep in the sample produce spots close to the UAF PSF, while those in the vicinity of the coverslip rather produce spots close to the EPI PSF. This effect is detrimental when emitters deposited at the coverslip are used for the calibration, as all the spots recorded during the acquisition are EPI PSFs. This, again, is likely to induce calibration biases for molecules far from the coverslip. Fig. 2.1 displays the difference between PSFs acquired at the coverslip and in the volume of the sample to illustrate the influence of all the previously mentioned effects.

2.1.2 Principle of the calibration using coated microspheres

We designed a fully experimental, sample-based calibration method to provide unbiased calibration results that can be used for 3D SMLM measurements. In this protocol, all the axial information needed is provided by the known geometry of the sample, and the acquisitions are performed in the nominal conditions, i.e. for a given objective at a given position and for given sample refractive index and fluorophore emission wavelength. This protocol was published in *Optics Letters* in 2018 [56].

More specifically, we used 15.0-µm (± 1.5 µm) diameter latex microspheres decorated with Alexa Fluor (AF) 647 dSTORM dyes at their surface. The sample preparation protocol is detailed in section B.2. A similar sample was used in [52], but only in confocal microscopy to measure the focal shift. Likewise, microspheres were used in 3D superlocalisation by Juette *et al.* [57]—although for the purpose of assessing the performance rather than calibrating the axial detection. The interest of such a sample relies on the

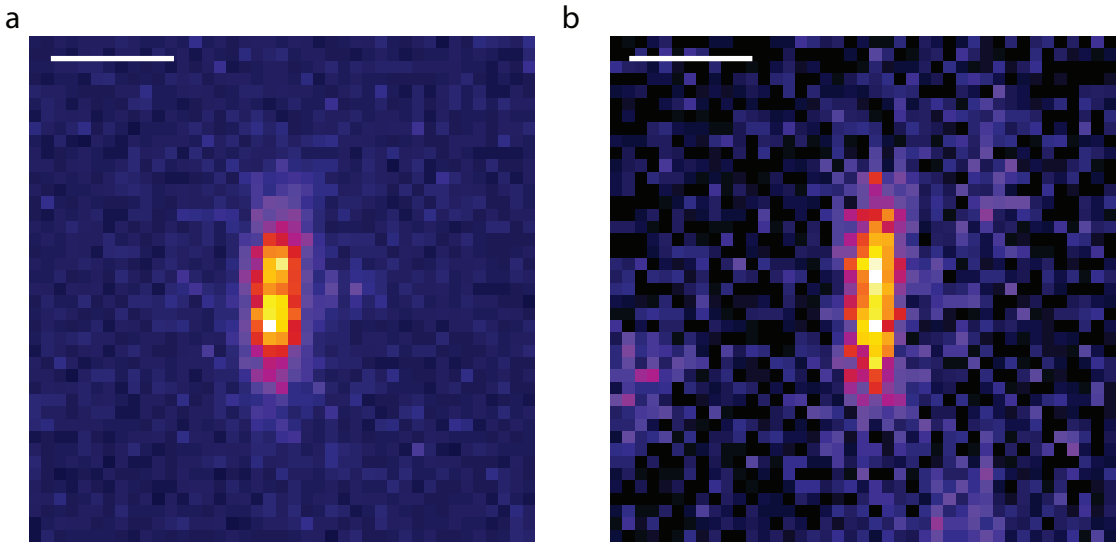

Figure 2.1 – Difference between experimental PSFs acquired from fluorescent beads at the coverslip and in the volume. The PSFs were acquired in the presence of a strong astigmatism aberration, with the source at the coverslip **(a)** or in 1 µm deep in the volume of the sample **(b)**. In both cases, the emitter was located 600 nm above the focus plane. Note that the PSF acquired at the coverslip exhibits two lobes, unlike that recorded in the volume. This is due to the effect of spherical aberration on the PSF shape. Scale bars: 1 µm.

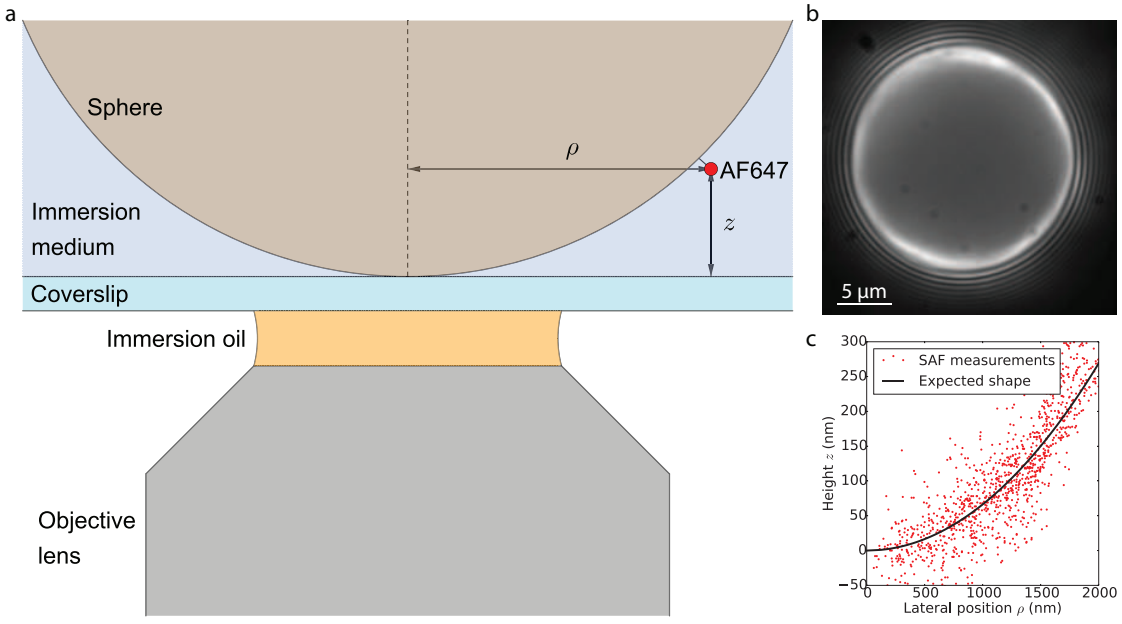

Figure 2.2 – Principle of the calibration protocol. **(a)** Schematic of the sample of coated microspheres deposited on a coverslip. **(b)** Raw diffraction limited wide field image of a microsphere acquired in its equatorial plane (used to determine the radius and the centre of the microsphere). **(c)** Depth profile detected with DONALD. The red circles correspond to the experimental data, and the black line stands for the curvature expected for a sphere of the measured radius.

fact that, once the lateral position of the centre (x_0,y_0) and the radius R of each microsphere are known, the depth of any molecule can be calculated from its measured lateral position (x,y) using the following equation (Fig. 2.2a):

$$\rho^2 + (R - z)^2 = R^2 \tag{2.1}$$

where $\rho = \sqrt{(x - x_0)^2 + (y - y_0)^2}$ is the lateral radial position to the centre of the microsphere. This directly gives the height z of the molecule assuming that only the lower part of the microsphere is imaged (which is reasonable since R is typically much higher than the depth of field of the system):

$$z = R - \sqrt{R^2 - \rho^2} \tag{2.2}$$

2.1.3 Experimental results

In order to characterise the sample and verify the accordance of our geometrical model with the actual shape of the sample, we first performed DONALD 3D acquisitions. We assumed that the SAF ratio curve was valid, and that DONALD could be used without calibration, which is a reasonable hypothesis considering that the SAF decay curve was experimentally verified (see Fig. 1.22). Thus, it provides a reliable method to verify the sample shape. As seen on the ρ-z profile (Fig. 2.2c), the microspheres exhibit the expected curvature in the probed area. Especially, they do not seem to significantly flatten out at the contact point with the coverslip.

Having verified the validity of the geometry of the sample, we carried out acquisitions to obtain the calibration curve of an astigmatism-based PSF shaping detection scheme. The aberration was created by a cylindrical lens added in the detection path with a spacing of approximately 800 nm between the two focal lines. The focus (average point between the two focal lines) was set at 400 nm beyond the coverslip. We performed dSTORM acquisitions according to the protocol detailed in section A.2 and processed the data using a home-written Python code to extract the x and y positions of each spot, as well as their widths w_x and w_y, via a gaussian fitting (as explained in section A.3). Both the lateral and axial drifts were corrected using a cross-correlation algorithm, and the lateral deformation of the image induced by the astigmatism was accounted for. The corresponding width map and ρ-z profile are presented in Figures 2.3a and 2.3b respectively. Using x, y, x_0, y_0 and R, we determined the value of the depth z of each molecule, which allowed us to plot the calibration curve (w_x, w_y) as a function of z. For the statistical pooling of the localisation data, we analysed three different microspheres for a total of approximately 20.000 localisation events. To reduce the influence of statistical uncertainties, the data was divided in 40 nm depth slices (using a sliding window pooling), each slice containing between 100 and 1.000 localised points.

As a comparison, we also conducted an acquisition on a sample of 20-nm diameter fluorescent beads deposited on a glass coverslip. The object plane was scanned through

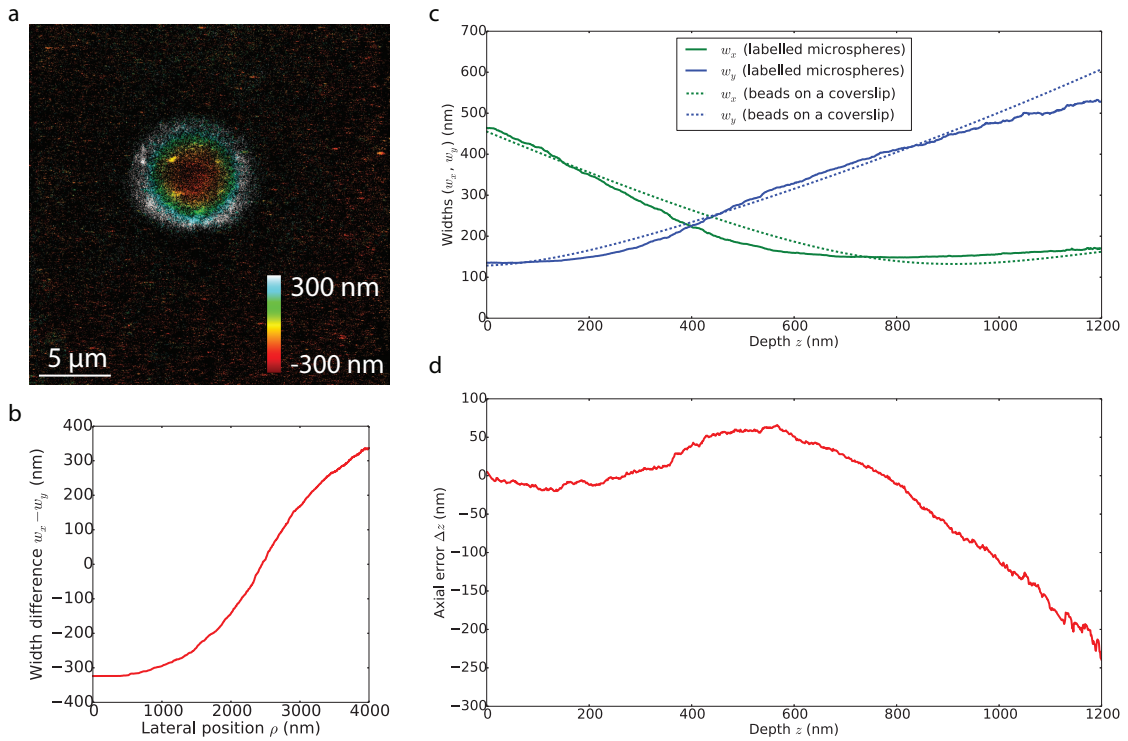

Figure 2.3 – Results obtained with the calibration protocol. **(a)** Colour-coded map of the width difference $\Delta w = w_x - w_y$ of the PSFs induced by the astigmatism. Note that the radius appears lower than in Fig. 2.2c since the depth of imaging limits the observation to a small portion of the sphere near the contact point with the coverslip. **(b)** Width difference Δw profile as a function of the lateral position obtained from the sphere displayed in **(a)**. **(c)** Calibration curve showing the widths w_x and w_y obtained by analysing the data acquired from the labelled microspheres sample as a function of the distance to the coverslip. The comparison with the method using fluorescent beads at the coverslip is also displayed. The abscissa of the latter calibration method was translated so that the two curves coincide at 10 nm depth with a focus at 400 nm (thus corresponding to the same experimental configuration). **(d)** Error made on the measured axial position when using immobilised fluorescent beads on a coverslip to perform the calibration, showing the difference between the two calibration curves displayed in **(c)**.

the sample by moving the objective by 25-nm steps thanks to a piezoelectric stage, and the axial positions were corrected in order to take into account the focal shift. For each position of the objective, 25 fluorescent beads were imaged over 200 frames to reduce the statistical fluctuations by averaging. In order to compare the two methods, this calibration curve was translated using a common reference: when the focus is set 400 nm deep in the sample, the aberrations are the same for the 20-nm fluorescent beads as for fluorophores at $z = 10$ nm with the calibration technique using the labelled microspheres. The abscissa was thus shifted so that the curve overlaps with the microspheres calibration curve at 10 nm depth, corresponding to the same experimental configuration.

Thanks to the previously described method, we obtained the calibration curve of the astigmatism and compared it to the method using fluorescent beads deposited on a coverslip (Fig. 2.3c), which yields significantly different results. Note that because the

experiment was performed in the nominal conditions, a single acquisition provides a calibration valid over the whole axial detection range of the instrument, namely 1.2 µm. The difference between the two methods is mainly due to the influence of spherical aberration arising from the index mismatch on the PSF shapes, which is not considered in the latter case. The resulting axial bias (Fig. 2.3d) proves to behave in a very non-linear way (especially, it is either positive or negative depending on the depth), reaching values as large as 200 nm over a 1200 nm range. Such a result is in agreement with previous studies quantifying the effect of spherical aberration in calibration experiments [53, 54, 58], both in terms of curve shape and magnitude.

To illustrate the importance of this difference, we performed measurements on a COS-7 sample labelled with AF647-phalloidin to image the actin network (Fig. 2.4a–b). The slice profile presented in Fig. 2.4c highlights the axial bias that arises from the effect of spherical aberration when using fluorescent beads immobilised on a coverslip to perform the calibration. The axial bias is even more clearly visible on Fig. 2.4d–e, where the localisation results are plotted for a centrosome aligned in the x-z plane. Centrosomes are expected to display an isotropic shape, which is the case with the microspheres calibration, while the calibration using fluorescent beads induces a noticeable ellipticity of the structure.

One of the key features of our technique is its precision, that makes it especially suitable for super-localisation experiments. The statistical uncertainty σ_z on the value of z calculated from equation (2.2) decreases as R increases. Indeed, the lower the local slope of the sphere surface, the lower the influence of the lateral localisation precision. As it is necessary to image a whole microsphere to measure its radius and centre, the optimal microsphere diameter one should choose to achieve the best precision is equal to the size of the field of view. Assuming that the centre and the radius positions can be estimated with precisions around 50 nm, a 15 µm diameter microsphere yields axial precisions σ_z down to 15 nm over a 1.2 µm axial range. It should be noted that since the number of localised molecules on the microsphere is around 20.000, the localisation precision has a much lower influence on the value of σ_z than any error on the measurement of the radius or the centre of the sphere.

2.1.4 Outlooks

This fully experimental method was published in *Optics Letters* in January 2018 [56]. It can be used to obtain the unbiased calibration curve of any PSF-shaping-based axial detection scheme in 3D SMLM. While it does not require any computation, device interfacing or modification of the optical setup, it accounts for both the focal shift and the effect of spherical aberration on the PSFs by performing acquisitions in the nominal experimental conditions, as all the axial information relies on the controlled geometry of the sample. These features make it suitable for a broad range of uses in SMLM as it could be used in dSTORM, PALM and (DNA-)PAINT. Aside from calibration of PSF shaping methods, this technique could also be used as a means of experimental verification of the performances of 3D SMLM techniques that require no calibration or are already

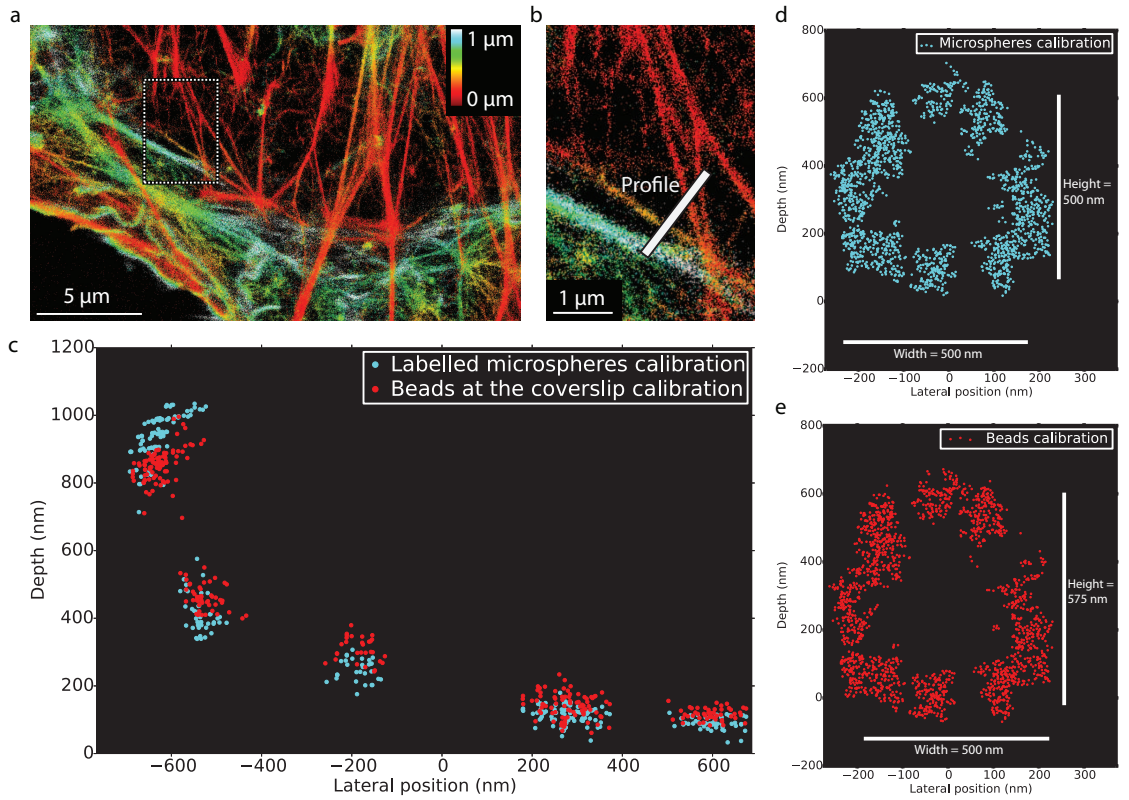

Figure 2.4 – Illustration of calibration biases on biological samples. **(a)** 3D (colour-coded depth) localisation image of actin labelled with AF647 in fixed COS-7 cells. **(b)** Zoom on the boxed region shown in **(a)**. **(c)** *x*-*z* profile of actin filaments along the axis displayed in **(b)**, comparing the two calibration methods. **(d–e)** Comparison of the 3D results using the two calibration methods on a centrosome along the *x*-*z* plane (CEP164 labelled with AF647, sample courtesy from Karine Monier, CRCL). Note the anisotropy of the structure with the calibration using fluorescent beads on the coverslip.

calibrated[2]. The method could be further improved by labelling the microspheres with several dyes to perform a calibration at different emission wavelengths (either sequentially or simultaneously), thus getting rid of the chromatic aberration influence, a major bottleneck for multiple colour/species 3D SMLM imaging. An interesting tool for this particular purpose is DNA-PAINT labelling: as reported in [59], DNA-PAINT docking sites can be attached on the biotin layer of the microspheres. The calibration acquisitions can then be performed sequentially with the different fluorophores of interest. Imaging the same beads to perform the multicolour calibration is a relevant solution since it eliminates the uncertainty on the measurement of the radius of the spheres as a potential source of slight bias.

[2]Moreover, as the use of the geometrical relation giving the axial position from the lateral information is not specific to single molecule experiments, the same type of sample could be used at wider depth ranges (up to several tens or hundreds of microns) with other imaging modalities, such as light-sheet microscopy, structured illumination, two-photon excitation or STED to calibrate the axial positioning for instance

2.2 Evaluation of the localisation precision

SMLM approaches are designed as imaging tools to perform 2D or 3D observations of relevant samples. This can be done in the framework of studies of biological processes or structures organisation and properties in material science. This can also find its use in the characterisation of fluorescent probes, fixation or labelling processes or even calibration samples that will later be used to verify the performances of other fluorescence microscopy methods. In any case, the performance of the method is capital information, as it defines its ability to effectively image the sample with sufficient precision to resolve the processes or structures of interest. The major factor defining the performances is the localisation precision[3], which is defined by four major points: the physical principle used to encode or extract the information (it determines the Fisher information available), the fluorescent molecules and the blinking regime (which define the number of photons per PSF, as well as the background amplitude), the optical setup (optical aberrations or camera noise, for instance, have some influence), and finally the software used to process the data and extract the information.

Aside from the localisation precision itself, the performance attainable in an acquisition also involves the stability of the setup, as instabilities (from mechanical, thermal or electromagnetic sources) are bound to cause a degradation of the resolution. In some cases, it may also depend on the label, and especially on its size, shape, degree of freedom and density. Finally, the measurement itself can sometimes induce a loss of information. In this section, we will tackle the question of the measurement of the performance of a method and propose different methods to decouple the influences of the different factors involved (localisation precision, stability of the setup, label geometry and measurement).

2.2.1 Theoretical expectation: Cramér-Rao Lower Bound

The simplest strategy to assess the localisation precision independently of the other parameters is perhaps to use a theoretical model. The main idea is to model the processes used to encode and retrieve the relevant information. This is done by defining the Fisher information matrix from the model—the Fisher matrix contains information about the statistical influence of the different parameters involved. Then, it is possible to derive a fundamental lower limit of the localisation precision, which is equal to the square root of the diagonal terms of the Fisher matrix [60]. This limit, called Cramér-Rao Lower Bound (CRLB), sets the best attainable precision[4] with a given method and for given signal levels (number of photons per PSF, number of background photons per pixel). It can prove a very powerful tool since it provides a priori knowledge about the expected precision for the method, provided simple and realistic models can be found for the PSFs (for instance isotropic 2D Gaussians) and the process used to extract the information (for example the difference between two photon counts in the case of DONALD). Examples of axial and

[3] The localisation precision σ is defined as the standard deviation of the distribution of the localisation positions when imaging a point source without any precision loss induced by drifts or instabilities.

[4] In this work, CRLB values will be expressed as localisation precisions, i.e. standard deviations of the position distributions.

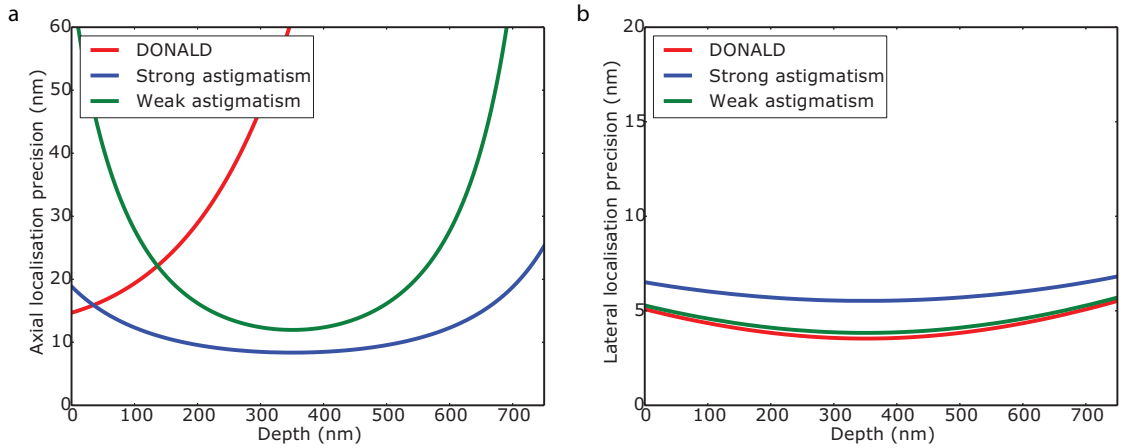

Figure 2.5 – Axial **(a)** and lateral **(b)** CRLB calculations for DONALD and astigmatic imaging. Parameters were set to match realistic experimental conditions with AF647 fluorophores. The CRLB values for astigmatism were calculated in for two aberration values, expressed as the spacing between two focal lines. The strong astigmatism corresponds to a 800-nm spacing, the weak corresponds to a 300-nm spacing, and the axial position of the focal plane was set to 375 nm.

lateral CRLB calculations in the cases of DONALD and astigmatic imaging are provided in chapter C, and displayed in Fig. 2.5.

The Fisher information can furthermore be used to optimise the performances of a system, for instance by choosing the aberration amplitude that maximises the precision in PSF shaping axial detection methods (see Fig. 2.6). It can even be used to design new detection strategies: for instance, in [34], the authors calculate the PSF shape optimising the localisation precision in 3D tracking, while in [61], Shechtman *et al.* derive from the spectral dependence of an SLM the PSF maximising the spectral specificity between two selected fluorescence wavelengths.

In many cases, experimental precisions relatively close to the CRLB value can be achieved. Still, calculating a CRLB requires skills in statistical theory in order to establish the Fisher matrix. Realistic noise models have to be used, as well as signal levels matching those obtained in experimental conditions. Finally, the CRLB only provides a lower bound; it does not provide the actual localisation precision for a given system. This is due to the approximations made to establish a simple model to derive the CRLB value. In particular, it is ill-suited for dealing with optical aberrations. Although modifications can be brought to the model to adapt the PSF shapes, the effect of optical aberrations is often unpredictable, as they come from both non-idealities of the optical elements used in the detection setup, potential misalignment, as well as from the sample itself. In other words, fitting a mathematical model to the PSFs is extremely difficult, all the more as they often prove dependent on their position in the field, as well as on the sample. This non-ideality can be source of precision loss, which is not accounted for by the CRLB calculation.

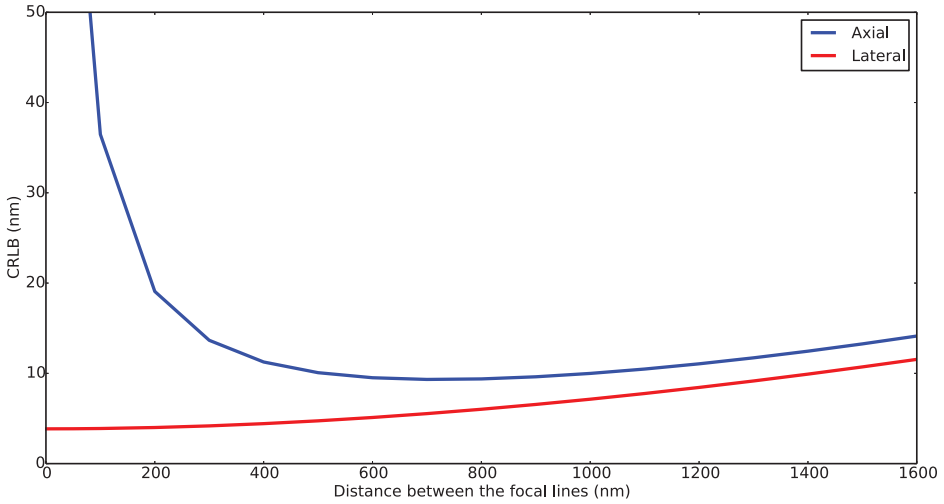

Figure 2.6 – Best CRLB value in astigmatic imaging over the capture range as a function of the aberration amplitude. The axial and lateral CRLB values are displayed for a set of parameters matching realistic experimental conditions with AF647 fluorophores. The astigmatism amplitude is expressed as the spacing between the two focal lines. Note that the axial precision presents an optimum around 800 nm between the two focal lines.

2.2.2 Experimental measurement of the localisation precision

Another approach consists in experimentally measure the localisation precision. This is probably the most relevant method, as it directly reflects the performance of the system—i.e. the resolution that can be expected when performing an acquisition. Still, the results of an experimental performance measurement have to be considered with extreme care, as it is the results of several factors: the localisation precision itself, but also the stability of the setup and the size, shape and degree of freedom of the fluorescent sources imaged. Although the actual resolution of the super-localisation image is what matters most eventually, it is relevant to seek to decouple the different elements contributing to the performance. Indeed, some of them may vary from one acquisition to the other, such as the amplitude of the drift (if it is not completely corrected by the processing software), or from one sample to the other, such as the size and shape of the label. For instance, the performance measured on a sample labelled with AF647-phalloidin might not reflect the expected performance for a sample immunolabelled with AF647, as the phalloidin toxin is much shorter (a few nanometres) than the construction consisting of a primary and a secondary antibodies (10–15 nm). Besides, decoupling the different factors contributing to the resolution can provide leads to improve the method—for example, if residual drifts are identified as sources of performance deterioration, it may be beneficial to seek to improve the stability of the optical system or the efficiency of the drift correction algorithm. Finally, performance measurements may involve unknown data, such as the size of the protein labelled. These are delicate to handle when trying to interpret the results.

In this section, we will present two approaches commonly adopted in the literature to measure the performances of a method: biological samples, and calibration samples.

We will explain how they can provide information about the localisation precision, as well as their weaknesses.

2.2.2.1 Biological samples

It is possible to use biological samples as performance measurement samples rather than for the study of processes of interest. In this case, the size and shape of the imaged proteins have to be known, which is generally done using measurements previously obtained with other methods. Two approaches are available: either point-like objects (i.e. objects displaying sizes well below the expected localisation precision) are used to directly measure the width of the localisation distribution histogram, or objects of known sizes are imaged to assess the resolution.

The first approach might be the simplest to understand, if not to achieve. Indeed, finding a suitable sample is very challenging, as both the sizes of the protein and the label must be significantly inferior to the expected precision. Still, several possibilities can be mentioned: first, actin filaments can be labelled with phalloidin-AF647. As their diameter is around 5–9 nm [62], and as the size of the toxin is but a few nanometres, the diameter is expected to be around 10 nm. This is not sufficient to stand for a point-like object for standard 2D SMLM imaging (the precisions are rather around 5 nm with organic dyes), but it can be valid for axial detection methods that typically do not exhibit as good a precision. In particular, it can be useful when imaging at important depths (beyond a few µm), where significantly degraded localisation precisions can be expected due to signal loss, important background levels as well as optical aberrations—this approach was followed in [42].

Other suitable structures include clathrin coated pits—the thickness of the light chain layer is expected to be below a few nanometres—or Gram-negative bacteria, in which the membrane is only a few nanometres thick. Still, the labelling strategy may play an important role, as if the linker is larger than a few nanometres the hypothesis of a point-like source is bound to be inadequate. This is illustrated in Fig. 2.7, which shows an x-y slice of a clathrin sphere in 2D SMLM. Although the localisation precision (previously measured on fluorescent beads) is below 10 nm, the standard deviation of the localisation distribution is found to be around 17 nm, which is consistent with the expected size of the label and the localisation precision.

Resorting to fluorescent proteins rather than organic dyes might be a sound strategy here. This presents two major advantages: first, fluorescent proteins are known to be much closer to their targets than organic dyes attached through immunolabelling. Second, as the photon count per PSF is much lower, the localisation precision is significantly worse. As a consequence, the performance is more likely to be dominated by the localisation precision itself rather than by the stability of the setup or the size of the label. Still, inferring the localisation precision that would be obtained with brighter fluorophores from measurements performed with dim fluorescent proteins might be somewhat hazardous.

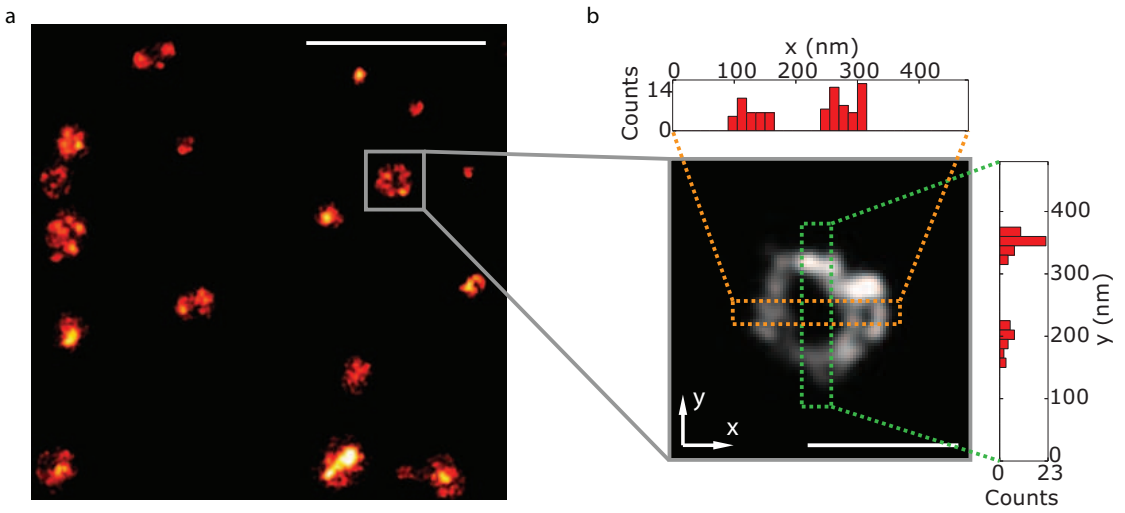

Figure 2.7 – Measurement of the performance of a 2D SMLM setup on immunolabelled clathrin coated pits (fixed COS-7 cells with the Heavy chain and the Light chain clathrin immunolabelled with AF647). **(a)** 2D SMLM image of clathrin coated pits. **(b)** x-y slice in the equatorial plane of the boxed clathrin sphere in **(a)** alongside with the histograms plotted along centred lines. The standard deviations of the different peaks are around 17 nm. Scale bars: 1 µm **(a)**, 250 nm **(b)**.

The second possibility is to use biological structures of known size and geometry in order to measure the resolution. This knowledge can be obtained through the use of other detection methods, for instance electron microscopy. Microtubules have been used to assess the resolution of a method by visualising the hollowness [47]. Indeed, when the resolution is sufficient, the line profile plotted perpendicular to the axis of a microtubule displays two peaks corresponding to the two edges of the cylinder (see Fig. 2.8). Then the distance between the two peaks can be measured. It is directly linked to the localisation precision: the further the peaks, the lower the localisation precision, as explained in Fig. 2.9.

This method, however, suffers from several drawbacks, as it heavily relies on the assumptions made on the sizes of the microtubules and the labels—which are not known with extreme precision. If the diameter is assumed to be 55 nm instead of 60 nm for instance, the results would be altered.

Other samples can be used in a similar way, especially Nuclear Pore Complexes (NPC), which are composed of two 100-nm diameter rings separated by 50 nm, each ring featuring eight sites [63]. As they seem to be quite reproducible, and as their size matches typical resolutions found in SMLM, they can prove useful too. Still, they remain limited by the same problems as those encountered with microtubules: the size of the label as well as their geometry have to be known in order to obtain reliable results.

2.2.2.2 Calibration samples

Biological samples being ill-suited in many cases for localisation precision measurements, an alternative is to resort to dedicated calibration samples, i.e. samples specif-

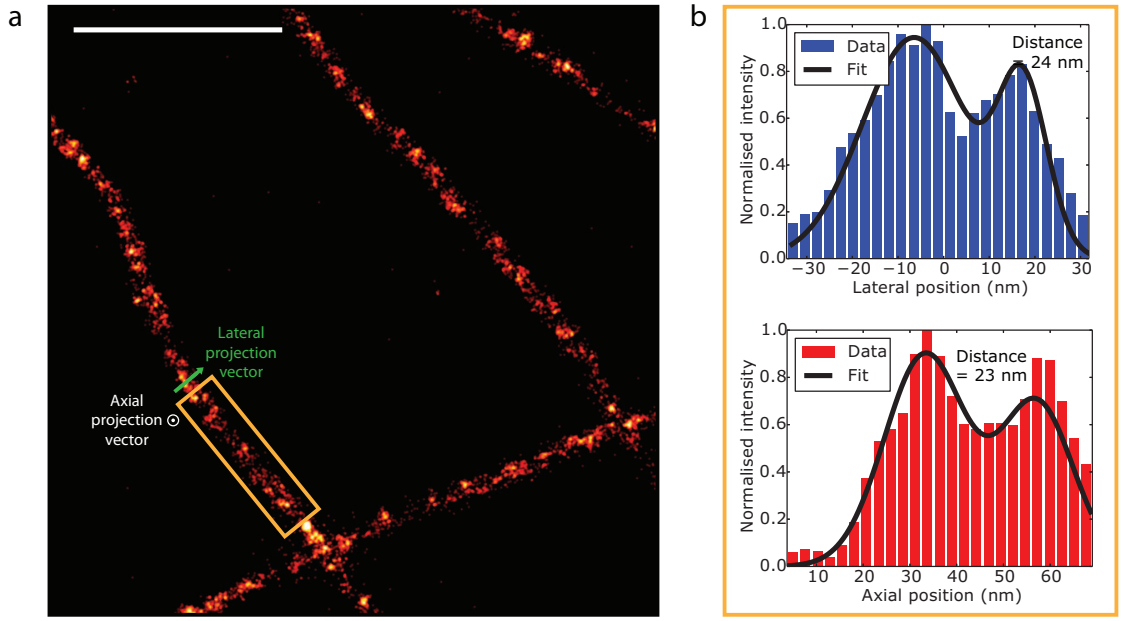

Figure 2.8 – Measurement of the performance of a 2D SMLM setup on immunolabelled microtubules (fixed COS-7 cells with the α-tubulin immunolabelled with AF647). **(a)** 2D SMLM image of microtubules. **(b)** Lateral and axial histograms plotted in the yellow boxed region, along the displayed projection vectors (horizontal for the lateral profile, vertical for the axial profile). Scale bar: 1 µm.

ically designed for performance measurements. An example of calibration sample is the 15-µm microspheres decorated with AF647 molecules that was presented in section 2.1. However, although they can be used for biases assessment, they are not adapted for localisation precision measurements, as the localisations seem rather broadly distributed. This may be due either to the thickness of the biotin layer (which is unknown but could a priori be as large as a few tens of nanometres) or to the roughness of the spheres, which may be bumpy locally[5]. Much like in the case of biological samples, two strategies are available: either a direct distribution width measurement on isolated point-like sources, or a resolution assessment on a sample of controlled geometry.

The simplest way to produce a sparse set of point-like (i.e. well below the Airy radius) emitters is to deposit fluorescent nanobeads on a coverslip, as detailed in section B.3. As their diameter typically ranges from 20 nm to 100 nm, they are generally not below the localisation precision value. This is not problematic, however, since emitters are randomly distributed in the beads, which results in a substantial averaging of the position[6]. Still, for large beads (100 nm for instance), the size might be an issue because it is not significantly below the Airy radius—this implies that the spot is not a

[5] This would induce a dispersion of the localisation results rather than biases, as the results are averaged radially over the spheres.

[6] Assuming a single fluorophore randomly located in a filled sphere, the mean square distance to the centre reads: $\sqrt{\frac{3}{5}}R$. Then, assuming $N = 5000$ emitters (for 5000 photons collected per frame in the PSF, which is a realistic hypothesis), the mean square distance of the centre of the measured distribution to the

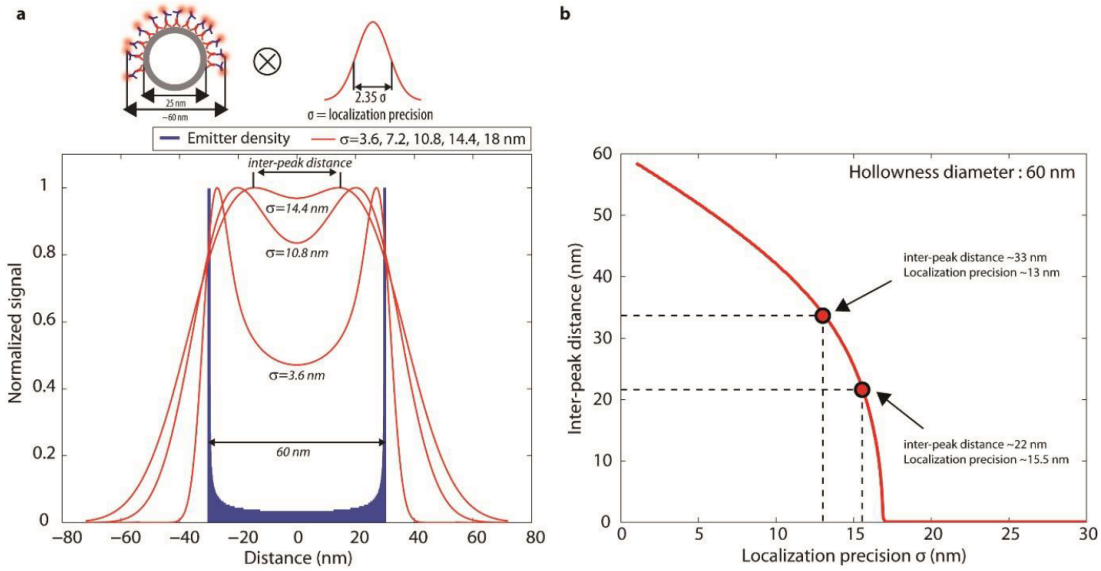

Figure 2.9 – Estimation of the localisation precision from the visualisation of the hollowness of microtubules. **(a)** Top: hypotheses made for the modelling of the microtubules (dyes attached through immunolabelling are distributed along a circle with a 60-nm diameter, and the image obtained is the convolution of this distribution with a Gaussian function featuring a standard deviation equal to the localisation precision). Bottom: projection of the distribution (blue) and profile obtained (red) fir different values of the localisation precision. Note that the distance between the two peaks decreases as the localisation precision increases. **(b)** Correspondence between the inter-peak distance and the localisation precision. This curve is used to deduce the localisation precision from the measured distance between the peaks. Source: Bourg *et al.*, *Nature Photonics* (2015) [47].

PSF strictly speaking, but rather the convolution of the PSF with a 100-nm sphere. Using smaller beads (for example 40-nm diameter or below) for performance assessment is thus recommended.

Acquisitions can be performed on such a sample in nominal conditions: especially, the illumination power should be adjusted so that the fluorescence of the beads matches realistic signal levels in biological samples (for instance, AF647 generally emit 8000–10000 photons per PSF within one ON cycle in a standard dSTORM buffer). Then the localisation distribution is retrieved for each bead from the localisation list, and the standard deviation can be measured, both in the lateral and in the axial directions (in 3D SMLM). If necessary, a clustering algorithm can be used to pool the distributions obtained for many beads. This method has the advantage of enabling a straightforward decoupling between the localisation precision itself, and the stability of the setup, as the drifts can be tracked frame per frame if the number of beads in the imaged field is sufficient: this is illustrated in Figure 2.10b–c. Besides, it also allows to evaluate the impact of the number of fluorescence photons emitted (see Fig. 2.10b,d). Finally, as mentioned

centre of the bead reads: $\sqrt{\frac{3}{5N}}R$. Even for a 100-nm nanobead, this results in a 1.1-nm mean error, which can be considered negligible.

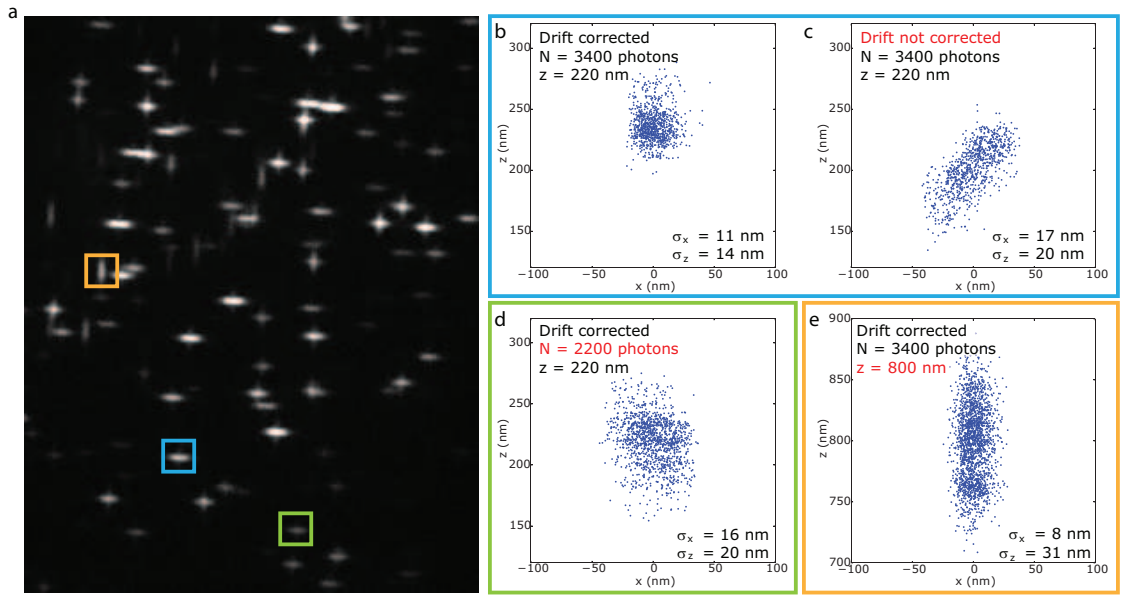

Figure 2.10 – Measurement of the performances using fluorescent beads. 40-nm fluorescent beads were randomly deposited on unlabelled fixed COS-7 cells: they are thus distributed at random heights. **(a)** Astigmatic image of such a sample. **(b–e)** Analysis and decoupling of several factors. The x-z localisation scatter plots are shown for different beads, and the resulting lateral and axial standard deviations σ_x and σ_z measured are displayed. The control configuration is shown in **(b)**, and different parameters are varied in **(c–e)**. **(b,c)** show the influence of the stability of the setup on the same bead by correcting the drifts frame-per-frame over the whole field or leaving them uncorrected. **(b,d)** illustrate the influence of the number of photons collected by comparing drift-corrected results on two beads at the same height with different brightnesses. **(b,e)** display the influence of the axial position on the lateral and axial precisions by comparing drift-corrected results on two beads of similar brightnesses at different depths.

previously, the size of the emitters is not a potential source of error as it can be in performance measurements carried out on biological samples (see section 2.2.2.1).

Fluorescent beads are not always the ideal sample, however. The first problem that has to be mentioned is the fact that they are only deposited on the coverslip rather than properly attached. Thereby, some of them might diffuse locally during the acquisition, thus altering the localisation results. Provided the motion is large enough to be resolved (i.e. larger than the localisation precision), the localisation results can be discarded for the diffusive beads through data processing. Another downside of fluorescent beads is the fact that they do not blink as SMLM fluorescent probes do. This can prove problematic if the background signal must be removed: this is generally achieved by removing pixel per pixel the temporal median of the previous and next frames to get rid of static signals and keep only temporally varying fluorescence. However, this is not possible with non-blinking sources, which implies that other strategies have to be used (see appendix A.3.2)—otherwise, the measurements performed on the PSFs might be subject to biases, especially when performing photon counting. This problem can be circumvented by replacing the fluorescent beads with SMLM fluorophores attached to the coverslip (for instance AF647-streptavidin deposited on a biotin-coated coverslip), which also presents

the advantage of reproducing realistic experimental conditions more exactly.

Finally, fluorescent beads deposited on a coverslip does not enable axially resolved measurement. For example, they cannot provide the measurement of the localisation precision curve (whether lateral or axial) for molecules distributed in all the axial extent of the capture range. In order to solve this issue, we have proposed to deposit the fluorescent beads on unlabelled fixed cells (see the protocol detailed in section B.3.4). An example is given in Figure 2.10a. As the beads randomly deposit on the top of the cells, this produces single emitters roughly randomly distributed in the axial direction when imaging the edge of a cell—this allows the axially resolved measurement of the 3D localisation precision, as illustrated in Fig. 2.10b,e. This method also has the advantage of inducing realistic sample-induced optical aberration in the detection to match typical experimental conditions more closely. An alternative would be to resort to the so-called dip coating method [64], which consists in dipping the coverslip in a polymer to create steps of controlled heights on which the fluorescent beads can then be dropped[7].

Finally, dedicated nanostructures can be used as calibration samples. For instance, nanorods with two fluorophores (or DNA-PAINT binding sites) at the edges allow the measurement of the resolution of the method—either the lateral resolution if they are laid on the coverslip, or the axial resolution if they are raised perpendicular to the surface. Naturally, this requires that the nanorulers have the right size to match the resolution of the system. One should also ensure that the signal levels emitted by the probes match those obtained in typical biological acquisitions. Other structures can also be used, such as tetrahedra. Still, a commonly encountered problem with such calibration nanostructures is the reproducibility of their size and shape: some exhibit variations up to 25 %, which makes the assessment of the resolution more difficult.

2.3 Biological and chemical applications in DONALD

SMLM unlocks a broad range of applications by allowing imaging the organisation of proteins or molecules at nanometre scale, well below the diffraction limit. Still, due to the relative complexity of 3D super-localisation imaging, some of these studies require specific strategies, whether for the labelling, the acquisition or the analysis of the localisation data. In this section, we will present different studies that we carried out in collaboration with teams in biology or chemistry using DONALD. This will allow us to illustrate the 3D SMLM-related non-idealities encountered, as well as their effect on the studies. Thus, we will also describe the different developments that had to be performed to come up with adapted sample preparation and imaging schemes. We will also describe the data analysis codes that we specifically designed to assess the validity of the biological or chemical hypotheses that were to be verified.

A feature shared by these three applications is the fact that the required precision is around or below 10 nm, i.e. below the axial localisation precision. This implies that the

[7] Note that the refractive index of the polymer has to match that of the imaging buffer or the biological sample to avoid the effect of spherical aberration.

position must be measured from a large set of molecules in order to reduce the error on the assessment of the mean position. DONALD is especially suited in this case due to the absolute axial information that it provides: as the reference of the coverslip is known, and as the results are not subject to axial detection biases, the molecules detected can readily be pooled and analysed. On the contrary, the same measurements would be far more challenging using relative detection methods such as PSF shaping: the use of fiducial markers would be mandatory in order to correct axial detection biases (as mentioned in section 1.6.1), but also to assess the position of the coverslip in order to merge the results obtained on different fields of view before performing the statistical analysis. This feature illustrates the usefulness of the SAF reference to make acquisitions more reproducible and reliable—this will be exploited in chapter 3 to correct the detection biases inherent in PSF shaping methods.

2.3.1 Assessing the penetration of antibiotics in *Staphylococcus aureus* bacteria

The first application was carried out in collaboration with Rym Boudjemaa, Karine Steenkeste and Marie-Pierre Fontaine-Aupart (Institut des Sciences Moléculaires d'Orsay, France). The study was set in the framework of the investigation of antibiotics ineffectiveness in the treatment of *Staphylococcus aureus* infections [65]. Indeed, *Staphylococcus aureus* is a pathogenic bacterium that can provoke serious human infections. In particular, they are often observed to cause implant-related infections due to their capacity to organise in biofilms—cell aggregates presenting modifications of membrane properties that decrease bactericidal activity. Even in the absence of biofilm formation, few antibiotics are efficient against *Staphylococcus aureus* infections because of its capacity to develop resistance[8] to bactericidal agents. Daptomycin is one of the few antibiotics still able to efficiently treat staphylococcal infections. It is a molecule consisting of a hydrophylic part and a lipophilic tail that interacts with the cell membrane to form pores from which ions leak, leading to cell death. Although daptomycin is believed to be efficient against *Staphylococcus aureus* bacteria independently of their growth phase (exponential phase or stationary phase), treatment failure in stationary phase and biofilms is observed in a certain number of cases, even on non-resistant strains.

The goal of this study was to identify the origin of this tolerance[9] in order to propose treatment modifications capable of improving bactericidal efficacy. Several hypotheses could be considered: first, daptomycin could be unavailable in stationary phase and biofilms due to low diffusion—thus, it would not be able to reach the cells. Previously Fluorescence Recovery After Photobleaching (FRAP) results obtained with fluorescently labelled daptomycin had led to dismiss that hypothesis, as the fluorescence recovery was found to be only around 40 %, which implies that a significant proportion of the antibiotics effectively binds to the cells [65]. A second possibility was that antibi-

[8] The term *resistance* refers to genetic mutations developed by the bacteria to withstand the effect of drugs.

[9] The word *tolerance* designates the capacity to withstand bactericidal activity through non-genetic modifications (for instance due to environment-related modifications of the membrane properties).

otics reaching the cells were unable to penetrate inside the outer cell wall[10] to bind to the inner membrane. We investigated this hypothesis by resorting to DONALD imaging to image the nanoscale 3D localisation of fluorescently labelled daptomycin and link it with the known position of the membrane.

More precisely, stationary phase non-resistant *Staphylococcus aureus* samples were grown and BODIPY FL-labelled daptomycin was added[11]. Still, BODIPY FL is ill suited for SMLM, as it exhibits poor photophysical properties (low signal, low blinking, high photobleaching) in imaging buffer. Thus, we resorted immunolabelling to attach AF647 instead: we used a Rabbit primary antibody that binds to BODIPY FL and quenches its fluorescence, and a goat anti-rabbit AF647 secondary antibody fragment. The size of the whole construction is expected to be around 10 nm large. No residual fluorescence signal from the BODIPY FL was observed when exciting the sample at 488 nm, which means that the antibodies effectively reached their target and bound to the daptomycin.

However, when imaging the AF647 molecules in a standard dSTORM buffer composed of Tris, NaCl, glucose, cysteamine, glucose oxidase and catalase, we found that a large part of the cells were killed during the acquisition[12], probably due to deprivation of oxygen, thus potentially altering the results. We therefore performed several tests with various buffer compositions; we eventually found that by removing the cysteamine and keeping the rest of the buffer unchanged, the photophysical performances were still sufficient to perform the acquisitions, and that most cells were still alive after two hours of acquisitions on different fields of view.

We performed the acquisitions in TIRF configuration to image the lower part of the bacteria, i.e. their contact point with the coverslip. The goal was to measure the distribution of the AF647 molecules to determine whether the daptomycin was localised at the membrane—in which case it would be expected to appear 30 nm deep in the sample at the contact point—or randomly located inside the cell wall, which would imply a distribution between 0 nm and 40 nm, with a mean value around or below 20 nm (see Fig. 2.11a). The 3D DONALD images (Fig. 2.11b) were analysed thanks to a similar algorithm as that used for the calibration microspheres in section 2.1 to define radial ρ slices and plot the axial profile (see Fig. 2.11c). At $\rho = 0$, i.e. at the contact point with the coverslip, the average axial position of the AF647 molecules was found to be 33 nm $\pm$ 3 nm, which is consistent with the hypothesis that the drug actually reaches its target and binds to the membrane. As a comparison, we also performed measurements with vancomycin instead of daptomycin. Vancomycin is known to be a cell wall-targeting antibiotic, and was measured only 20 nm $\pm$ 3 nm above the coverslip on average (in the same labelling and imaging conditions). This result is consistent with the hypothesis of a random distribution in the cell wall.

[10] As a Gram-positive bacterium, the outer envelope of *Staphylococcus aureus* is composed of a cell wall (40-nm thick) that surrounds the membrane. Daptomycin can be effective only if it binds to the membrane to form pores.

[11] It should be noted that the BODIPY FL molecule is grafted on the hydrophilic part of the daptomycin rather than on the lipophilic tail that is supposed to interact with the membrane.

[12] This was observed using a cell death marker, propidium iodide.

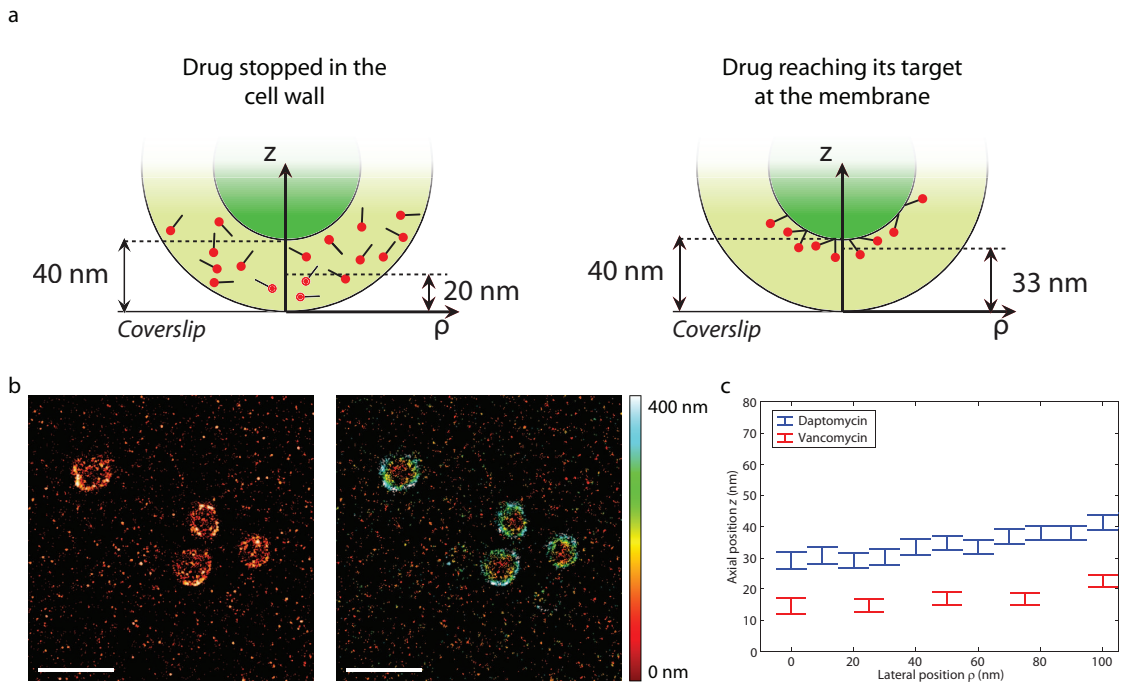

Figure 2.11 – 3D localisation of daptomycin in *Staphylococcus aureus* using DONALD. **(a)** Illustration of the two studied hypotheses: either the antibiotics is stopped in the cell wall, or it effectively reaches its target at the membrane. **(b)** 2D SMLM (left) and 3D DONALD images (colour-coded depth, right) of cells with AF647-labelled daptomycin. **(c)** Radial profile of the mean height of the AF647 molecules in the presence of daptomycin or vancomycin. Note that the mean height follows the curvature of the sphere-shaped cells, and that fluorophores are detected 33 nm deep in the case of daptomycin, and 20 nm deep in that of vancomycin. Scale bars: 2 µm.

It should be noted that DONALD is especially suited for this application due to its ability to provide absolute axial information. Without the knowledge of the position of the coverslip (for instance with a PSF shaping-based 3D approach), this would require a fine correction of the axial drift and the measurement of the position of the coverslip (using fiducial markers for example) with a precision of the order of a few nanometres.

Once the hypothesis of daptomycin being stopped in the cell wall and not being able to reach its membrane target was discarded, complementary studies were performed to identify the origin of daptomycin treatment failure. The membrane damage rate was found to be significantly lower in stationary phase and biofilms than in exponential phase. This correlated with the chemical composition of the membrane: high saturated fatty acid content and low branched chain fatty acid content were linked with decreased bactericidal efficiency [65]. Consequently, it was proposed to associate daptomycin delivery with branched chain fatty acids loads in order to decrease the tolerance and improve the efficacy of the treatment.

This work was published in *Antimicrobial Agents and Chemotherapy* in May 2018 [65]. More specifically, I worked in close collaboration with Rym Boudjemaa, and I contributed to the development of the labelling strategy and the dedicated imaging buffer,

as well as to the acquisitions. Finally, I wrote the software used to analyse the localisation results.

2.3.2 Imaging the structure of adhesion proteins in podosomes

Biological applications were also carried out using DONALD, especially for the study of adhesion processes and structures. In collaboration with Anaïs Bouissou, Renaud Poincloux and Isabelle Maridonneau-Parini (Institut de Pharmacologie et de Biologie Structurale, Toulouse, France) among others, we performed experiments to understand the generation of protrusion and traction forces in podosomes of human macrophages [66]. Podosomes are adhesion structures found in several particular types of cells, such as macrophages, neurons and tumour cells. They exhibit a ring shape and a diameter around 1 µm. They are involved in the process of adhesion to surfaces, as they are at the origin of the generation of protrusion forces. The main goal of this mechanobiological study was to determine where protrusion and subsequent traction forces are localised, which proteins are involved in the process, and how they organise spatially in 3D to produce the forces.

Previous measurements had been performed on a dedicated instrument called Protrusion Force Microscope—basically an Atomic Force Microscope scanning a thin Formvar membrane on which the sample was deposited, so that the tip could sense the deformation of the membrane and translate them into force measurements. The results proved that the forces exerted in a single podosome consist of a protrusion force at the core of the podosome towards the substrate on the one hand, and on the other hand a traction force at the outer ring directed towards the cell [66]. Further investigation was carried out by studying the role of different proteins of interest suspected to be involved in the force generation process: talin, vinculin and paxillin. Samples ware prepared in which each of these proteins was knocked out and imaged with the Protrusion Force Microscope, which evidenced lowered protrusion forces.

The last step of the study consisted in determining the spatial organisation of each protein of interest in the podosomes and to link them to hypothesised roles for each of them. As the 3D structure had to be known with nanometre precision, and as the axial information had to be intrinsically linked to the position of the coverslip, DONALD seemed to be the most relevant imaging method. First, the fixed podosome samples had to be labelled to allow imaging of the different proteins. Different samples were therefore produced: on each of them, the F-actin was labelled using phalloidin-AF488 to provide a common reference and allow the localisation of the podosomes, and the protein of interest (paxillin, vinculin, talin-N, talin-C or F-actin) was immunolabelled thanks to a primary antibody and an AF647 secondary antibody. The acquisitions were performed in epifluorescence illumination configuration with a standard dSTORM imaging buffer according to the following protocol: first, the sample was briefly shone at low 488-nm illumination power to record a diffraction-limited image where the actin cores of the podosomes were identifiable. Then, a high 637-nm illumination power was used to induce

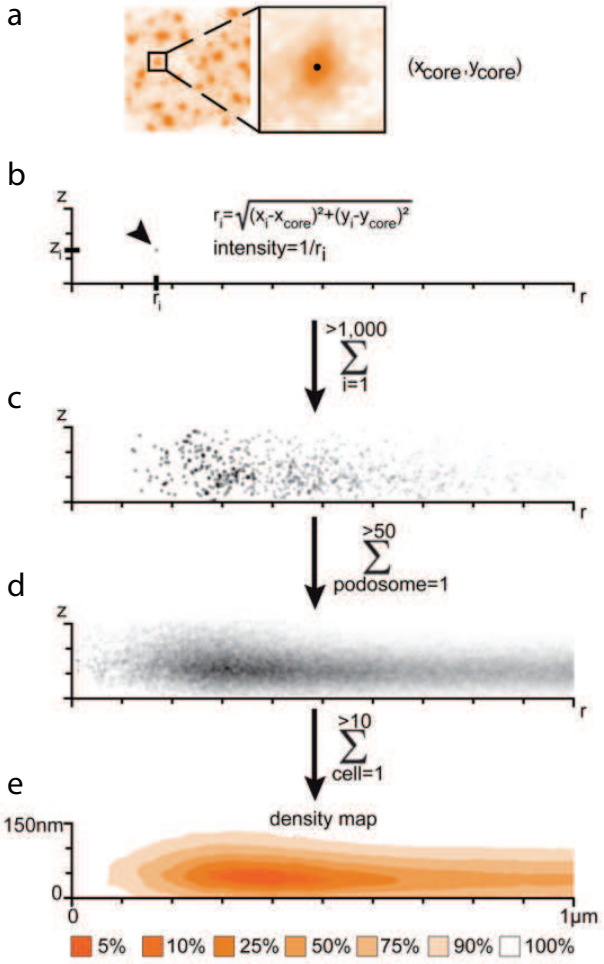

Figure 2.12 – Processing workflow used to calculate the density maps of the different proteins in podosomes. **(a)** Wide-field image of the actin distribution and zoom on a podosome. The lateral coordinates of the centre of each podosome is calculated using this image. **(b)** Radial-axial (z-r) scatter plot for one localisation i at (x_i,y_i,z_i) of the protein of interest labelled with AF647. To normalise the plot, the localisation is weighted according to its radial position (the closer to the centre of the podosome, the higher the weight). **(c)** Scatter plot obtained considering all the localisations in a single podosome. **(d)** Scatter plot obtained by pooling the data for all the podosomes in several fields of view. **(e)** Density map calculated from the scatter plot **(d)**. The density is expressed as a normalised volume containing a certain number of localisations—thus, the lower the volume, the more concentrated the localisations. Source: adapted from Bouissou *et al.*, *ACS Nano* (2017) [66].

most of the AF647 molecules in the dark state and achieve single molecule regime. The frames were acquired and processed to retrieve the DONALD information.

Once the 3D localisation data was available, it could be analysed using a radial distribution calculation. More precisely, the lateral radial distance r to the centre of the podosome was calculated for each localisation, much like in the cases of the calibration spheres (see section 2.1) and the *Staphylococcus aureus* bacteria (see section 2.3.1). By pooling the results obtained for all the podosomes on several fields of view, a large statis-

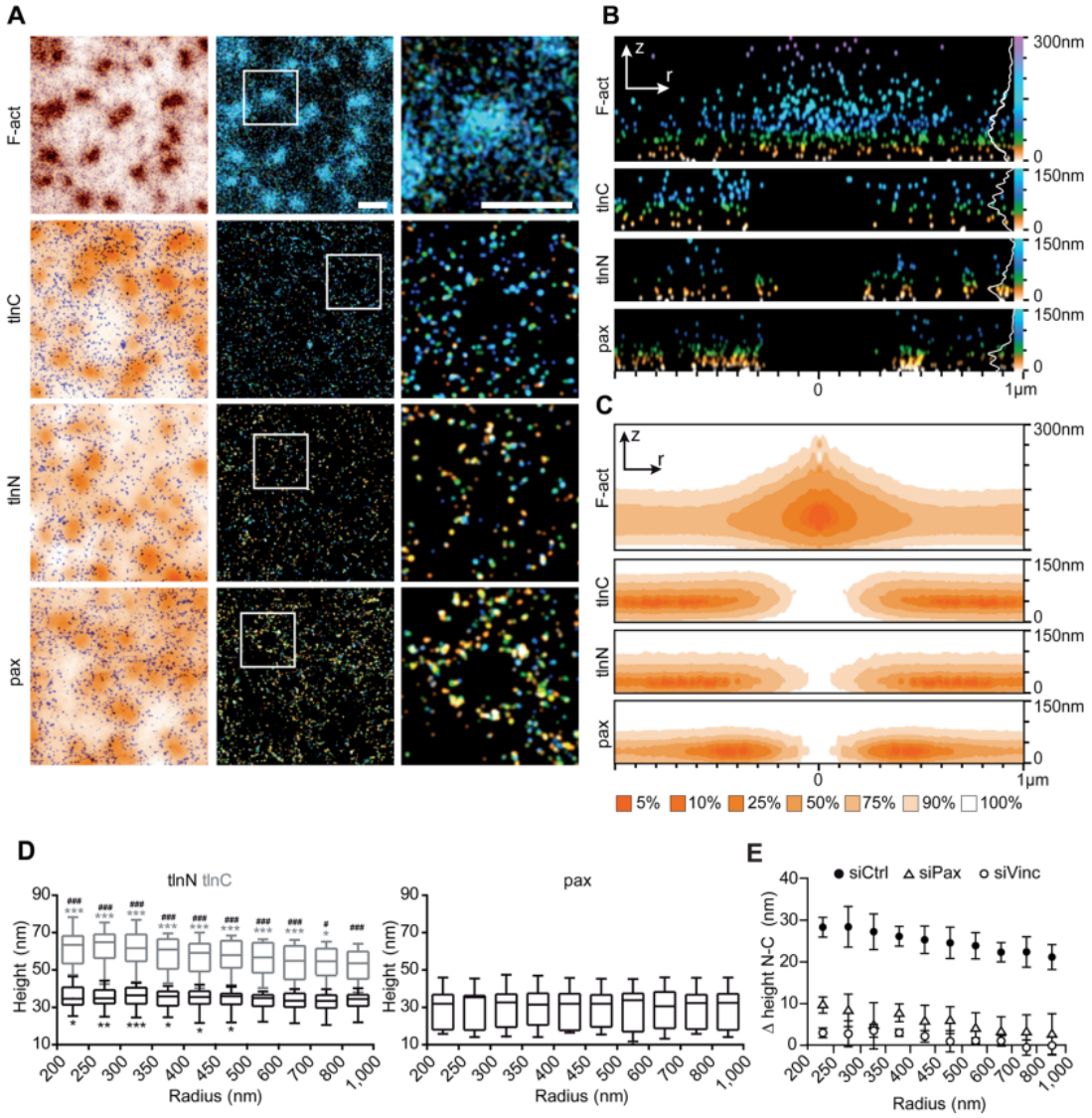

Figure 2.13 – 3D distributions of F-actin, talin-N, talin-C and paxillin in podosomes imaged with DONALD. **(A)** SMLM images obtained for each protein. The left row displays the 2D AF647 localisations (blue) overlaid on the diffraction-limited AF488 actin images (red-orange). The middle row displays the 3D AF647 localisations (colour-coded depth), and the right row shows zooms on the boxed regions of the middle row. **(B)** *z*-*r* views of the 3D images displayed in **(A)**. **(C)** Corresponding *z*-*r* density maps (pooled for many podosomes). **(D)** Mean height radial profiles of talin and paxillin. **(E)** Mean axial extension of the talin (i.e. axial distance between talin-N and talin-C) for the control cells (siCtrl) and those featuring knocked down paxillin (siPax) and vinculin (siVinc). Scale bars: 1 µm. Source: Bouissou *et al.*, *ACS Nano* (2017) [66].

tical set was obtained, which could be used to calculate the local density. This processing workflow is illustrated in Fig. 2.12.

Following this protocol, we imaged the 3D spatial distributions of the F-actin and the paxillin, as well as the two ends of the talin (N-terminal and C-terminal). The results presented in Fig. 2.13: while the N-terminal of the talin always remains close to the

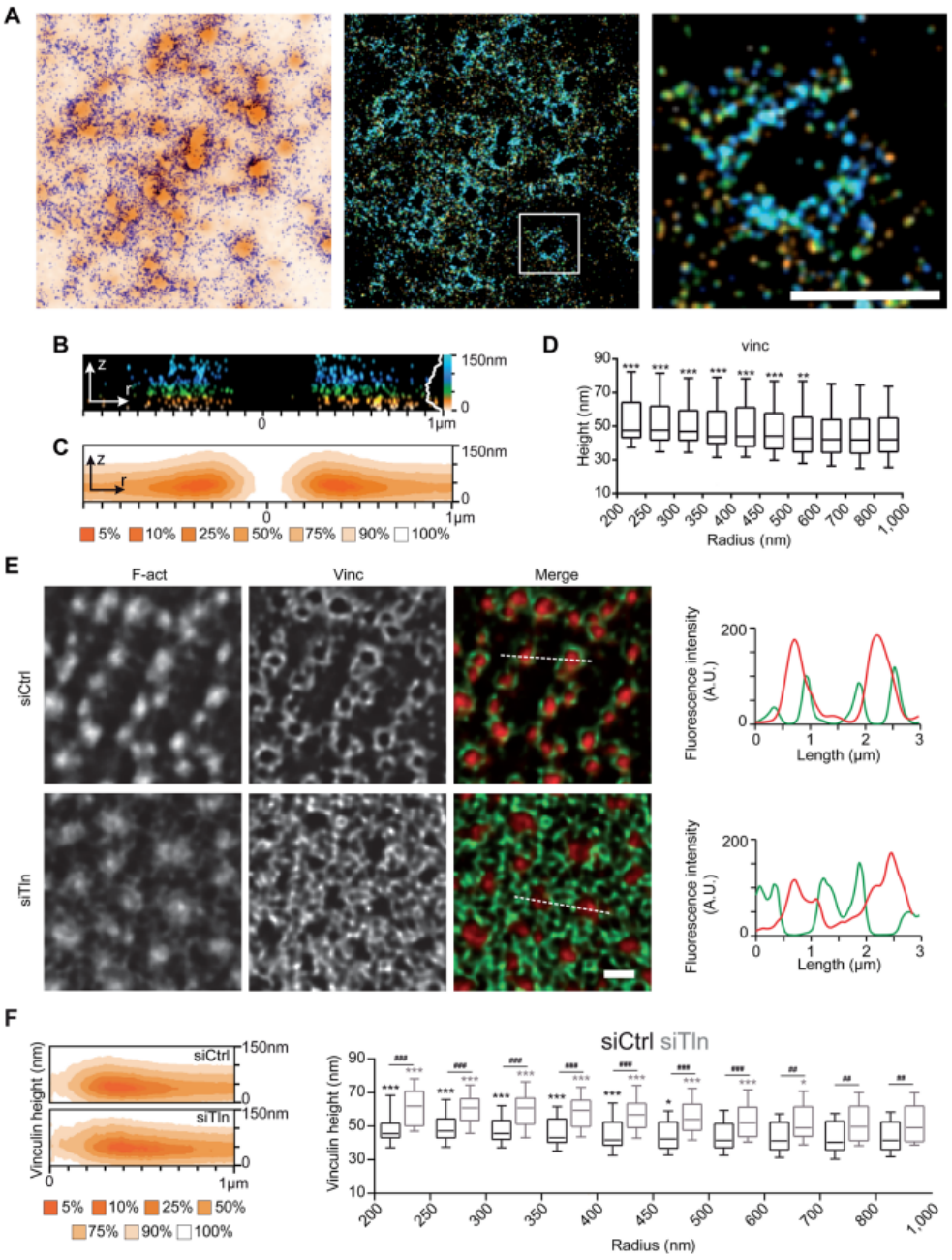

Figure 2.14 – 3D distribution of vinculin in podosomes imaged with DONALD. **(A)** SMLM images obtained for vinculin. Left: 2D AF647 localisations (blue) overlaid on the diffraction-limited AF488 actin image (orange). Middle: 3D AF647 localisations (colour-coded depth). Right: zoom on the boxed region of the middle image. **(B)** *z*-*r* views of the 3D image displayed in **(A)**. **(C)** Corresponding *z*-*r* density map (pooled for many podosomes). **(D)** Mean height radial profile vinculin. **(E)** Left: 2D SMLM images of the distributions of actin and vinculin, and corresponding merged image (red: actin, green: vinculin). The images are displayed for two conditions: standard samples (siCtrl) and talin-depleted samples (siTln). Right: actin and vinculin distribution profiles plotted along the dotted lines. **(F)** Left: *z*-*r* density maps plotted for siCtrl and siTln samples. Right: corresponding mean height profiles. Scale bar: 1 µm. Source: Bouissou *et al.*, *ACS Nano* (2017) [66].

coverslip (35 nm ± 1 nm), the C-terminal is located higher, around 61 nm ± 2 nm on average. Still, an interesting feature is that the mean height of the talin-C rises from the edge to the centre of the podosomes (Fig. 2.13D–E), indicating a continuous stretching of the protein from the edge to the core, probably under an increasing tension.

Then, we set out to assess the roles of vinculin and paxillin in the stabilisation of actin. We performed DONALD imaging of samples in which the vinculin or the paxillin were knocked down (siVinc and siPax respectively). The results presented in Figure 2.13E indicate that in the absence of either of the two proteins, the axial extension of the talin is dramatically reduced (4 nm and 6 nm between the N and C terminals for siVinc and siPax respectively). This indicates that both vinculin and paxillin contribute to the stabilisation of the talin stretching—this corroborates the results obtained in Protrusion Force Microscopy, which stressed the vastly reduced protrusion force exerted by siVinc and siPax podosomes.

Finally, we deemed relevant to assess the 3D localisation of vinculin, as we did for talin and paxillin (Fig. 2.12). The results are displayed in Figure 2.14A–D: the axial distribution is rather broad with a mean height value measured 52 nm ± 3 nm above the coverslip, i.e. between the talin-N and the talin-C. Also, much like talin-C, vinculin appears to rise near the F-actin core. This might indicate that vinculin binds to certain sites exposed by stretched talin. To verify this hypothesis, talin-depleted samples (siTln) were produced and imaged: the morphology of the podosomes seemed significantly altered (see Fig. 2.12E), with a displacement of vinculin towards the edges of the ring. Finally, the height of vinculin in siTln podosomes was found to be higher than in regular cells (see Fig. 2.12F). Together, these two elements suggest that in the absence of talin, vinculin binds to other proteins, such as actin.

This mechanobiological study of human macrophage podosomes through complementary imaging approaches—Protrusion Force Microscopy and DONALD—allows to infer the origin of adhesion force generation. The protrusion force exerted by the central F-actin column is associated with a traction force at the ring, resulting in increasing talin stretching from the ring to the core. This stretching offers binding sites for vinculin, which contributes to the stabilisation of the talin extension, alongside paxillin. This model is summarised in Figure 2.15.

Understanding the mechanobiological model underlying force generation in podosomes is likely to enlighten how cells move and adhere, and sense their environment. Our conclusions may prove useful in explaining several processes such as cell adhesion and migration, cancer cell invasion or axon growth. My contribution to this work, which was published in *ACS Nano* in April 2017 [66], mainly consisted in running the acquisitions, as well as processing the data.

2.3.3 Localising kindlin inside integrin focal adhesions

As DONALD is especially relevant to image the 3D architecture of adhesion structures and processes, we continued in this field in collaboration with Thomas Orré, Olivier

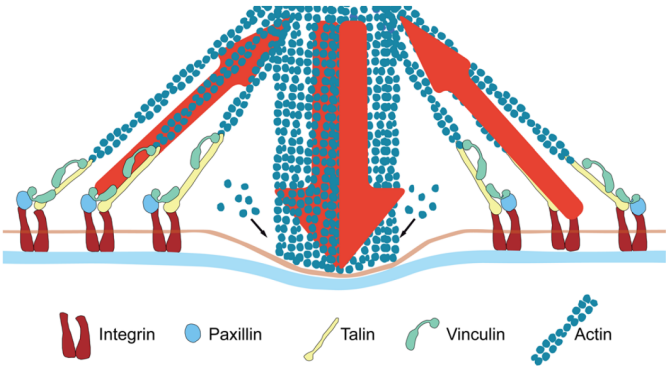

Figure 2.15 – Protein organisation and force generation model in podosomes. The arrows represent force generation (protrusion force directed towards the substrate at the centre due to actin polymerisation, and traction force directed towards the cell at the ring. The traction force is associated with talin stretching, which offers binding sites to vinculin. This, alongside with the effect of paxillin, contributes to the stabilisation of the structure and help force generation. Source: Bouissou *et al.*, *ACS Nano* (2017) [66].

Rossier and Grégory Giannone (Interdisciplinary Institute for Neuroscience, Bordeaux, France). This work aimed at determining the role and the structure of kindlin in focal adhesions, as well as its involvement in integrin activation. Much like podosomes (see section 2.3.2), focal adhesions are structures involved in cell adhesion processes: more precisely, they form a connection between the extracellular matrix and the cytoskeleton, and play a capital role in signalling. They are composed of a large assembly of various proteins, although they are very different from podosomes, both in terms of shape and size. They organise in different nanoscale axial layers connected together, as described in the previous work of Kanchanawong *et al.* [67]; still, the interaction of kindlin with the integrin layer remains poorly understood.

Previous parts of the study were carried out in sptPALM using mEos2-labelled proteins to study diffusion and immobilisation inside focal adhesions. They proved that kindlin controls immobilisation and activation of integrin inside focal adhesions. Kindlin was also found to mostly follow a free diffusion regime at the plasma membrane, both inside and outside focal adhesions—even though inhibition of the interaction between integrin and kindlin further increased the diffusive kindlin fraction, thus highlighting the role of the mutual interaction between the two proteins. Eventually, the PH domains in kindlin were found to be crucial in membrane recruitment, as the deletion of the domain vastly reduced this recruitment.

We then used DONALD to assess the 3D distribution of kindlin and investigate the role of transitions between the different layers present in focal adhesions in kindlin function. Still, mEos2 proved an unsuited fluorescent probe for DONALD due to its low fluorescence and poor blinking behaviour. We rather resorted to fixed cells in combination with dSTORM labelling. We used GFP-labelled proteins instead of mEos2-labelled,

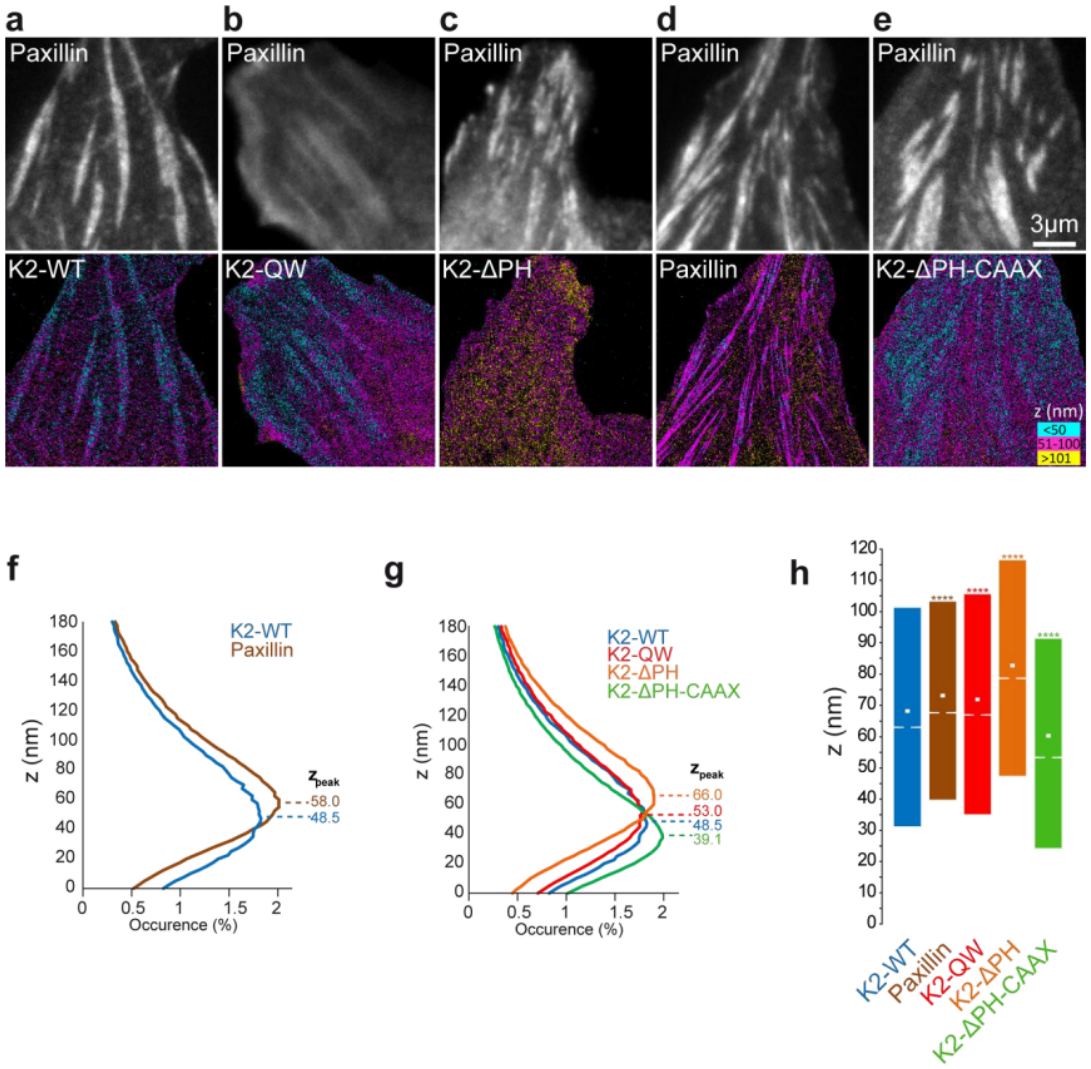

Figure 2.16 – 3D distribution of paxillin and talin in focal adhesions. **(a–e)** Top: diffraction-limited images of RFP-labelled paxillin (note that focal adhesions are clearly identifiable). Bottom: 3D DONALD images of the distribution of AF647 (cyan, magenta and yellow stand for three classes of axial positions). Five different conditions were studied: kindlin-2 wild type (K2-WT), kindlin-2 in modified cells to reduce the interaction between kindlin and integrin (K2-QW), kindlin-2 in modified cells to delete the PH domains of kindlin (K2-ΔPH), paxillin in wild type cells (paxillin), and kindlin-2 in modified cells presenting the ΔPH mutation as well as another mutation to restore the membrane association of kindlin (K2-ΔPH-CAAX). **(f–g)** Histograms of the axial distributions of the different conditions in focal adhesions. **h** Box plots of the axial distributions (notch: median, square: mean, edges: 25 % and 75 % percentiles). Source: Orré *et al.* (2018, submitted) [68].

and we then attached AF647 anti-GFP nanobodies[13] [69]. Besides, paxillin was labelled with RFP to provide a common reference between the different samples and to allow focal adhesion identification. Acquisitions were preformed in TIRF excitation configuration in

[13] It should be noted that anti-GFP nanobodies quench the fluorescence of the GFP.

a standard dSTORM buffer. First, samples were briefly shone with a low power 532-nm illumination to record the RFP diffraction-limited image. Then a high power 637-nm illumination was used to achieve single molecule regime and image AF647 molecules.

The results are presented in Figure 2.16. Inside focal adhesions, paxillin was found to be localised 58 nm above the coverslip on average, i.e. in the upper boundary of the integrin layer. Similarly, kindlin-2 was located in the integrin layer (48.5 nm), close to the membrane. Inhibition of the binding between kindlin and integrin (K2-QW) did not significantly modify this localisation, whereas PH domains deletion (K2-ΔPH) induce a major redistribution of the kindlin. This suggests that binding partners for kindlin-2 are mostly in the integrin layer. It also proves that this localisation is not dominated by binding with integrin, but rather by the PH domains. Further investigation was performed by restoring the membrane association of K2-ΔPH thanks to the addition of a CAAX sequence (K2-ΔPH-CAAX), which resulted in a membrane diffusion increase and a close association to the membrane in the integrin layer (39 nm above the coverslip on average), as well as significant enrichment in focal adhesions. These results seem to indicate that kindlin recruitment in focal adhesions requires membrane recruitment and diffusion through the PH domain.

Considering the experiments carried out and the conclusions obtained throughout this work, a model can be hypothesised to explain the role of kindlin in integrin activation inside focal adhesions. The colocalisation of kindlin with paxillin, which is found in the integrin layer, indicates the crucial role of the interaction between kindlin and paxillin. Indeed, it seems reasonable to assume that binding to paxillin in the integrin layer helps create a pool of immobile kindlin for integrin to interact with. The immobile integrin-kindlin complexes would allow local talin interaction to further enhance integrin activation.

The results presented here were submitted in *Nature Communications* in 2019 [68]: I contributed to the development of the labelling strategy, performed the dSTORM acquisitions and wrote the data analysis codes used to assess the 3D distribution of the proteins of interest in dSTORM experiments. These conclusions could prove useful in understanding the probing and signalling processes occurring in focal adhesions, and more precisely the mechanisms of communication between the different layers. This is bound to find applications in the study of cell migration, proliferation and differentiation.

2.4 Conclusion

This chapter devoted to the presentation of characterisation strategies and applications in 3D SMLM has enabled us to highlight a need for reliable protocols. First, we have tackled the question of axial calibrations, that are required in most three-dimensional approaches. We have proposed a simple protocol that efficiently uses the known geometry of a dedicated 15-µm microspheres calibration sample to obtain the axial information. As the acquisitions are performed in nominal acquisition conditions, the calibration re-

sults produced faithfully account for the effect of the spherical aberration—unlike the protocol using fluorescent beads deposited on a coverslip usually reported in the literature. We have explained the principle and the sample preparation, as well as the algorithm used to process the data. We have then characterised the sample and illustrated the difference between the two calibration protocols, thus emphasising the interest of our method to eliminate sources of axial biases. Then, we have set out to propose solutions to evaluate the performances of SMLM methods. This is necessary, as it determines their suitability for biological applications requiring a certain resolution or imaging range. We have exposed different approaches, from theoretical modelling to biological samples or dedicated calibration samples. In particular, we have proposed a protocol to obtain isolated sources distributed in the volume, which is ideal to measure the evolution of the 3D localisation precision over the whole imaging range. Overall, we have found that the most reliable protocols are those that enable the decoupling of the different factors involved in the final performance. This allows to separately assess the contributions of the encoded information, the number of photons, the stability of the setup and the size of the target. Eventually, we have focused on several state-of-the-art biological or chemical applications carried out in DONALD. This has allowed us to present the sample preparation, labelling, acquisition and processing protocols specifically developed for these studies. We have also highlighted the need for statistical analysis of localisation data due to the required precision of the measurements. In that regard, the reproducibility of the measurements appears a crucial factor.

Both the calibration method, the performance measurement protocols and the applications of DONALD for acquisition of reliable data pertain to the same effort to make 3D SMLM more easily applicable. In this framework, identification and elimination of potential sources of error and biases are important steps, as these errors currently represent major hindrances to the generalisation and the uniformisation of SMLM approaches in cell biology. The question of the reproducibility will be thoroughly investigated in the next chapter, where we will introduce a method to readily eliminate axial detection biases.

Chapter 3

Combining PSF shaping and SAF: DAISY

In spite of its relative versatility, implementation straightforwardness and capability in terms of capture range as well as lateral and axial precisions, PSF shaping is often hindered several experimental bottlenecks. Most of them stem from the fact that the axial positions are measured relative to the focus plane, which leaves the technique sensitive to axial drift, axial chromatic aberration and sample tilt. While the former is likely to induce a loss of resolution, the latter two result in axial biases, thus hampering the reproducibility of experiments and jeopardising colocalisation experiments (this was mentioned in section 1.6.1). In other words, in most cases, 3D super-localisation imaging based on uncorrected PSF shaping is bound to be limited in precision and accuracy by the non-idealities of the setup. Correction strategies have been developed to suppress these effects, but in many cases even identifying or measuring their influence can be challenging as it requires modifications of either the setup or the sample, or both.

The most satisfying strategy is probably the use of fiducial markers placed inside the sample: they enable both the tracking of the axial drift and the assessment of the axial chromatic aberration—note that multicolour markers have to be used with this end in view—the sample tilt and the field-dependent aberration-induced bias. Nevertheless, their use is far from easy: nanorulers are difficult to come by and require a preparation step that is not compatible with all samples, while fluorescent beads are subject to photobleaching in most super-localisation experiments due to their duration—this can be overcome by using a dedicated spectral channel for the markers [70] or by exciting them off-resonance, although this imposes constraints on the labelling, not to mention that the effects to be detected may be wavelength-dependent, in which case they have to be assessed at the very fluorescence wavelength.

On the contrary, DONALD exhibits very little sensitivity to both axial drift, axial chromatic aberration and sample tilt due to the fact that it yields results independent from the focus position, i.e. the only reference is the coverslip itself. As the SAF decays sharply with the depth, though, it becomes somewhat unreliable after roughly 300 nm,

hence the limitation of its application to membrane-related phenomena (see section 2.3). Still, its performances near the coverslip make it a very powerful tool to provide the reference that PSF shaping lacks. From that point of view, we thought that the SAF could bring much to PSF measurement-based 3D imaging by coupling the two complementary information sources. To come up with a proof of principle, we chose to use the most simple PSF shaping implementation, namely astigmatism. We built a dual-view setup that provides the SAF absolute information using a photon comparison between an UAF and EPI paths on the one hand, and on the other hand the astigmatism information based on PSF engineering using a cylindrical lens. We called this technique Depth Astigmatic Imaging with SAF Yield (DAISY). Most of the work that will be presented in this chapter was published in *Nature Communications* in April 2019 [71].

The main concept of that method is similar to the use of fiducial markers for the correction of the shortcomings of the axial detection. However, instead of using markers introduced in the sample on purpose, we use the very detected single molecules as references taking advantage of the SAF detection, which provides their unbiased positions.

3.1 Principle, advantages, experimental setup and position calculation

Although the experimental setup is very close to that of DONALD, DAISY should rather be seen as a means to improve a versatile and precise PSF shape measurement approach by providing it with the absolute reference brought by the SAF. Still, the SAF detection imposes that a dual-view setup be built. This we saw as an opportunity to use the available photon budget in a different way compared to most (single-view) PSF shaping setups.

3.1.1 Determination of the astigmatism amplitude and experimental setup

The axial precision of each PSF shape measurement method depends on the amplitude of the aberration: for instance, a low astigmatism creates little distortion of the spots, making the assessment of the height less precise; on the contrary, a high astigmatism results in strongly aberrated PSFs, making the calibration curve steeper and thus the measurement more precise (this is illustrated in Fig. 3.1). Similarly, the axial precision is determined by the spacing between the two focal planes in biplane imaging, and by the rotation speed of the helix (in terms of angle per axial displacement) in double helix PSF. Nevertheless, the axial precision also deteriorates as the signal to noise ratio decreases, which is a crucial parameter to consider, as high aberrations induce strongly deformed PSFs. For too large aberrations, this spreading of the photons is actually detrimental to the localisation precision since the shape sensitivity improvement does not compensate the SNR loss. In other words, there is an optimum to be found between the two competing effects. Using the results published in [72] dealing with the cases of biplane, astigmatism and double helix, we illustrate this for the particular case of astigmatic imaging in Fig. 3.2. As the theoretical results obtained by the authors in that article are not con-

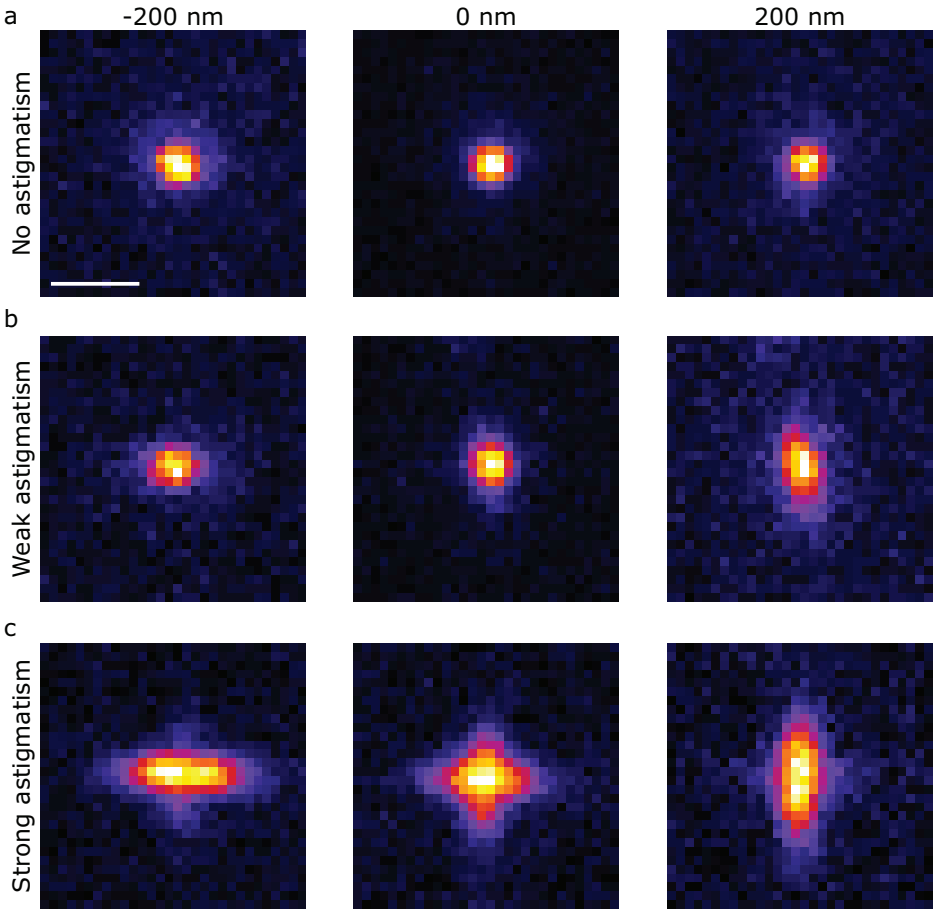

Figure 3.1 – Influence of the astigmatism amplitude on the PSF shapes. Experimental PSFs are displayed for three axial positions, and in three cases—no astigmatism, weak astigmatism (350 nm between the two focal lines), and strong astigmatism (800 nm between the two focal lines) in **(a)**, **(b)** and **(c)** respectively. Scale bar: 1 µm.

fronted with experimental data, they remain but an ideal; still, they have the advantage of highlighting the parameters influencing the precision. In the case of astigmatism, the optimum of the precision can be obtained analytically: more precisely, the optimal spacing between the two focal lines equals twice the depth of field (see section C for a detailed explanation of the CRLB calculations).

Aside from the best attainable precision value over the capture range (i.e. the precision at the focus in most cases) displayed in Fig. 3.2, it is crucial to consider also the size of the capture range and the variation of the precisions, both lateral and axial, with the axial position. A typical example is double helix PSF: by tuning the aberration amplitude, the axial precision can be changed. The higher the aberration, the higher the sensitivity (i.e. the angle covered per axial displacement) and thus the lower (i.e. the better) the axial precision. Still, the capture range cannot be better than the axial range over which the helix covers an angle of 2π, and this range decreases as the aberration amplitude increases—the axial precision typically diverges at the edges of the capture range

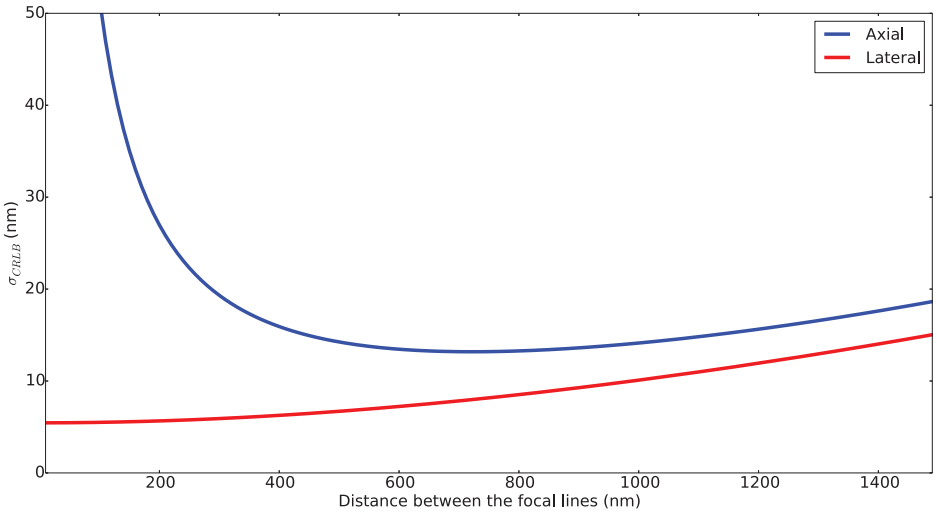

Figure 3.2 – Influence of the astigmatism amplitude on the axial and lateral Cramér-Rao Lower Bound (CRLB) theoretical limits for 2750 photons per PSF. The best achievable value over the whole imaging range (i.e. the value at $z = 0$ in most cases) is plotted as a function of the astigmatism amplitude, expressed as the spacing between the two focal lines in nm. Note that the axial precision displays a minimum around 800 nm. Typical values found in the literature are often around 350 nm.

due to the indeterminacy of the angle between the top and bottom edges of the range in terms of PSF angle. This results in an intrinsic coupling between the best precision on the one hand, and the capture range and the precision curve flatness on the other hand. The case of astigmatism is slightly different from that of double helix PSF, however, as the capture range and flatness generally improve with the aberration amplitude, at least for reasonable values of astigmatism[1] (see Fig. 3.3). We found that the optimal astigmatism value in terms of axial performance, i.e. the best compromise between the axial precision at the focus, the capture range and the localisation flatness was that corresponding to the best achievable precision, i.e. a 800-nm distance between the two focal lines.

In practise, this value is seldom used in the literature, mainly because it corresponds to a rather high amount of aberration (see Fig. 3.1), which induces a large lateral resolution loss, as illustrated in Fig. 3.4. PSF shaping typically causes lateral resolution losses significantly worse than the CRLB, which may be due to the fact that in most cases, the fitting method used to provide the lateral position does not take into account the aberrations—in other words, the fitted function is not a realistic experimental PSF, hence the precision is decreased. In our case, as we set out to develop a dual-view setup composed of an unaberrated EPI fluorescence path and an astigmatic UAF path, less than half the total number of photons collected is used for the PSF shaping. As a result, the lateral precision cannot be degraded by more than a factor $\sqrt{2}$ compared to 2D SMLM.

[1] It should be noted that the results presented in Fig. 3.3 are slightly different from those reported in [73]—especially in terms of axial variation of the axial precision and of capture range. This may be due to the PSF model assumed by Rieger and Stallinga, as strongly astigmatic PSFs might not be ideally described by anisotropic 2D Gaussian functions, in particular near the focus.

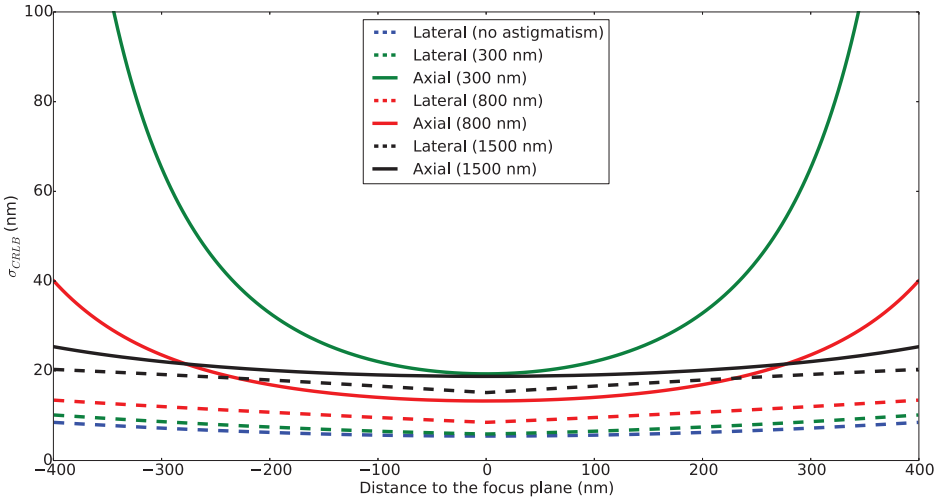

Figure 3.3 – Lateral and axial precisions for different astigmatism amplitudes as a function of the axial position. This gives additional information compared to Fig. 3.2 as the capture range and the flatness of the localisation precision curves can be assessed for different astigmatism values.

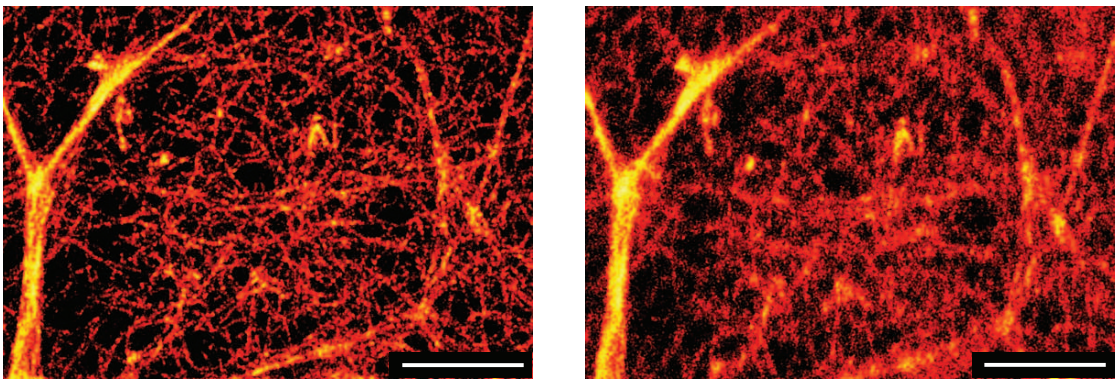

Figure 3.4 – Lateral resolution loss induced by the astigmatism. The same field of actin labelled with phalloidin-AF647 in a COS-7 cell (see section B) was imaged without astigmatism (left) and with a strong astigmatism (right), i.e. 800-nm spacing between the two focal lines. The resolution loss due to the astigmatism is clearly visible on the sub-network. Scale bar: 2 µm.

This represents a noticeable difference as a strong astigmatism can spoil the lateral resolution by potentially more than a factor 3. Thus, this experimental configuration allows us to tune the axial detection almost independently of the lateral performance.

The setup is presented in Fig. 3.5a. It largely resembles the DONALD setup as the fluorescence is split in two paths using a non polarising beam splitter, and a physical mask is placed in a relay plane of the BFP to remove the SAF components on the UAF path only. Nevertheless, unlike DONALD, it comprises a cylindrical lens placed in the UAF path in order to create the astigmatism. The focal length of the cylindrical lens and its position were calculated to optimise the axial detection, i.e. to obtain a 800-nm spacing between the two focal lines. The cylindrical lens was thus fabricated for this precise purpose: it features a focal length of -3500 nm. The z position of the cylindrical

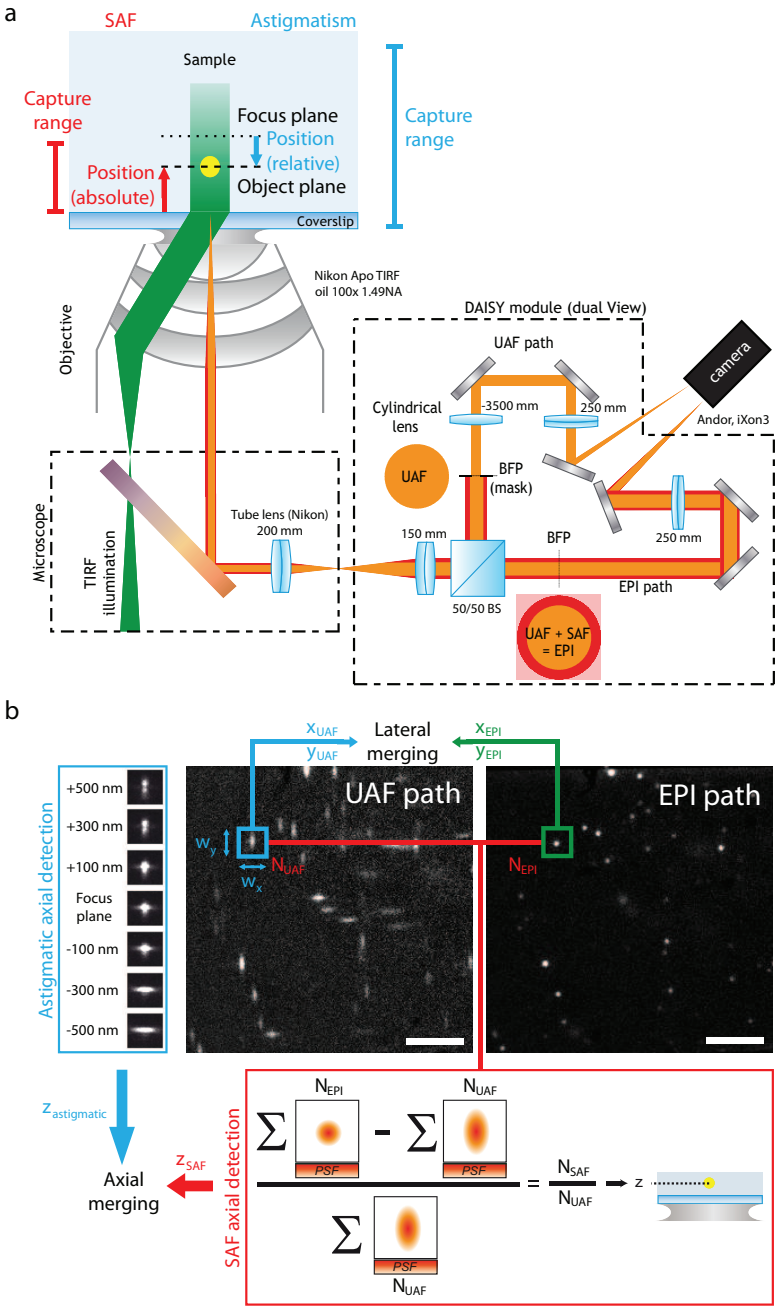

Figure 3.5 – Experimental setup used in DAISY. **(a)** The DAISY module is placed between the microscope and the camera. After the beam splitter cube (BS), the UAF path contains a cylindrical lens, as well as a physical mask in a relay plane of the back focal plane of the objective to block the SAF photons. These two elements are not present in the EPI detection path, which comprises both the UAF and SAF components. The images are formed on the two halves of the same camera. **(b)** UAF and EPI frames recorded by the camera on a given field (COS-7 cells, α-tubulin immunolabelling, Alexa Fluor 647, see section B) are also displayed (top right corner). For each PSF, the x and y widths are measured to obtain the astigmatic axial information, and the numbers of UAF and EPI photons are used to retrieve the SAF axial information. Finally, the axial astigmatic and SAF positions are merged together. Similarly, lateral positions are obtained by merging the lateral positions from the UAF and EPI paths.

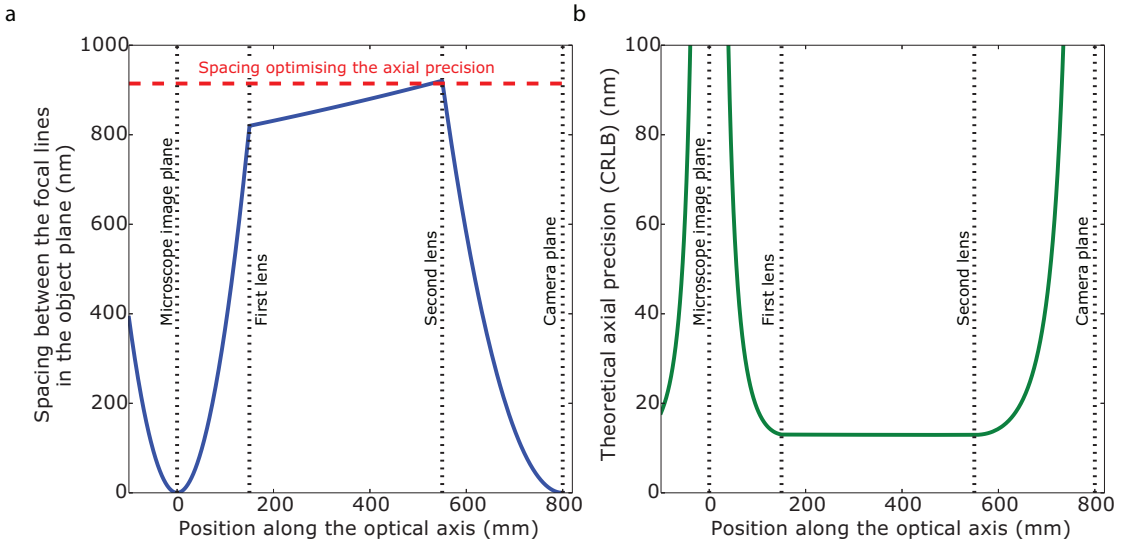

Figure 3.6 – Calculation of the optimal position of the cylindrical lens for DAISY. **(a)** Evolution of the spacing between the two focal lines (i.e. the astigmatism amplitude) as a function of the position of the cylindrical lens along the optical axis in the detection setup (solid blue line). The spacing that optimises the precision, which corresponds to twice the depth of field, is displayed in red dashed line. The positions of the microscope first image plane (in other words the entrance of the DAISY module), the two lenses in the module and the camera plane, are displayed in black dotted lines. **(b)** Theoretical axial precision (solid green line) as a function of the position of the cylindrical lens along the optical axis in the detection setup. The positions of the microscope first image plane, the two lenses in the module, and the camera plane, are displayed in black dotted lines. Note that the position of the cylindrical lens matters little as long as it is placed between between the two lenses (in the collimated part of the beam). See section C.2 for more details about the calculation of the precision according to the astigmatism amplitude. A number of photons equal to 2750 per PSF (typical value for AF647) was assumed.

lens has little influence as long as it is placed in the collimated part of the beam (see Fig. 3.6). Still, several details have to be noted: first, the cylindrical lens must be placed after the mask as it is bound to ruin the conjugation between the BFP and the mask plane otherwise. Second, the best position for the cylindrical lens is in theory the Fourier plane itself as it is the only position where the cylindrical lens can apply a deformation of the PSFs without deforming the field itself (this issue will be dealt with in section 3.2); however, in our case this position is not accessible since the mask is already placed in the Fourier plane. Finally, we chose to use a negative focal length in order for the cylindrical lens to move the focus in the depth of the sample rather than inside the coverslip, which would not be useful. Still, the spacing between the EPI and UAF paths can be adjusted thanks to a translation stage on which the last lens of the UAF path (250 mm focal length) is mounted.

A comparison between the axial CRLB values expected in DAISY and standard astigmatism is shown in Figure 3.7. While the optimal precision (i.e. the precision near the focus) is very similar in both configurations, DAISY is expected to exhibit a better capture range. This is due to two factors: first, the strong astigmatism offers a better

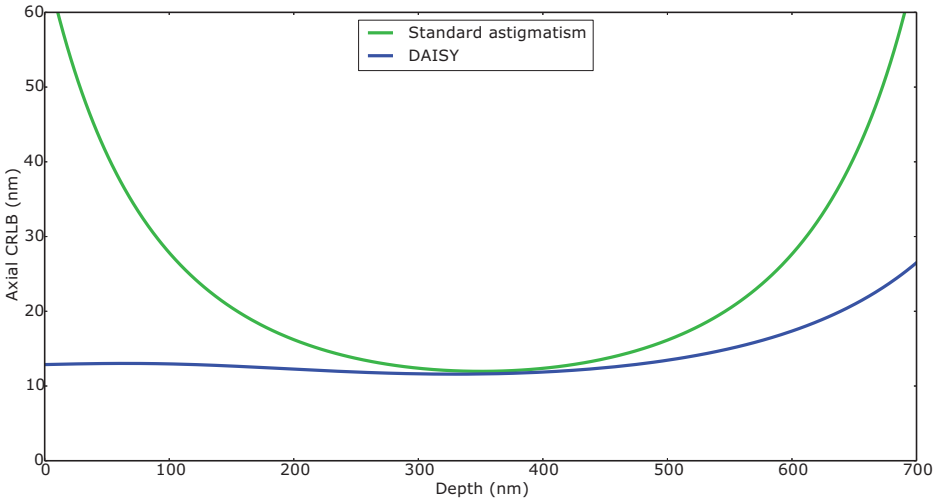

Figure 3.7 – Comparison between the axial CRLB values for DAISY and a standard single-path astigmatic detection. The spacing between the two focal lines is 800 nm for DAISY and 300 nm for standard astigmatism. Besides, the standard astigmatism uses all the photons available (without splitting the signal as in DAISY). The precisions are calculated for typical signal and background levels corresponding to AF647 (5500 total photons collected per molecule). The focal plane is placed at $z = 350$ nm.

precision curve flatness (see Fig. 3.3), and second, the SAF detection contributes to the improvement of the localisation precision near the coverslip—mostly in the first 200 nm.

3.1.2 Acquisition, localisation and position calculation workflows

The camera acquires two frames of the same field, one containing the UAF and SAF components, and the other, the UAF photons only. The latter also contains the astigmatism information. The processing workflow is detailed in section A.3.2. First, the frames are pre-processed to remove the out-of-focus static fluorescence background, which could induce biases during the calculation of the UAF and EPI photon counts. On each half of the frame, the PSFs are detected thanks to a lower threshold, and for each UAF PSF, the corresponding EPI PSF is found.

Then the UAF and EPI lateral positions are assessed thanks to a centroid calculation. On the UAF positions, we apply an affine transformation to correct the field deformation induced by the cylindrical lens (as it is not placed in the Fourier plane, such a deformation is inevitable). A more detailed description of the calculation of the transformation is given in section 3.2, and the accuracy of this correction is assessed in section 3.3. This allows x^{EPI} and x^{UAF} on the one hand, and y^{EPI} and y^{UAF} on the other hand to be merged (see Fig. 3.5b) according to their theoretical localisation precisions:

$$x^{\mathrm{DAISY}} = \left(\frac{x^{\mathrm{UAF}}}{\left(\sigma_x^{\mathrm{UAF}}\right)^2} + \frac{x^{\mathrm{EPI}}}{\left(\sigma_x^{\mathrm{EPI}}\right)^2} \right) \Bigg/ \left(\frac{1}{\left(\sigma_x^{\mathrm{UAF}}\right)^2} + \frac{1}{\left(\left(\sigma_x^{\mathrm{EPI}}\right)^2\right.} \right) \tag{3.1}$$

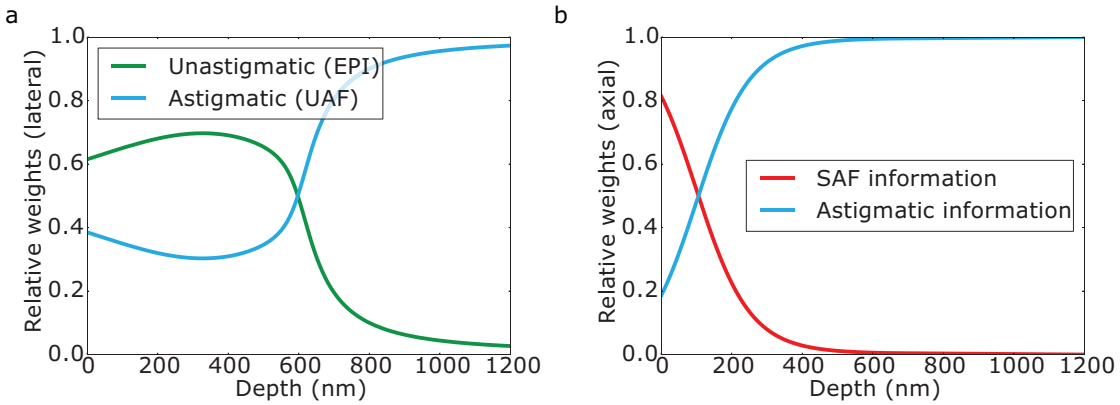

Figure 3.8 – Relative weights of the UAF and EPI lateral positions **(a)** and of the SAF and astigmatic axial detections **(b)** used to merge the positions in DAISY (see equations (3.1), (3.2) and (3.8)).

$$y^{\mathrm{DAISY}} = \left(\frac{y^{\mathrm{UAF}}}{\left(\sigma_y^{\mathrm{UAF}}\right)^2} + \frac{y^{\mathrm{EPI}}}{\left(\sigma_y^{\mathrm{EPI}}\right)^2} \right) \Bigg/ \left(\frac{1}{\left(\sigma_y^{\mathrm{UAF}}\right)^2} + \frac{1}{\left((\sigma_y^{\mathrm{EPI}}\right)^2} \right) \tag{3.2}$$

where σ_i^{UAF} and σ_i^{EPI} are the localisation precisions (i.e. the standard deviations of the positions) in the direction i for the UAF and EPI detections respectively. This combination optimises the final precision, i.e. it provides the best precision attainable from the two sources given their respective uncertainties. Note that, as the experimental localisation precisions may be different from the CRLB expectations, it may be more relevant to use the experimental precisions to determine the relative weights (see section 3.6). Fig. 3.5b illustrates the principles of the detection and information merging processes for both the lateral and axial, and the relative weights are plotted as a function of the axial position in Fig. 3.8a.

Finally, the lateral positions are drift-corrected using a temporal cross-correlation algorithm, as explained previously (see part 1.5).

As for the axial detection, the SAF requires a counting of the EPI and UAF photon numbers N^{EPI} and N^{UAF}. This is obtained thanks to a signal integration on a 2-µm wide square region centred on the centre of mass of the PSF performed on the filtered frame (i.e. after removing the temporal median of the last 10 frames). From these measurements, the so-called SAF ratio is expressed as follows:

$$\rho^{\mathrm{SAF}} = \frac{N^{\mathrm{SAF}}}{N^{\mathrm{UAF}}} = \left(\frac{N^{\mathrm{EPI}}}{N^{\mathrm{UAF}} \alpha_{\mathrm{RT}}} - 1 \right) \beta_{\mathrm{mask}} \tag{3.3}$$

where α_{RT} is a factor added to correct the non-ideality of the beam splitter, which does not display a reflection/transmission ratio equal to 1 exactly. This factor is obtained by removing the physical mask and counting the photons on fluorescent beads at the coverslip for instance—α_{RT} must verify $N^{\mathrm{EPI}} = N^{\mathrm{UAF}}$ when the mask is removed. β_{mask} is a correction factor that accounts for the fact that the mask does not have exactly the

right diameter—consequently, it either allows some SAF photons in the UAF PSFs, or discards some UAF photons on the UAF path. Once the reflection/transmission correction is measured, β_{mask} can be assessed using a sample of fluorescent beads deposited at the coverslip, for which the expected SAF ratio is known (see equation 3.5). For example, the value expected for 40-nm diameter fluorescent beads emitting at 680 nm is $\rho^{\text{SAF}} = 0.85\exp\left(-\frac{40/2}{0.24\times 680}\right) = 0.75$. These two correction factors have to be calibrated for each fluorescence wavelength, but they remain perfectly stable over time (in other words, they are calibrated once and for all) provided the temperature of the objective lens does not vary.

Then the SAF position is calculated using an analytical formula:

$$\rho^{\text{SAF}} = 0.85\ \exp\left(-\frac{z}{0.24\lambda_{\text{fluo}}}\right) \tag{3.4}$$

Hence:

$$z = 0.24\lambda_{\text{fluo}}\ln\left(\frac{0.85}{\rho^{\text{SAF}}}\right) \tag{3.5}$$

where λ_{fluo} is the mean fluorescence wavelength, and z the depth of the molecule in the sample, 0 being the sample/coverslip interface.

This analytical formula was obtained by fitting the theoretical curve presented in Fig. 1.22 with a decaying exponential[2]. Note that both the factors 0.85 and 0.24 in equation 3.4 depend on the numerical aperture objective and the indices of the glass coverslip and the imaging buffer—we used a 1.49 NA APO-TIRF 100x Nikon objective, a 1.51 glass index and a 1.335 buffer index.

The astigmatism information is extracted thanks to the Gaussian fitting performed on the UAF PSFs, which allows the measurement of the widths w_x^{UAF} and w_y^{UAF} (these widths are defined as the x and y standard deviations of the optimal 2D Gaussian). The correspondence is then found with the calibration table, which is established using the 15 µm diameter microspheres coated with fluorophores, as described in section 2.1 as well as in [56]. This accounts for the effects of both the SAF and spherical aberration on the PSF shape itself. Several methods are available to find the correspondence with the width lookup table. We typically use a least squares minimisation using an error function defined as the square of the width differences:

$$\varepsilon = \left(w_x^{\text{UAF, experimental}} - w_x^{\text{UAF, calibration}}\right)^2 + \left(w_y^{\text{UAF, experimental}} - w_y^{\text{UAF, calibration}}\right)^2 \tag{3.6}$$

Another possibility is to define the anisotropy of the PSF: $\Delta w^{\text{UAF}} = w_x^{\text{UAF}} - w_y^{\text{UAF}}$ and minimise this anisotropy:

[2] The fitted function matches the theoretical curve very closely.

$$\varepsilon = \left(\Delta w^{\text{UAF, experimental}} - \Delta w^{\text{UAF, calibration}}\right)^2 \tag{3.7}$$

The latter seems to yield better precision near the focus, but performs poorly at the edges of the capture range because of the defocus behaviour. Indeed, it causes PSF widths to roughly increase linearly with the depth: thus, the anisotropy varies little away from the focus, which results in a poor sensitivity.

Before the two axial information sources can be merged, the axial astigmatic positions must be corrected using the SAF reference in order to account for axial detection biases such as drift, chromatic aberration and sample tilt. This is achieved by performing a spatially and temporally resolved cross-correlation between $z^{\text{astigmatic}}$ and z^{SAF}. This correction algorithm is explained in section 3.2.

The merged DAISY position is obtained thanks to a linear combination of $z^{\text{astigmatic}}$ (after the correction) and z^{SAF} weighted according to their theoretical uncertainties. The formula is similar to that used for the lateral merging (equations 3.1 and 3.2):

$$z^{\text{DAISY}} = \left(\frac{z^{\text{SAF}}}{\left(\sigma_z^{\text{SAF}}\right)^2} + \frac{z^{\text{astigmatic}}}{\left(\sigma_z^{\text{astigmatic}}\right)^2}\right) \Bigg/ \left(\frac{1}{\left(\sigma_z^{\text{SAF}}\right)^2} + \frac{1}{\left(\sigma_z^{\text{astigmatic}}\right)^2}\right) \tag{3.8}$$

The relative weights used in the axial position merging are displayed in Fig. 3.8b. It should be noted that as the UAF and EPI lateral positions on the one hand, and the SAF and astigmatism positions on the other hand are merged together, the total photon loss is minimal: it ranges from $0.5\times0.85/(1+0.85) = 23\%$ for molecules at the coverslip to almost zero for fluorophores beyond 500 nm. Instead of being wasted compared to single view PSF shaping implementations, the photon budget is rather used differently. Less than half the collected photons are used for the astigmatic localisation, but this is made up for by the strong aberration, which greatly increases the sensitivity. Similarly, the UAF photons contribute little to the lateral localisation, but as the EPI path is unastigmatic, the lateral performance is not degraded compared to a standard single view setup using a weak PSF shaping. The exhaustive measurement of the localisation performances and the comparison with standard astigmatic imaging will be presented in part 3.3.

At the end of the position computation process, several filtering steps are performed in order to remove false detections. The main criteria are the UAF photon number (typically 500 photons minimum for AF647), the EPI PSF width ($110\text{ nm} < \sqrt{w_x^{\text{EPI}} w_y^{\text{EPI}}} < 350\text{ nm}$) and the EPI PSF aspect ratio ($0.67 < w_x^{\text{EPI}}/w_y^{\text{EPI}} < 1.5$).

3.2 Correction software

As described in part 3.1, the DAISY setup was designed to optimise the 3D localisation precision as well as the capture range—this will be thoroughly characterised in section 3.3. Still, the main point of DAISY is not to achieve the best possible precision.

Indeed, in most cases, the resolution and the relevance of the results are not limited by the precision itself, but rather by experimental axial non-idealities that induce losses of resolution and biases in the localised data. The best documented of these limitations is the drift, which must be corrected in order to save the resolution. The lateral drift is often induced by the mechanical relaxation of the stage on which the sample is placed, or by the weight of the stage itself if it is not perfectly horizontal. In those cases, the drift curve generally exhibits a relatively similar behaviour from one acquisition to the other, with speeds typically around 100 nm per minute, which results in total displacements superior to 1 µm in typical dSTORM experiments. If the stage is motorised, the electronic noise might add to the low frequency mechanical drift higher frequencies, which are bound to be more difficult to track as they require thinner temporal slices to increase the bandwidth.

In order to correct the lateral drift, we use the redundant cross correlation (RCC) algorithm published in [11] performed on the localised positions, although a direct cross correlation algorithm might be sufficient, or even better in the rare cases where a sudden, large shift occurs. The slice width is typically set between 500 and 2000 frames (which corresponds to 25–100 s with an integration of 50 ms), and the localisations are binned in images with 50 nm large pixels before the cross correlation is calculated. The problem of the lateral drift correction was mentioned in part 1.5, and a drift measurement for a typical dSTORM acquisition was presented in Fig. 1.11, alongside a comparison between the images before and after the lateral drift correction.

3.2.1 Lateral correction

The lateral detection can further be hampered by the field deformation. Any dual-view setup requires a correction to make up for the translation, rotation and potentially reflection between the two images. This is mathematically represented by an orthogonal transformation, i.e. a linear transformation with a determinant equal to ±1. Nevertheless, the PSF shaping also induces a field deformation if the shaping element is not placed in the Fourier plane (to our knowledge, only adaptive optics-based setups verify this condition), as mentioned in section 3.1. The exact deformation pattern depends on the shaping applied: the more complex the wavefront pattern, the more complex the deformation. In the particular cases of biplane imaging and astigmatism, it can be apprehended rather simply. In biplane imaging, as the two images have different conjugations, they exhibit slightly different magnifications. Similarly, in astigmatic imaging, the cylindrical lens changes the effective focal length along one axis only, hence a magnification difference between x and y (see Fig. 3.9).

Although the magnification difference could be assessed (for instance using fluorescent beads) to come up with an anisotropic x-y pixel size, the translation and rotation components would still need to be addressed. Instead, we chose to perform a global correction by simultaneously measuring the translation, rotation and magnification. For that purpose, we supposed an affine transformation, i.e. a combination of these three components, for a total of five degrees of freedom (x and y translations, rotation an-

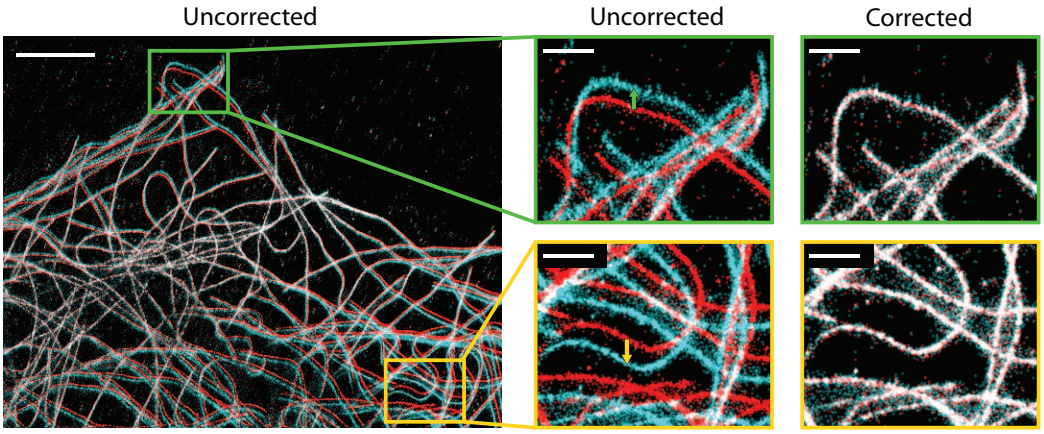

Figure 3.9 – Illustration of the image lateral field deformation induced by the astigmatism. For the same acquisition (COS-7 cells, α-tubulin labelled with AF647, see section B), 2D images were reconstructed from the lateral positions measured on both the astigmatic UAF (in cyan) and the unastigmatic EPI (in red) detection paths of our setup. The whole field and zooms on the boxed regions are displayed, both before (left and centre) and after (right) the correction. Note the deformation along the vertical axis, whereas the horizontal axis is almost unchanged. Note also that while the two images are superimposed at the centre, the discrepancy increases towards the edges. Scale bars: 5 µm (left), 1 µm (right insets).

gle, x and y magnifications). In order to obtain the optimal transformation, the EPI and UAF localisations were binned in two 2D images, which were smoothed according to their localisation precisions. Then, the UAF image was applied an affine transformation with a certain set of parameters and the resulting image was cross-correlated with the EPI image. This operation was done for several parameter sets corresponding to all the possible combinations over a reasonable range with a certain discretisation step. The optimal transformation was chosen as that maximising the cross-correlation. For the sake of both calculation time and precision, we performed several iterations (typically 10) with a small number of combinations (5 values for each parameter, for a total of 3125 combinations), starting from a wide parameter range with a rough precision. At the end of each iteration, a new parameter range was set around the position of the optimum, and the precision was refined.

Running this algorithm on the data notably provided the x-y magnification difference, which is around 4 %. Although this value remains stable over time, the algorithm should be used for each acquisition as the translation component is likely to slightly change, especially if the temperature is not perfectly stable or if the detection setup was re-aligned shortly before the acquisition. The correction code performs well, as displayed in Fig. 3.9, with final discrepancies typically below 7 nm (see part 3.3 for a thorough characterisation of the final accuracy).

This algorithm is very stable, if a bit slow; its efficiency could be improved by fitting the multi-dimensional cross-correlation curve around the maximum to improve the precision for each iteration, thus allowing to reduce the number of iterations. Another possibility would be to perform a least-squares calculation on the very localisations rather

than on the images.

3.2.2 Axial correction

The astigmatic axial detection also needs to be corrected before it can be merged with the SAF. As mentioned previously, the main issues encountered are the relativity of the information, the drift, the chromatic aberration and the sample tilt. We designed an algorithm that assesses and corrects all these problems at once. In the end, the $z^{\text{astigmatic}}$ values are thus expected to be absolute, achromatic and insensitive to the axial drift and the sample tilt. This is obtained using the SAF positions as absolute references, as explained in the section 3.1. The main idea is very similar to using fiducial markers at known heights as references. Still, here we intend to use every single localisation as a reference, which is very powerful since it provides a vastly superior number of references, distributed in all the field and through the whole capture range.

The algorithm is fed with the z^{SAF} and $z^{\text{astigmatic}}$ of all the detected molecules, as well as with the x and y positions. The first step is to filter the data to restrict the calculation to the range where the SAF is efficient: only the molecules verifying $z^{\text{SAF}} \in [-50\text{ nm}, 300\text{ nm}]$ are kept. Of course, molecules cannot be located at $z < 0$, but due to the localisation uncertainty, they can be detected at negative depths. Filtering out all molecules verifying $z_{SAF} < 0$ would alter the measurement statistics.

Then, we removed the tilt: the $z^{\text{SAF}} - z^{\text{astigmatic}}$ axial discrepancy was calculated for each molecule from the data verifying $z^{\text{SAF}} \in [-50\text{ nm}, 300\text{ nm}]$. The spatially resolved axial discrepancy information was used to calculate the tilt by fitting a plane $P(x, y) = ax + by + c$ (with a, b and c parameters to adjust) to the data, which provided the tilt direction and amplitude. The astigmatic positions were corrected in accordance with this result. For this step, we used the median of the absolute value of the discrepancy as the error function to be minimised:

$$\varepsilon = \text{median}\left(\left|z^{\text{SAF}} - P(x, y)\right|\right) \tag{3.9}$$

where x and y describe the lateral position of the molecule.

We found this error function to be better than the mean of the square discrepancies because it is far less sensitive to aberrant values coming from the inevitable false positive detections. Like for the lateral deformation correction algorithm, we divided this correction in several iterations, starting from a broad range with a rough precision for the (a,b,c) parameter set, and restricting the calculation near the optimum position and refining the precision after each iteration—once again, this could be improved for the sake of calculation speed, although this step requires only a few minutes on a standard computer.

Note that this step not only corrects the tilt, but also the offset. In other words, at the end of this step, the corrected astigmatic values are absolute (i.e. referenced directly to the coverslip) and achromatic, as the chromatic aberration can be seen as a sim-

ple translation of the focus plane between two acquisitions at two different fluorescence wavelengths.

After the tilt correction data was divided in subsets of 1000 frames and distributed in series of 3D images with 100 nm lateral and 15 nm axial pixel sizes, each of them corresponding to a 1000 frame subset. For each subset, the SAF and astigmatism 3D images were cross-correlated allowing only axial displacements to maximise the overlap, which brought the correction to be applied to the astigmatic positions for the subset. Then the results obtained for all the subsets were pooled and interpolated to generate the axial drift curve.

Both the sample tilt and axial drift corrections were applied to the whole set of data rather than to the $z^{\mathrm{SAF}} \in [-50\ \mathrm{nm}, 300\ \mathrm{nm}]$ subset, which is used only to perform the calculation. The final accuracy of the correction appears to be typically better than 3 nm (this was obtained by measuring the height of fluorophores deposited at the coverslip outside of cells).

It is worth noting that the 1000-frame division corresponds to a 50-s sampling of the axial drift (with 50-ms exposure time). This value seems reasonable given the slow evolution of the drift: it is the result of a compromise between the bandwidth of the correction (a finer sampling allows a better correction of higher drift frequencies) and the robustness of the algorithm (if the amount of data is too low, the algorithm may not adequately converge or provide a wrong value). Shorter slices might be used with higher density samples or non-blinking sources (a 50-frame division is sufficient with fluorescent beads for instance). Similarly, acquisitions featuring a lower SNR or photon number would require larger pixels or larger slices to compensate the influence of the localisation precision worsening. The algorithm could be improved thanks to a sliding window frame division to enhance the sampling (for instance, 1000-frame subsets could be sampled every 50 frames).

This so-called DAISY correction algorithm is released on Github as an open source code available at the following address: https://github.com/ClementCabriel/DAISYcorrection, alongside with a few uncorrected data sets taken on biological samples. Although the code requires data acquired with a DAISY setup as both the SAF and PSF shaping information sources are used, we believe that the whole approach developed is rather general in PSF shaping experiments. Thus, we are convinced that it could benefit the community by highlighting the hindrances inherent in PSF shaping and the means available to overcome them. For instance, the algorithm could be adapted with minimal effort for another implementation using a different information source than SAF to provide the reference.

3.3 Characterisation and performances

The first step after setting up the experiment was to evaluate the performances of DAISY in terms of precision and capture range. With this end in view, a reliable calibration sample featuring sources distributed trough the whole capture range was needed. As

mentioned in section 2.2.2.1, biological samples are not the best solution to measure the localisation precisions per se considering that the dispersion of the position distribution produced results from other factors aside from the localisation precision, such as the size of the labelled protein, the size and geometry of the label, as well as its degree of freedom in rotation—note that most of these elements are poorly documented in the field of super-resolution microscopy. Calibration samples, on the contrary, are designed to allow the measurement of the performances of the setup itself, i.e. the combination of the localisation precision and the setup stability or correction algorithm accuracy (see section 2.2.2.2).

3.3.1 Localisation precision

To assess the lateral and axial localisation precisions, we used fluorescent beads randomly distributed in the volume of the sample. This can be obtained by embedding them in an agarose gel, as described in [47], but we found that the gel is somewhat fragile: after a few minutes, the network seems to start collapsing and consequently, the beads tend to diffuse locally, which is unsuited for precision measurements. We rather chose to take unlabelled fixed COS-7 cells and add 40-nm diameter dark red fluorescent beads (the sample preparation protocol is detailed in section B.3.4). Beads stuck on the upper side of the membrane were thus located at random heights. Several 500-frame acquisitions were performed on different fields in the same conditions with a fixed focus plane, 50 ms exposure time and 150 EMCCD gain. A low illumination power (0.025 kW.cm^{-2}) was used in order to match the level of emission of the beads with that of AF647 in typical dSTORM acquisition conditions. More precisely, our reference is set to be 2750 photons per UAF PSF (and 2750–5100 photons per EPI PSF depending on the height of the source). The acquisition protocol is explained in appendix A.2.3. Measuring the performances on beads emitting the same number of photons is crucial as, according to CRLB calculations, the precision is expected to vary proportionally to $1/\sqrt{N}$ where N is the number of photons per PSF. Note that this sample is quite realistic as both the signal and the background noise (i.e. the amount of out-of-focus light collected) are close to typical experimental dSTORM conditions, not to mention that the biological structures induce slight aberrations, just as they would in dSTORM acquisitions on biological samples.

The frames were processed according to the workflow defined in sections 3.1 and 3.2: the field deformation and the lateral drift were corrected before merging the lateral positions, and similarly the axial astigmatic positions were corrected before being merged with the SAF information. Finally, the filters were applied to remove false positive detections as well as overlapping PSFs.

We processed the localisation lists with a home-made clustering algorithm that detected the clusters, filtered them to remove the beads that were too bright or too dim, as well as those too close to their neighbours and those that diffused during the acquisition. Then, for each bead and each frame, the values of z^{DAISY}, x^{DAISY} and y^{DAISY} were measured and the localisation precisions (noted σ_z and σ_{xy}) were calculated as the standard deviations of the statistics. For the lateral precision, we kept only the worst value

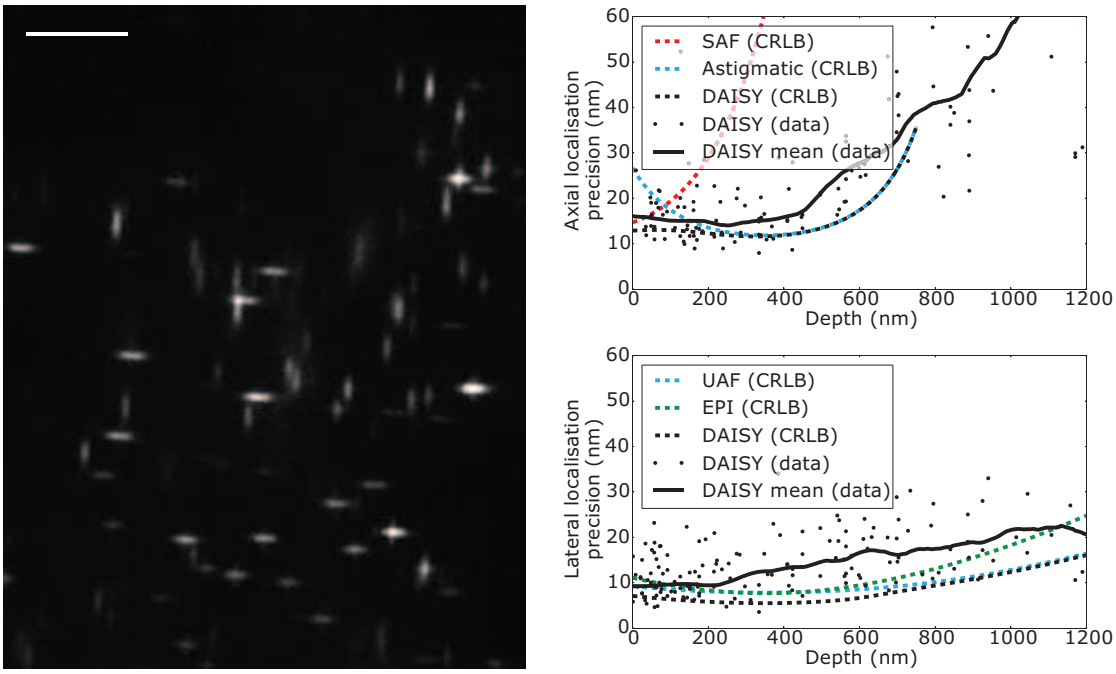

Figure 3.10 – Measurement of the localisation precisions. Left: UAF frame taken on one field of view (40-nm diameter dark red fluorescent beads deposited on fixed unalbelled COS-7 cells, see section B.3.4). Right: axial (top) and lateral (bottom) experimental precisions plotted as a function of the mean z. The data of five different fields were pooled. Each circle stands for one bead, and the solid black curve represents the sliding window average of the data point cloud over a ±50 nm range. The experimental data represent $\sigma_z^{\mathrm{DAISY}}$ and $\sigma_{xy}^{\mathrm{DAISY}}$ respectively. The dashed lines stand for the CRLB values for each detection modality taken separately and for their merging, i.e. for σ_z^{SAF}, $\sigma_z^{\mathrm{astigmatism}}$ and $\sigma_z^{\mathrm{DAISY}}$ on the one hand, and for $\sigma_{xy}^{\mathrm{SAF}}$, $\sigma_{xy}^{\mathrm{astigmatism}}$ and $\sigma_{xy}^{\mathrm{DAISY}}$ (see section C for more information about the CRLB calculations). Scale bar: 5 µm.

between σ_x and σ_y. The experimental localisation precisions are displayed in Fig. 3.10 as a function of z, i.e. the mean value of z^{DAISY} for the bead, alongside with the calculated CRLB values for typical experimental parameters.

Taking advantage of the SAF, the DAISY detection performs well close to the coverslip. After 200 nm, the axial precision is mostly provided by the astigmatism, which does not vary too steeply thanks to the high astigmatism value chosen (see Fig. 3.3). Besides, though the UAF contributes little to the lateral detection, as mentioned in section 3.1, the lateral precision curve remains quite flat over the whole imaging range. In the end, DAISY maintains weakly anisotropic localisation precision in the first 600 nm—this represents a noticeable improvement compared to standard astigmatic imaging, which typically features σ_z values around twice to thrice σ_{xy} and a somewhat reduced detection range (typically ±250 nm around the focus plane). DAISY can still be used up to 1 µm, if with a degraded axial localisation.

We measured the precisions on fluorescent beads only in the far red domain ($\lambda_{\mathrm{fluo}} \approx$ 680 nm). For different wavelengths, the localisation precision should change only slightly. The differences are expected to come mainly from three elements. The first is the

SAF decay, which is sharper at shorter wavelengths (see equation 3.4), thus yielding a better precision near the coverslip, but a quicker dwindling as the depth increases. The second element is linked to the depth of field, which is shorter at shorter wavelengths. This causes the astigmatic PSFs to distort more quickly—here again, this should bring a better precision near the focus, but a sharper deterioration of the axial precision away from the focus. Finally, as the EPI PSFs are narrower at shorter wavelengths, the lateral precision should be better near the coverslip, although it is expected to deteriorate more quickly away from the coverslip due to the limited depth of field. Note that imaging at a different wavelength requires the use of an astigmatism calibration curved performed with the corresponding fluorophore. Note also that the values of the coefficients α_{RT} and β_{mask} (see equation 3.3) are wavelength-dependent and should be calibrated for each fluorescence wavelength. The challenges of multicolour imaging will be more thoroughly detailed in part 3.4.

The performances of DAISY in terms of localisation precision, however, can be highly dependent on several factors, from the size of the spots to the number of photons per PSF. One particular point that has to be considered is the density of active molecules per frame. Indeed, as all localisation-based super-resolution techniques, DAISY fundamentally relies on the single molecule regime hypothesis. In case it is not fully achieved, some localisations may be rejected by the filtering steps performed (see section 3.2) based on the PSF shapes especially, but overlapping spots that are not discarded may lead to axial and lateral mislocalisations.

To assess the impact of the molecule density per frame on the localisation performance of our algorithm and filtering, we simulated DAISY PSFs on a 30 µm x 30 µm field with 100 nm pixels. The PSFs were simulated as elliptical Gaussians for the UAF channel and circular Gaussians for the EPI channel with realistic PSF sizes matching those of experimental data obtained with AF647. All the sources were considered at the coverslip (z = 0 nm) and all the PSFs had the same intensity (2750 UAF photons, 2750–5100 EPI photons depending on the axial position of the source). In order to decouple the effect of the molecule density from the localisation precision, we did not add background or Poisson noise. The lateral positions were uniformly distributed over the field. The number of PSFs per frame ranged from 1 (1.1 10^{-3} molecules.µm^{-2}) to 1000 (1.1 molecules.µm^{-2}), as illustrated in Figure 3.11. The generated positions were recorded for later use.

Then the localisation was run on the generated data and the filters (size and anisotropy of the unastigmatic EPI PSFs, distance between PSF neighbouring pairs) were applied and the number of remaining detections was compared to the number of generated molecules to calculate the fraction of missed/discarded localisations (Fig. 3.12a). Among the remaining localisations, those displaying a 3D distance to the expected position superior to 50 nm were flagged as wrong detections and their fraction among all the localisations after filtering was displayed in Fig. 3.12a in the cases of the SAF and astigmatic detections. Finally, the lateral and axial (for the SAF and the astigmatic detections) median distances to the expected positions were displayed in Fig. 3.12b.

As expected, the numbers of missed/discarded localisations and wrong detections

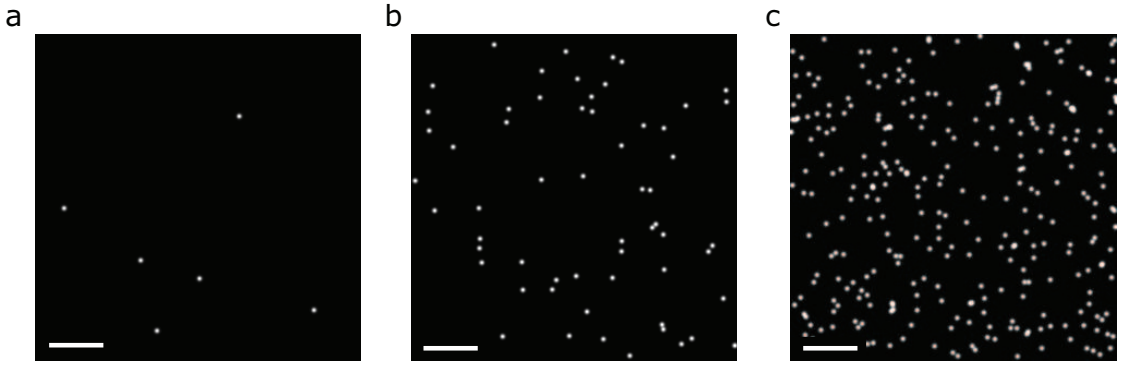

Figure 3.11 – Variation of the density of active molecules per frame. Examples of simulated EPI frames are displayed for three cases: low density (6.7 10^{-3} molecules.µm^{-2}), average density (6.7 10^{-2} molecules.µm^{-2}) and high density (0.33 molecules.µm^{-2}) in **(a)**, **(b)** and **(c)** respectively. Scale bars: 5 µm.

increase with the density, but the latter remains quite low for reasonable densities (under 15 % below 0.3 molecules.µm^{-2}). Similarly, the lateral and axial position discrepancies increase with the density. Realistic dSTORM conditions correspond to densities around 10^{-2}–10^{-1} molecules.µm^{-2}. At such densities, the number of missed/rejected localisations can account for up to 40 % of the total number of localisations, but the number of wrong detections remains minimal (below 4 %). Besides, the errors on the measured positions are rather low (inferior to 4 nm in the lateral and 1 nm in the axial direction, both in SAF and astigmatism).

These results can prove useful to optimise the acquisition conditions—especially the composition of the imaging buffer in dSTORM, the concentration of imager strands in DNA-PAINT or the activation power in PALM, as well as the exposure time for all these methods. In DNA-PAINT acquisitions, relatively high molecule densities (up to 0.3 molecules.µm^{-2}) can be used to speed up acquisitions, as long as the localisation error remains below the localisation precision. On the contrary, in PALM experiments, the number of photoactivable molecules is often low and in order to minimize the number of missed/discarded molecules, the molecule density should be kept low (inferior to 3 10^{-2} molecules.µm^{-2}). Depending on the sensitivity of the fluorophores used to photobleaching, dSTORM acquisitions can match either of the two previously described cases.

3.3.2 Lateral registration accuracy

Secondly, we wanted to assess the lateral registration error in order to ensure that the EPI and the corrected UAF positions are aligned before they are merged together. For this purpose we used different samples: first, we performed the measurement on 40-nm diameter dark red fluorescent beads stuck at the coverslip, using the standard protocol described in section B.3.3. A low illumination power was used in order to match the level of emission of the beads with that of AF647 (see section A.2.3). The results are presented in Fig. 3.13a1–2, and a comparison with the case of DONALD (i.e. a dual-view setup without PSF shaping, see section 1.6.3.2) is provided in Fig. 3.13a3. The residual

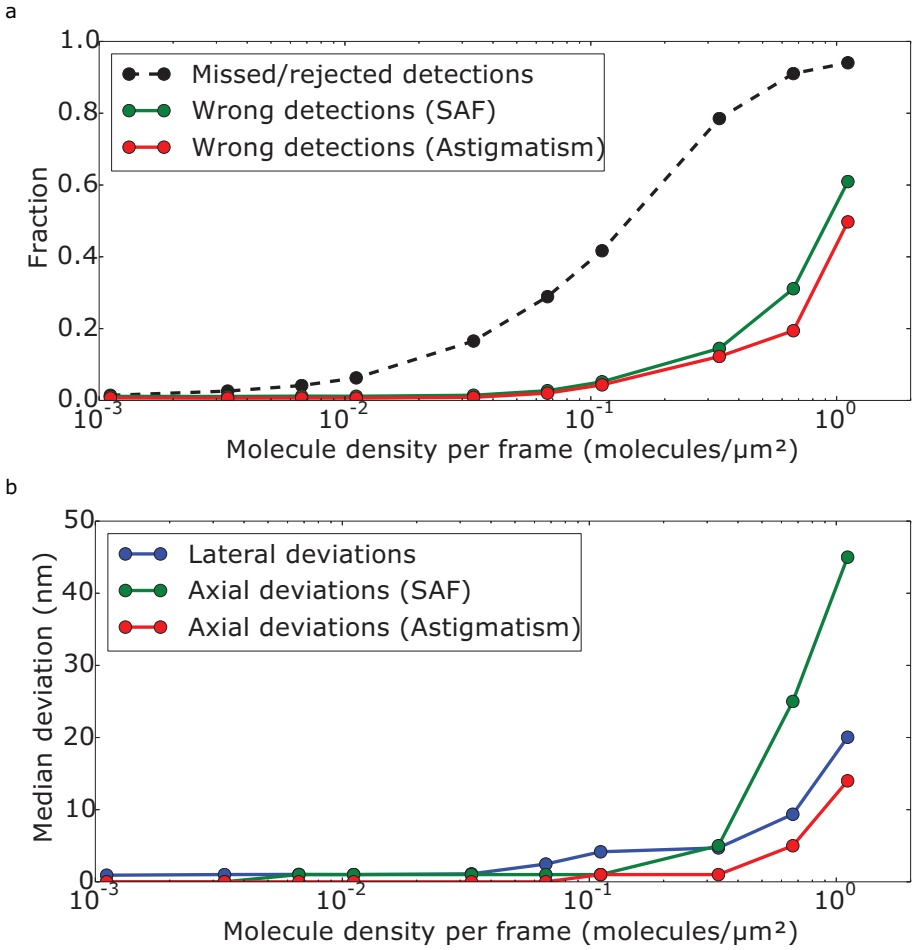

Figure 3.12 – Influence of the molecule density per frame on the localisation computation. **(a)** Fraction of localisations missed or discarded (black dashed line) and fraction of wrong detections (blue and red solid lines) as a function of the molecule density on each frame. **(b)** Median lateral and axial discrepancies between the real and the measured positions as a function of the molecule density on each frame.

discrepancies are slightly superior for DAISY (7 nm) than for DONALD (4 nm). We analyse these results as a proof that our correction algorithm provides a correction accuracy (4 nm) significantly lower than the localisation precision (10 nm at best), but we also hypothesise that our lateral localisation could exhibit a slight PSF shape-dependent lateral bias that would induce higher discrepancies for aberrated PSFs—the centroid detection is known to be biased by the coma aberration for instance. Another explanation would simply be a residual effect of the localisation precision (which is significantly worse with astigmatic PSFs). In any case, one should keep in mind that potential field distortions are bound to be also present in standard (i.e. single channel) astigmatic imaging, in which case they can be neither detected nor corrected because of the lack of reference channel. Thus, our dual-view system allows to mitigate this bias, if not correct it fully. Note that the Fig. 3.13a1 does not seem to show any regular pattern (i.e. the residual registration error does not seem to be field-dependent), which we interpret as a proof that the

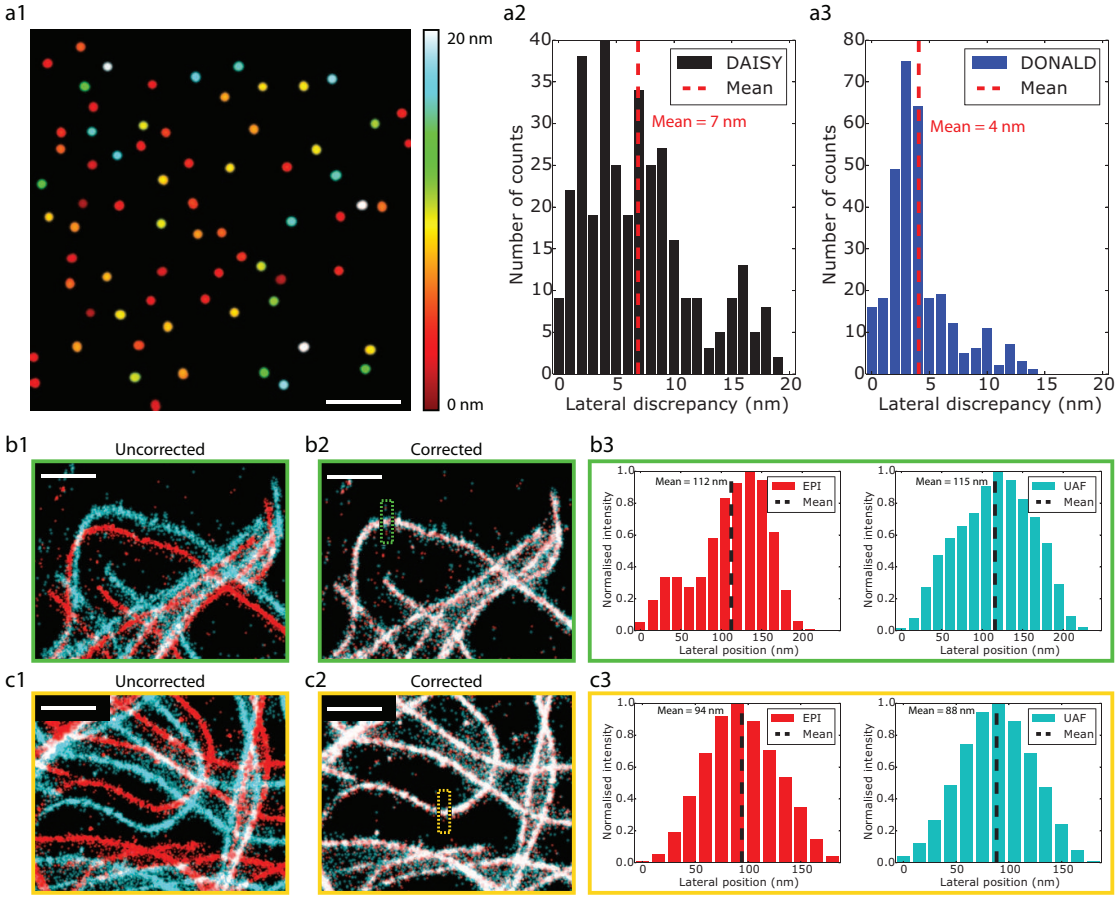

Figure 3.13 – Measurement of the residual lateral registration error after the correction. **(a)** Measurement on 40-nm diameter dark red fluorescent beads deposited at the coverslip (three acquisitions on different fields were stacked): **(a1)** Map of the residual lateral error in DAISY, **(a2)** Residual lateral error histogram obtained with DAISY. As a comparison, the same measurement is provided for a DONALD acquisition (i.e. the same dual-view setup without the cylindrical lens) in **(a3)**. In both cases, the axial positions were averaged over 500 frames to mitigate the influence of the localisation precision. **(b–c)** Measurements performed on the two microtubules regions of interest presented in Fig. 3.9: **(b1–c1)** Superimposed 2D maps (red: EPI path, cyan: UAF path) before running the correction algorithm. The images display large discrepancies (around 500 nm) due to the magnification difference between the x and y axes. **(b2–c2)** Superimposed 2D maps after the correction, **(b3–c3)** EPI and UAF profiles along the axes displayed in **(b2–c2)** respectively after correction. The residual discrepancy is below 6 nm. Scale bars: 5 µm **(a)**, 1 µm **(b)**.

correction algorithm does not leave uncorrected translation, rotation or magnification difference between the UAF and EPI channels.

To further evidence the performance of our correction in terms of lateral registration error, we also measured the lateral discrepancies on a biological sample: we used the microtubules regions of interest presented in Fig. 3.9 to plot the histograms on both channels after correction (Fig. 3.13b–c). This gave values below 6 nm, which is consistent with those obtained on fluorescent beads.

3.3.3 Axial correction performance

Then, the performance of the axial DAISY correction code had to be verified to make sure that the registration precision between the astigmatic and SAF positions is accurate enough to enable their merging. In particular, we wanted to evidence the efficiency of the chromatic aberration, axial drift and sample tilt correction.

3.3.3.1 Chromatic aberration

The chromatic aberration is typically assessed using either one source able to emit at different wavelengths, or several colocalised single colour sources. The first possibility is very straightforward to achieve using multicolour beads, but can also be carried out by resorting to a biological sample with a given protein labelled with DNA-PAINT docking strands and imaging it sequentially with two different imagers. The second possibility (i.e. using colocalised single colour sources) is obtainable by labelling with two different fluorophores the α- and the β-tubulin, or the light chain and the heavy chain in clathrin for example.

We first performed experiments on tetraspeck beads deposited on a coverslip, according to the sample preparation protocol detailed in section B.3.1. The acquisitions were done at low illumination powers (typically 0.025 kW.cm^{-2}) with 100 ms exposure time and 150 EMCCD gain. The beads were excited sequentially at 637 nm, 532 nm and 488 nm, and the data were processed using the DAISY correction algorithm. The results are presented in Fig. 3.14a. While the uncorrected results exhibit axial discrepancies as large as 70 nm, the residual error after the DAISY correction is below 4 nm. It is worth noticing that before the correction the red wavelength appears below the green and blue, which is consistent with the dispersion curve of the objective. Nevertheless, the value is sizeable considering that the objective is apochromatic.

We performed similar measurements on a biological sample—more specifically COS-7 cells having the α-tubulin and the β-tubulin labelled with AF555 and AF647 respectively: the chromatic shift is consistent with the previous results (around 70 nm before the correction, and below 5 nm after).

3.3.3.2 Axial drift

The axial drift can be observed in a very similar way as the lateral drift: Fig. 3.15a presents typical astigmatism results obtained without any correction—the effect of the drift on both the resolution and the bias are clearly visible. Running the DAISY correction algorithm on the data enables the measurement of the drift curve: Fig. 3.15b–c shows typical examples obtained with a biological sample over one dSTORM acquisition and tetraspeck beads in a several hour-long tracking experiment. The drift values during the course of one acquisition are generally large (amplitudes beyond 200 nm have been observed), and almost always superior to the localisation precision, which implies that the resolution of uncorrected acquisitions is bound to be limited by the very drift. Of course, this strongly depends on the optical setup, and especially the stability of the

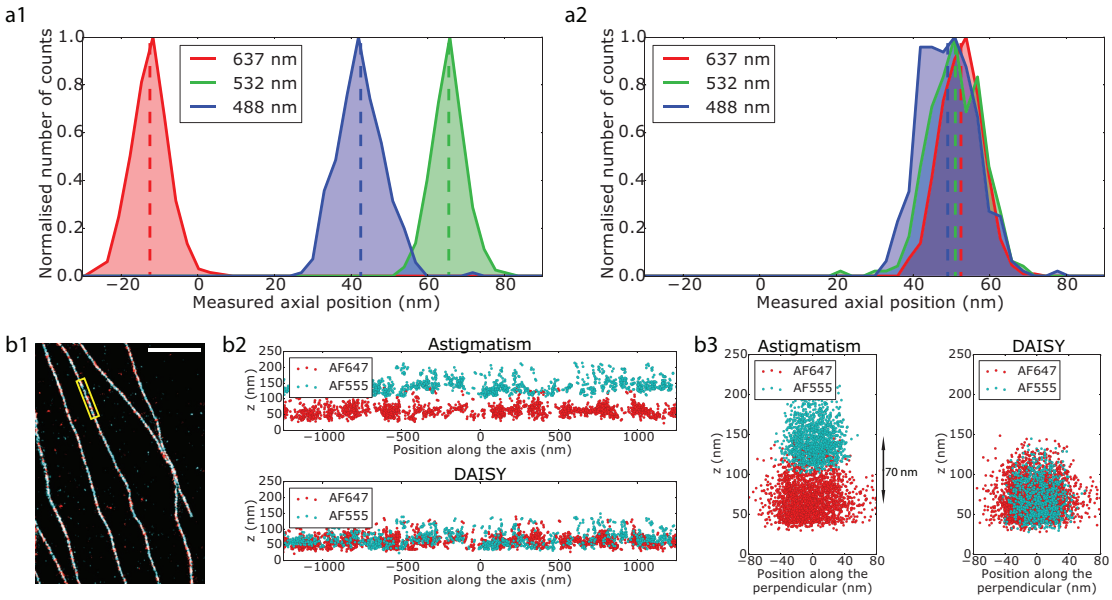

Figure 3.14 – Illustration of the chromatic aberration and measurement of the DAISY chromatic correction accuracy. **a** Histograms of the localised positions measured on tetraspeck beads sequentially shone with 637 nm, 532 nm and 488 nm lasers. The solid lines represent the localisation distributions, and the dashed lines stand for the mean values for the different acquisitions. The results are displayed before (**a1**) and after (**a2**) the correction. Even for the uncorrected results, the sample tilt and the axial drift were accounted for in order to decouple the effect of the axial chromatic aberration from the other detection biases. **b** Measurement of the chromatic aberration on a biological sample. **(b1)** 2D localisation image of microtubules (COS-7 cells, α-tubulin labelled with AF555 and β-tubulin labelled with AF647, see section B) sequentially imaged in two different colours (red: AF647, cyan: AF555). The x-z **(b2)** and y-z **(b3)** profiles of the boxed microtubule are plotted for both standard astigmatic imaging and DAISY. Scale bar: 2 µm.

stage and the axial locking system. Even slight temperature changes (less 1°C) can induce sizeable focus shifts. Nevertheless, the DAISY algorithm is able to measure and correct these drifts to preserve the resolution, as shown in Fig. 3.15a2–3.

3.3.3.3 Sample tilt

Finally, we had to characterise the correction of the sample tilt. Such tilts can be quite difficult to evidence in biological samples, where no references at known positions are available. The most straightforward way to highlight this effect is simply by using beads deposited on a coverslip and measuring their 3D positions. If the sample is placed perfectly horizontally, the depth differences between the different beads are only due to field-aberration induced biases; however, a tilt would induce a slope in the measured axial positions. We prepared a sample of 40-nm according to the standard protocol described in section B.3.3 and imaged them according to the protocol detailed in appendix A.2.3. Using a clustering algorithm, we measured the mean x^{DAISY}, y^{DAISY}, $z^{\text{astigmatism}}$ and z^{DAISY} values for each bead in order to suppress the influence of the localisation precision. Fig. 3.16 presents the corresponding results: discrepancies as large as

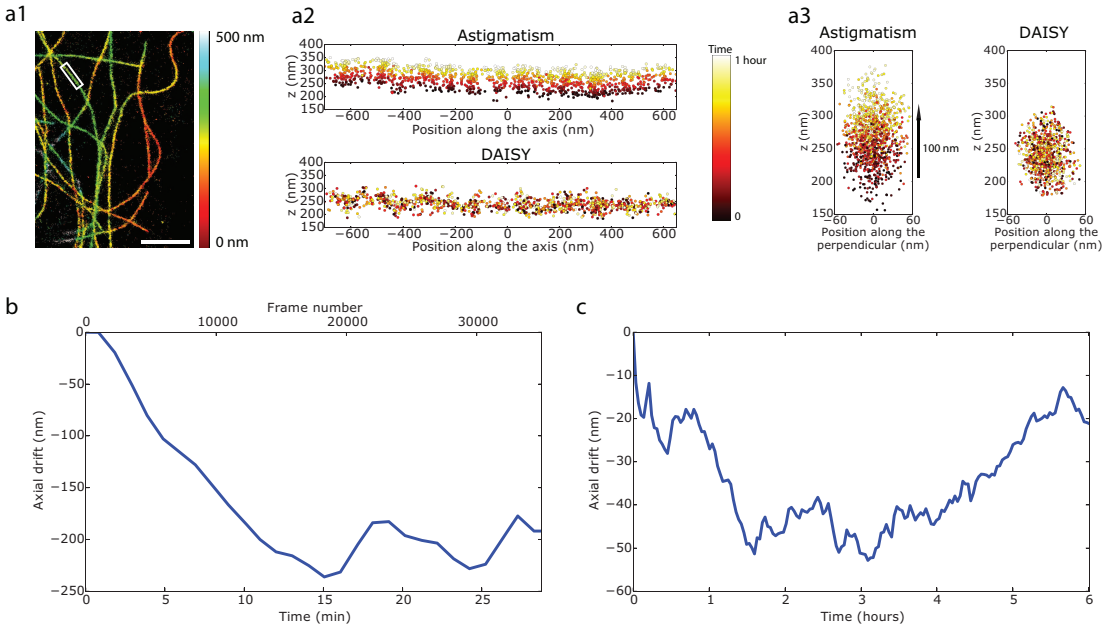

Figure 3.15 – Illustration of the effect of the axial drift. **(a1)** Depth map of microtubules (COS-7 cells, α-tubulin labelled with AF647, see section B). The x-z **(a2)** and y-z **(a3)** profiles of the boxed microtubule are plotted for both standard astigmatic imaging and DAISY. The time is colour-coded over one hour to highlight the effect of the drift over time. **(b)** Drift curve plotted over a whole acquisition on a biological sample (*E. coli* bacteria, LPS labelled with AF647). **(c)** Tracking of the axial drift over several hours on tetraspeck beads deposited on a coverslip.

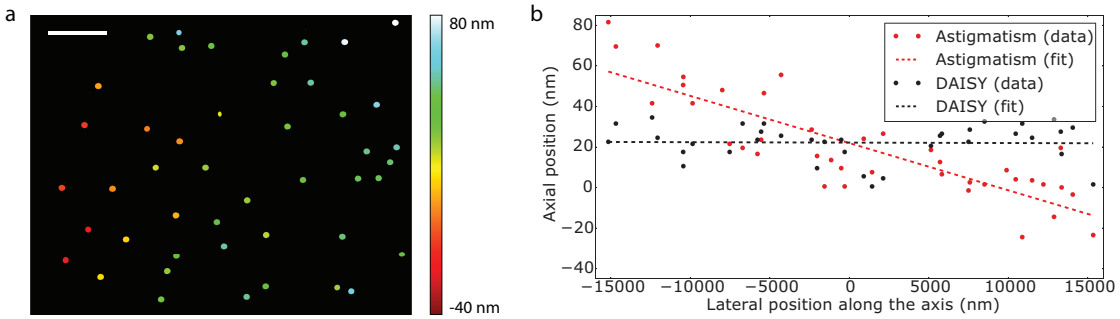

Figure 3.16 – Observation and correction of the sample tilt. **(a)** Image of the $z^{\text{astigmatic}}$ positions in a field of 40-nm fluorescent beads deposited on a coverslip. Note the tilt from the bottom left to the top right corner. **(b)** Comparison of the $z^{\text{astigmatic}}$ and z^{DAISY} positions versus the lateral positions projected along the tilt axis, which highlights the slope induced by the tilt. Scale bar: 5 µm.

70 nm over a 30-µm wide field of view are visible in standard astigmatism. Even though this corresponds to a very slight angle around 0.1°, the effect on the results is obvious. On the contrary, the remaining error after the DAISY correction is very small, below 2 nm over the same field. Consequently, this correction can be considered very accurate to make up for the impact of the tilt.

3.3.3.4 Field-varying aberrations

Having measured very satisfactory results for the correction applied to the axial astigmatic positions using the SAF references in terms of chromatic aberration, axial drift and sample tilt, we furthermore deemed necessary to assess the influence of one last axial bias source that could be anticipated for PSF shaping experiments—the influence of the field-varying aberrations on the PSFs. Indeed, in addition to the aberration deliberately applied in the detection path, other aberrations contribute to modifying the shapes of the PSFs. Most of these aberrations are expected to stem from the objective and the lenses used in the detection setup, and their amplitude is known to be non-uniform over the imaged field [74]. They thus induce field-varying biases in the PSF shaping detection, with amplitudes as large as 100 nm over one field of view reported by von Diezmann *et al*. Although we do not actively perform corrections of these biases, they are expected to have a lower influence in DAISY compared to standard astigmatism. The first explanation to this is the high astigmatism amplitude that we use (800-nm spacing between the focal lines compared to 350-nm, which is a typical value found in the literature). In other words, the PSFs are more strongly aberrated than in standard astigmatic imaging, hence a lesser sensitivity to field aberrations. Besides, the SAF detection relies on an intensity measurement; consequently, it is not expected to be sensitive to PSF shapes, even though it could exhibit field-varying biases if the camera sensitivity was not spatially uniform, or in case the detection setup exhibits partial vignetting somehow.

To assess the influence of these field-varying biases, we imaged 20-nm diameter dark red fluorescent beads (see the sample preparation and acquisition protocols in appendices B.3.3 and A.2.3 respectively). Using again a clustering algorithm, we measured the mean values of x^{DAISY}, y^{DAISY} and z^{DAISY} over 500 frames for each bead. As a comparison, we then repeated the same experiment with a standard astigmatism setup featuring a 350 nm spacing between the two focal lines, and we measured the mean values of x, y and z (calculated using a calibration curve acquired beforehand) for each bead.

The results are presented in Fig. 3.17: DAISY reduces the field-varying biases by almost a factor 2. One could notice that a solution to purposely reduce the influence of these biases would be to perform a spatially resolved calibration, as described in [74]. Still, von Diezmann use beads deposited on a surface, which, as mentioned in part 2.1 and in [53, 54, 56], does not take into account the effect of spherical aberration on the PSFs. In other words, the calibration would require sources distributed at all (x,y,z) positions. This condition is very demanding: a solution would be to use optical tweezers to move fluorescent beads through all the imaged volume, much like in [54]. Another possibility would be to use a sample featuring structures at known heights, such as nanostairs or DNA origamis. Finally, a machine learning algorithm could help create a (x,y,z)-resolved PSF database by accumulating results acquired on many samples.

3.3.3.5 Axial registration accuracy

Eventually, we considered useful to quantify the axial registration error, i.e. the discrepancy between z^{SAF} and $z^{\mathrm{astigmatism}}$ after the DAISY correction. This we did using once

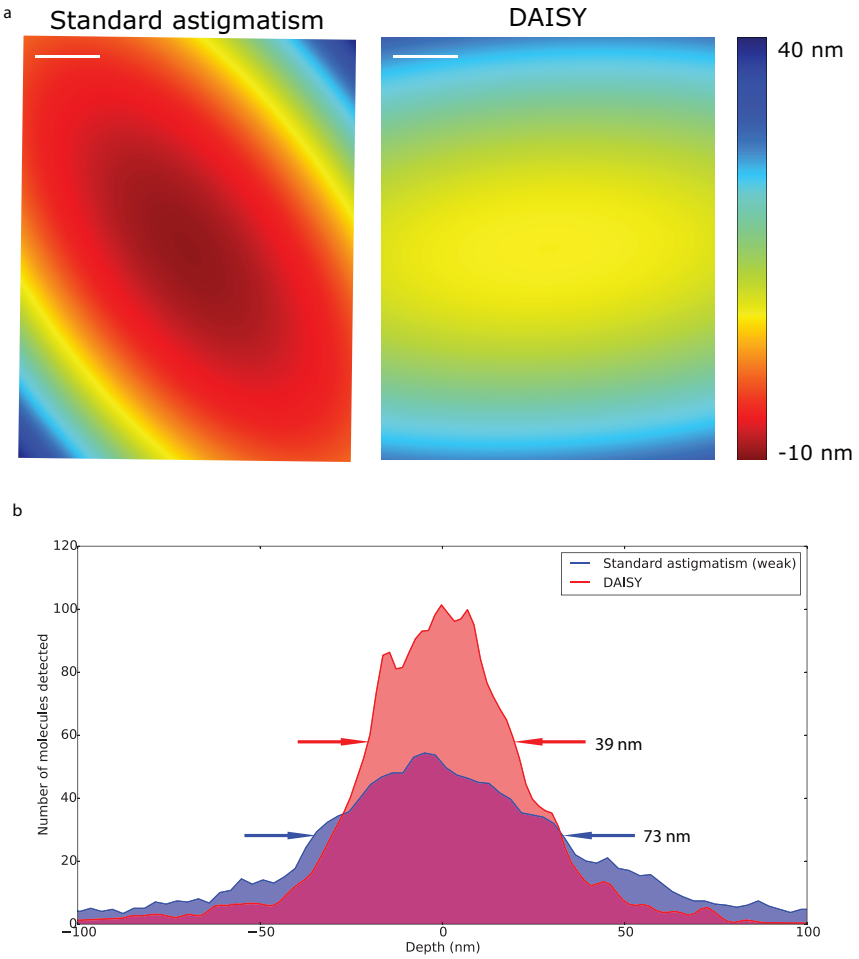

Figure 3.17 – Influence of the remaining field aberrations on the axial detection after tilt correction. **(a)** Interpolated depth maps of the axial positions measured for a sample of 20-nm dark red fluorescent beads deposited on a coverslip and averaged over 500 frames to suppress the influence of the localisation precision. The results are plotted for both a typical astigmatism-based imaging (300 nm spacing between the two focal lines, close to the values encountered in the literature) and for DAISY. **(b)** The depth histograms are plotted over the 25-µm wide field for both the typical astigmatic detection and for DAISY. The displayed widths stand for the full widths at half maximum. Scale bars: 5 µm.

again using 40-nm diameter dark red fluorescent beads imaged over 500 frames, either directly stuck on a coverslip or deposited on COS-7 cells so that they are located at different heights (see the preparation and acquisition protocols in parts B.3.3, B.3.4 and A.2.3).

The results are displayed in Fig. 3.18: in both cases, the axial correction algorithm seems very accurate (1 nm average discrepancy at the coverslip, and 3 nm in the volume, which is well below the localisation precision), in accordance with the performances measured for the DAISY correction software. The histograms exhibit a certain dispersion of the values around the mean value, however (the measured standard deviations are 24 nm and 29 nm respectively for beads on the coverslip and in the volume). This could be due to the fact that the beads have a diameter of 40 nm, hence they are not point sources and

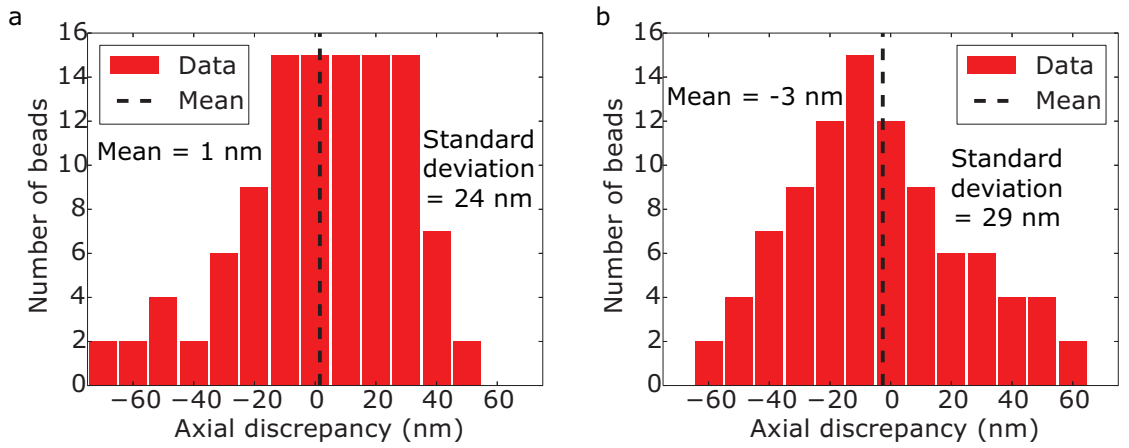

Figure 3.18 – Measurement of the residual axial registration error after the correction. **(a)** Histogram of the residual axial discrepancy (i.e. $z^{\text{astigmatic}} - z^{\text{SAF}}$) obtained with 40-nm diameter dark red fluorescent beads deposited at the coverslip. **(b)** Histogram of the residual axial discrepancy (i.e. $z^{\text{astigmatic}} - z^{\text{SAF}}$) obtained with 40-nm diameter dark red fluorescent beads randomly distributed in the volume and imaged over a 500-nm range above the coverslip. In both cases, the axial positions were averaged over 500 frames to mitigate the influence of the localisation precision.

the spot shapes are not exactly PSFs—in this case, better results could be obtained using a sample of sparsely distributed docking sites for DNA-PAINT labels in the solution. As the dispersion of the values increases for beads in the volume, it could also be attributed to either the decay of the SAF signal in the volume, which causes the SAF localisation precision to become non-negligible, or the influence of the previously mentioned field-dependent aberrations, which induce biases in the astigmatic positions according to the position in the field. This effect is present in conventional single-view PSF shaping imaging too, but it is difficult to detect unless a specifically designed calibration sample is used. The dispersion due to field-dependent aberrations could be mitigated by using a spatially resolved PSF calibration, as in [74].

3.4 Multicolour imaging: stakes and challenges

Once we ensured that the performances of the implementation, setup and correction algorithm were a priori sufficient for 3D super-localisation, we set out to use DAISY for relevant biological studies. Most applications require multicolour imaging in order to analyse the interaction between different proteins through colocalisation evaluation. Multicolour SMLM imaging raises various issues, from the choice of efficient fluorophores to the labelling or the density of active molecules per frame. Whether it requires a simultaneous time-resolved observation of the different species or it can be performed on a fixed sample by imaging the species sequentially, the identification of the molecules is often spectral, although other methods will be presented in chapter 4. This means that, even in a simple case where the identification is trivial, the collected fluorescence may present different wavelengths.

3.4.1 Setup-related challenges

Although DAISY is able to handle—and even especially suited for—multicolour imaging, some preliminary calibration steps are necessary. First, the fluorescence wavelength must be known for each molecule since this knowledge is used for the SAF detection, as formulated in equation 3.4. The SAF detection also requires the specific measurement of the correction factors α_{RT} and β_{mask} applied to the SAF ratio (see equation 3.3), as these two factors are wavelength-dependent. These results can be obtained in a rather straightforward way: α_{RT} only requires removing the physical mask and measuring the intensities on both fluorescence paths for each PSF. No particular constraint is imposed on the sample except that the fluorophore used must be the same (or at least have the same fluorescence wavelength) as that which will be used for biological acquisitions. The measurement of β_{mask}, on the contrary, requires fluorophores stuck at the coverslip. This is not especially easy to achieve: if no fluorescent beads at the right wavelength are available, the best solution is probably to coat a coverslip with biotin and add streptavidin-conjugated fluorophores in dSTORM experiments, or to place docking sites at the coverslip and add the right imager in DNA-PAINT experiments.

The astigmatic detection is also wavelength-dependent: more specifically, aside from the chromatic focal shift, the very PSF shape depends on the fluorescence wavelength, as mentioned at page 93, which is due to the fact that the depth of field is linked to the wavelength—not to mention that unintended optical aberrations in the detection setup are too. Consequently, it is necessary to perform a spectrally-resolved astigmatism calibration. This is quite easy to achieve using the calibration protocol relying on the large microspheres coated with fluorophores [56]. Indeed, one simply needs to use the desired streptavidin-conjugated fluorophores to the biotin-coated microspheres.

Another problem is bound to arise when imaging a fixed sample by sequentially exciting at different laser wavelengths: the images have to be laterally positioned so that the imaged fields are perfectly superimposed. One should notice, however, that this challenge is not linked to multicolour imaging as the lateral chromatic aberration seems to be negligible (i.e. below the lateral localisation precision) on most SMLM setups, but rather to sequential imaging as shifts between the images are bound to stem from the drift. Still, a lateral translation coefficient has to be applied in order to match the images. Depending on the sample, calculating this factor can be more or less straightforward.

The most simple case is that where common structures are available: for instance, if the α- and β-tubulin or the heavy chain and the light chain of clathrin are labelled with two different fluorophores, running a simple cross-correlation algorithm on the final 2D super-localisation images allowing only lateral translation directly yields the x and y shift. Typical examples are those presented in Fig. 3.14b and Fig. 3.23.

A more subtle case is that of only roughly colocalised proteins, such as adducin and β2-spectrin in axons (see Fig. 3.22), which alternate along the filaments with a periodicity around 200 nm. Cross-correlating the structures on the high resolution images would result in incorrectly superimposing the rings formed by the two proteins. A possible

solution is thus to perform the cross-correlation on a low resolution image where the alternating rings are not visible, such as the raw diffraction-limited image or the super-localised image blurred with a 200-nm standard deviation Gaussian filter. In this case, the rough shape of the sample is used rather than the fine structure at the protein scale.

Finally, if no common structures are available between the images reconstructed at different excitation wavelengths, adding fiducial markers in the sample may be useful. This solution is not ideal nonetheless: as fluorescent beads do not blink, they are likely to prevent the SMLM reconstruction of neighbouring structures. Besides, they are subject to photobleaching in long dSTORM or DNA-PAINT experiments. Finally, they increase the complexity of the sample preparation step. Another possibility that does not involve any sample modification is to add to the drift curve obtained for each acquisition the total (i.e. final) drift values of the previous acquisitions. This is sufficient if the acquisitions are chained without any delay. Finally, one could record diffraction-limited images at low illumination powers with each excitation laser before starting each SMLM acquisition, which would allow to track the lateral drift between the different acquisitions by running a cross-correlation algorithm between the diffraction-limited images recorded at different times.

3.4.2 Choice of the labels

Aside from this issue, DAISY is highly insensitive to chromatic effects once the required calibrations are performed, as both the SAF correction factors and the astigmatism calibration are stable in the course of months or even years. Having dealt with the problems related to the setup, the last step before imaging multicolour samples was the labelling. Overall, we found that the main hindrance to multicolour bioimaging was the choice of the fluorophores based on their photophysical properties in the imaging buffer. More specifically, we noticed that the best dSTORM fluorophores—i.e. those exhibiting low ON state times, high photon emission rates per ON/OFF cycle and low photobleaching—were almost exclusively in the far red fluorescence domain. This makes multicolour labelling very challenging as multiple far red fluorophores would be simultaneously excited by the 637-nm laser, thus preventing sequential acquisitions. Although some methods are available for simultaneous demixing (see chapter 4), we chose to limit our observations to sequential multicolour imaging first.

AF647, CF647 both exhibit a very satisfactory photophysical behaviour in our standard dSTORM imaging buffer. CF660C, CF680 and Cy5 also perform well. AF680, on the contrary, exhibits a poor performance, with a low photon count and a noticeable photobleaching.

In the green-excitable domain, most fluorophores that we tested exhibit poor blinking performance and high photobleaching sensitivity. Only AF555 seemed valid, even though it is less than ideal as the labelling seems to progressively detach from the binding sites over time when the laser beam is shone on the sample. Experimentally, from the beginning of the acquisition (i.e. from the moment the laser power is increased to achieve single molecule regime) the amount of non-specific signal gradually increases.

In the meantime, the specific signal dwindles: the number of imaged molecules actually localised on their target drops. After about ten minutes, almost no specifically bound probes remain. It would be interesting to quantify this process, for instance using the SQUIRREL algorithm (see [75], Supplementary Note 11).

Finally, in the blue-excitable domain, we found that no fluorophore is really suited for dSTORM imaging, not even AF488 or Atto488, even using a different buffer such as that containing ascorbic acid and methyl viologen mentioned in [47].

In this regard, DNA-PAINT could be a sound alternative to dSTORM, even if it induces much more background light: indeed, in this binding/unbinding regime, the blinking is mostly defined by the chemical affinities of the DNA strands rather than the photophysical behaviour of the fluorescent molecules. Photobleaching is furthermore almost negligible. Thus, cyanines, rhodamines and oxazines are expected to exhibit differences mostly in terms of photon counts, allowing the use of efficient sets of well spectrally resolved fluorophores.

3.5 Biological applications

Thanks to its insensitivity to axial detection biases, DAISY is especially suited for reproducible bioimaging. In particular, the results of sequential acquisitions on different regions of interest can easily be pooled together without the need to apply axial corrections, for instance to match the focal planes. As mentioned in section 3.4, sequential multicolour acquisitions are also vastly facilitated provided that a satisfactory fluorophore set is available. In this part, we will show results acquired on various biological samples, both to verify the performances on standard ones and to study relevant biological or chemical questions requiring reliable 3D single molecule imaging.

3.5.1 Standard biological test samples

First, we used fixed COS-7 cells as test samples, as this is often done in SMLM development articles. Commonly encountered labellings include tubulin, actin, clathrin coated pits, mitochondria and nuclear pore complexes. We mainly focused on the first three.

Tubulin is perhaps the most frequently presented: aside from the facts that the labelling step is very simple to perform and that very specific antibodies are commercially available, microtubules can be used to assess the resolution to some extent. Indeed, two close filaments can be distinguished or not depending on the resolution of the technique. This method is far from ideal, however, as it relies on finding the right zone to perform the measurement. Besides, to adjust the size of the integration area, a compromise has to be found, as a short length could provide too low a number of localisations, while a long one would imply integrating over a zone where the microtubules are not straight or not horizontal. Finally, the ground truth (i.e. the actual positions of the microtubules) is not known a priori.

Another method based on measuring the hollowness of microtubules exists, which was described in section 2.2.2.1, Figure 2.9. The main idea is to measure the apparent diameter of microtubules, which results from a combination of the diameter of the very filaments, the size of the label and the localisation precision—the better the precision, the more clearly the hollowness is resolved, and thus the more distant the two peaks of the localisation histogram. Note that as the localisation precision is expected to be both z-dependent and slightly anisotropic, the hollowness is expected to be somewhat elliptical rather than circular, as well as more or less clearly resolved at different positions in the capture range. Such a method has the advantage of being especially adapted in the precision range of most 2D or 3D dSTORM imaging experiments, hence a good sensitivity to the precision. Still, it also suffers from major drawbacks. The first is very similar to that previously mentioned: in order to have enough localisation events to plot a statistically significant distribution, it is necessary to integrate over a certain length along the filament, which can cause a dramatic effect on the visibility of the hollowness if the filament is not perfectly straight or horizontal. Besides, the precision value that can be extracted from the diameter measurement is quite sensitive to hypotheses made on the sizes of the microtubules and the label, while neither of them is very well documented in the literature.

Nevertheless, we chose to use this method to extract a localisation precision value, which we intend to compare to those measured on fluorescent beads (see Fig. 3.10). We thus imaged COS-7 cells labelled with AF647 on the α-tubulin. The results are presented in Fig. 3.19: we deduce from those measurements that the 3D localisation precision at 40 nm depth for that experiment is around 14–16 nm, which is consistent with the values obtained on fluorescent beads.

We furthermore resorted to actin imaging to evaluate the 3D resolution. This is rather straightforward, as one simply needs to distinguish two filaments of the sub-network to prove the resolution power of the instrument. This is expected to be simpler than with microtubules, as the phalloidin-conjugated labels used to stain the actin are known to be much shorter than antibody-conjugated fluorophores, which results in the probes being much closer to their targets. Moreover, the phalloidin-AF647 especially is known to exhibit a PAINT behaviour. Such a transient binding/unbinding regime allows much longer acquisitions due to the reduced influence of the photobleaching, at the cost of a higher background intensity. This is useful for resolution measurements as it allows one to integrate the localisations over a shorter area. The results are presented in Fig. 3.20: DAISY is sufficient to clearly resolve sub-network filaments as close as 27 nm in xy and 55 nm in axial—although it would most likely be possible to resolve closer filaments in the axial direction providing a suitable zone can be found.

We eventually used DAISY for reproducible and reliable sequential multicolour imaging, first on a standard cytoskeleton labelling (tubulin and actin): the image is displayed in Fig. 3.21. We chose to image both species with a PAINT labelling so that we could acquire for a long time (about one hour for each colour) without having to worry

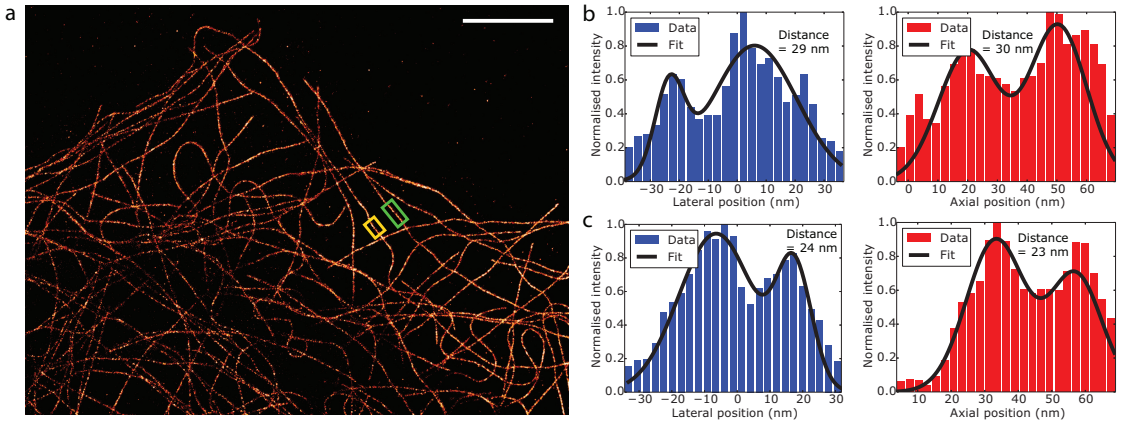

Figure 3.19 – Visualisation of the hollowness of microtubules to measure the localisation precision. **(a)** 2D super-localised image of COS-7 cells with α-tubulin labelled with AF647 (see section B). The acquisition is the same as that presented in Fig. 3.9. The lateral (blue) and axial (red) histograms are then plotted in the green boxed region **(b)** and in the yellow boxed region **(c)**. Both the experimental data and the fitted profile with a double Gaussian function are displayed, as well as the distance between the two Gaussian peaks. The hollowness is clearly visible, and the distance between the peaks corresponds to a localisation precision around 14–16 nm (see Ref. [47], **Supplementary Fig. 7**). Scale bar: 5 µm.

about photobleaching, which is a real challenge in multicolour imaging, as mentioned in part 3.4. This protocol can prove tricky to put into action, though, as the phalloidin-AF647 is first imaged in the standard dSTORM buffer, whereas the DNA-PAINT probe is imaged in a different, dedicated buffer. It is thus necessary to remove the buffer, rinse the sample and add a new buffer between the two acquisitions without changing the field of view—this is still feasible if one handles the tools carefully.

3.5.2 State-of-the-art biological and chemical studies

In collaboration with the team of Christophe Leterrier (Aix-Marseille Université), we also visualised the periodic sub-membrane scaffold present along the axon of cultured neurons [76]. We imaged the 3D organisation of two proteins within this scaffold: adducin (labelled with AF647) that associates with the periodic actin rings, and β2-spectrin (labelled with AF555) that connect the actin rings (Fig. 3.22a–c). The lateral resolution allowed us to easily resolve the alternating patterns of adducin rings and β2-spectrin epitopes and their 190 nm periodicity (Fig. 3.22d) [77]. Thanks to the axial resolution of DAISY, we were also able to resolve the sub-membrane localisation of both proteins across the whole diameter of the axon at 600 nm depth (Fig. 3.22e).

Finally, we illustrate the performances in terms of localisation precision and colocalisation suitability by performing acquisitions on living *E. coli* bacteria adhered to a coverslip. The envelope of bacteria was labelled with both AF647 and AF555 using a click chemistry process (see section B) [16, 78]. This study results from a collaboration with the team of Boris Vauzeilles, Aurélie Baron and Marie-Ange Badet-Denisot (Insti-

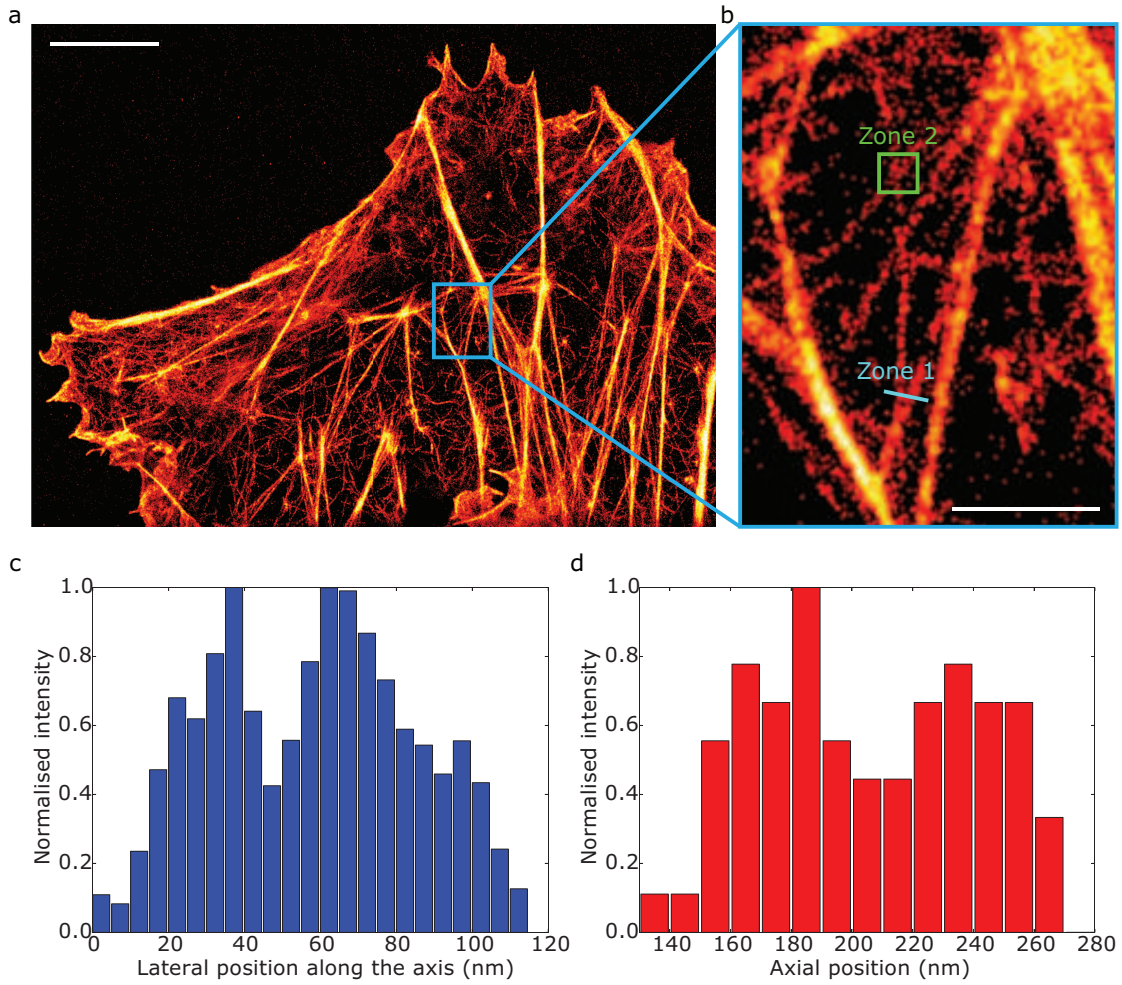

Figure 3.20 – DAISY imaging of actin and measurement of the 3D resolution in COS-7 cells labelled with phalloidin-AF647 (see section B). **(a)** 2D image of the field of view. **(b)** Zoom on the boxed region displayed in **(a)**. **(c)** Lateral histogram of the localisations along the axis displayed in **(b)** (zone 1). **(d)** Axial histogram along a vertical axis in the area displayed in **(b)** (zone 2). Scale bars: 5 µm **(a)**, 1 µm **(b)**.

tut de Chimie des Substances Naturelles, CNRS, France, and Laboratoire de Synthèse de Biomolécules, Institut de Chimie Moléculaire et des Matériaux d'Orsay, Université Paris-Sud, France). Since the lipopolysaccharide (LPS) layer is thin in Gram-negative bacteria, this is a good sample to observe the influence of the localisation precision. We present in Fig. 3.23a–b 2D and 3D images of a region of interest and in Fig. 3.23c an x-z slice along the line displayed in Fig. 3.23a. The measured diameter of the bacterium is around 1 µm but it does not exhibit a strong loss of resolution at its edges. To evidence this, we also plotted the lateral and axial histograms in the boxed regions (Fig. 3.23c). The axial standard deviations were found to be respectively around 30 nm and 45 nm at the bottom and at the top of the cell, while lateral standard deviations were around 27 nm in both colours. Taking into account the size of the LPS layer (<10 nm), of the label—i.e. the DBCO-sulfo-biotin and streptavidin-AF construction—(10 nm) and the effect of the

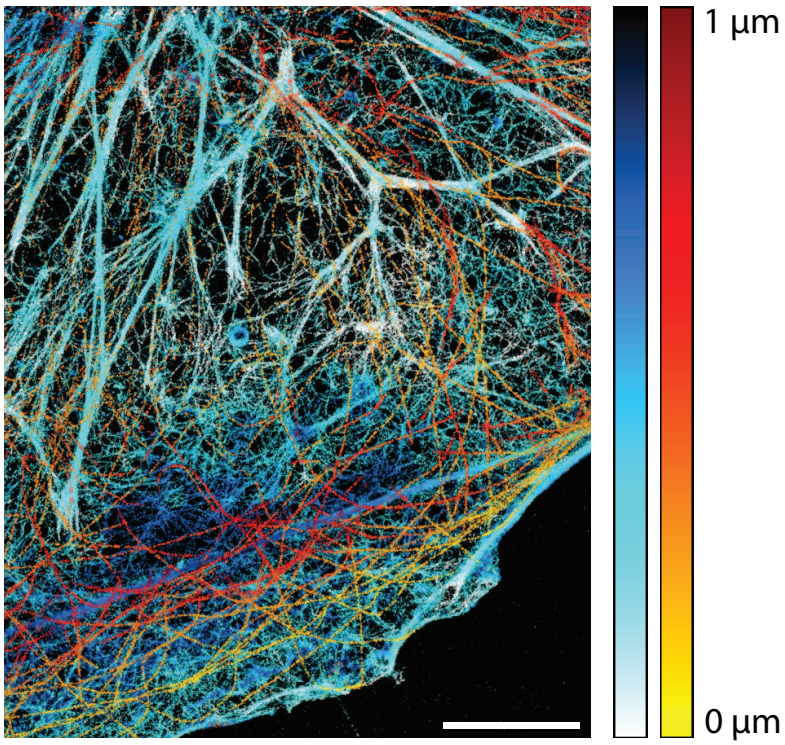

Figure 3.21 – Dual-colour sequential imaging of the cytoskeleton of COS-7 cells. The actin was labelled with phalloidin-AF647 and the α-tubulin was labelled with DNA-PAINT secondary antibodies and imaged with a 560-nm-excitable imager (see section B). The 3D DAISY image is displayed (colour-coded depth: cyan–blue for actin, red–yellow for tubulin). Scale bar: 5 µm.

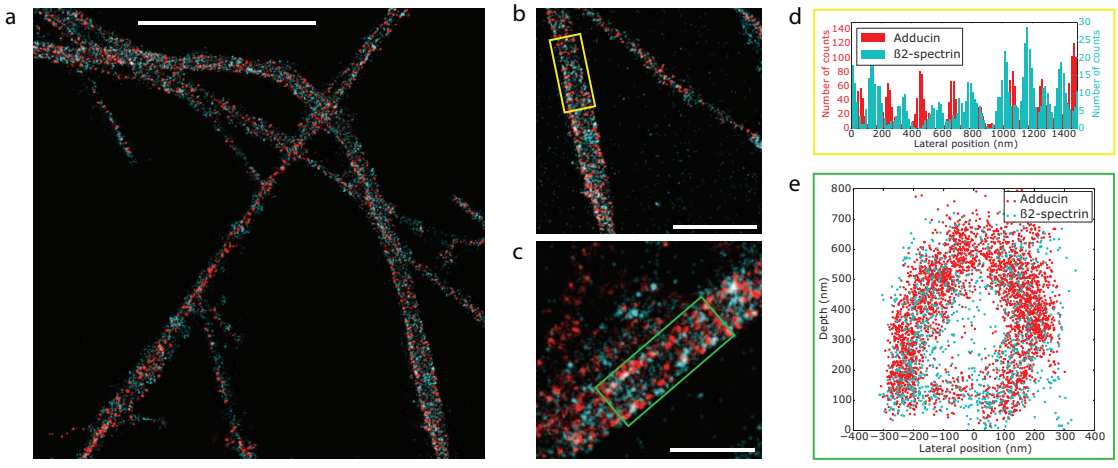

Figure 3.22 – Multicolour imaging of the sub-membrane scaffold in axons of rat hippocampal neurons where the adducin and the β2-spectrin were labelled with AF647 and AF555 respectively (see section B). **(a–c)** 2D dual-colour (red: AF647, cyan: AF555) of various regions of interest. **(d)** Lateral profile along the axis of the yellow box displayed in **(b)**. **(e)** x-z slice along the green box displayed in **(c)**. Scale bars: 5 µm **(a)**, 2 µm **(b)**, 1 µm **(c)**.

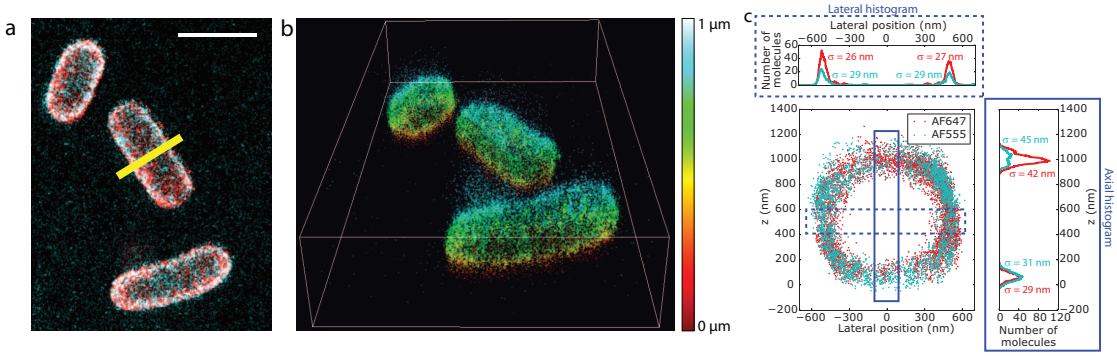

Figure 3.23 – 3D multicolour imaging of living *E. coli* bacteria where the LPS layer was labelled using a click chemistry process (see section B). **(a)** 2D SMLM image of living *E. coli* bacteria labelled with both AF647 (red) and AF555 (cyan) at the membrane. **(b)** 3D view of the field displayed in **(a)**. The depth is colour-coded (one single colour map is used for both AF647 and AF555). **(c)** x-z slice along the line displayed in **(a)** and axial and lateral profiles in the boxed regions. The σ values stand for the standard deviations of the distributions. Scale bar: 5 µm.

curvature of the bacterium over the width of the area used for the analysis (10 nm), these values are consistent with the localisation precision curves plotted in Fig. 3.10.

As a comparison, the results obtained on the same sample with uncorrected astigmatism and with DONALD are provided in Fig. 3.24. Like DAISY, DONALD features an absolute detection, insensitive to both chromatic aberration and axial drift. However, the axial precision of DONALD deteriorates sharply with the depth due to the decay of the SAF signal; thus the top half of the sample (beyond 500 nm) is hardly visible, whereas DAISY clearly permits of imaging up to 1 µm. Uncorrected astigmatism has the same capture range as DAISY, but since it lacks the absolute information, it exhibits an axial shift between the two colours as well as a broadening of the histogram widths due to the axial drift.

The goal will be to eventually characterise the density of the DBCO-sulfo-biotin labelling. In other words, we aim at determining how many sugar molecules were incorporated to the LPS per area unit versus the concentration of sugar in the solution during the culture. This could be achieved by first counting the number of detections over the whole imaging range for each bacterium. This amount would then have to be divided by the number of localisations obtained for one isolated binding site. Indeed, one biotin binding site is expected to be linked to only one streptavidin molecule, but each streptavidin molecule could carry several AF647 molecules, not to mention that, due to the blinking, each AF647 is bound to be detected several times before photobleaching. This measurement could be performed by dramatically reducing the concentration of DBCO-sulfo-biotin in order to keep only a few isolated binding sites for the streptavidin-AF647 per cell. Taking advantage of the resolution power of DAISY, these sites could be distinguished and counted. Note that this solution does not require multicolour imaging, but strongly relies on the fact that the capture range of DAISY is around 1 µm, which is sufficient to image the whole bacteria without missing localisation events. Finally,

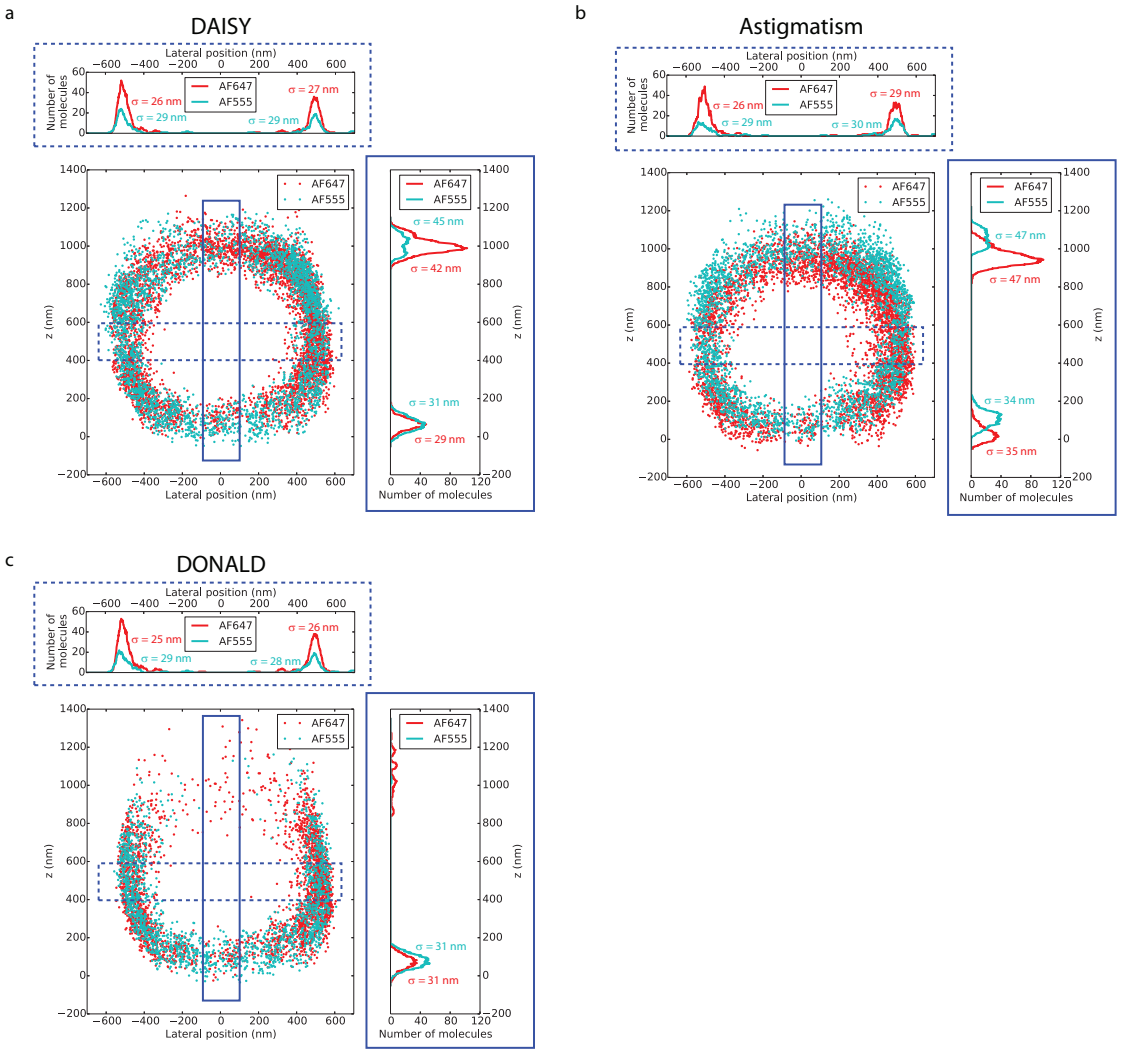

Figure 3.24 – Comparison of the 3D performances of **(a)** DAISY, **(b)** uncorrected astigmatism and **(c)** DONALD on a sample of living *E. coli* bacteria labelled with AF647 and AF555 at the membrane (see section B). The sample and the region of interest are the same as those shown in Fig. 3.23. The *x*-*z* slices along the line displayed in Fig. 3.23a and the axial and lateral profiles in the boxed regions are plotted. The σ values stand for the standard deviation of the distributions. Like DAISY, DONALD features an absolute detection, insensitive to both chromatic aberration and axial drift. However, the axial precision deteriorates sharply with the depth due to the decay of the SAF signal; thus the top half of the sample (beyond 500 nm) is hardly visible. Uncorrected astigmatism has the same capture range as DAISY, but since it lacks the absolute information, it exhibits an axial shift between the two colours as well as a broadening of the histogram widths due to the axial drift.

this approach relies on the hypothesis that no molecule is missed during the acquisition, which is not really the case in most dSTORM acquisitions (see part 3.3 and Fig. 3.12). This implies that it would be necessary to either reduce the density of active molecules per frame (for instance using PALM or DNA-PAINT rather than dSTORM), or at least assessing the proportion of missed events.

3.6 Improvement prospects

In spite of the benefits brought by DAISY compared to uncorrected standard astigmatic imaging, the method still remains hampered by various bottlenecks. In this section, we will list them and propose improvement prospects.

3.6.1 Suppression of remaining biases and inaccuracies

The first element that has to be mentioned is the merging of the positions, both lateral and axial. As described in part 3.1 and Fig. 3.8, we used the theoretical precisions to determine the relative weights of the different sources of information (see equations 3.1, 3.2 and 3.8). Although this is simple to implement, this is probably not the best solution, as the experimental precisions may differ from the CRLB predictions. In particular, the the UAF positions are significantly worse than the theoretical expectation; thus, the DAISY lateral positions would be roughly equal to the EPI positions: $x^{\mathrm{DAISY}} \approx x^{\mathrm{EPI}}$ and $y^{\mathrm{DAISY}} \approx y^{\mathrm{EPI}}$. Note that it may be possible to improve the UAF lateral detection, for example using cubic spline algorithms, as the experimental precisions obtained are still far from the CRLB. In that case, the UAF contribution to the lateral detection may not be negligible any more.

The influence of field aberrations on the PSF shapes is another issue. They induce field-varying biases that are bound to result in axial offsets, but also variations of the slope of the $w_{x,y}^{\mathrm{UAF}}(z)$ calibration curve [74]. We measured the offsets for fluorescent beads located at the coverslip (Fig. 3.17) and noticed that the values were non-negligible (around 15–20 nm over one field of view, which is of the same order as the axial localisation precision). Obviously, they result in field-varying axial discrepancies between the SAF and astigmatic positions, as the two have different sensitivities to the effect of aberrations (especially, the SAF is almost insensitive to PSF shapes): the axial registration error was found to be around 25–30 nm (Fig. 3.18).

This point was discussed in section 3.3: even though the problem is not specific to DAISY—on the contrary, standard PSF shaping does not even allow the assessment of these discrepancies, while DAISY not only highlights them, but also suppresses them partially—correcting it would bring a major improvement. As mentioned at page 102, this would require performing a calibration on a sample featuring point sources distributed over the whole (x,y,z) imaging volume. The easiest solution would thus probably be to stack results obtained through acquisitions performed on different fields of view in order to have enough detections to retrieve a statistically sufficient data sample. A machine learning approach could help by systematically recognising PSFs acquired in all acquisitions processed—on both biological and calibration samples—and feeding them to a large (x,y,z)-resolved PSF dictionary. Note that one dictionary should be built per fluorophore, or at least per fluorescence wavelength. Although this requires more acquisitions, the spectral differences could actually be used to discriminate different fluorophores (for instance CF647 and CF680) simultaneously excited at the same wave-

length and thus present on the same frames. The question of simultaneous demixing will be dealt with more thoroughly in chapter 4.

3.6.2 Extension of the capture range

Another shortcoming of DAISY is the fact that it is limited to imaging near the coverslip. Indeed, due to the sharp decay of the evanescent field, almost no SAF signal is left after roughly 500 nm, which essentially turns DAISY into a mere dual-view strong astigmatic imaging setup by forbidding the SAF-astigmatism cross-correlation-based correction. While we do not have a solution to retrieve SAF signal from the volume of the sample, we can propose a means to improve the imaging range of the technique by stacking sequential acquisitions performed at different focus positions. The main concept is not new [79], but what makes DAISY especially suited for this is that the first slice is intrinsically self-referenced thanks to the SAF information. This reference will then be transferred to the subsequent slices using once again a sample-based 3D cross-correlation algorithm to perfectly superimpose the structures. Of course, it requires that two successive acquisitions contain common features—in other words, there must be a certain overlap between the axial imaging ranges.

Since the SAF signal quickly decays with the depth in the first 500 nm above the coverslip, the absolute reference is accessible only in the first slice. Still, as it provides unbiased results, the top of this first slice serves as an absolute reference for the next slice, which is matched to the previous using a sequential lateral, then axial position cross-correlation algorithm. In other words, the first 1 µm unbiased slice is interlaced with the following one, which contains the positions between 600 nm and 1.6 µm typically (as described in the schematic in Fig. 3.25a). The absolute reference is thus transferred from the first slice onto the second, which becomes insensitive to axial detection biases. Similarly, the third slice, containing positions from 1.2 µm to 2.2 µm typically, is intertwined with the second by position cross-correlation and thus it also benefits from the absolute reference and the bias insensitivity that it brings. Several slices can be recorded and merged together to obtain an extended depth image—still, this is limited by photobleaching (although this can be mitigated by using (DNA-)PAINT labelling), as well as aberrations inherent in depth imaging, which cause the axial and lateral precisions to deteriorate away from the coverslip. Moreover, registration errors are likely to add as the number of slices increases, so using fiducial markers might be necessary to merge more slices. We illustrate the method with a single-colour acquisition series (COS-7 cells, α- and β-tubulin labelled with AF647) in Fig. 3.25b–d: the stack of the three slices (Fig. 3.25e) obviously shows information in deep regions (beyond 1 µm) that would not be accessible with a single acquisition. We then imaged a dual-label tubulin-clathrin sample (COS-7 cells, light chain and heavy chain clathrin labelled with AF647, α- and β-tubulin labelled with 560-nm-excitable DNA-PAINT imager) in three sequential acquisitions while shifting the focus by 600 nm between each of them to obtain a 3D dual-colour 2-µm imaging range set of data (Fig. 3.25f). Aside from the fact that no axial mismatch between the subsequent acquisitions is observed, the localisation precision remains satisfactory after

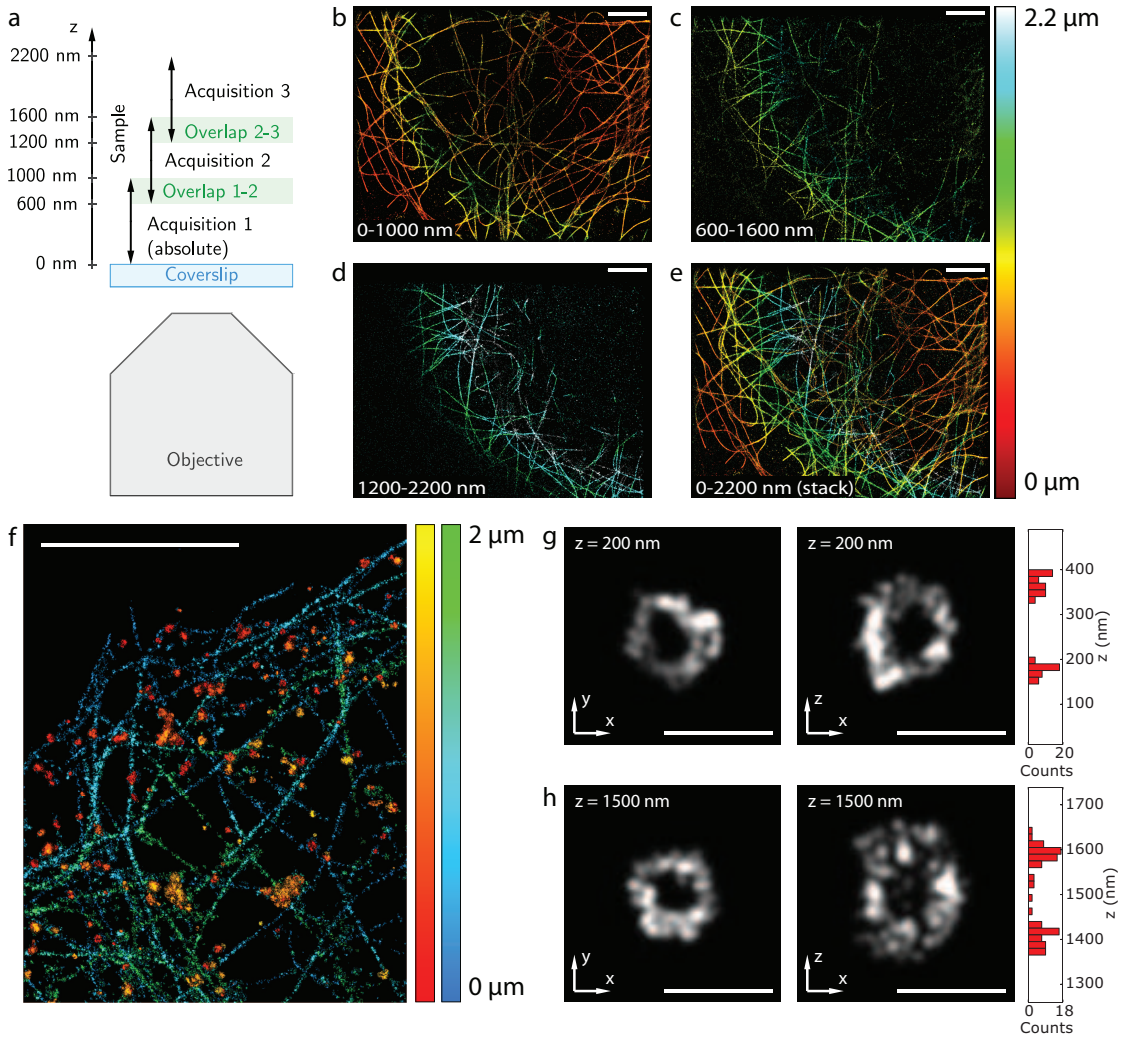

Figure 3.25 – Extended depth imaging principle and results. **(a)** Description of the acquisition protocol: several sequential acquisitions are performed at different focus positions with a sufficient overlap between them to enable the stitching of the different slices (the focus is typically shifted by 600 nm between successive acquisitions, while the capture range is around 1 µm for each acquisition). **(b–d)** 3D images reconstructed from single-colour tubulin acquisitions performed at three different focus positions (COS-7 cells, α- and β-tubulin labelled with AF647). **(e)** Final 3D image obtained by stitching the three consecutive acquisitions. The total range is around 2.2 µm. **(f)** 3D extended range dual-colour image of clathrin (red-yellow) and tubulin (blue-green) obtained from three sequential acquisitions (for each colour) at different heights (COS-7 cells, heavy chain and light chain clathrin labelled with AF647, α- and β-tubulin labelled with a 560-nm excitable DNA-PAINT imager). **(g–h)** x-y and x-z slices of two clathrin spheres taken from **(f)** at two different depths (200 nm and 1500 nm). The axial histograms of the x-z images are displayed on the right, and the lateral histograms are displayed in Fig. 3.26. Scale bars: 5 µm **(b–f)**, 250 nm **(g–h)**.

1.5 µm as it is limited only by the effect of spherical aberration and sample-induced aberrations. To evidence this, we measured the dispersion of the localisations on two clathrin spheres located close to the ventral membrane (200 nm depth) and the dorsal membrane

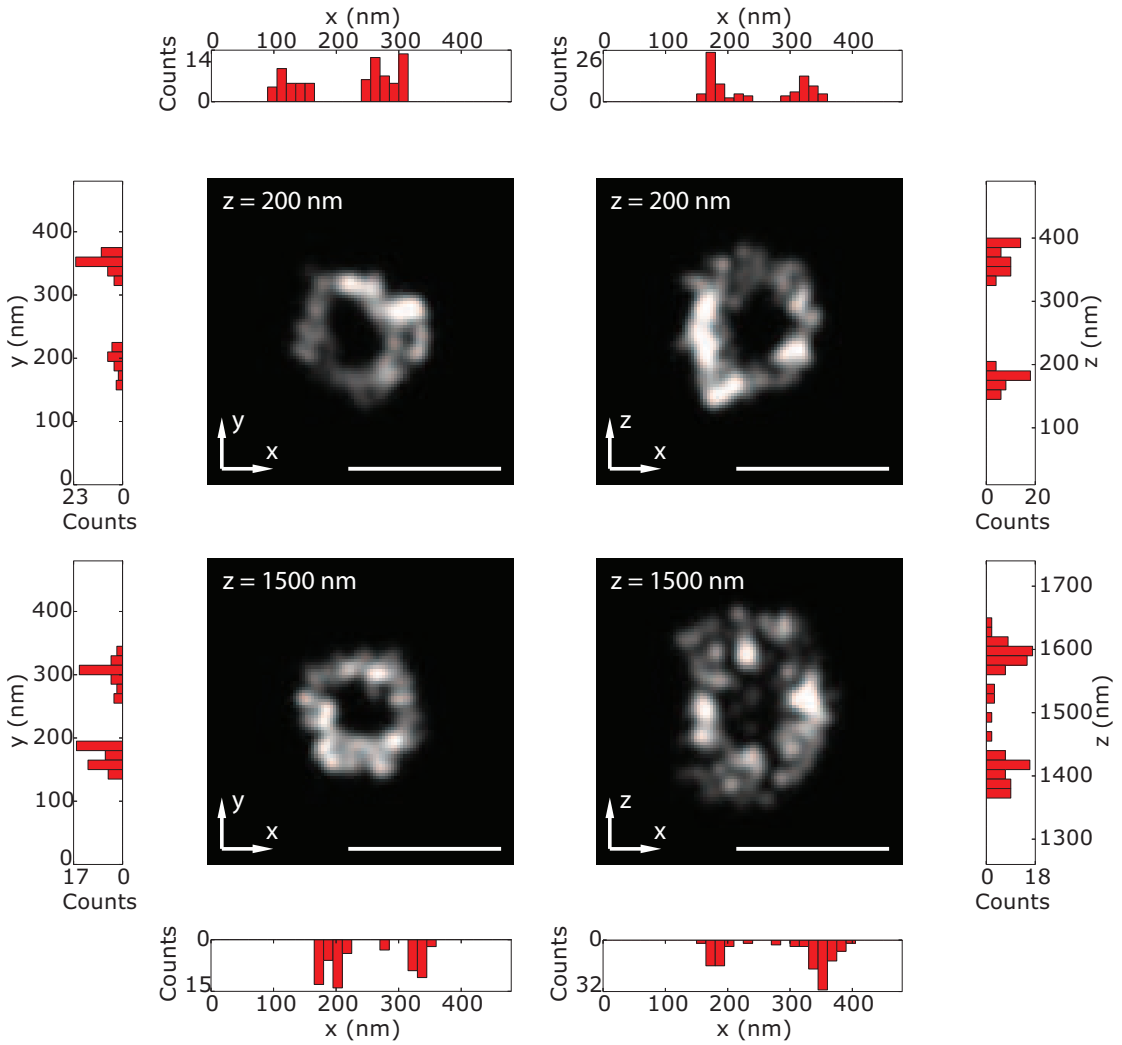

Figure 3.26 – Lateral and axial histograms plotted on the clathrin spheres presented in Fig. 3.25g–h. The histograms are plotted along lines at the centre of the spheres to highlight their hollowness. Scale bars: 250 nm.

(1500 nm depth) respectively (Fig. 3.25g–h, Fig. 3.26). The lateral and axial standard deviations were found to be 16 nm in xy and 17 nm in z at 200 nm depth, and 20 nm in xy and 27 nm in z at 1500 nm depth—as expected, the axial precision is more affected by the effect of the aberrations in the volume than the lateral precision.

3.6.3 Enhancement of the SAF detection

As the performances of DAISY in terms of axial biases correction relies on the measurement of the SAF positions, it would also be tempting to seek to improve the precision of the SAF detection. Even if the characterisations performed in section 3.3 did not seem to evidence any significant inaccuracy of the astigmatism correction, lowering σ_z^{SAF} would benefit DAISY by improving the axial precision near the coverslip, i.e. in the first 300 nm.

There are very few ways to enhance the SAF signal: the most obvious is perhaps to increase the numerical aperture of the system in order to collect more SAF photons. This can be done using a higher-numerical-aperture objective and results in a global increase of the SAF ratio ρ^{SAF}, which impacts the sensitivity of the axial detection by reducing the sensitivity to photon noise. We could use a 1.70-numerical-aperture Olympus APO TIRF objective but had little time to characterise its effect on the SAF detection. Nevertheless, several elements have to be mentioned: first, high-numerical-aperture objectives typically induce very strong field aberrations, and especially a sharp radial astigmatism component. These aberrations have to be corrected if the precision is to be improved, as it would cause the astigmatic detection to deteriorate if left uncorrected. Using adaptive optics could be a viable solution here. Also, one should keep in mind that the phase of the SAF signal varies from the inner limit of the SAF part in the back focal plane to the outer (the so-called Goos-Hänchen effect [80]). Thus, all the components are not phase-matched, which induces a broadening of the PSFs compared to a corrected 1.70 NA detection. This effect is bound to be more visible with high numerical aperture values. Once again, adaptive optics may be a sound strategy to suppress this effect.

Finally, working with high numerical apertures imposes several experimental constraints. No matter how mundane these problems, care should be taken to them: first, the sapphire coverslips used with the 1.70-numerical-aperture objective are very expensive. Besides, the immersion oil used to match the index is both very volatile—it evaporates and crystallises fast—and very toxic.

Eventually, increasing the numerical aperture to enhance the SAF collection is probably not worth the investment in terms of work and cost unless one plans to couple it with PSF shaping, in which case it could open new perspectives, especially in terms of aberration correction and new PSF shaping patterns.

3.6.4 Alternative labelling and demixing strategies for multicolour imaging

DAISY could furthermore benefit from the improvement of multicolour labelling and detection. Indeed, very few dSTORM fluorophores outside of the red range perform well [81], least of all those excited around 488 nm. Even AF555 suffers from a problem of loss of specificity during the acquisition—this was mentioned in section 3.4, page 105. As a result, dSTORM multicolour imaging is challenging with two spectrally resolved molecules, and quite hazardous with more. Multicolour labelling limitations are not specific to DAISY; on the contrary, they are bound to be recurrent in SMLM, no matter which implementation is chosen.

One possibility would be to use PAINT imagers: their photophysical behaviour is expected to be less critical a parameter regarding both blinking and bleaching times. Still, PAINT typically generates a strong diffuse signal coming from the volume of the sample, which would impact the localisation precision negatively. Besides, DNA-PAINT imagers is still not commercially available, thus strongly restricting the possibility to use them instead of dSTORM.

We propose another solution based on the use of several labels in the red range. As their excitation wavelengths are expected to be too close not to excite them all at once, strategies have to be developed to demix the acquisition. In other words, it is necessary to come up with a solution to identify each molecule on each frame. This can be done spectrally [61,82–84], but we also propose another method based on other photophysical properties. More precisely, the PSF size (which reflects the fluorescence wavelength), the lifetime of the ON state and the number of photons emitted per time unit in the ON state can be used to discriminate different molecules. These modalities will be more exhaustively described and characterised in chapter 4. Nevertheless, it should be noted that simultaneous multi-species imaging brings new challenges in terms of density of active molecules per frame, especially in dSTORM (see the assessment of the influence of the molecule density on the localisation in section 3.3 and Fig. 3.12).

3.6.5 Three-dimensional imaging in state-of-the-art studies

The improvement of simultaneous multicolour demixing capabilities could also benefit DAISY for time-resolved imaging of living samples. We did not investigate this field of application—aside from the *E. coli* bacteria, which were living but immobile once adhered to the coverslip, all samples presented in chapter 3 were fixed. Still, biological studies in 3D SMLM commonly resort to PALM and/or single particle tracking in living samples to have access to the dynamics of processes of interest. DAISY being limited to imaging close to the coverslip, it could be used to study phenomena related to adhesion and motility for instance [66,68].

Another potential field of application for DAISY is the characterisation of 3D calibration samples, as developed in parts 2.1 and 2.2.2.2. Such samples are necessary when developing a setup or a detection modality, whether to perform an axial calibration or to measure the resolution or localisation precision at different heights. In order for them to provide relevant results, their geometry (i.e. their spacing for nanorulers, their diameter for microspheres coated with fluorophores or their heights for fluorescent beads distributed in the volume) has to be known. However, this is not easily accessible in most cases due to either the intrinsic randomness of the sample or the lack of sufficient reliability of the sample—nanorulers often exhibit a certain size dispersion, while microspheres tend to slightly flatten out near the contact point with the coverslip, probably due to their own weight. This lack of information is often difficult to make up for as it requires a complementary measurement with an already calibrated method on the same field of view.

DAISY, on the contrary, presents an alternative approach where two complementary sources of axial information are intrinsically present already. Typically, the SAF can be readily used once the α_{RT} and β_{mask} are measured, which only requires beads on a coverslip. Thus, it is possible to characterise the sample using the SAF and then use this knowledge of the sample to perform either the calibration of the astigmatism or the measurement of the localisation precision for example. It is worth noticing that this approach is quite general, and could be transposed to methods other than astigmatism, or

even other than PSF shaping: coupling the SAF with any other axial detection modality would bring the same benefit for sample calibration.

3.7 Conclusion

In this chapter, we have introduced DAISY as a method to improve reliability and reproducibility in 3D SMLM experiments in an effort to make them more easily applicable. It relies on two complementary axial information sources: an astigmatic detection on the one hand, and a SAF measurement on the other hand. Thanks to the dual-view configuration of the detection setup, the axial and lateral precisions can be optimised independently. While astigmatism offers a good axial precision over the whole capture range, SAF brings an absolute reference that is used to correct axial detection biases inherent in relative axial methods, especially PSF-shaping-based. This is done by applying a cross-correlation correction algorithm that uses each localised molecule as a reference. We have demonstrated the capabilities of DAISY in terms of 3D localisation precision, and evaluated its insensitivity to axial drift, chromatic aberration and sample tilt. Finally, we have applied DAISY to multicolour three-dimensional imaging in state-of-the-art biological and chemical applications.

The approach that we described in this work published in *Nature Communications* in April 2019 [71] seems quite general to us. Indeed, using a detection modality as a reference fed to another is very common in microscopy, whether in correlative imaging or in SMLM, where fiducial markers can be used as references imaged in a different spectral channel [70] or with a complementary phase detection [85] for instance. DAISY uses the very molecules instead of fiducial markers, but the approach of correlating complementary information sources in simultaneous acquisitions is similar. Thus, it would be tempting to transpose this strategy to other detection modalities, by coupling the SAF detection with other PSF shaping patterns such as double helix, which offers a better precision curve flatness across the capture range at the cost of a necessarily reduced density of active molecules per frame to match the single molecule regime condition. It would even be feasible to adapt the wavefront shaping to the density of molecules—due to the photophysical processes involved, dSTORM tends to produce a large active fluorophores density at the beginning of the acquisition, and a slow decrease of the density afterwards because of photobleaching—by changing the pattern during experiments, as demonstrated in [36]. Of course, this strategy requires adaptive optics, but it allows a wide range of wavefront patterns, ranging from astigmatism [29] to double helix [30], saddle-point [34] or tetrapod of various kinds [35].

Aside from PSF shaping, SAF could benefit other 3D SMLM methods. In particular, methods based on interferometry and phase measurements—either shape- or intensity-encoded—are known to produce the best localisation precisions available in 3D SMLM. Notable examples include iPALM [38], ModLoc [41] and SELFI [42]. Such techniques have the advantage of exhibiting little sensitivity to aberrations and providing very precise measurements of the positions of emitters, but they are extremely sensitive to the

stability of the setup, especially axial drifts, as well as to chromatic aberrations and sample tilt. While these problems are typically dealt with by using fiducial markers to track the drift, coupling these detection strategies with a complementary SAF detection might prove a viable alternative by providing another way to recover the missing information without having to resort to fiducial markers added in the samples.

Chapter 4

Multicolour demixing in SMLM

Fluorescence microscopy often heavily relies on the use of multiple labelling. Indeed, one of its major advantages is the possibility to specifically label different targets with different probes, which can be imaged independently from each other to a certain extent. Whether it is based on immunolabelling, click chemistry or transfection to create cell lines expressing fluorescent molecules, the target to be labelled is often largely independent from the fluorescent probe used to image it—endogenous fluorescent markers and PAINT lipidic markers being notable exceptions. This makes fluorescence microscopy a very versatile and powerful tool for both biological and material chemistry studies, as it makes it possible to image different targets on the same field and merge the images in a straightforward way. Such a possibility is very useful since the distribution of a certain molecule relative to other species is much more informative than its absolute position alone. Indeed, this reflects the interactions between the different molecules, as well as the cellular context of the processes of interest. Moreover, functional information can be obtained by varying the conditions (such as knocking out a certain protein) and evaluating the effect of the modifications on a species relative to an unchanged reference (as illustrated in parts 2.3.2 and 2.3.3).

A simple way to enable independent imaging of different probes in the same sample relies on spectrally separated fluorophores, which can be distinguished through their different excitation and/or fluorescence wavelengths. The different images can be acquired either sequentially using a temporally separated excitation, or simultaneously through different spectral channels in the detection setup. Finally, this is compatible with live cell imaging. Although increasing the number of channels is often challenging due to the spectral overlap between the probes (most fluorescent molecules have broad excitation and emission spectra), wide-field or confocal microscopy can provide information on three to four species on the same sample, which is sufficient for many applications. Indeed, even if the application requires the assessment of many proteins, it is often easier to image multiple samples with only a common reference and one or two proteins of interest labelled in each sample than labelling both the reference and all the targets of interest in the same sample. For example, in [66], in order to measure the spatial distributions of talin, vinculin and paxilin relative to the actin reference, three se-

ries of samples were prepared: talin-AF647/actin-AF488, vinculin-AF647/actin-AF488 and paxilin-AF647/actin-AF488 (see section 2.3.2). As a consequence, it is seldom necessary to image more than three species on the same sample, which is perfectly feasible in wide-field or confocal imaging.

The same type of imaging is possible in SMLM; however, this raises specific challenges. First, as the excitation powers used are generally quite high, the residual absorption of fluorophores far from their absorption peak can induce blinking or photobleaching due to the excitation by other lasers (for instance, a 532-nm laser used to image AF555 may slightly excite AF647 molecules). Besides, some blinking strategies such as dSTORM and DNA-PAINT rely on the use of specifically prepared imaging buffers, which may have to be different for different fluorophores. For example, AF647 works well with a buffer composed of Tris, NaCl, glucose, cysteamine, glucose oxidase and catalase, whereas AF488 is best imaged in a buffer comprising Tris, HCl, ascorbic acid, methyl viologen, glucose, cysteamine, glucose oxidase and catalase [47]. Moreover, few molecules exhibit satisfactory blinking behaviours: in PALM, they are concentrated in a spectral domain ranging from 488-nm to 561-nm excitations, while in DNA-PAINT and (d)STORM, most molecules are excited with 561-nm to 637-nm excitations wavelengths. Finally, SMLM experiments are generally long, which makes sequential multicolour imaging somewhat counterproductive. All these factors contribute to the difficulty of performing multi-species sample studies in SMLM, hence the need to develop alternative strategies.

4.1 Motivation and state of the art

Taking into account the fact that most efficient fluorophores are concentrated in a small fraction of the accessible spectrum, a great deal of effort was made to come up with methods achieving high spectral resolutions. The goal of these developments was to enable imaging of samples labelled with several spectrally close probes. One of the first published techniques, called SR-STORM, makes use of a prism placed in the detection setup to induce a dispersion of the fluorescence light [83,84]. On the camera, this results in a lateral displacement of the spot on the camera, as well as a spreading due to the spectral width of the fluorescence. In order to retrieve the spectral information, it is necessary to measure the lateral displacement relative to a reference. This is done through a dual-objective setup that uses one objective lens to perform the 2D/3D imaging in a dedicated detection setup, while the other objective lens sends the fluorescence signal in the spectral detection setup (see Fig. 4.1). The comparison of the lateral positions of each PSF on the two images yields the displacement due to the dispersion. Finally, using a correspondence curve obtained thanks to a calibration of the system, the central fluorescence wavelength is obtained for each PSF and the corresponding molecule is identified. This techniques displays a spectral resolution below 10 nm. Identification of four fluorophores in the [660 nm, 700 nm] fluorescence wavelength domain is demonstrated with minimal cross-talk (a few percent only).

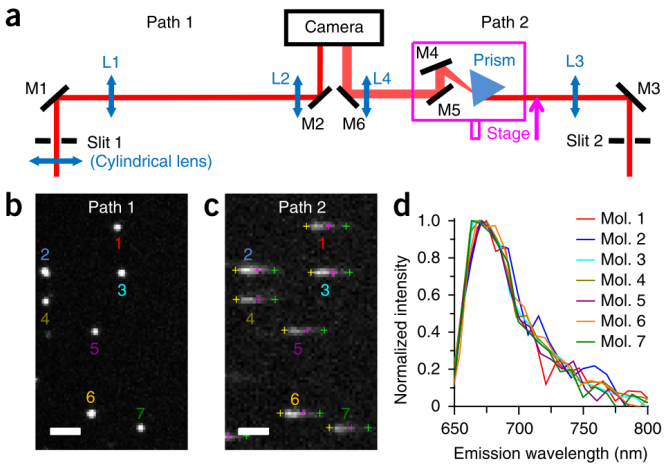

Figure 4.1 – Principle of SR-STORM. **(a)** Optical setup: two fluorescence beams are collected by two opposite objectives. One of them (left) is used for the 3D detection, while the other (right) comprises a prism to create a wavelength-dependent translation of the spots. **(b–c)** Frames recorded on the left and the right paths. Yellow, magenta and green crosses respectively indicate the expected positions for 647, 700 and 750 nm for each molecule. **(d)** Measured spectra of the different molecules visible in **(b–c)**. Scale bars: 2 µm. Source: Zhang *et al.*, *Nature Methods* (2015) [83].

Another approach based on the use of a dichroic mirror in the detection setup exists [82]. The fluorescence light is split in two channels by a long-pass dichroic mirror centred roughly at the middle between the fluorescence wavelengths of the different fluorophores of interest. The images are formed on the two halves of a camera and the localisation is performed. Once the correspondence between the PSFs of the two images is done, it is possible to calculate the intensity ratio between the two channels for each PSF. This ratio depends on the fluorescence wavelength: it is close to 1 for a wavelength near the centre of the dichroic mirror cut-off value, and to zero and infinity (or the contrary) far below and far above the cut-off wavelength. This spectral specificity can be used to identify spectrally close molecules that were calibrated beforehand to find their intensity ratios—this is displayed in Fig. 4.2. Such a ratiometric method is based on a photon counting for each PSF rather than on a position measurement, and is thus expected to be less limiting in terms of active molecule density per frame, and less sensitive to aberrations and wobble effects. This so-called SD-dSTORM method is able to clearly resolve 50-nm spaced fluorophores, and a 3-colour proof of principle with CF568 (excited with a 568-nm laser), CF647 and CF680 (excited with a 643-nm laser) was demonstrated in [86].

Many elements in an optical setup are likely to exhibit spectrally-varying responses. In particular, SLMs are highly chromatic as they intrinsically induce an Optical Path Difference (OPD), which results in a phase difference inversely proportional to the wavelength. This was used in [61] to produce spectrally-varying PSFs thanks to an SLM placed in the fluorescence path. Although the standard microscope PSF already contains spectral information (see section 4.2), the SLM can be used to optimise the spectral specificity

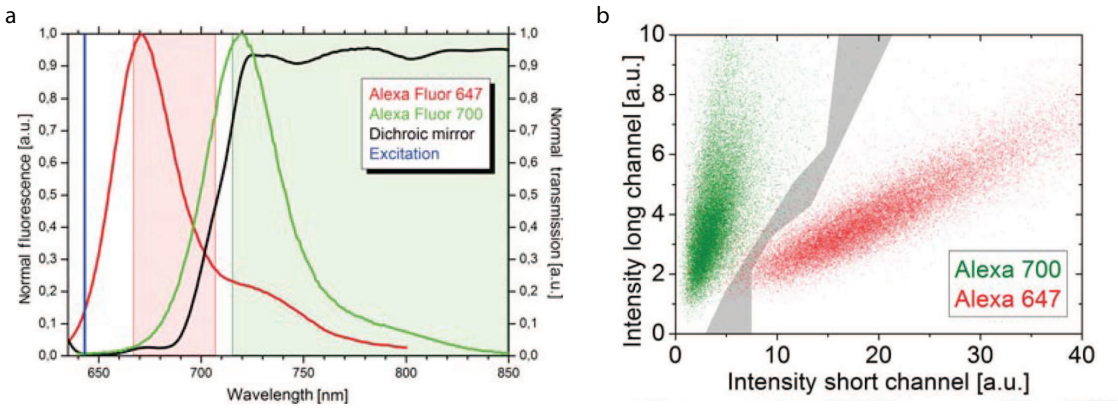

Figure 4.2 – Principle of SD-dSTORM. **(a)** Fluorescence spectra of AF647 and AF700. The common excitation wavelength and the transmission of the dichroic mirror placed in the detection setup are also displayed. **(b)** Scatter plot of the intensities collected in each of the detection channels (long-pass and short-pass channels). The calibration results obtained for AF647 and AF700 are displayed. Two zones are clearly identifiable, and molecules in the grey area are to be discarded to avoid cross-talk. Source: adapted from Lampe *et al.*, *Biol. Cell* (2012) [82].

for the desired wavelength set. Shechtman *et al.* calculated the Fisher information to find the optimally varying 3D PSF for a given couple of fluorescence wavelengths. This results in tetrapod PSFs with an orientation that varies with the wavelength (see Figure 4.3). It should be noted, however, that the final PSFs are very wide (5 µm radius typically), which makes them ill-suited for most applications apart from 3D Single Particle Tracking. To mitigate this issue, the authors also used another spectrally dependent wavefront shaping pattern that induces only a slight lateral spreading of the PSFs according to their wavelength. Although it has the advantage of begin compatible with super-localisation imaging, as the PSFs are relatively similar to standard PSFs, the spectral specificity is not as good as that of the rotating tetrapods. Still, the authors demonstrate simultaneous dSTORM imaging of AF532 (excited with a 514-nm laser line) and AF647 (excited with a 641-nm laser line).

More recently, several strategies were developed to extract specific information from other properties than the fluorescence wavelength. Shechtman *et al.* conceived a deep-learning algorithm that learns to recognise PSFs acquired with different fluorophores [87]. This can later be used to identify and categorise PSFs localised in simultaneous multicolour experiments. Such an algorithm is very powerful since it is likely to use all the information available, from the shape of the spots at different defocus values to the brightness. However, the inherent drawback is that no feedback is returned as to which features actually provide significant information and which are unnecessary to measure. In other words, one cannot hope to simplify the code to get rid of unspecific information. Another problem linked to this method is that since the information used is not known, it is necessary to perform a potentially long learning stage for each condition. For instance, changing the objective lens may induce a different aberration set and thus change the spot shapes, while modifying the excitation power is bound to alter the

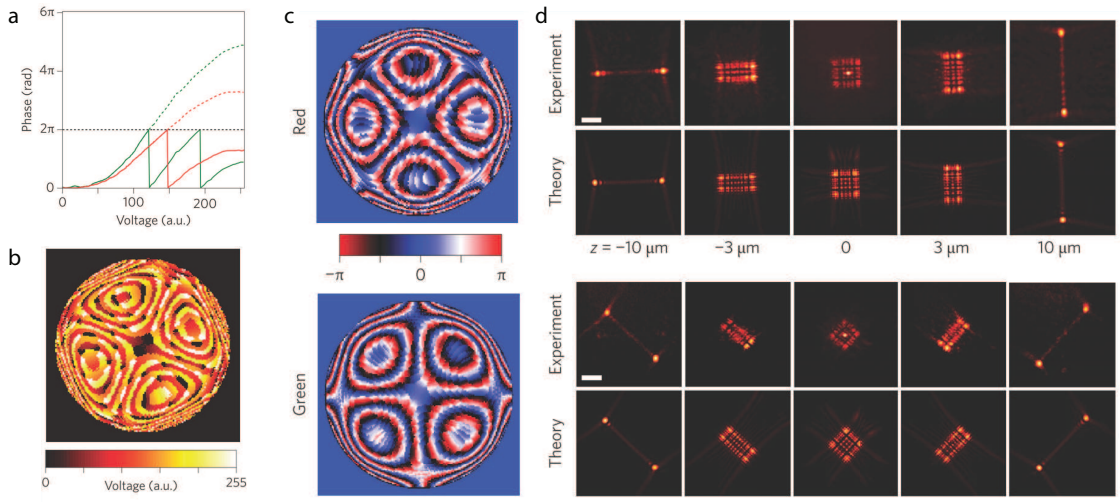

Figure 4.3 – Principle of spectrally-dependent PSF shaping. **(a)** Spectral dependence of the SLM response: the phase shift is displayed as a function of the applied voltage for two wavelengths: 559 nm (green) and 699 nm (red). **(b)** Optimised voltage pattern applied for the creation of spectrally-dependent PSF shaping. **(c)** Corresponding phase shift patterns for the red and green wavelengths. **(d)** Resulting theoretical and experimental PSFs for the two wavelengths, and for different defocus values. Scale bars: 5 µm. Source: adapted from Shechtman *et al.*, *Nature Photonics* (2016) [61].

fluorescence brightness of each PSF. To mitigate this issue, the authors propose to use again an SLM so as to optimise the spectral specificity of the detection setup, very much like in [61]. They illustrate the capabilities of this technique on isolated Qdots, but do not show dSTORM or DNA-PAINT data in biological samples.

In [88], the intensities of the different excitation lasers are sine-wave-modulated at different frequencies—typically integer fractions of the acquisition frequency to facilitate the demodulation step while respecting the Nyquist criterion. For each molecule, the temporal profile of the fluorescence intensity is extracted and its frequency is measured by Fourier analysis of this temporal signal (see Fig. 4.4). Such a method, however, presents major drawbacks that severely limit its potential applications. The first is related to the time scales involved: as the temporal profile must be sampled over several frames (at least three for two-colour acquisitions), the effective acquisition time for one frame is at least tripled compared to standard imaging. Still, it is necessary that the fluorophore remain active over at least one full cycle—and preferably over several cycles. This implies that either the exposure time has to be reduced at the cost of a noise increase, or the fluorophores have to exhibit long ON times, which typically limits labels to DNA-PAINT. The second drawback of this method is that the specificity is introduced in the excitation, thus restricting its use to clearly spectrally resolved molecules. This makes it especially hazardous to use with more than two colours, both because of the overlap of the absorption spectra and of the difficulty to find a suitable set of fluorophores with decent photophysical properties for super-localisation.

Finally, two teams also developed strategies based on the temporal blinking be-

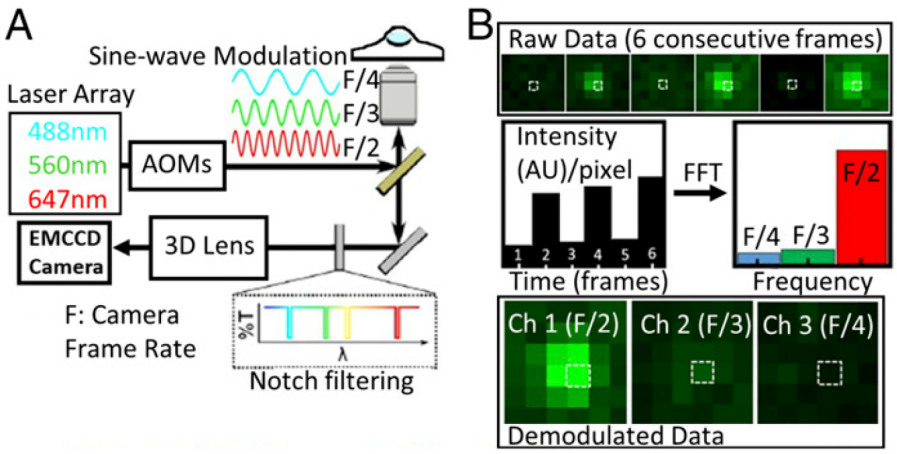

Figure 4.4 – Principle of demixing through temporal modulation/demodulation of the excitation. **(A)** Schematic of the optical setup. Three excitation lasers are sine-wave modulated at different frequencies, and the camera is synchronised with the modulation frequencies. **(B)** For each molecule, the temporal fluorescence emission (top panel) is analysed through Fourier analysis to extract the temporal spectrum components (middle panel) and separate the emission into three frequency channels (bottom panel), which correspond to the different excitation modulations. Source: Gómez-García *et al.*, *PNAS* (2018) [88].

haviour of the sources [89, 90]. Although they also use complementary spectral criteria to perform the discrimination, the authors study both the ON and OFF times. The temporal emission profile of a given source is tied to its chemical structure, and is thus a priori likely to yield specific information. This specificity can in some cases be optimised through label engineering: for instance, Wade *et al.* use specifically designed DNA strands featuring controlled numbers of bases that define the binding times of the probes (this is illustrated in Figure 4.5). Nevertheless, the temporal behaviours of the fluorescent sources, whether (d)STORM or PALM molecules, (DNA-)PAINT imagers, Qdots or crystal defects, is defined by a Poisson statistics due to the stochastic nature of the ON/OFF processes involved. This creates a spreading of the ON and OFF times and causes the specificity to deteriorate—unless the probes imaged feature very different lifetimes, which is likely to create issues due to the density of active molecules per frame. Both techniques seem to allow precise identification of many different sources imaged simultaneously; still, proofs of principle were performed only on isolated emitters which can be distinguished from each other. Such a condition is necessary to associate the repeated ON/OFF cycles to each molecule: otherwise, only one ON cycle could be associated to each localisation, making the ON time measurement less precise and preventing the OFF time measurement, not to mention that the quantitative aspect of the detection would be lost, as each molecule would be detected a random number of times. Besides, the time scales involved seem to be incompatible with dense samples imaging. Finally, extracting the specificity of dSTORM and PALM probes seems difficult with these methods, as the ON and OFF times are typically not very different from one molecule to the other.

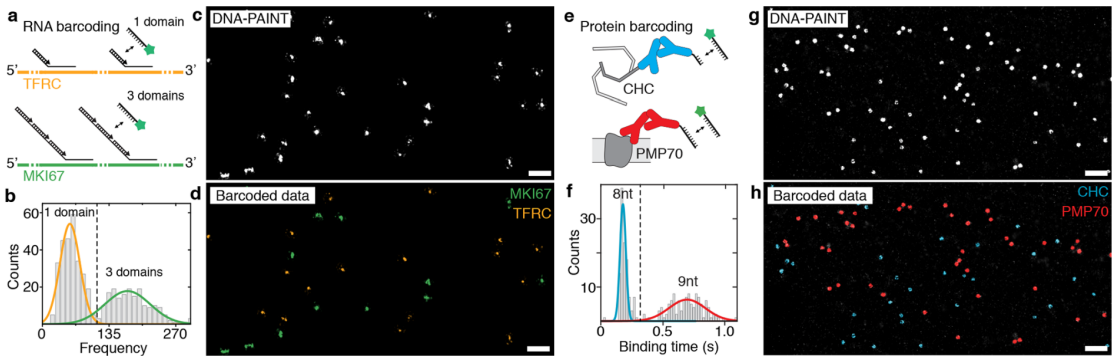

Figure 4.5 – Principle of binding kinetics engineering. The demixing of the binding frequencies is presented in **(a–d)**, while the demixing of the binding times is presented in **(e–h)**. **(a)** Illustration of the differences between two RNA species (TFRC and MKI67) in terms of number of binding sites. **(b)** Corresponding binding frequency histogram. The higher the number of binding sites, the greater the probability for a DNA strand to attach, and thus the higher the blinking frequency. The two species can be identified through calibration. **(c)** Standard DNA-PAINT image, where the two species imaged simultaneously are undistinguishable. **(d)** Demixed DNA-PAINT image, where the two species are demixed. **(e)** Different proteins (CHC and PMP70) can be labelled with docking sites of different lengths. **(f)** Corresponding binding time histogram. The longer the strands, the stronger the chemical affinity, and thus the longer the binding time. The two species are distinguishable from the histogram. **(g)** Standard DNA-PAINT image, where the two species imaged simultaneously are undistinguishable. **(h)** Demixed DNA-PAINT image, where the two species are demixed. Scale bars: 1 µm. Source: adapted from Wade *et al.*, *Nano Letters* (2019) [89].

Overall, most of the demixing methods mentioned impose the use of a dedicated excitation and/or detection setup. Some are especially expensive and tricky to align, such as those based on the use of a dual-objective setup [83, 84] or an SLM [61, 87]. Still, even those that are not [82, 88, 90] require a particular setup, which makes them incompatible with most commercial SMLM microscopes, as well as some home-made microscopes that rely on the use of a conflicting excitation or detection module. Although the method proposed by Wade *et al.* [89] does note require a dedicated hardware strategy, it heavily relies on the use of specifically engineered DNA-PAINT strands featuring controlled numbers of DNA bases in order to display the desired binding durations and frequencies.

Consequently, there exists the need to develop straightforward methods enabling the demixing of simultaneous acquisitions. Even though high performance techniques are available, experimentally simpler approaches could unlock a broad range of applications insofar as they could be used on most routinely used microscopes. We propose two novel post-processing-based approaches that allow one to perform a demixed detection from simultaneously acquired data with minimal constraint on the acquisition conditions—potentially rendering them applicable to data previously recorded on the same setup. The first is based on the detection of the PSF widths, thus reflecting the fluorescence wavelength. The second relies on the measurement of the temporal emission profile of a molecule to extract both its ON time and its fluorescence photon flux. These two elements are fluorophore-specific for a given set of experimental conditions,

and can therefore be used to identify different molecules without the need to resort to spectral identification—making it even possible to isolate spectrally indistinguishable molecules. Each of these methods use free information, i.e. information already present in the data regularly acquired that only need to be extracted and compared to calibration results to be put to use. We demonstrate their capabilities for 2D two-species simultaneous SMLM imaging using commercially available dSTORM fluorophores on standard biological samples.

4.2 PSF width filtering

Optical systems exhibit wavelength-dependent responses. Hence, the PSF of any microscope carries information about the fluorescence spectrum. In practise, due to the high number of photons collected per PSF, the spatial distribution of the light reflects the average fluorescence wavelength, i.e. the weighted average of the fluorescence spectrum. In the case of an ideal, unaberrated imaging system, the spatial standard deviation w of the PSF is proportional to the Airy radius:

$$w \propto \frac{1.22\lambda_{\text{fluo}}}{2\text{NA}} \tag{4.1}$$

where λ_{fluo} and NA are the average fluorescence wavelength and the numerical aperture of the objective, respectively. In other words, the diameter of the spot contains information about the fluorescence wavelength: the shorter the wavelength, the narrower the PSF. We set out to use this feature to retrieve information about the fluorescence wavelength and thus enable demixing of simultaneous multicolour experiments through a software-based method which we call Spot width Evaluation for Spectral Assignment in Multicolour Experiments (SESAME).

4.2.1 Principle and optical system

As we aim at imposing as little constraint on the experimental setup as possible so that SESAME can be used in combination with other methods, we used a standard microscope to perform the acquisitions (Fig. 4.6a): the excitation path consists of two lasers (532 nm and 637 nm) combined with a laser dichroic mirror, and a beam expander. The detection path is composed of the objective lens (Nikon APO TIRF x100 1.49 NA, oil immersion) and a beam expander to match the total magnification to the pixel size of the camera[1] (ORCA-Flash4.0, Hamamatsu).

Experimentally, however, optical aberrations are likely to induce an additional deformation of the PSFs. This can be due to simple defocus obviously, but also to non-idealities of the detection setup (especially the objective lens). To come up with a proof of

[1] The total magnification of the detection path is calculated so that one pixel on the camera corresponds to 108 nm in the object plane to optimise the lateral localisation precision. Note that a simpler solution for the detection setup would be to use a 60x magnification objective lens. This would produce the right magnification factor without the need to add lenses in the detection setup. As a consequence, the camera could be placed directly at the end of the microscope.

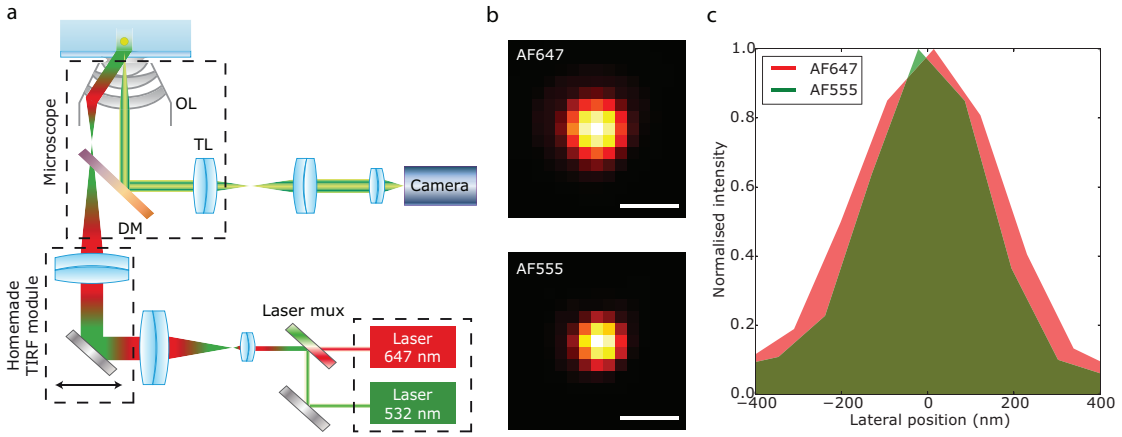

Figure 4.6 – Principle of SESAME. **(a)** Optical setup used for the SESAME acquisitions. The excitation consists of two lasers (637 nm, Obis 637LX, 140 mW, Coherent; and 532 nm, Verdi G5, 5 W, Coherent), a laser dichroic beam splitter (Laser mux), a beam expander, a home-made TIRF module, a dichroic beam splitter (BS) (LF405/488/532/635-A-000, Semrock) to separate the fluorescence, and an objective lens (OL) (Nikon APO TIRF x100 1.49 NA, oil immersion). The detection path is merely composed of the tube lens (TL) of the microscope (Nikon Eclipse Ti inverted microscope), an afocal system to adapt the magnification and a SCMOS camera (ORCA-Flash4.0, Hamamatsu). **(b)** Experimental PSFs obtained from AF647 (λ_{fluo} = 680 nm) and AF555 (λ_{fluo} = 580 nm). **(c)** Lateral profiles plotted from the PSFs displayed in **(b)**. Note that the PSFs are wider for AF647 than for AF555. Scale bars: 500 nm.

principle, we first minimised their importance as much as possible. With this end in view, we carried out acquisitions using TIRF illumination to perform an optical sectioning—although other methods such as structured illumination or light sheet excitation may also work. This strongly reduces the excitation far from the coverslip, and thus removes most molecules that are out of the imaging plane. It should be noted that optical sectioning is a very widespread method, and is thus not expected to significantly reduce the field of application of SESAME. Besides, we restricted the acquisition to a rather narrow field of view (28 µm square) to minimise field-varying optical aberrations. This is not sufficient to remove all aberrations, but our aim was mainly to get rid of varying aberrations. To account for the remaining, we performed a calibration of the PSF shapes with the fluorophores interest.

We illustrate the principle of the spectral dependence of the standard PSF shape with by imaging two different fluorophores at different wavelengths in the previously mentioned acquisition conditions (Fig. 4.6b–c).

For the purpose of using the PSF shape to spectrally resolve fluorophores, the widths first have to be calibrated for the species of interest. This step is necessary, as optical aberrations are likely to induce a broadening of the PSFs compared to theoretical expectations (see Fig. 4.7). We thus imaged fixed COS-7 cells in which the Heavy chain clathrin was labelled with AF647, and we processed the acquired frames by performing a 2D Gaussian fitting on the PSFs. The standard deviation w of the fitted Gaussian was taken as an estimator of the PSF width (see part 4.2.2 for more details about the localisa-

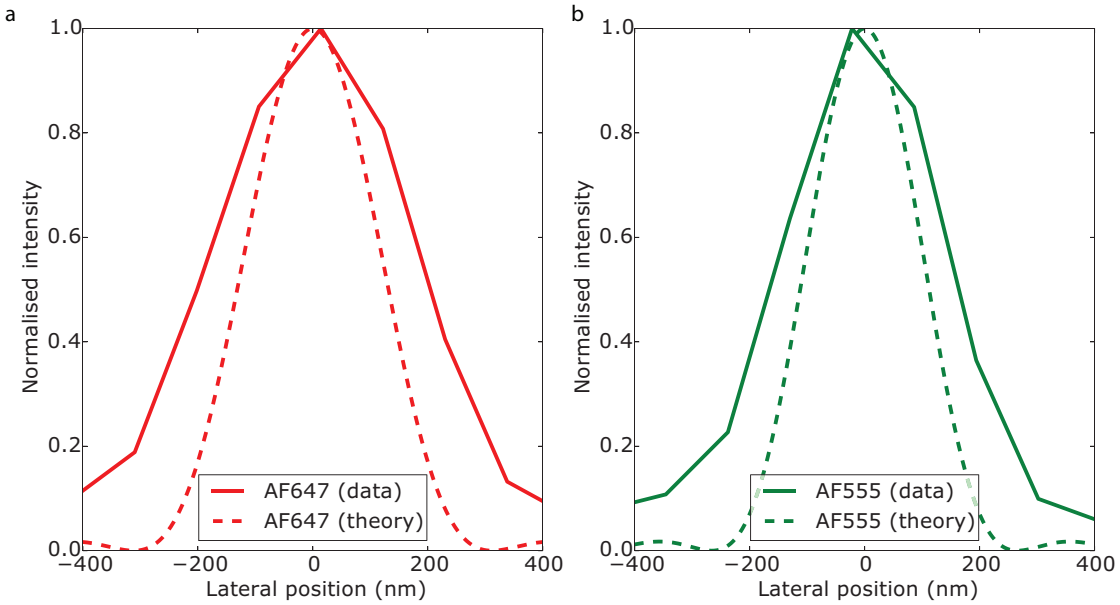

Figure 4.7 – Comparison between the theoretical and experimental PSF widths for AF647 **(a)** and AF555 **(b)**. The experimental PSFs are in the focus plane, and the numerical aperture of the detection setup is 1.33. Note that the experimental PSFs are slightly wider than the theoretical expectations, probably due to the optical aberrations of the detection path (especially the objective lens).

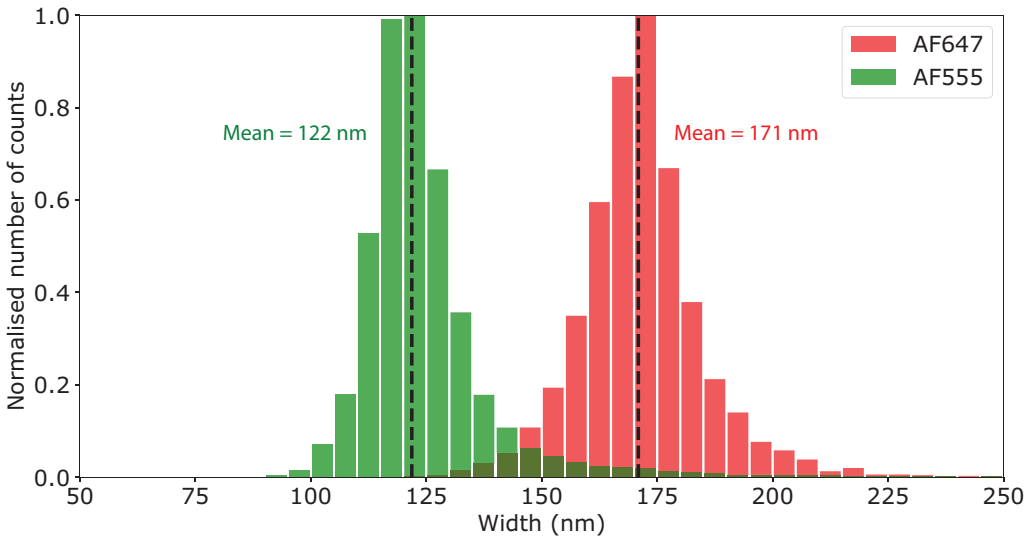

Figure 4.8 – Calibrations used for SESAME with AF647 and AF555. Two samples (fixed COS-7 cells labelled with AF555 on the α-tubulin, and fixed COS-7 cells labelled with the AF647 on the Heavy chain clathrin) were imaged and localised with the SESAME software.

tion code and the w measurement). We then performed a similar calibration for AF555 using fixed COS-7 with the α-tubulin labelled. The measured distribution of the values of w is represented in Fig. 4.8 for each species: two peaks are clearly distinguishable, if not totally separated.

4.2.2 Processing software

We thus built a post-processing strategy that aims at recovering the spectral information contained in the unengineered PSFs and use it for the demixing of simultaneous SMLM acquisitions. This consists in a home-written Python code, which we intend to release on Github soon. The script contains several major steps, from the localisation to the filtering of the data and the assignment of each PSF to a species based on the results of the calibration acquisitions. The processing workflow is exhaustively detailed in appendix A.3.3, but the main steps are explained below.

First, each frame is pre-processed by removing the static fluorescence background without altering the PSFs. The spots are detected using a wavelet filtering. Each PSF is characterised using an anisotropic Gaussian fitting to retrieve the PSF positions and widths w_x and w_y. A photon counting is also performed to determine the number of photons N.

A filtering step based on photon number, PSF widths and PSF anisotropy is then operated to get rid of false positive detections and strongly defocused PSFs. The lateral drift is corrected thanks to a sample-based cross-correlation algorithm.

Then, each PSF needs to be assigned to one fluorophore based on its width. This is done using the results of the single-colour calibration acquisitions (see section 4.2.1 and Fig. 4.8). In order to identify the domains corresponding to each fluorophore of interest, we use a k nearest neighbours algorithm. For each pixel in the (w_x,w_y) space[2], the algorithm finds the 50 nearest neighbours from the calibration localisation lists and uses them to calculate the local density of each species i (with $i \in [\text{AF555}, \text{AF647}]$ for instance). From the densities, a probability $p_i(w_x, w_y)$ of belonging to the species i is calculated. The probabilities verify:

$$\sum_i p_i(w_x, w_y) = 1 \quad \forall (w_x, w_y) \tag{4.2}$$

In particular, for the AF555/AF647 couple, this results in:

$$p_{\text{AF555}}(w_x, w_y) + p_{\text{AF647}}(w_x, w_y) = 1 \quad \forall (w_x, w_y) \tag{4.3}$$

It is then possible to calculate domains for each species. The least stringent filtering is to simply assign the (w_x,w_y) pixel to the fluorophore that has the highest probability (in the case of a dual-colour acquisition, this corresponds to taking a lower bound probability threshold equal to 0.5). The advantage of this filtering is that it does not induce any localisation discard, as every (w_x,w_y) pixel is assigned a species; still it is not expected to give an optimal cross-talk value. Another solution is thus to exclude from the domains

[2]We consider the x and y widths rather than the average width $w = \sqrt{w_x w_y}$ in order to account for a potential pixel size discrepancy between the x and y directions. Still, the difference between the two is typically minimal. Hence, in sections 4.2.1, 4.2.3 and 4.2.4, we chose to represent w rather than (w_x,w_y) for the sake of simplicity.

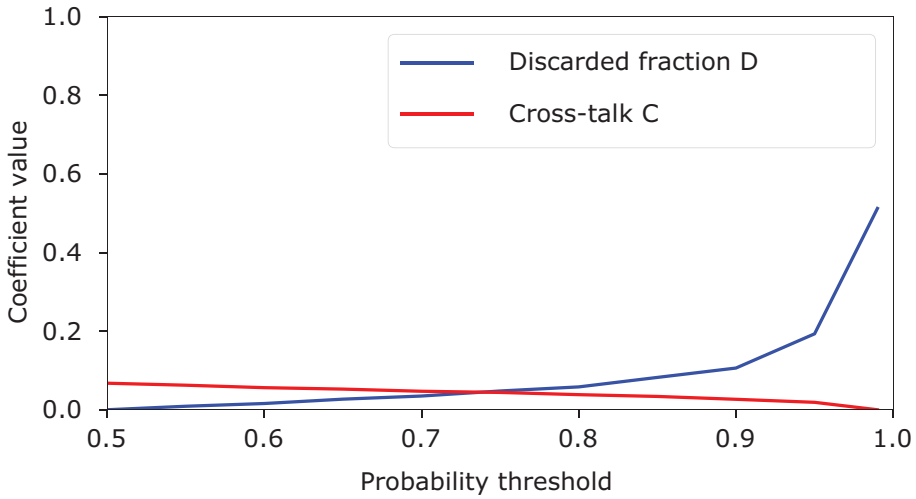

Figure 4.9 – Evolution of the cross-talk and the discarded fraction of SESAME as a function of the filter stringency.

any (w_x,w_y) pixel where no species has a probability high enough to be considered unambiguous. For instance, in the particular case of dual-colour acquisitions, probabilities below a certain threshold (between 0.5 and 1) can be discarded in order to optimise the specificity, which comes at the cost of a certain localisation loss proportion. This will be explained more in detail in part 4.2.3 and Fig. 4.9.

Eventually, the values of w_x and w_y of each PSF recorded during a simultaneous multicolour acquisition are used to distribute the detected molecules in the corresponding categories according to the domains delimited from the calibration results.

4.2.3 Characterisation and performances

As the recorded PSFs result from the optical transfer function of the microscope without any kind of shaping, which is the main advantage of SESAME, they are not expected to be optimal—this causes the detection to be slightly less specific than in [61]. Nevertheless, by applying numerical filters, it is possible to retrieve highly specific information. Two figures are especially relevant to evaluate the effect of a given filter: the fraction of discarded molecules D and the cross-talk between the two species C (i.e. the fraction of misidentified molecules). The more stringent the filtering, the lower the cross-talk, which comes at the cost of a higher rejected fraction. The influence of this probability threshold is illustrated in Fig. 4.9 for the case of the AF555/AF647 couple: in accordance with expectations, as the threshold increases, the cross-talk falls, while the discarded proportion rises. A typical SESAME filter is presented in Fig. 4.10: it corresponds to a threshold value of 0.8, and produces a cross-talk equal to $C = 4.1$ % and a discarded fraction $D = 5.5$ %.

Having addressed the calibration step, we then applied it for the identification of molecules in simultaneous dSTORM acquisitions: we imaged fixed COS-7 cells where

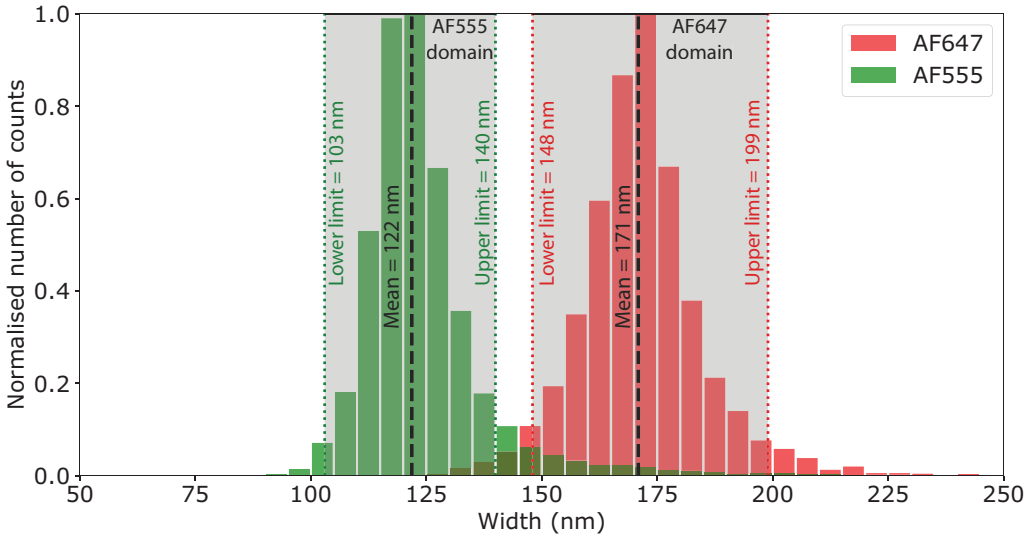

Figure 4.10 – Domains calculated from the calibration acquisitions for a typical SESAME filter (probability threshold equal to 0.8). The domains are represented in grey. Localisations that do not fit in any of the domains are to be discarded.

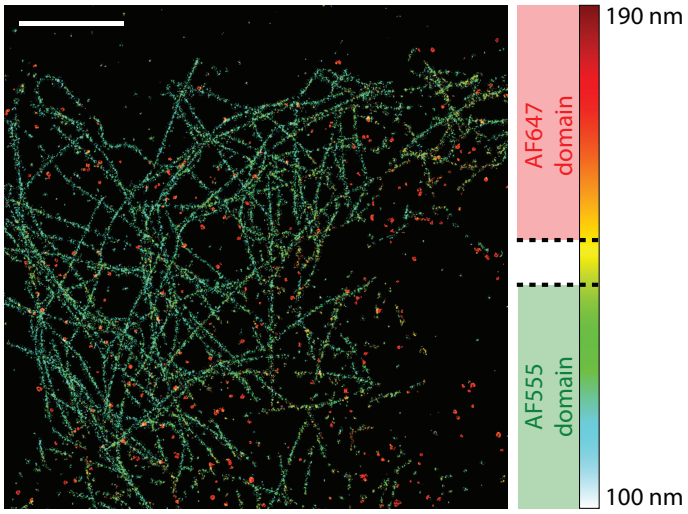

Figure 4.11 – PSF width SMLM map obtained from a dual-colour AF647/AF555 sample (fixed COS-7 cells with the α-tubulin labelled with AF555 and the Heavy chain clathrin labelled with AF647, imaged with simultaneous TIRF 637-nm and 532-nm excitations). The PSF width w is colour-coded from 100 nm to 190 nm. In red and green are represented the domains determined from the calibration acquisitions that are to be applied in order to perform the demixing. Scale bar: 5 µm.

the Heavy chain clathrin and the α-tubulin were labelled with AF647 and AF555 respectively. The sample was shone in TIRF illumination with 637-nm and 532-nm lasers simultaneously. The acquired frames were processed according to the workflow described previously (see part 4.2.2).

Figure 4.11 displays the width map that is produced by the localisation software. In

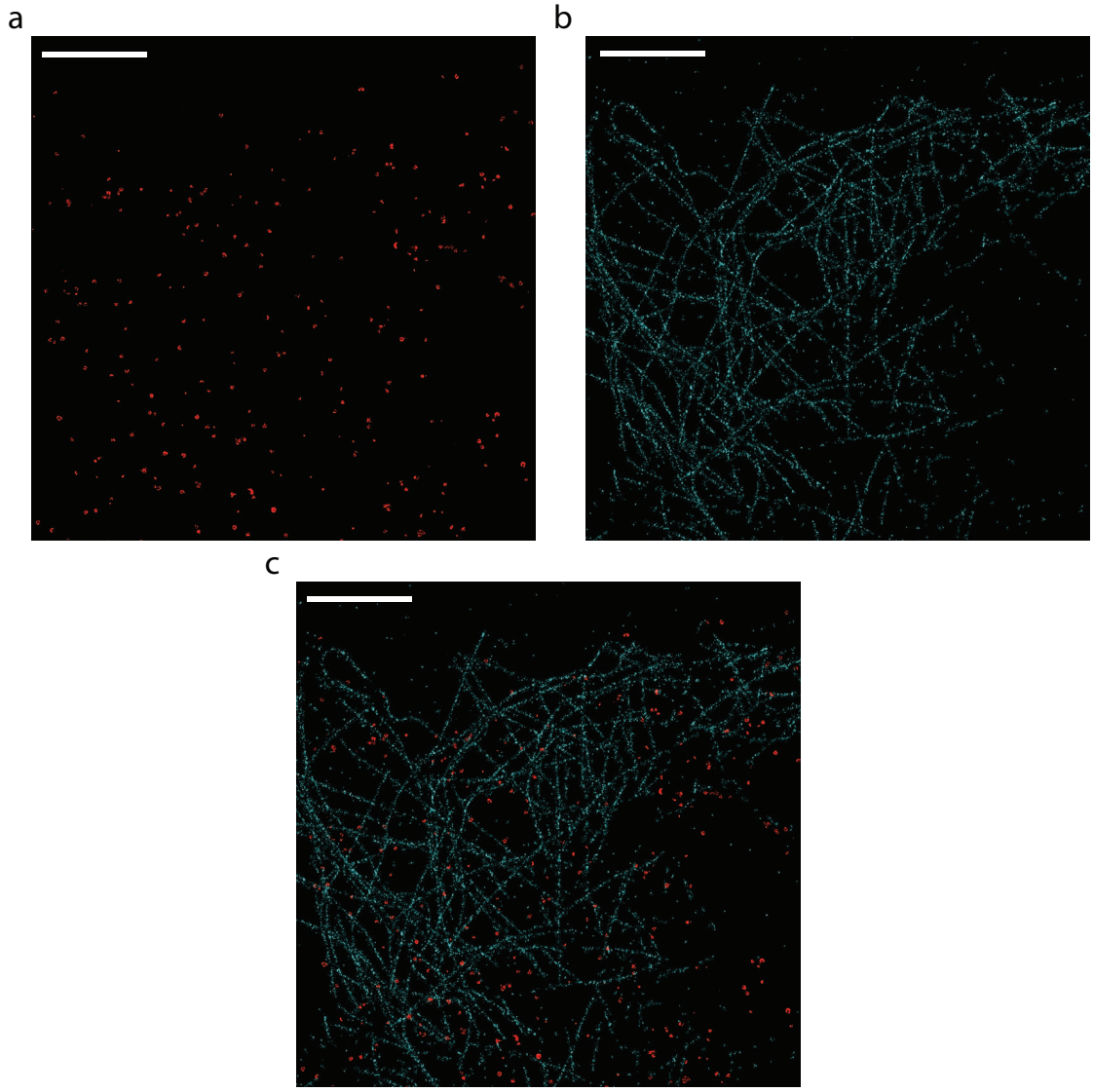

Figure 4.12 – Demixed SESAME 2D SMLM images obtained from the dual-colour AF647/AF555 sample displayed in Fig. 4.11 (fixed COS-7 cells with the α-tubulin labelled with AF647 and the Heavy chain clathrin labelled with AF555, imaged with simultaneous TIRF 637-nm and 532-nm excitations). **(a)** and **(b)** display the images identified as AF647 (red) and AF555 (cyan) respectively using the filter shown in Fig. 4.10. **(c)** shows the merging of the two maps (in other words, the demixed dual-colour map). Scale bars: 5 µm.

other words, it contains all the localisations obtained before the identification of the fluorophores. Two populations are clearly visible—narrow spots (tubulin) are AF555, while broader (clathrin) correspond to AF647. After running the demixing algorithm with the typical filtering obtained from the calibration data, we could separate the two species to reconstruct a highly specific dual-colour 2D super-localisation image[3] (Fig. 4.12).

[3]One could notice that the AF555 image displays a somewhat patchy tubulin network. This is also observed when imaging a single-colour AF555 sample, and can probably be attributed to the antibody used. In any case, it does not stem from the demixing process itself—the discarded fraction being around 5.5 %,

After this proof of pinciple, we set out to assess the influence of potential experimental hindrances. More precisely, we studied field-varying aberrations and defocus. Tackling the issue of field-dependent aberrations, which create non-uniform PSF deformations over the field of view (this problem was studied in the case of DAISY in part 3.3.3.4), could also improve the specificity of the measurements. We measured the influence of field-varying aberrations on the PSF widths using 40-nm fluorescent beads deposited on a coverslip (see appendix B.3.2 for the preparation protocol) for different field of view sizes. To decouple the influence of field-varying aberrations from the width measurement inaccuracy (which is linked to the number of signal photons and to the background), we acquired 300 frames and we used a clustering algorithm to identify the beads. Then, we averaged the measured widths for each bead. As a comparison, we also display in Figure 4.13 the unaveraged results: as expected, the effect of field-varying aberrations is all the more significant as the field of view is large. Besides, they seem to account for a significant part of the PSF size distribution width, especially on a large field of view. If left uncorrected, spatial variations of the PSF width could hamper the demixing by increasing the cross-talk between the different channels. A solution to tackle this problem would be to perform a spatially-varying PSF size calibration. Modifications of the optical setup, for instance through adaptive optics, could also help reduce these aberrations.

Another limitation of SESAME might be the defocus, which causes the PSFs to broaden depending on their axial position. Although it is possible to tackle this problem by using optical sectioning at the excitation, as we demonstrated previously, this can be inadequate in some cases where one needs as important an axial capture range as possible. If optical sectioning cannot be performed, the effect of the defocus is bound to decrease the specificity of the detection. Complementary characterisations need to be carried out to assess precisely the impact of the defocus on the PSF shapes and on the specificity of the detection for each fluorophore set. As illustrated in Figure 4.14, the optical sectioning brought by the TIRF excitation causes the spot width distribution to change only slightly. The histogram seems a little broader, which results in a slightly increased cross-talk, as displayed in Figure 4.15. Still, SESAME may still be usable without optical sectioning provided the spectral spacing between the fluorophores is large enough, much like with the AF647/AF555 couple.

4.2.4 Outlooks

These results demonstrate the ability of SESAME to extract information from the PSF widths using commercially available dSTORM probes on a standard SMLM microscope featuring no PSF shaping or dispersive element in the detection setup. This additional information is free, as it does not induce any performance loss. Naturally, there are many improvement perspectives: first, it could be used with other fluorophore sets. In

the effect of the demixing is almost negligible on the final spatial resolution of the image.

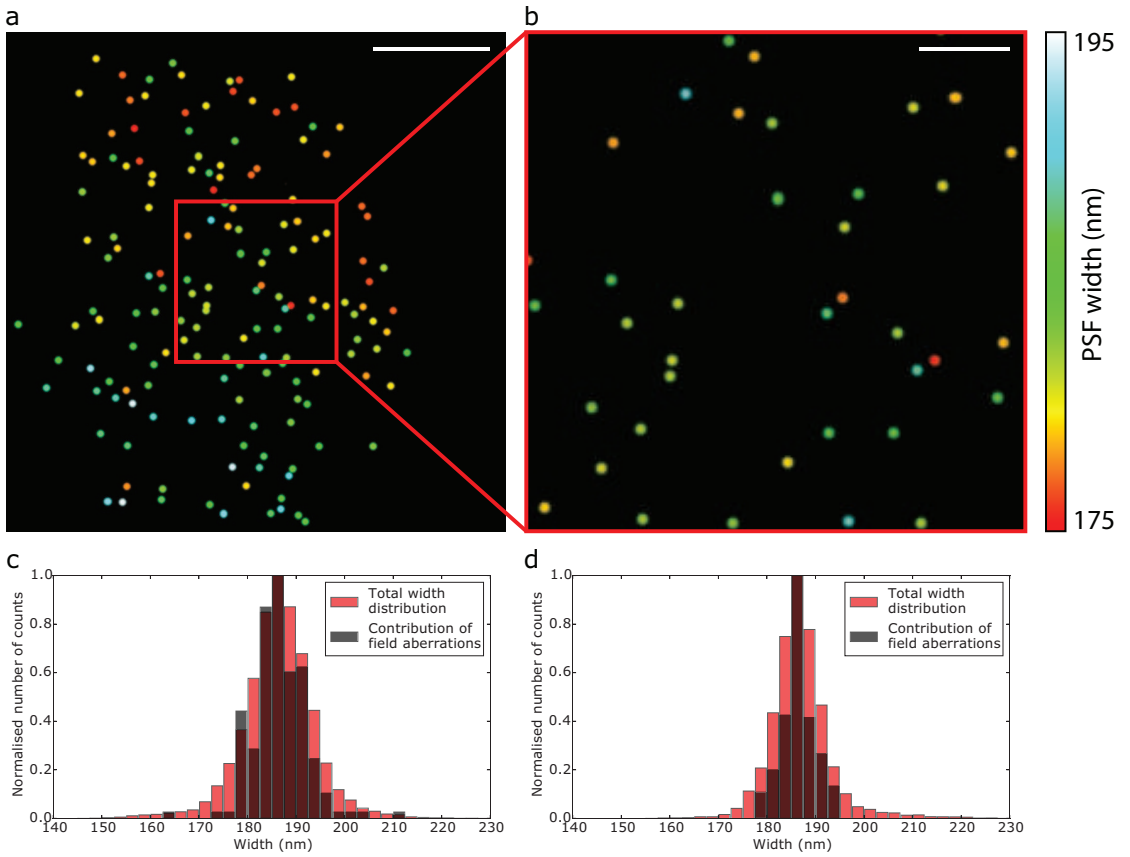

Figure 4.13 – Influence of field-varying aberrations on PSF widths. Spot size measurements were performed on dark red 40-nm fluorescent beads deposited on a coverslip. **(a)** and **(b)** display PSF width maps on a large (85-µm wide) and a standard (27-µm wide) fields of view respectively. **(c)** and **(d)** show the PSF width histograms corresponding to **(a)** and **(b)** respectively. The contribution of field-varying aberrations (obtained by averaging the measured widths for each bead over 300 localisations) is displayed in black, while the total unaveraged distribution is shown in red as a comparison. Scale bars: 20 µm **(a)**, 5 µm **(b)**.

particular, to make up for the mediocre photophysical behaviour of AF555[4], it could be replaced with CF568, which seems to exhibit much superior performances, even with a 532-nm excitation. As its fluorescence wavelength is higher than that of AF555, for the purpose of maintaining a significant spectral spacing, it could be used in combination with CF660C or CF680 rather than AF647.

Provided a suitable set of spectrally resolved dSTORM molecules could be found, it would even be possible to detect more species, probably up to three—more than four would be challenging in terms of fluorescence wavelength spacing as well as PSF density per frame. Besides, it could be used with labelling strategies other than dSTORM, especially DNA-PAINT and PALM. It is worth noticing that SESAME is a priori perfectly suitable for live cell studies relying on multicolour single particle tracking.

[4]The photophysical performances of AF555 explain the lack of homogeneity of the microtubules displayed in Figures 4.11 and 4.12.

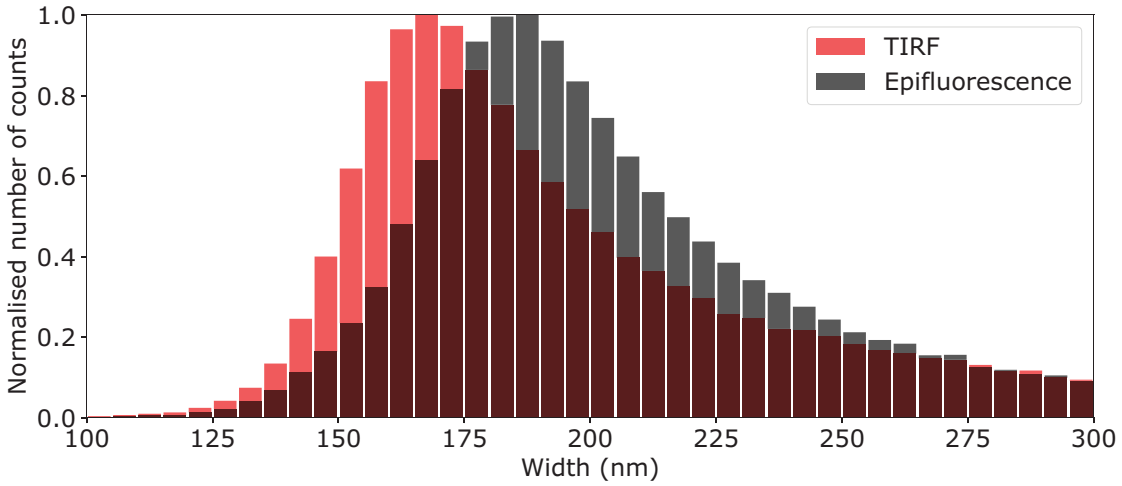

Figure 4.14 – Influence of the sectioning depth on the PSF width. The same sample (fixed COS-7 cells, α-tubulin labelled with AF647) was imaged on the same field of view, first in epifluorescence excitation, and then in TIRF. Even though the recorded PSF widths are slightly lower in TIRF, the effect of the sectioning on the spot sizes does not seem large enough to prevent the use of SESAME in epifluorescence excitation, i.e. without optical sectioning.

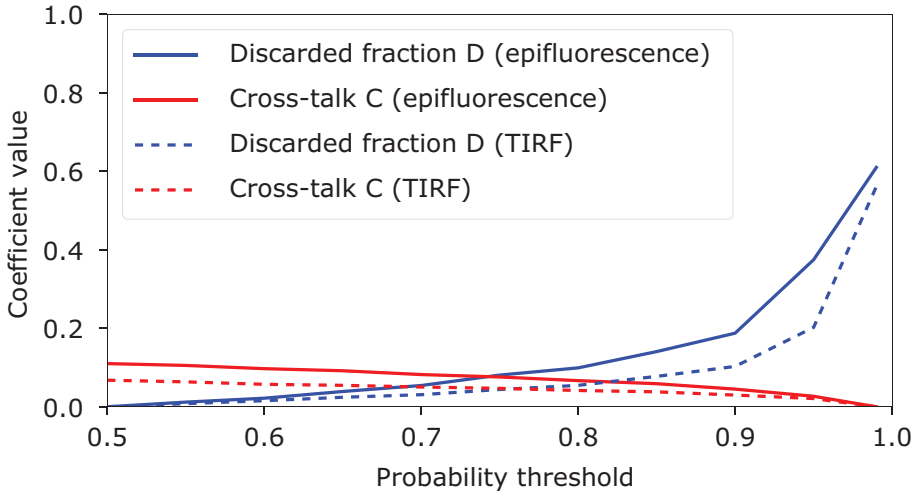

Figure 4.15 – Influence of the sectioning depth on the cross-talk. The cross-talk and the discarded fraction are compared for the AF647/AF555 couple for two illumination schemes: standard epifluorescence and TIRF.

The performances demonstrated with the AF647/AF555 couple in terms of discarded fraction and cross-talk are sufficient for many applications; still, some might require better specificity. One solution to improve the precision of the assessment of the width is to use brighter fluorophores or to reduce the background signal: while this is rather evident, this is not always easily achievable. One can imagine other ways to improve the demixing, though: for instance, using higher magnification detection systems may be relevant. Indeed, oversampled PSFs could bring an improvement of the measurement of w. SESAME could further be enhanced by using a cross-correlation-based

algorithm with experimentally acquired PSFs to assess the shapes more reliably than with a Gaussian fitting.

As mentioned in section 4.2.3, field-varying aberrations are currently one of the factors limiting the specificity of the detection. They could be reduced through modifications of the detection setup—in particular, adaptive optics could be useful here. Another approach would be to perform a spatially resolved PSF width calibration.

Finally, SESAME could be coupled with other detection modalities, especially 3D SMLM through intensity-based methods such as DONALD, iPALM or ModLoc—PSF shaping-based axial detection being potentially more hazardous due to its unavoidable effect on the PSF sizes. Aside from the obvious advantage that it would yield the complementary axial information which is crucial for many applications, it could also benefit the demixing itself by alleviating the need for optical sectioning. Indeed, if the axial position is accessible, one could acquire an axially resolved calibration for SESAME (instead of a global as we proposed previously). Then, the molecules localised in a multicolour simultaneous experiment would first have to be localised in 3D and the SESAME calibration matching their axial position would be used for the demixing. This is expected to enhance the performances of SESAME, i.e. lowering the cross-talk and the fraction of discarded localisations. More importantly, if this is feasible, optical sectioning becomes unnecessary, as the effect of the defocus is accounted for in the axially resolved PSF width calibration. Note, however, that coupling SESAME with 3D SMLM methods might be challenging since the axial detection itself is spectrally dependent in some cases.

Aside from these considerations related to the development of the technique, SESAME could naturally be used for biological applications. As it currently remains restricted to acquisitions using optical sectioning, it could prove useful in combination with TIRF for neurobiology as well as bacterial imaging—much like DAISY. As it is a priori compatible with acquisitions on live cells, it may also benefit adhesion or motility studies.

4.3 Lifetime and fluorescence intensity measurement

Note: the work described in this section 4.3 is currently being patented to protect its use. Therefore, this part of the manuscript should remain confidential until the acceptance of the patent.

Each fluorescent molecule has its own chemical properties, which define its spectral characteristics (i.e. its absorption and emission spectra), but also many other features, such as its brightness, ON and OFF states times, photobleaching time, etc.[5] Spec-

[5] In this part, we will present mostly dSTORM results; still, the principle of the technique is more generally applicable in SMLM, and can be easily be transposed to (DNA-)PAINT. In this case, the ON and OFF states are replaced with the docked and diffusive states (DNA-PAINT results will be briefly presented in section 4.3.3: see Figures 4.27 and 4.28). It can also be used in combination with PALM, but in this case the dynamics of the fluorescent proteins is mostly defined by the photobleaching time.

trally close molecules can exhibit very different behaviours in that regard. These properties often depend on the composition of the imaging buffer and on the power and wavelength of the excitation, but they can be assessed through software analysis.

We developed a data analysis method which measures the ON state time of the probes as well as their fluorescence photon flux and uses this information for identification of molecules simultaneously acquired on the same frames. As mentioned in part 4.1, the use of the ON state has already been reported on isolated sources [89, 90], but it has never been demonstrated for structural imaging (i.e. with a dense labelling). As for the fluorescence intensity, only Comtet *et al.* [90] assessed it, but the results do not seem to show any difference in intensity between the studied species, thus it cannot be used in the framework of demixing in that specific case.

We call our approach PHotophysics-based Allocation for Nanoscopy through inTensity and On time Measurement (PHANTOM). Much like SESAME, PHANTOM does not require modifications in the excitation or detection setups.

4.3.1 Principle and optical system

To come up with a proof of principle for PHANTOM, we performed acquisitions on a standard microscope equipped with a single 637-nm laser. As the photophysical behaviour of a fluorescent probe is expected to be dependent on the local excitation power density (this will be more thoroughly studied in part 4.3.3), it is important to use as homogeneous an excitation pattern as possible, at least until the effect of the excitation power density can be assessed. Several methods are available to produce a highly homogeneous excitation over the imaged field [91, 92], but for the sake of simplicity, and as we aim at imposing as little constraint on the setup as possible, we chose to produce a standard Gaussian epifluorescence illumination and restrict the acquisition to a relatively small field of view (28 µm × 28 µm).

The detection path is composed of two lenses to match the right magnification for the whole detection system (one pixel on the camera corresponds to 108 nm in the object plane), and a physical mask placed in a relay plane of the back focal plane to get rid of the SAF component[6] (see part 1.6.3). Given that the dynamics of dSTORM probes corresponds to times of the order of tens of milliseconds[7], one needs to have a sufficient camera frame rate. We thus used an sCMOS camera with a 10-ms integration time[8] in

[6] The SAF component is unwanted in this case because it adds a dependence of the fluorescence intensity on the axial position, which is bound to induce a loss of specificity if not accounted for. Here, the fluorescence intensity should be as uniform as possible to optimise the specificity. Note that a simpler solution for the detection setup would be to use a 1.33-numerical-aperture objective with a 60x magnification. This would produce the right numerical aperture and magnification factor without the need to add lenses or masks in the detection setup. As a consequence, the camera could be placed directly at the end of the microscope.

[7] DNA-PAINT imagers generally exhibit slightly longer binding times, around a few hundred milliseconds, although this strongly depends on the DNA strands used.

[8] In these experiments, the integration time could not be reduced below 10 ms due to acquisition software limitations. Still, as the typical integration times with fluorophores such as AF647 or CF647 can be as low as 30 ms, it would be relevant to decrease the integration time to improve the temporal resolution. Still, the

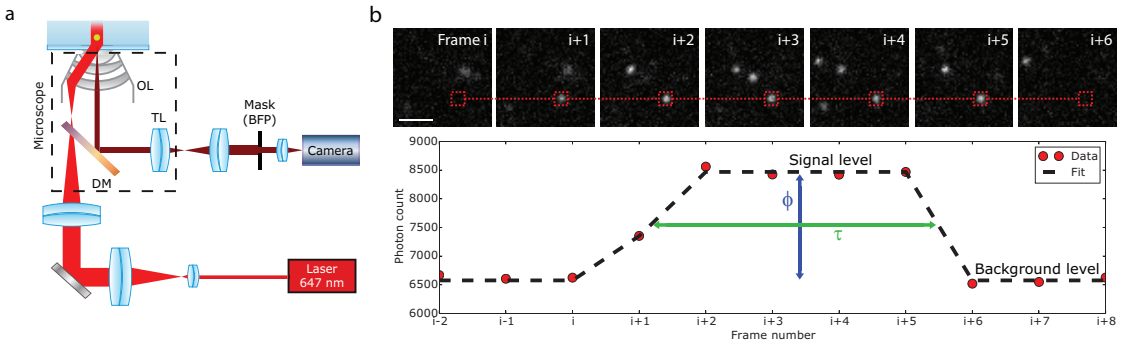

Figure 4.16 – Principle of PHANTOM. **(a)** Optical setup used for the PHANTOM acquisitions. The excitation consists of a 637-nm laser (Obis 637LX, 140 mW, Coherent), a beam expander, a dichroic beam splitter (BS) (LF405/488/532/635-A-000, Semrock) to separate the fluorescence, and an objective lens (OL) (Nikon APO TIRF x100 1.49 NA, oil immersion). The detection path is merely composed of the tube lens (TL) of the microscope (Nikon Eclipse Ti inverted microscope), two lenses to match the magnification with the camera pixel size, a physical mask placed in a relay plane of the back focal plane (BFP) to block the SAF component, and an SCMOS camera (ORCA-Flash4.0, Hamamatsu). **(b)** Principle of the measurement of τ and ϕ. The top row shows a zoom on a region of interest on the raw acquired frames (fixed COS-7 cells with the α-tubulin labelled with CF680 and the Heavy chain clathrin labelled with AF647). For each PSF, the number of photons is measured by integration in the same area on the previous and next slices to generate the temporal intensity profile, which is displayed in the bottom row. The profile is fitted to extract the ON state time τ (defined as the full width at half maximum of the top plateau) and the photon flux ϕ (defined as the photon count difference between the top plateau and the background level). Scale bar: 2 µm.

continuous acquisition mode to remove any delay between the consecutive frames. The experimental setup is depicted in Fig. 4.16a.

From the series of frames acquired, the temporally resolved emission profile of each fluorophore can be extracted and fitted to retrieve the lifetime of the ON state τ and the fluorescence intensity[9] ϕ (see Fig. 4.16b). More information will be given about the data processing software in section 4.3.2.

As the ON state time and the fluorescence photon flux are dependent on the excitation and the detection setups, the first step is to perform the calibrations that will then be used for the demixing of simultaneous multi-fluorophore acquisitions. These calibra-

exposure time should not be reduced too dramatically, as it is necessary to perform the localisation, which requires PSFs to be identified among the background noise. It is also worth mentioning that the choice of the integration time should be matched to the excitation power density used since the ON time of a molecule decreases as the excitation power increases.

[9]We call *fluorescence intensity* or *fluorescence photon flux* the number of photons collected on each frame for a given PSF. Note that this is proportional to the integration time. We performed all the acquisitions with a 10-ms exposure time, but if the integration time was to be varied, it may be more relevant to normalise the fluorescence intensity by dividing it by the integration time—i.e. to express it as the number of photons collected per time unit. It is also worth noticing that we study only the number of fluorescence photons collected by the optical system. This is dependent on the numerical aperture of the detection system, on the transmission characteristics of the dichroic filter used, as well as of the light loss due to the lenses and mirrors. Thus, it is necessary to perform calibrations on the setup that is to be used for the multi-species acquisitions in order to account for all these factors.

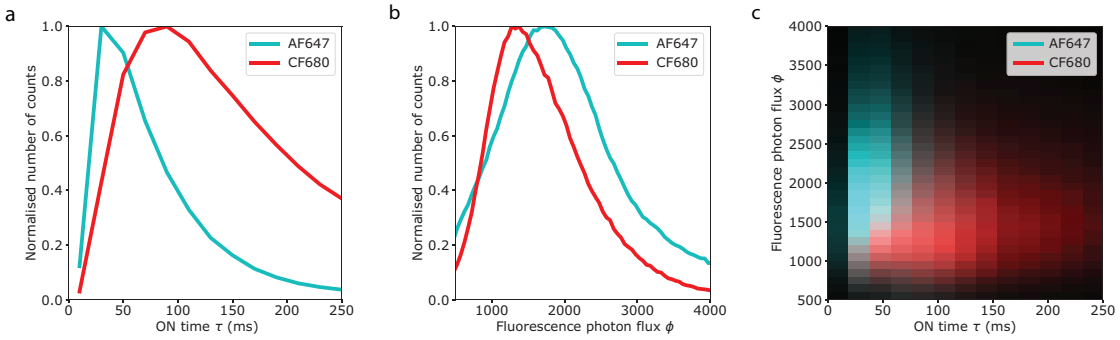

Figure 4.17 – PHANTOM calibration of AF647 and CF680. **(a)** Histogram of the ON times. **(b)** Histogram of the fluorescence intensities. **(c)** 2D histogram (plotted as a density map) of the values of τ and ϕ. Note that the density map carries more information than the 1D histograms (which are only projections of the 2D histogram), but for the sake of clarity we will show the 1D τ and ϕ histograms whenever comparisons of different conditions have to be performed.

tions are typically done in the nominal acquisition conditions. Especially, they have to be acquired with the same excitation in terms of laser wavelength, beam size, excitation power, and with the same imaging buffer[10]. To illustrate the differences between fluorophores in terms of τ and ϕ, we performed acquisitions on single-label samples. We used fixed COS-7 cells with either the Heavy chain clathrin labelled with AF647 or the α-tubulin labelled with CF680. Fig. 4.17 shows the results of the calibration acquisitions that will be used to determine the domains corresponding to each fluorophore. Note that Fig. 4.17c displays a certain degree of specificity between the two species: AF647 corresponds to low ON times and high photon fluxes, whereas CF680, on the contrary, is associated to high ON times and low fluorescence intensities[11].

4.3.2 Processing software

We designed a home-written Python code to perform the localisation and measure the values of τ and ϕ from the frame stack. It consists of several major steps: after a preprocessing stage, the localisation is performed on each frame and the temporal profile of the emission is extracted for each PSF. A fitting is performed on every profile to calculate the values of the ON state time and the fluorescence intensity. The localisation list is filtered to get rid of false positive detections, the lateral drift is corrected and the PSFs present on subsequent frames are recombined. Finally, each molecule is assigned a species based on the results obtained from the calibration acquisitions. Most of these operations use CPU parallelisation to improve the calculation speed. The exact processing workflow is exhaustively detailed in section A.3.4, but the main steps are described below.

[10] The photophysical properties of fluorescent molecules (especially dSTORM probes) is dependent on the chemical composition of the imaging buffer. Thus, it is important to always use either freshly prepared buffer or sealed samples in order to avoid buffer oxygenation.

[11] This is probably due to the fact the CF680 is more off-resonance than the AF647 with a 637-nm excitation, which results in a lower photon absorption and thus a lower fluorescence. As the molecules cycle more slowly between the ground state and the excited state, the time it takes to reach the OFF state is also higher.

First, each frame is pre-processed by removing the static background locally without altering the signal contained in each PSF. The spots are detected using a wavelet filtering. Each PSF is characterised using a Gaussian fitting to retrieve the PSF positions and widths w. For each PSF on the frame i, a photon counting is also performed in every frame from $i-100$ to $i+100$ to extract the temporal intensity profile. This profile is fitted around the frame i with a modified rectangular function to allow one intermediary position between the background and the top plateau level at the rising edge, and one another at the falling edge[12] (see Fig. 4.16b, frame $i+1$). The values of τ (defined as the full width at half maximum between the two edges) and ϕ (defined as the difference between the top plateau and the background level) can thus be extracted.

A filtering step based on PSF widths and PSF anisotropy is then operated to get rid of false positive detections. The lateral drift is corrected thanks to a sample-based cross-correlation algorithm.

A recombination algorithm is used to group all the detections corresponding to one single molecule in one ON cycle (for instance, in Fig. 4.16b, the localisations in the dotted boxed region are grouped for the frames $[\![i+1, i+5]\!]$) and average the localisation data over the cycle. This recombination step is important because it makes up for the low integration time, which results in relatively low numbers of photons per frame per PSF. By averaging the results over the whole ON cycle, the measurement of the localisation data is made more precise. Besides, it saves the quantitative aspect of the localisation—otherwise, molecules featuring long τ values would be counted several times, and would contribute to altering the statistics of the τ distribution.

Finally, the values of τ and ϕ are used to distribute the detected molecules in the corresponding categories according to the domains delimited from the calibration results. These domains are automatically determined using a k nearest neighbour algorithm to calculate the likelihood of a molecule belonging to either of the species. The domains are generated excluding too unspecific regions (i.e. probabilities too low or too undecided between the different species). In order to identify the domains corresponding to each molecule, we use a k nearest neighbours algorithm—much like in the SESAME algorithm (see part 4.2.2). For each pixel in the (τ,ϕ) space, the algorithm finds the nearest neighbours from the calibration localisation lists and uses them to calculate the local density of each species i (with $i \in$ [AF647, CF680] for instance). From the densities, a probability $p_i(\tau, \phi)$ of belonging to the species i is calculated. The probabilities verify:

$$\sum_i p_i(\tau, \phi) = 1 \quad \forall(\tau, \phi) \tag{4.4}$$

In particular, for the AF647/CF680 couple, this results in:

$$p_{\mathrm{AF647}}(\tau, \phi) + p_{\mathrm{CF680}}(\tau, \phi) = 1 \quad \forall(\tau, \phi) \tag{4.5}$$

[12] The molecule is expected to switch ON or OFF at a random time. Thus, in most cases, it emits photons only on a fraction of the integration time on the first and last frames of its ON cycle.

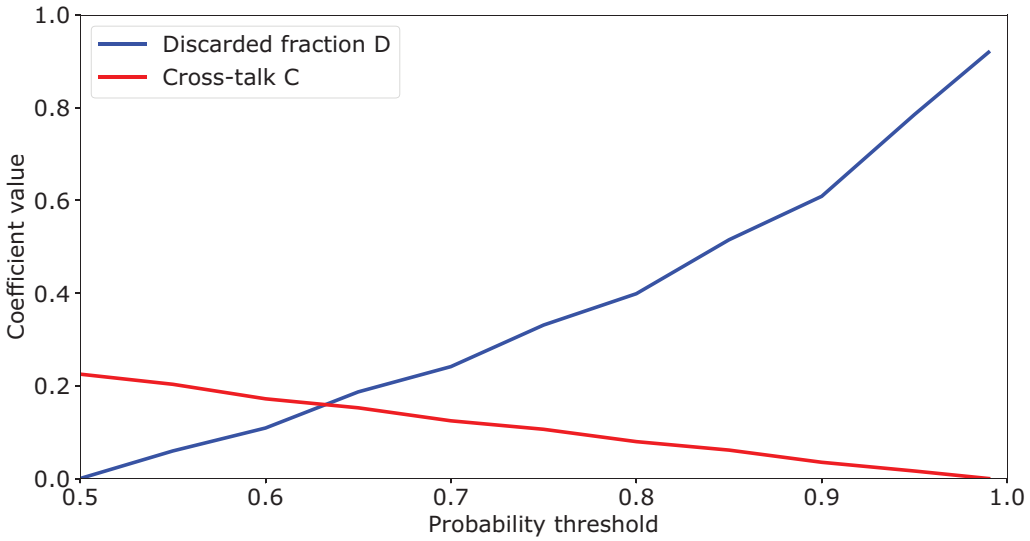

Figure 4.18 – Evolution of the cross-talk and the discarded fraction of PHANTOM as a function of the filter stringency.

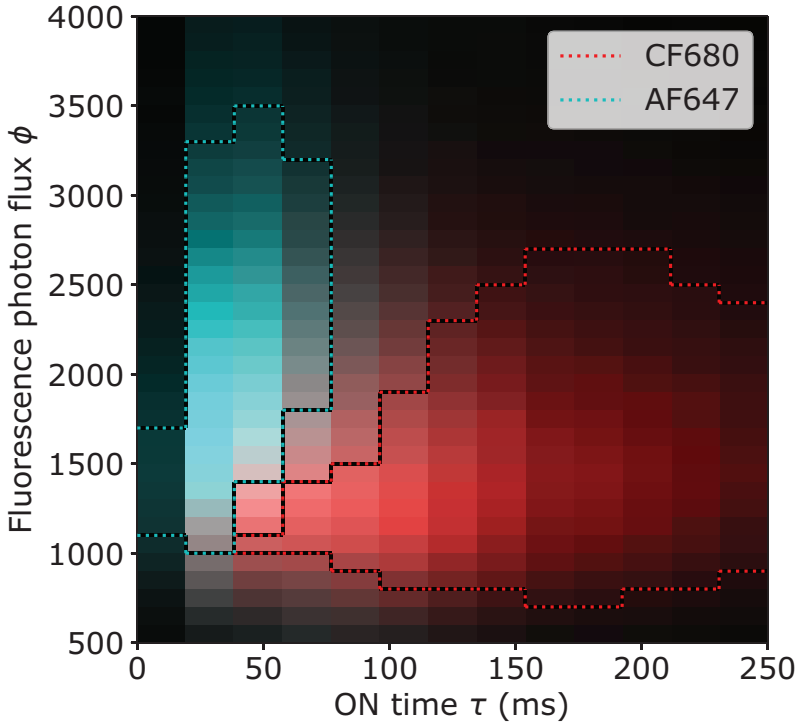

Figure 4.19 – Domains calculated from the calibration acquisitions for a typical PHANTOM filter (probability threshold equal to 0.7). The raw calibration data are displayed in cyan (for AF647) and in red (CF680) as density maps (in other words, 2D histograms). The domains calculated from the calibrations are represented in dotted lines. Localisations that do not fit in any of the domains are to be discarded.

It is then possible to calculate domains for each species. The least stringent filtering is to simply assign the (τ,ϕ) pixel to the fluorophore that has the highest probability (in the case of a dual-colour acquisition, this corresponds to taking a lower bound probability threshold equal to 0.5). The advantage of this filtering is that it does not induce any localisation discard, as every (τ,ϕ) pixel is assigned a species; still it is not expected to give an optimal cross-talk value. Another solution is thus to exclude from the domains any (τ,ϕ) pixel where no species has a probability high enough to be considered unambiguous. For instance, in the particular case of dual-colour acquisitions, probabilities below a certain threshold (between 0.5 and 1) can be discarded in order to optimise the specificity, which comes at the cost of a certain localisation loss proportion.

Eventually, the values of τ and ϕ of each PSF recorded during a simultaneous multicolour acquisition are used to distribute the detected molecules in the corresponding categories according to the domains delimited from the calibration results.

4.3.3 Characterisation and performances

Several factors have an influence on the capabilities of PHANTOM. After having shown the principle of the demixing to produce multicolour images from simultaneous acquisitions, we will assess the importance of these factors.

In order to perform the demixing, it is first necessary to set the probability threshold (see part 4.3.2). Much like in the case of SESAME, the value of this threshold determines both the fraction of discarded molecules D and the cross-talk between the channels C. The effect of the threshold is illustrated in Fig. 4.18 for the case of the AF647/CF680 couple: in accordance with expectations, as the threshold increases, the cross-talk falls, while the discarded proportion rises. To come up with a proof of principle for the AF647/CF680, we set a typical PHANTOM filter corresponding to a threshold value of 0.7 (see Fig. 4.19). This results in a cross-talk equal to $C = 12.4$ % and a discarded fraction $D = 24.1$ %.

From these calibration results, it is possible to produce demixed localisation data. To illustrate this, we imaged fixed COS-7 cells where the Heavy chain clathrin and the α-tubulin were labelled with AF647 and CF680 respectively. Both fluorophores were excited with a single 637-nm laser line in epifluorescence illumination configuration, exactly like for the calibration acquisitions. We processed the data with the PHANTOM software (see part 4.3.2) to first produce the (τ,ϕ) map presented in Fig. 4.20. On the image, two species are clearly distinguishable: the clathrin (AF647) features low ON times and high fluorescence photon fluxes, while the tubulin (CF680) corresponds to high τ and low ϕ values. Using the domains presented in Fig. 4.19, this image can be demixed in order to identify the two species with quite a satisfactory specificity (Fig. 4.21).

Having demonstrated the feasibility of the photophysics-based demixing of simultaneous acquisitions with spectrally close fluorophores, we set out to evaluate the in-

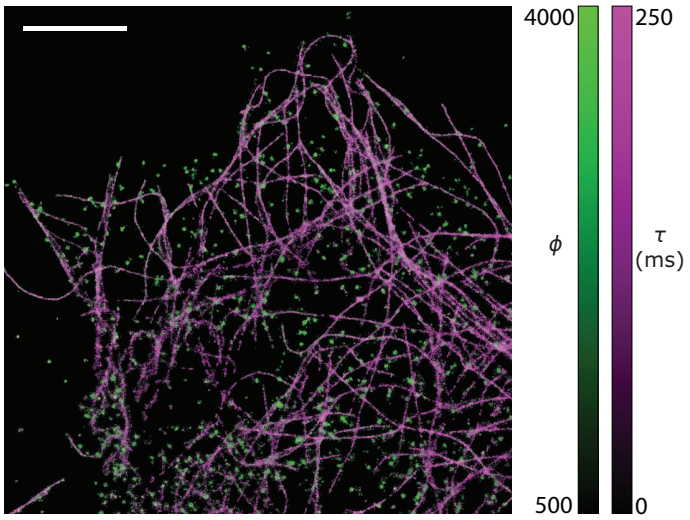

Figure 4.20 – (τ,ϕ) SMLM map obtained from a dual-colour AF647/CF680 sample (fixed COS-7 cells with the α-tubulin labelled with CF680 and the Heavy chain clathrin labelled with AF647, imaged with a single 637-nm excitation). τ and ϕ are displayed in magenta and green respectively, and the intensity encodes their values. Note that the two species are clearly distinguishable: the clathrin spheres (AF647) exhibit high photon fluxes and low ON times, while the tubulin network (CF680) corresponds to low ϕ and high τ values. As a consequence, they appear rather green and magenta, respectively. Scale bar: 5 µm.

fluence of several major parameters that may influence the results. The first complementary characterisation aims at determining the effect of the excitation power on the values of τ and ϕ. We imaged fixed COS-7 cells where the α-tubulin was labelled with CF680. We performed several acquisitions with different 637-nm excitation powers and we processed the data according to the PHANTOM workflow. The results are presented in Fig. 4.22: as expected, the ON time decreases and the fluorescence intensity increases as the excitation power increases. This could be used to improve the specificity of the demixing by selecting an excitation power that minimises the overlap of the (τ,ϕ) values for the species of interest. Still, it should be noted that too low excitation powers are likely to threaten the single molecule regime, while too high can induce phototoxicity in living cells and require that the acquisition frame rate be high enough, not to mention that the maximum output power of the laser itself might be a limiting factor.

Although the global excitation power obviously influences the ON time and the fluorescence photon flux, what actually defines the photophysical behaviour of a molecule is the local power density. Even if the excitation path is well aligned, there may be significant excitation power inhomogeneities across the imaged field due to Gaussian shape of the beam, but also to a speckle effect if the excitation peak is narrow. We performed measurements to assess their local impact on the values of τ and ϕ. The results presented in Fig. 4.23 seem to indicate a relatively strong impact of the Gaussian beam shape, as the radial component seems prevailing, with deviations to the mean values of τ and ϕ around 23 % and 14 % respectively over the 25-µm wide field of view. On the contrary,

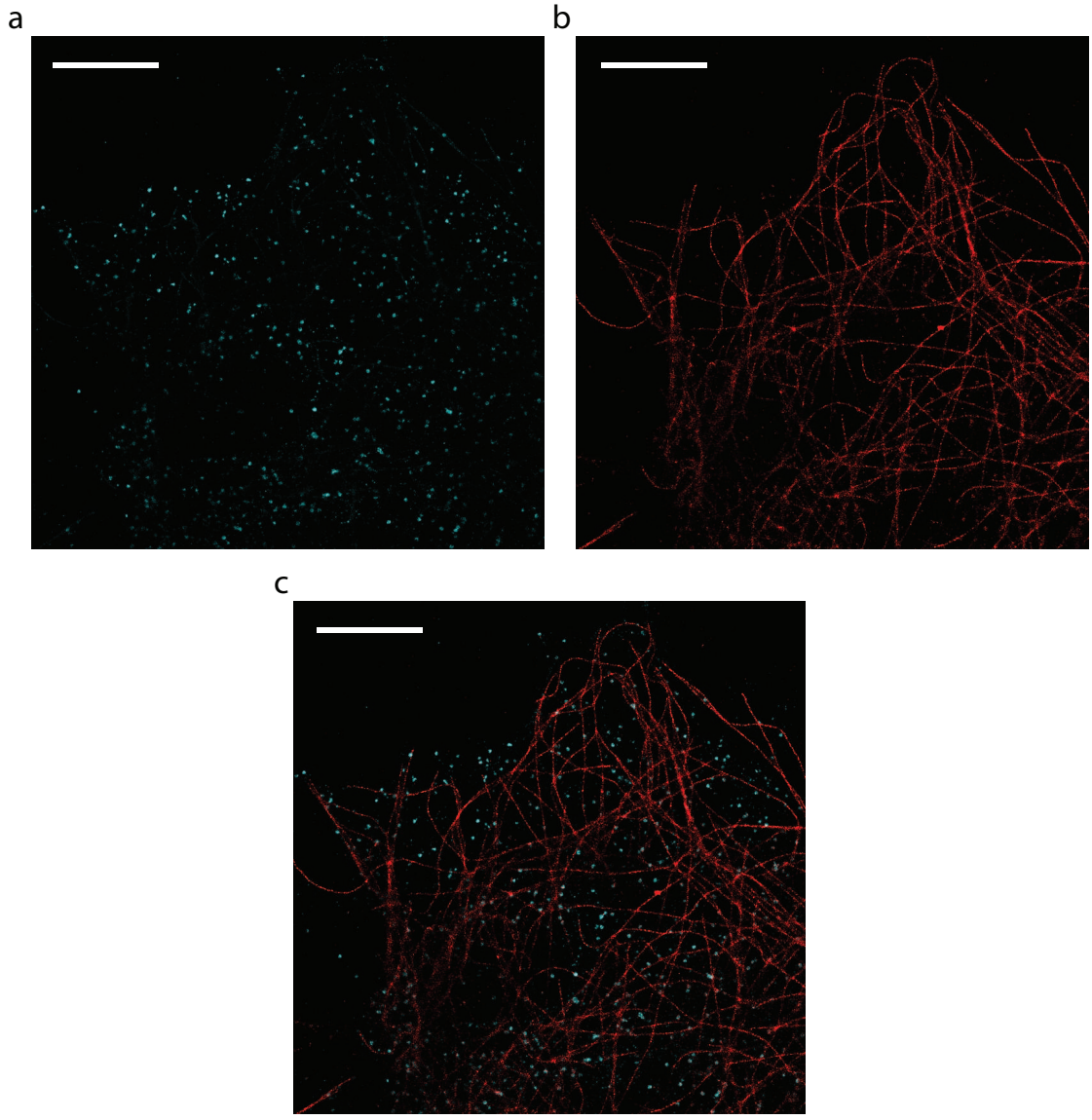

Figure 4.21 – Demixed PHANTOM 2D SMLM images obtained from the dual-colour AF647/CF680 sample displayed in Fig. 4.20 (fixed COS-7 cells with the α-tubulin labelled with CF680 and the Heavy chain clathrin labelled with AF647, imaged with a single 637-nm excitation). **(a)** and **(b)** display the images identified as AF647 (cyan) and AF555 (red) respectively using the filter shown in Fig. 4.19. **(c)** shows the merging of the two maps (in other words, the demixed dual-colour map). Scale bars: 5 µm.

the speckle pattern exhibits a less significant effect. It is worth noticing that the variations of ϕ and $1/\tau$ are correlated, much like they respond to global power variations (see Fig. 4.22), which corroborates our hypothesis that local power variations impact the photophysical behaviour. Naturally, the specificity of the properties are affected negatively by these local variations.

In order to make up for this effect, we applied local corrections based on the maps presented in Fig. 4.23. The specificity of τ and ϕ was found to be slightly enhanced, as

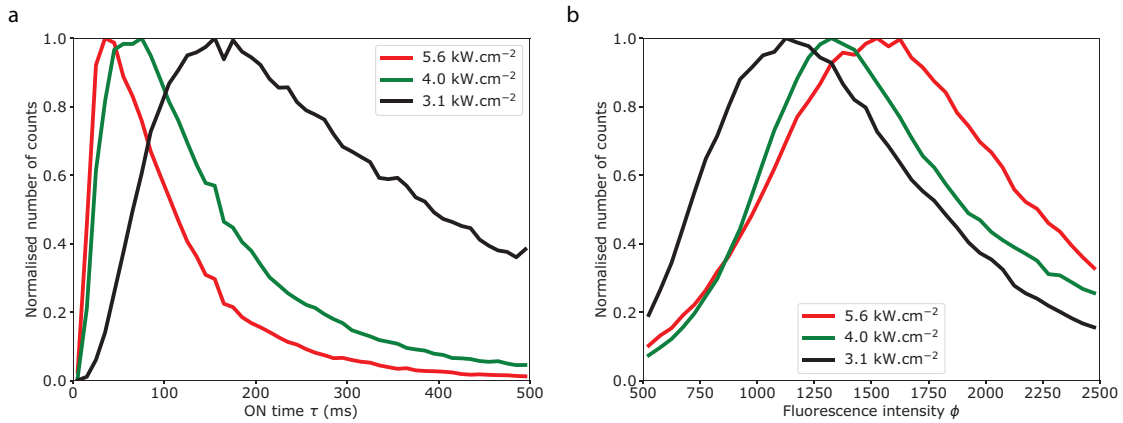

Figure 4.22 – Influence of the global excitation power on the PHANTOM results for CF680 (fixed COS-7 cells with the α-tubulin labelled with CF680). The τ **(a)** and ϕ **(b)** histograms are plotted for different laser output levels, which are converted into average power densities over the imaged field of view.

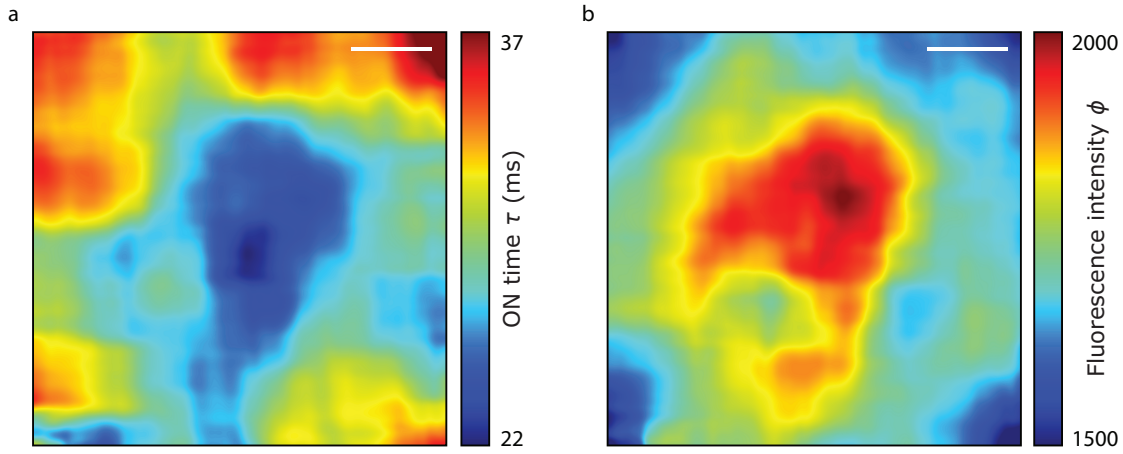

Figure 4.23 – Influence of the local excitation power on the PHANTOM results (fixed COS-7 cells with the α-tubulin labelled with AF647). The interpolated τ **(a)** and ϕ **(b)** maps are plotted over a field of view for an average power density over the field of view equal to 4 kW.cm^{-2}. Scale bar: 5 µm.

well as the cross-talk and the discarded fraction (see Fig. 4.24). Still, the improvement seems minimal considering the apparent amplitude of the local variations. We did not have time to pursue this characterisation, but there seems to be room for improvement here.

After this characterisation of the spatial homogeneity of the photophysical properties, we set out to assess the temporal stability of the ON time and fluorescence photon flux. A priori, a temporal evolution could be expected, as the chemical composition is not perfectly stable over time. Indeed, if the sample is not sealed, contact with air might induce oxygenation of the buffer. Even if it is sealed, the reactions triggered by the optically induced photochemical reactions are likely to slightly modify the buffer. We thus

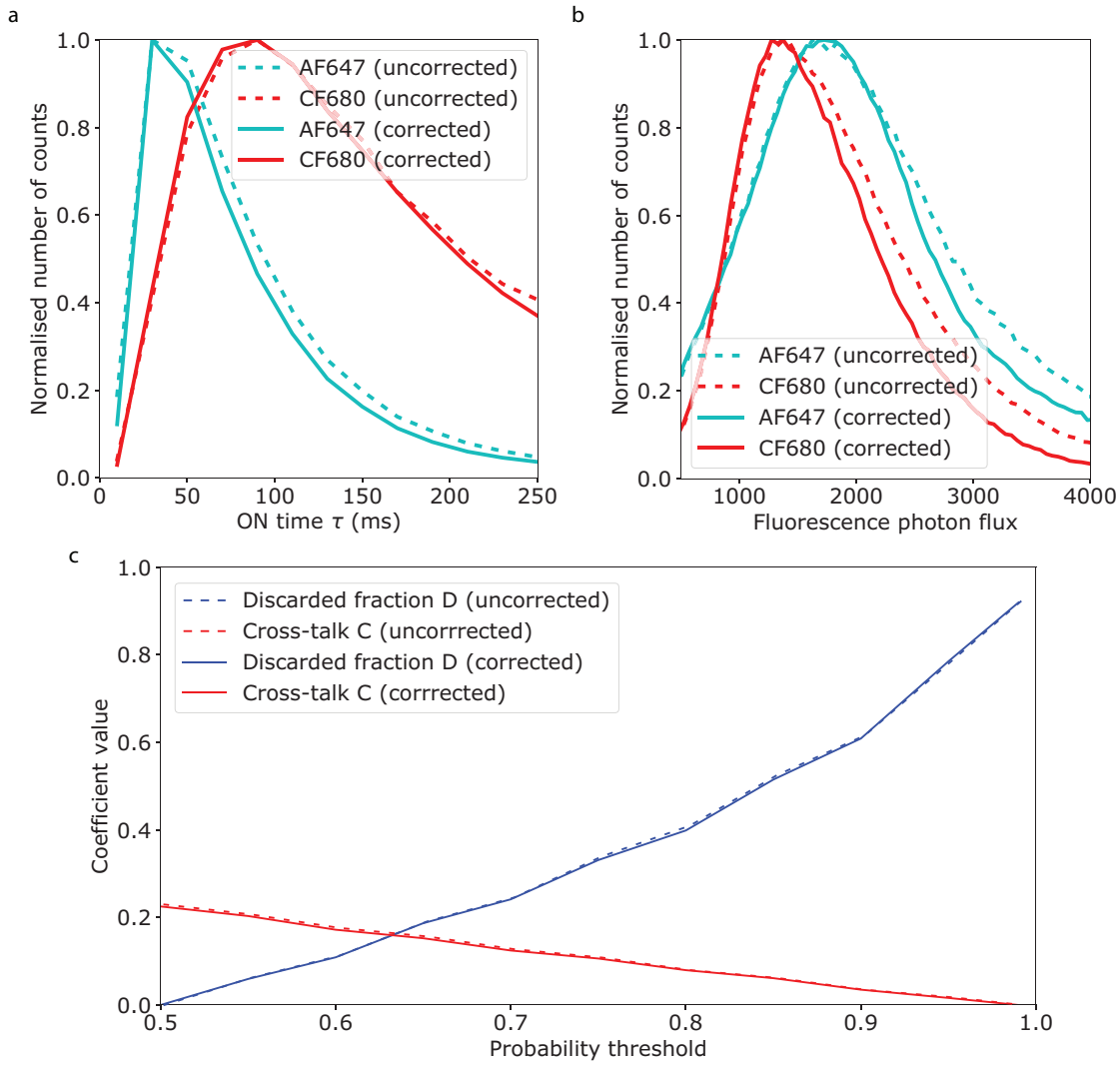

Figure 4.24 – Influence of the local correction on the PHANTOM results (fixed COS-7 cells with either the Heavy chain clathrin labelled with AF647 or the α-tubulin labelled with CF680). The histograms of τ **(a)** and ϕ **(b)** calculated over the whole field of view are plotted before and after the applying the local correction maps. Similarly, the cross-talk and discarded fraction calculated over the whole field of view are displayed in **(c)**.

imaged fixed COS-7 cells where the Heavy chain clathrin was labelled with AF647. The coverslips were unsealed and we used the usual dSTORM imaging buffer. We tracked the evolution of τ and ϕ from the beginning of the acquisition (i.e. from the moment the single molecule regime is achieved). Fig. 4.25 displays the results of this study: they do not seem to show significant temporal evolution of the photophysical properties, at least for dSTORM fluorophores[13] over the one acquisition time (typically around 15 minutes). This is rather reassuring because otherwise, a time-resolved calibration may be necessary to improve the demixing, at the cost of more complex data acquisition and processing

[13] A very similar behaviour was observed for AF555, CF647, CF660C and CF680, even if we do not present the results here.

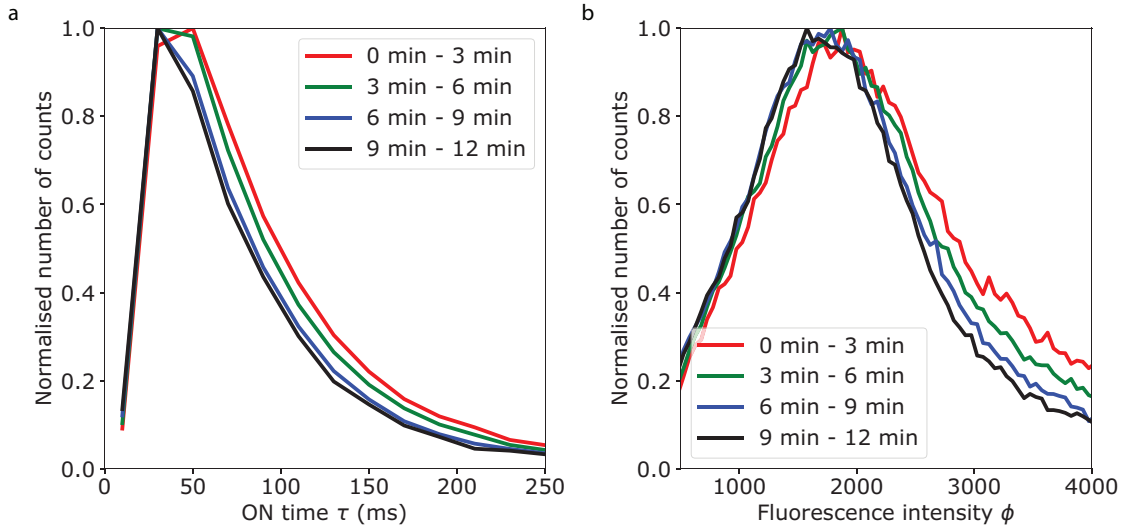

Figure 4.25 – Temporal evolution of the PHANTOM characteristics (fixed COS-7 cells with the Heavy chain clathrin labelled with AF647). The acquisition is divided in 3-minute long slices, and the histograms of τ **(a)** and ϕ **(b)** are plotted for the different slices.

workflows. Nevertheless, it is worth noticing that we only studied the dynamics of the blinking at macroscopic time scales, while there might be local effects over time scales below τ that might cause slight emission properties changes over one ON cycle—although this would probably be very difficult to probe, and even more so to correct.

The characterisations presented in all this section were performed with AF647 and/or CF680, but we also screened other commercially available dSTORM fluorophores. Indeed, the choice of the fluorophore set is a very straightforward way to optimise the specificity of the PHANTOM identification. Fig. 4.26 presents the results of the τ and ϕ measurements obtained with AF555, CF647, AF647, CF660C and CF680[14]. The histograms show significant differences that could be exploited to enhance the multi-species simultaneous detection. Overall, we found that the optimal couple was AF647/CF680. Although AF555/AF647 probably offers the best specificity, we chose not to use AF555 due to its poor stability over time in imaging conditions (see section 3.4, page 105). Still, it may prove useful for three-species simultaneous imaging (with AF555/AF647/CF680 or AF555/CF647/CF680).

We also evaluated the ON times and fluorescence intensities of mono-label probes, i.e. antibodies conjugated with one single fluorescent molecule. However, they showed very little difference in terms of photophysical properties, and could thus not be exploited to improve the demixing. Similarly, mouse antibody conjugated- and rabbit antibody conjugated AF647 exhibited highly similar properties, which tends to prove that

[14]The last four molecules were excited with the 637-nm laser, but AF555 was excited with an additional 532-nm laser (Verdi G5, 5 W, Coherent). The average 532-nm power density over the field of view was 8 kW.cm^{-2}, compared to 4 kW.cm^{-2} for the 637-nm laser (4 kW.cm^{-2} at 532 nm is not sufficient to achieve single molecule regime with AF555).

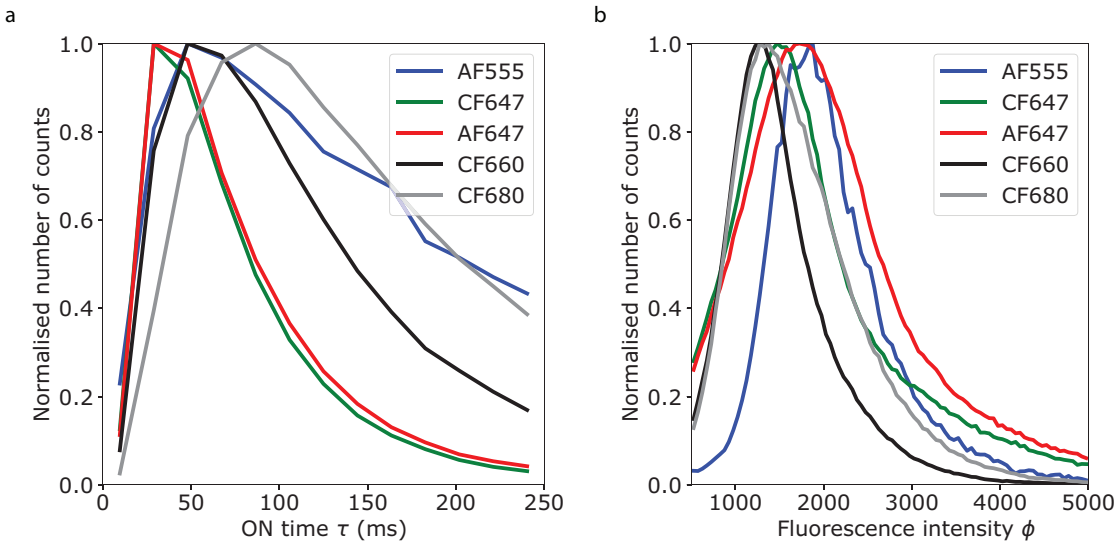

Figure 4.26 – PHANTOM characterisation of AF555, CF647, AF647, CF660C and CF680 (fixed COS-7 cells with the α-tubulin labelled with the fluorophore of interest). The τ and ϕ histograms are shown in **(a)** and **(b)** respectively.

these properties mostly depend on the fluorescent molecule itself rather than on the conjugating part or the target. Phalloidin-AF647 also showed a very similar behaviour compared to antibody-conjugated AF647, even if slight changes in the τ values could have been expected due to the PAINT-like binding/unbinding behaviour of the phalloidin to the actin.

Finally, we performed measurements on DNA-PAINT probes[15]. Due to the possibility to engineer the binding DNA strands in a controlled way to optimise the binding times [89], and to choose the fluorophore independently to tune the fluorescence photon flux, it appears a sound alternative to dSTORM, even if the secondary antibodies and the imagers are more difficult to obtain. Overall, the DNA-PAINT probes display significantly higher τ values[16], as displayed in Figure 4.27. While the fluorescence photon flux strongly depends on the excitation power, it seems more regular in DNA-PAINT, hence a better specificity. Overall, we found that the temporal profiles obtained with DNA-PAINT were far more regular than those obtained in dSTORM (see Fig. 4.27). This might be due to the fact that the single molecule regime is more convenient to achieve and to maintain over the time of one whole acquisition[17]. Otherwise, this could also be due to the previously mentioned chemical reactions induced by the optical transitions—this might result in a local modification of the buffer at time scales below τ.

[15] In DNA-PAINT, the choice of the fluorescent molecule is not expected to be as crucial as in dSTORM. For this characterisation, we used Atto655-functionalised DNA-PAINT probes.

[16] In the case of dSTORM, τ refers to the duration of the ON time; for DNA-PAINT, it refers to the time over which the imager remains bound to the docking strand.

[17] Imperfect single molecule regime is bound to induce a major degradation of the performances in most SMLM techniques. In the case of PHANTOM, the tails of the PSFs tend to create unwanted signal in the integration area, which impacts the photon count temporal profile.

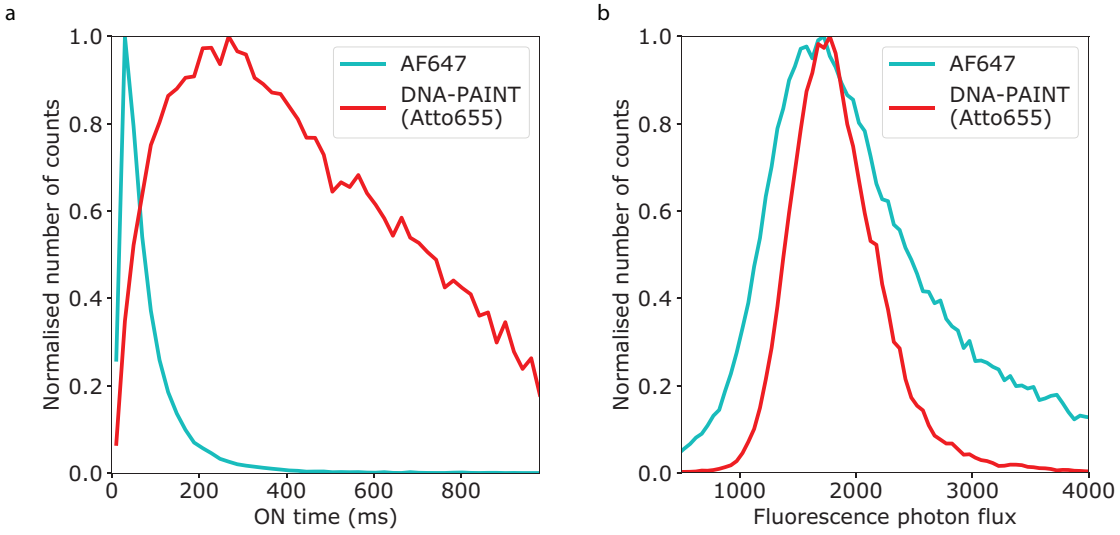

Figure 4.27 – PHANTOM characterisation of DNA-PAINT labelling (Atto655) and comparison with AF647. The τ and ϕ histograms are shown in **(a)** and **(b)** respectively.

4.3.4 Outlooks

Although we have demonstrated a proof of principle for PHANTOM and characterised several relevant factors influencing the results, there are many studies that remain to be performed. First, we only characterised a few commercially available dSTORM fluorophores. The fact that this was sufficient to produce an efficient dual-colour demixing ensures that it could be widely used with little modifications of the sample preparation protocols. Still, it would be tempting to try to find other suitable fluorophore sets compatible with PHANTOM imaging. This would require screening available fluorophores and determining the best combinations from the calibration results.

In dSTORM, CF568 might exhibit a certain degree of specificity compared to dark red fluorophores while maintaining satisfactory blinking properties, which could make it suited for three-species imaging. However, the best results may be obtained with specially designed probes. In particular, DNA-PAINT allows a certain degree of freedom for the engineering of the fluorophore and its binding strand. This could be used to identify spectrally indistinguishable species, thus eliminating chromatism-related problems at the excitation or the detection (such as the the axial chromatic aberration) and alleviating the need for spectrally separated super-resolution probes that is challenging in most multi-species SMLM experiments.

As the photophysical behaviour of the fluorescent molecules strongly depend on the chemical composition of the imaging buffer, there may be room for improvement of the specificity by optimising the buffer. We only used a standard dSTORM imaging buffer (see section A), but it would be possible to first vary the proportions of the different reagents and assess the effects of the modifications on the values of τ and ϕ. For example, a reduction of the cysteamine concentration is expected to increase the ON

times. Of course, it is also possible to use different buffer compositions, such as those published in [5, 81, 93, 94]. An exhaustive characterisation of the different buffers would be necessary though. Indeed, some of them might improve the specificity of the fluorophores regarding the PHANTOM detection at the cost of a degradation of the general blinking behaviour—for instance, a higher photobleaching rate, or a general decrease of the photon yield, which would affect negatively the localisation precision, or even a lower transition rate towards the OFF state which would make the single molecule regime more difficult to achieve.

Another lead to increase the performances of the PHANTOM detection is to improve the regularity of the temporal emission profiles. Overall, we found that a certain proportion of the recorded profiles exhibit relatively poor shapes. Whether it is due to unwanted signal coming from the tails of neighbouring PSFs or to the irregularity of the molecules themselves, some temporal profiles of dSTORM fluorophores seem rather uneven, with noticeable intensity fluctuations over one ON cycle. This causes an inadequacy of the fitted function[18] and results in poor τ and ϕ measurements. On the contrary, we found that DNA-PAINT fluorophores exhibit much more regular temporal profiles (see Figure 4.28), even if we were unable to determine if this was only due to the lower density of molecules (and thus the more complete single molecule regime) or if other phenomena were involved.

Once again, using DNA-PAINT labelling may be a viable solution. Nevertheless, it may also be possible to implement a filtering step in the PHANTOM algorithm to eliminate poor temporal profiles through conditions on the goodness of fit or on the temporal derivative of the profile.

One last possibility to enhance the results of the demixing is the improvement of the homogeneity of the excitation power density over the field of view. This was studied in section 4.3.3 (Figures 4.23 and 4.24): we found consequent local fluctuations of the photophysical behaviour due to both the Gaussian shape of the excitation beam and the speckle pattern created by the coherence of the excitation laser. Taking this into account, we applied local corrections to the measured values of the τ and ϕ, which resulted in a modest improvement of the specificity. There seems to be room for improvement here: the spatial resolution of the local interpolated correction map might have been inadequate (too low a resolution is bound to miss a certain part of the local variations, while too high a resolution makes the correction very sensitive to false detections). In any case, it seems more reliable to try to improve the homogeneity of the excitation before the acquisition than to perform post-processing corrections.

For the purpose of enhancing the regularity of the excitation profile, two elements have to be considered: first, the speckle pattern has to be removed. This can be done either by using a wide spectrum source, such as a lamp or a relatively broad spectrum

[18] The temporal profile is expected to be a rectangular function, with little temporal intensity fluctuation—in an ideal situation, only the Poisson noise due to the signal and the background should induce fluctuations.

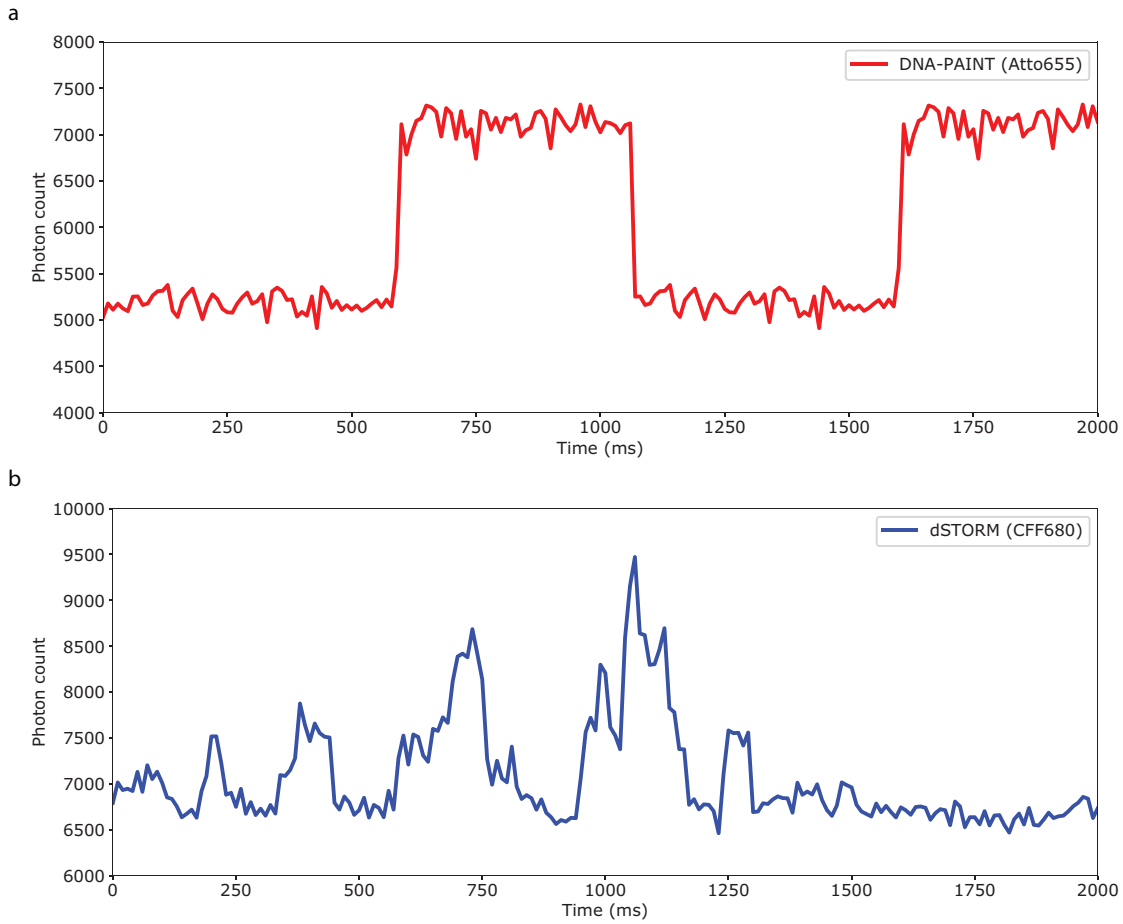

Figure 4.28 – Typical temporal emission profile obtained with DNA-PAINT (Atto655) **(a)** and comparison with a dSTORM profile (CF680) **(b)**. The irregularity of the dSTORM profile might stem from residual signal emitted by neighbouring PSFs (due imperfect single molecule regime), or to local evolutions of the chemical composition of the buffer over the duration of one ON cycle.

laser. However, this is not necessarily compatible with the required excitation for the chosen set of fluorophores. Another solution is to place a rotating diffuser in the excitation path [19]. This is not sufficient to achieve a homogeneous excitation pattern, however, as the noticeable radial dependence of the characteristics due to the Gaussian profile of the beam would be unaffected. To get rid of this dependence, several solutions might be employed. First, the beam could be expanded to reduce the variation of the power over the imaged field of view, although this induces a large waste of excitation power. Another solution is to use a narrow excitation beam and to scan it over the field of view within the acquisition time of one frame. This is done in [91]: by optimising the spatial distribution

[19] In order to avoid any divergence of the beam, the diffuser should ideally be placed near the focal point of the beam, i.e. between the two lenses composing the beam expander in the excitation path. Note that the rotation speed of the diffuser has to be adapted so that the speckle is effectively removed over the integration time of one frame. It should also be noticed that the rotation might induce mechanical vibrations of the optical table—these vibrations have to be dampened in order not to degrade the resolution in super-localisation acquisitions.

of all the laser power available, it produces a very homogeneous excitation—as well as a regular localisation precision over the imaged field. In the case of PHANTOM, this would also have the advantage of removing the previously mentioned speckle pattern without requiring the addition of a rotating diffuser. Of course, this would be perfectly valid in terms of optical setup, as PHANTOM does not impose constraints on the excitation scheme.

Aside from these possibilities of improvement of the demixing performances per se, PHANTOM could also be combined with other SMLM methods. This is especially true insofar as it is mostly a data processing-based strategy that is largely independent from the optical setup used. As long as two key points—the homogeneity of the excitation and the high acquisition frame rate—are respected, it can be coupled with most detection techniques without sacrificing the performances a priori. In particular, as it relies on photon counting, it could easily be coupled with PSF shaping methods[20] to bring complementary axial information. It could also be used in combination with a polarisation detection scheme to probe polarisation-related phenomena in either biological samples or materials, as proposed in [13, 14].

Interestingly, PHANTOM is also compatible with SESAME to some extent. A major hindrance is the fact that PHANTOM requires as homogeneous an illumination as possible, both in the lateral and in the axial directions. In other words, it is not very compatible with optical sectioning. For example, in TIRF configuration, molecules located far from the coverslip receive less excitation power than those close to the coverslip. This would cause their τ and ϕ to increase and decrease, respectively, even though they belong to the same species. Obviously, this broadening of the domains would lead to a deterioration of the specificity. As a consequence, the combination of PHANTOM and SESAME would require an epifluorescence illumination configuration. This would induce a broadening of the PSF size histograms and affect negatively the specificity of the SESAME detection—unless the sample does not feature fluorophores in the volume, which is the case for instance of adhesion structures such as focal adhesions or podosomes (see section 2.3). Nevertheless, considering the very low cross-talk between the AF647 and AF555 width obtained in TIRF configuration, this can be expected to be still usable without optical sectioning. The combination of SESAME and PHANTOM could thus enhance the demixing capabilities by extracting more fluorophore-specific information through software.

Still, there could be a potentially more relevant way to couple the two approaches: in the presence of optical sectioning at the excitation such as TIRF or light sheet, the SESAME algorithm could first be used to identify the species. Then, it would be possible to use the blinking characteristics τ and ϕ to assess the local power density, which is related to the axial position due to the confinement of the excitation. Naturally, the correspondence between (τ,ϕ) and the axial position would first need to be calibrated

[20] Unlike SESAME, which is based on a PSF shape measurement, PHANTOM is expected to be almost unaffected by PSF shaping. The only potential source of performance loss is the increased size of the PSFs that results in a lateral precision loss and imposes a reduction of the density of active molecules per frame to match the single molecule criterion.

for each fluorophore, but eventually this could yield spectrally-resolved 3D SMLM from simultaneous multicolour acquisitions based on a software approach.

Finally, PHANTOM is suited for simultaneous multicolour acquisitions on biological samples. This can solve drift issues inherent in sequential acquisitions, of course, but the main advantage of PHANTOM is that it permits imaging of spectrally close fluorophores—i.e. fluorophores that are excited by the same laser wavelength. For instance, we demonstrated the performances of the technique with the AF647/CF680 couple, which are both excited by the 637-nm laser. In other words, it would not be possible to perform sequential acquisitions on this couple. Such a feature represents a major advantage, as most efficient dSTORM fluorophores are in the orange to dark red part of the spectrum, which makes two-colour imaging challenging and three-colour almost impossible without resorting to demixing strategies. PHANTOM thus offers very satisfactory identification capabilities to produce demixed 2D SMLM images with two colours, and potentially up to three or four.

In terms of biological applications, this is particularly helpful since many studies are based on the colocalisation of two or three species, one of them standing for a known reference. Colocalisation experiments obviously benefit from the improvement of the localisation precision of every protein of interest, and PHANTOM allows the use of several efficient probes in the same experiment.

Besides, as the method is a priori compatible with live cell studies using multicolour single particle tracking, it could allow the simultaneous tracking and monitoring of different phenomena in the same sample. dSTORM may not be the best labelling strategy in this case due to its phototoxicity and to the need to permeabilise the cells for the probes to penetrate them in most cases. However, PHANTOM is also compatible with live-cell PAINT lipidic labels, as well as with PALM microscopy[21], which is much more adapted to live cell imaging.

4.4 Conclusion

In this final chapter, we have investigated the field of multicolour simultaneous SMLM experiments. Having identified the choice of the fluorescent molecules as a major bottleneck, we have found out that there exists the need for developing methods able to distinguish spectrally close labels. Various approaches are available in the literature, but most are experimentally demanding, which limits their use. Therefore, we have set out to develop simpler approaches to extract molecule-specific information immediately available from the acquisitions. We have developed two post-processing-based methods that do not require optical engineering of the excitation or the detection. As such, they are readily applicable on most home-made or commercial super-localisation microscopes, and compatible with various complementary detection modalities, such as 3D

[21] In the case of PALM, the fluorescence photon flux ϕ is unchanged compared to dSTORM or DNA-PAINT. The ON time τ, for its part, should be understood as the time between photoactivation (or photoconversion) and photobleaching.

or polarisation-resolved imaging. SESAME is based on the detection of the spot size of PSFs, which carries spectral information. PHANTOM uses the characterisation of the photophysical blinking behaviour of the molecules (ON state time and fluorescence photon flux) to identify different species without the need for spectral specificity. We have brought two-colour proofs of principle for both techniques and characterised their performances in terms of cross-talk between different channels and discarded fraction of molecules. We have thoroughly studied the impact of various factors on the specificity of the detection. Finally, we have proposed leads to improve the performances. We have furthermore discussed possibilities to extend the number of different species imaged simultaneously and to couple SESAME and PHANTOM with single particle tracking for live cell imaging or other SMLM detection modalities.

The work presented here is set in the framework of simplification of SMLM strategies to allow as broad a dissemination as possible. Much like the strategies presented in chapters 2 and 3 to make super-localisation experiments more reliable and reproducible, we believe that the simplification of the methods is a major lead to improve wide adoption and standardisation of SMLM to benefit high resolution and high specificity imaging in biology, chemistry and material physics.

Conclusion and perspectives

While single molecule localisation approaches brought new insights in fluorescence microscopy and unlocked previously inaccessible domains of investigation at the nanoscale, much remains to be done to make it routinely usable in cell biology. Indeed, if new optical setups have been specifically designed, many protocols used nowadays are inherited from standard diffraction-limited fluorescence microscopy. Thereby, non-idealities that were not noticeable have become limiting factors in SMLM, which offers high enough resolutions to investigate nanoscale structures and processes, but also highlights the many sources of errors that need to be overcome to achieve unbiased and reproducible imaging. Through this work, we have highlighted many of these non-idealities: from calibration and measurement protocols shortcomings to lateral and axial detection biases due to imperfect single molecule regime or to drifts, geometric and chromatic aberrations or sample tilt. Having identified the origins of these problems, we then set out to propose solution to overcome them.

In chapter 2, we identified the shortcomings of axial calibration protocols reported in the literature. Although correction protocols exist, they rely on modelling and simplifications of complex electromagnetic phenomena. We proposed an alternative fully experimental method based on the rather intuitive idea of imaging a sample of known geometry in standard conditions. We then tackled the issue of performance measurements in 3D SMLM. We presented theoretical approaches and sample-based measurements. We found out that biological samples are unsuited to this use in most cases due to the difficulty to decouple the influences of the localisation precision, the stability of the setup, the size of the labelled protein and the geometry of the label. We thus proposed to use dedicated calibration samples, which make the assessment of the influence of each of these factors more easily accessible. Finally, we presented three applications of DONALD led in collaboration with colleagues from biology and chemistry teams: we determined the localisation of antibiotics in *Staphylococcus aureus* cell walls to understand resistance to drugs, and we imaged the nanoscale architecture and the roles of different proteins in podosomes and focal adhesions, which finds applications in the field of cell adhesion, motility and migration.

The third chapter was devoted to the development of DAISY, through both optical

and software designs. We showed how the SAF absolute reference could help correct axial detection biases inherent in PSF shaping-based methods. More importantly, we presented a new approach that uses every single localisation through the acquisition as a reference provided to the correction software, which massively increases the statistical set compared to methods based on fiducial markers. Much like in the axial calibration protocol proposed in chapter 2, where all the relevant information was contained in the geometry of the sample to impose as little constraint on the imaging setup as possible, here we use DAISY to gather and process all the necessary information without imposing constraints on the sample preparation. Having characterised the performances of the method in comparison with standard astigmatic imaging and DONALD, we set out to use it for state-of-the-art applications in collaboration with biology and chemistry teams.

This allowed us to stress the many problems related to multicolour SMLM imaging—in particular, we found out that efficient fluorophores are generally very close spectrally, which vastly limits the possibilities to design fluorophores sets when aiming at imaging multiple species in the same sample. This led us to develop in the last chapter two novel post-processing methods to enable demixing of spectrally close fluorophores in the framework of simultaneous imaging. The two rely on the measurement of very different characteristics—SESAME uses the PSF size while PHANTOM is based on the assessment of the dynamic photophysical behaviour of the molecules. Still, they both share a similar strong point: they impose very little constraint on the optical setup, which makes them compatible with most other SMLM methods. The demixing performances achieved with standard commercially available dSTORM fluorophores appear particularly promising, as they could find a broad range of applications.

In spite of the advances presented in this thesis, many questions remain unanswered. It is our hope that they can be investigated to further push the understanding of the physical and chemical phenomena involved and their applications in superlocalisation microscopy.

In particular, if the calibration and performance measurement protocols proposed in chapter 2 are especially adapted for imaging near the coverslip, there is a need for the development of similar protocols in the framework of deep imaging. Imaging in thick samples is a major challenge in SMLM, but recently, several methods have been proposed to significantly increase the imaging range of 3D methods [37, 41, 42], up to a few tens of micrometres. While this unlocks new fields of investigation for biological questions, it also obviously requires robust methods to calibrate the axial detection and assess the 3D performances. Due to the strong effect of sample-induced aberrations, the preparation of such samples may bring new challenges—for instance, the degree of aberration may need to be controlled and quantified.

Even though a few leads remain to improve the performances of DAISY (such as the suppression of field-varying aberrations to reduce the consequent biases), we feel that it is a rather mature technique that can be readily coupled with other wavefront shaping patterns (double helix or tetrapod PSFs for instance), and applied to imaging of various samples. In particular, it could strongly benefit reproducible bioimaging thanks

to its insensibility to axial detection biases. Overall, we found out that the main limitations of DAISY when imaging biological samples were the very same as in standard 2D SMLM—namely, the difficulty to come up with a suitable set of efficient and spectrally separated fluorophores. Thereby, resorting to DNA-PAINT labelling, or coupling DAISY with demixing methods such as SESAME or PHANTOM is expected to bring significant improvements. Aside from bioimaging, DAISY could also be used as a means to measure and verify calibration samples, due to its reliability. Much like, in section 2.1, DONALD was used to verify the geometry of the microspheres before using them for the axial calibration of PSF shaping methods, one could imagine using DAISY to assess the geometry of samples that are intended to be used for other uses and with other techniques.

Finally, SESAME and PHANTOM seem very promising methods to us, as they could be coupled with most other SMLM modalities. Several questions require more thorough characterisation, though. Especially, SESAME would benefit from the use of a spatially-resolved PSF width calibration. Similarly, increasing the acquisition frequency and enhancing the illumination homogeneity through dedicated excitation approaches [91, 92] are bound to bring beneficial improvements in PHANTOM. Optimal fluorophore sets may be found thanks to a screening of the different molecules commercially available, but one can also imagine varying the chemical composition of the imaging buffer, or even engineering probes for this specific purpose. SESAME and PHANTOM could furthermore benefit from the coupling with other detection modalities—especially 3D SMLM. Finally, they are bound to find many relevant applications in the field of bioimaging, especially on living samples.

This work opens many perspectives for new development improvements and applications. Several leads seem of particular significance to us. First, adaptive optics might be a relevant complementary detection modality. Indeed, it could help correct spherical aberration as well as sample-induced ones, which are known to cause both precision degradation and axial biases. Interestingly enough, it could also be put to use to evaluate the amplitude of aberrations in biological samples, especially in the volume, and assess their influence on the PSFs. This approach is only seldom reported in 3D SMLM [37], but seems quite relevant to us. Aberrations measured this way could then be applied thanks to an SLM or a deformable mirror in order to mimic realistic aberrations in deep samples. High resolution imaging in the volume of samples (up to a few tens of micrometres) is a topical question in super-resolution fluorescence microscopy, as biological samples are known to exhibit different behaviours when adhered to a coverslip or in a realistic 3D environment. In that regard, characterising and applying realistic aberrations could vastly help the development of 3D SMLM in volume.

Adaptive optics could furthermore benefit DAISY in several ways. First, the wavefront pattern could be more finely adapted to imaging needs for a given application—for instance by tuning the astigmatism amplitude in order to match requirements in terms of axial and lateral precisions, as well as PSF size (this parameter is crucial to consider to achieve single molecule regime). Phase patterns applied through adaptive optics are also reported to be much cleaner (i.e. to generate much less residual aberration) than the

cylindrical lens we used. Besides, the variation of the the aberrations through the imaging field is still somewhat limiting in DAISY, and adaptive optics could be helpful here to perform a spatially-resolved aberration correction (adaptive optics methods are being developed to optimise the homogeneity of the correction through the field by using multiple guide stars for example). Different shaping patterns could also be used aside from astigmatism, and the phase pattern applied could even be modified during the course of the acquisition to optimise the precision for the temporally-varying density of PSFs [36].

More generally, we are convinced that adaptive optics is a very powerful tool for multi-modal SMLM. Indeed, in many cases, it is able to optimise the detection specificity by enhancing effects or extracting features. For example, we can mention the work of the team of W. E. Morener to precisely encode the polarisation [49] or the fluorescence wavelength [61] in the PSF shape. Using an SLM, similar complementary detection modalities could be readily developed, for example to probe local changes induced by the binding of probes to certain surfaces at the single molecule level.

Another major improvement lead is machine learning. Although such methods have to be used with care, as the reasoning followed by algorithms to identify relevant information is specific to the network itself, they can prove very powerful tools in some cases. The first use that we can propose for this approach is the learning of experimental PSFs. Indeed, spot shapes tend to be so difficult to predict that the only viable solution is often to simply measure them. Many effects can induce PSF deformations, from defocus and interface-induced spherical aberration to sample-induced aberrations, not to mention that spot shapes vary with the fluorescence wavelength and the lateral position in the imaging field most of the time. Accounting for all these effects represents a considerable amount of characterisation, and learning algorithms can be highly useful here. Indeed, they can be fed the results obtained over many acquisitions in nominal conditions to establish a PSF database that contains extensive knowledge about the influence of each factor. We are convinced that this approach could be strongly beneficial to enhance the precision of 3D and multicolour measurements.

Machine learning could furthermore be used in combination with SESAME and PHANTOM to gather information about the PSF shape as well as the lifetime and fluorescence intensity. This may be used for instance to identify more reliably overlapping PSFs during the localisation process and discard them. Spatially-resolved demixing of the acquisitions could also be performed this way in order to account for the variation of the spot shape and blinking behaviour across the imaged field. Interestingly enough, PHANTOM could benefit from such algorithms insofar as temporal profiles could be characterised more finely than we did during this work. The fitting function could be relevantly adapted to the shape of the profiles acquired experimentally, and contributions from neighbouring molecules could be identified to discard the corresponding localisations.

Finally, we would like to push further the characterisations and the applications in SESAME and PHANTOM. It would be interesting to evaluate the performances obtained with DNA-PAINT fluorophores and to find a set of labels that maximises the specificity

of the detection. Provided a suitable combination could be found, we would like to demonstrate the feasibility of the demixing in three- or even four-colour simultaneous acquisitions. Live cell imaging is also a challenging perspective, as both methods appear to be suited for time-resolved multi-species studies. Eventually, these detection modalities could also be used for functional imaging—for example to track binding of certain labels leading to modifications of the ON time or fluorescence photon flux.

Appendix A

Appendix: acquisition and processing protocols

In this appendix, we provide precise details about the optical hardware, as well as the protocols followed during the acquisitions. We also explain thoroughly the processing workflow to perform the localisation and extract the axial or multicolour information.

A.1 Optical setups

A.1.1 DONALD setup

The optical setup used for DONALD acquisitions is presented in Fig. 1.20. The excitation light can be provided by any of five lasers at different wavelengths: 637 nm (Obis 637LX, 140 mW, Coherent), 561 nm (Genesis MX 561 STM, 500 mW), 532 nm (Verdi G5, 5 W, Coherent), 488 nm (Genesis MX 488 STM, 500 mW, Coherent), and 405 nm (Obis 405LX, 100 mW, Coherent). The different wavelengths are combined thanks to different dichroic mirrors (LaserMux, Semrock). Two doublets (Thorlabs) are used to expand the beams and produce the required illumination field size, and a lens (Thorlabs) placed before the microscope focuses the beam in the BFP of the objective to produce a collimated beam after the objective. A home-made motorised TIRF stage (Thorlabs) allows to switch between epifluorescence or TIRF illumination by translation of the excitation beams in the BFP of the objective.

The microscope is a Nikon Eclipse Ti inverted microscope with a Nikon Perfect Focus System and a Nikon APO TIRF ×100 1.49 NA oil immersion objective lens (used with Nikon immersion oil). Depending on the excitation wavelength, two different dichroic cubes are used: either the Semrock LF405/488/561/635-A-000 (for 561-nm excitation) or the Semrock LF405/488/532/635-A-000 (for other excitation wavelengths).

The detection module is composed of a 150-mm lens (Thorlabs) to collimate the beam, a non-polarising 50/50 beam splitter (Thorlabs) and a 250-mm tube lens (Thorlabs) to create the image of the object plane in the plane of the 512×512-pixel EMCCD camera (iXon3, Andor). The mask placed in the back focal plane of the objective is a

custom made ring of approximately 4 mm diameter.

A.1.2 DAISY setup

DAISY acquisitions were carried out thanks to the optical setup presented in Fig. 3.5a. The excitation light can be provided by any of five lasers at different wavelengths: 637 nm (Obis 637LX, 140 mW, Coherent), 561 nm (Genesis MX 561 STM, 500 mW), 532 nm (Verdi G5, 5 W, Coherent), 488 nm (Genesis MX 488 STM, 500 mW, Coherent), and 405 nm (Obis 405LX, 100 mW, Coherent). The different wavelengths are combined thanks to different dichroic mirrors (LaserMux, Semrock). Two doublets (Thorlabs) are used to expand the beams and produce the required illumination field size, and a lens (Thorlabs) placed before the microscope focuses the beam in the BFP of the objective to produce a collimated beam after the objective. A home-made motorised TIRF stage (Thorlabs) allows to switch between epifluorescence or TIRF illumination by translation of the excitation beams in the BFP of the objective.

The microscope is a Nikon Eclipse Ti inverted microscope with a Nikon Perfect Focus System and a Nikon APO TIRF ×100 1.49 NA oil immersion objective lens (used with Nikon immersion oil). Depending on the excitation wavelength, two different dichroic cubes are used: either the Semrock LF405/488/561/635-A-000 (for 561-nm excitation) or the Semrock LF405/488/532/635-A-000 (for other excitation wavelengths).

The detection module is composed of a 150-mm lens (Thorlabs) to collimate the beam, a non-polarising 50/50 beam splitter (Thorlabs) and a 250-mm tube lens on each path (Thorlabs) to create the image of the object plane in the plane of the 512×512-pixel EMCCD camera (iXon3, Andor). The mask placed in the back focal plane of the objective is a custom made ring of approximately 4 mm diameter.

A.1.3 SESAME setup

The optical setup used for SESAME acquisitions is presented in Fig. 4.6a. The excitation light can be provided by two lasers at different wavelengths: 637 nm (450 mW, Errol), 532 nm (900 mW, Errol). The different wavelengths are combined thanks to a dichroic mirror (LaserMux, Semrock). Two doublets (Thorlabs) are used to expand the beams and produce the required illumination field size, and a lens (Thorlabs) placed before the microscope focuses the beam in the BFP of the objective to produce a collimated beam after the objective. A home-made motorised TIRF stage (Thorlabs) allows to switch between epifluorescence or TIRF illumination by translation of the excitation beams in the BFP of the objective.

The microscope is a Nikon Eclipse Ti inverted microscope with a Nikon Perfect Focus System and a Nikon APO TIRF ×100 1.49 NA oil immersion objective lens (used with Nikon immersion oil). A Semrock cube (LF405/488/532/635-A-000) is used to separate the fluorescence light from the excitation beams.

The detection module is composed of a 250-mm and then a 150-mm lenses (Thorlabs) to produce the right magnification factor at the detection and create the image of

the object plane in the plane of the 2048×2048-pixel SCMOS camera (ORCA-Flash4.0, Hamamatsu).

A.1.4 PHANTOM setup

PHANTOM acquisitions are carried out thanks to the optical setup presented in Figure 4.16a. The excitation light is provided by a 637-nm laser (450 mW, Errol). Two doublets (Thorlabs) are used to expand the beam and produce the required illumination field size, and a lens (Thorlabs) placed before the microscope focuses the beam in the BFP of the objective to produce a collimated beam after the objective.

The microscope is a Nikon Eclipse Ti inverted microscope with a Nikon Perfect Focus System and a Nikon APO TIRF ×100 1.49 NA oil immersion objective lens (used with Nikon immersion oil). A Semrock cube (LF405/488/532/635-A-000) is used to separate the fluorescence light from the excitation beams.

The detection module is composed of a 250-mm and then a 150-mm lenses (Thorlabs) to produce the right magnification factor at the detection and create the image of the object plane in the plane of the 2048×2048-pixel SCMOS camera (ORCA-Flash4.0, Hamamatsu). In the relay plane of the BFP, we placed a custom made ring-shaped physical mask of approximately 4 mm diameter to remove the axial dependence due to the SAF.

A.2 Acquisition protocols

A.2.1 DONALD acquisitions

For DONALD acquisitions, we use a standard dSTORM buffer (Smart kit, Abbelight). The focus plane is set approximately at the coverslip. Then the sample is briefly shone in epifluorescence excitation configuration at low illumination power (approximately 0.025 $kW.cm^{-2}$) to record the diffraction-limited wide field images for each wavelength of interest. Still in epifluorescence excitation configuration, the illumination power is then increased up to 4 $kW.cm^{-2}$ typically to achieve single molecule regime. Once a sufficient density of active molecules per frame (roughly 1 molecule per μm^2 per frame) is obtained, the excitation is generally switched to TIRF configuration, and the acquisition is started with a 50-ms exposure time and an EMCCD gain equal to 150. The number of images recorded strongly depend on the sample and the labelling, between 15.000 and 60.000 frames. When imaging dark red fluorophores (such as AF647), a low power (0.002 to 0.025 $kW.cm^{-2}$) 405-nm illumination is sometimes used together with the 637 laser beam in order to bring a fraction of the fluorophores back from the dark state to the ON state.

The frames are recorded thanks to a Python custom written piece of software.

A.2.2 DAISY acquisitions on dSTORM/DNA-PAINT samples

DAISY acquisitions are also performed using the Abbelight Smart kit as dSTORM imaging buffer. The focus plane is set approximately 400 nm above the coverslip, which corresponds to focal positions around 0 nm and 800 nm above the coverslip respectively. Then the sample is briefly shone in epifluorescence excitation configuration at low illumination power (around 0.025 kW.cm^{-2}) to record the diffraction-limited wide field images for each wavelength of interest. Still in epifluorescence excitation configuration, the illumination power is then increased up to 4 kW.cm^{-2} typically to achieve single molecule regime. Once a sufficient density of active molecules per frame (roughly 1 molecule per 4 µm^2 per frame) is obtained, the acquisition is started (still in epifluorescence excitation configuration) with a 50-ms exposure time (or a 100-ms exposure time in the cases of AF555) and an EMCCD gain equal to 150. The number of images recorded strongly depend on the sample and the labelling, between 20.000 and 90.000 frames. When imaging dark red fluorophores (such as AF647), a low power (0.002 to 0.025 kW.cm^{-2}) 405-nm illumination is sometimes used together with the 637 laser beam in order to bring a fraction of the fluorophores back from the dark state to the ON state.

Multicolour dSTORM experiments are done sequentially, starting from the higher wavelengths: for instance, when imaging a sample labelled with AF647 and AF555, once the diffraction limited images are recorded a high power 637-nm excitation is used to image AF647 until photobleaching, and then a high power 532-nm excitation induces the blinking of the AF555, which can be imaged.

Dual-colour dSTORM/DNA-PAINT experiments are slightly different in terms of acquisition protocol. First, the dSTORM acquisitions are performed (using the Abbelight Smart kit as imaging buffer): the dSTORM image is recorded at low illumination power (around 0.025 kW.cm^{-2}), and then the excitation power is increased up to 4 kW.cm^{-2} typically to achieve single molecule regime. Once a sufficient density of active molecules per frame (roughly 1 molecule per 4 µm^2 per frame) is obtained, the acquisition is started (still in epifluorescence excitation configuration) with a 50-ms exposure time and an EMCCD gain equal to 150. The number of frames recorded is around 60.000–90.000, and a low power (0.002 to 0.025 kW.cm^{-2}) 405-nm illumination is used together with the 637 laser beam in order to bring a fraction of the fluorophores back from the dark state to the ON state. Once most molecules are photobleached, the dSTORM buffer can be removed without moving the sample (for this purpose, we use unsealed sample holders). Then the dilution of DNA-PAINT imagers (typically 0.5 nM diluted in Ultivue imaging buffer) is added and we wait a few minutes for the imagers to diffuse and penetrate inside the cells. The DNA-PAINT diffraction-limited image is recorded using a brief low power illumination in epifluorescence excitation mode, and the excitation power is increased to achieve single molecule regime. The excitation is set to a steep angle epifluorescence configuration to limit background fluorescence signal, and the acquisition is started with a 100-ms exposure time and an EMCCD gain equal to 150.

The frames are recorded thanks to a Python custom written piece of software.

A.2.3 DAISY acquisitions on fluorescent beads samples

DAISY performance measurements and drift tracking experiments carried out on fluorescent beads samples were done using a solution of PBS with 5 % glucose to mimic the refractive index of the dSTORM buffer without inducing blinking. The excitation was adjusted (typically around 0.025 kW.cm^{-2}) to match the fluorescence emission level of AF647 (2750 photons per UAF PSF and 2750–5100 photons per EPI PSF depending on the height of the source). Measuring the performances on beads emitting the same number of photons is crucial as, according to CRLB calculations, the precision is expected to vary proportionally to $1/\sqrt{N}$ where N is the number of photons per PSF. Unless otherwise stated, the exposure time was set to 50 ms, the EMCCD gain was equal to 150, and 500 frames were recorded per field of view.

The frames are recorded thanks to a Python custom written piece of software.

A.2.4 SESAME acquisitions

For SESAME acquisitions, we use a standard dSTORM buffer (Smart kit, Abbelight). The focus plane is set approximately at the coverslip. Then the sample is briefly shone in epifluorescence excitation configuration at low illumination power (around 0.025 kW.cm^{-2}) to record the diffraction-limited wide field images for each wavelength of interest. Still in epifluorescence excitation configuration, the illumination power is then increased up to 4 kW.cm^{-2} with each wavelength (637 nm and 532 nm excitations are performed simultaneously) to achieve single molecule regime. Once a sufficient density of active molecules per frame (roughly 1 molecule per µm^2 per frame) is obtained, the excitation is switched to TIRF configuration, and the acquisition is started with a 50-ms exposure time. The number of frames recorded is set to 45.000. No 405-nm excitation was used.

The frames are recorded the Neo software provided by Abbelight.

A.2.5 PHANTOM acquisitions

PHANTOM acquisitions also used the Abbelight Smart kit as dSTORM imaging buffer. The focus plane is set approximately at the coverslip. Then the sample is briefly shone in epifluorescence excitation configuration at low 637-nm illumination power (around 0.025 kW.cm^{-2}) to record the diffraction-limited wide field image. Still in epifluorescence excitation configuration, the illumination power is then increased up to 4 kW.cm^{-2} to achieve single molecule regime. Once a sufficient density of active molecules per frame (roughly 1 molecule per µm^2 per frame) is obtained, the acquisition is started with a 10-ms exposure time (still with an epifluorescence excitation). The number of frames recorded is set to 90.000. No 405-nm excitation was used.

The frames are recorded the Neo software provided by Abbelight.

A.3 Localisation software

The processing software consists of custom written Python scripts.

A.3.1 DONALD software

The EPI and UAF frames are first pre-processed by subtracting the pixel per pixel temporal median of the last 10 frames to remove the static background. Then the PSFs are detected using a second order wavelet filtering [55] associated to an intensity lower threshold. PSFs closer than 1 µ are discarded to avoid mislocalisations due to imperfect single molecule regime. Each PSF is localised thanks to a circular Gaussian fitting to assess its lateral position (x,y). To find the correspondence between the spot pairs, for each detected UAF PSF, the EPI PSF is searched in a 2 µm × 2 µm square area centred on the UAF detection, and taken as the nearest neighbour if several EPI PSFs are detected in the area. The lateral positions detected on the EPI and UAF frames are then recombined to improve the lateral localisation precision by considering the average between the two[1]:

$$x = \frac{x^{\mathrm{EPI}} + x^{\mathrm{UAF}}}{2} y = \frac{y^{\mathrm{EPI}} + y^{\mathrm{UAF}}}{2} \tag{A.1}$$

Then, the numbers of EPI and UAF photons are measured through an intensity integration over a 1.3 µm × 1.3 µm square area centred on the PSF: this provides the EPI and UAF numbers of photons N^{EPI} and N^{UAF}. These steps are sequentially performed for each acquired frame of the series, which provides a localisation list containing the values of x, y, N^{EPI} and N^{UAF} for each PSF on each frame. Finally, the lateral drift is corrected (see section 1.5, Fig. 1.11).

The last step is to calculate the SAF ratio $\rho^{\mathrm{SAF}} = \frac{N^{\mathrm{EPI}}}{N^{\mathrm{UAF}}} - 1$ and correct it by applying the correction factors α_{RT} and β_{mask} to make up for the non-idealities of the detection setup (see equation (3.3)):

$$\rho^{\mathrm{SAF}} = \frac{N^{\mathrm{SAF}}}{N^{\mathrm{UAF}}} = \left(\frac{N^{\mathrm{EPI}}}{N^{\mathrm{UAF}} \alpha_{\mathrm{RT}}} - 1 \right) \beta_{\mathrm{mask}} \tag{A.2}$$

The theoretical axial dependence of the SAF ratio can be approximated by assuming an exponential decay, which fits the theoretical curve (Fig. 1.22) very well:

$$\rho^{\mathrm{SAF}} = 0.85 \exp\left(-\frac{z}{0.24 \lambda_{\mathrm{fluo}}} \right) \tag{A.3}$$

This can also be written:

$$z = 0.24 \lambda_{\mathrm{fluo}} \ln\left(\frac{0.85}{\rho^{\mathrm{SAF}}} \right) \tag{A.4}$$

The last equation is used to calculate the axial position from the intensity measurements.

[1] The optimal merging formula should take into account the photon numbers, as described in section 3.1, equations (3.1) and (3.2). Still, as the EPI and UAF photon numbers are not considerably different, this approximation is acceptable.

At the end of the position computation process, several filtering steps are performed in order to remove false detections. The main criteria are the UAF photon number (typically 500 photons minimum for AF647), the EPI PSF width (110 nm $< \sqrt{w_x^{\mathrm{EPI}} w_y^{\mathrm{EPI}}} <$ 350 nm) and the EPI PSF aspect ratio ($0.67 < w_x^{\mathrm{EPI}}/w_y^{\mathrm{EPI}} < 1.5$).

A.3.2 DAISY software

The EPI and UAF frames are first pre-processed by subtracting the pixel per pixel temporal median of the last 10 frames to remove the out-of-focus static background[2]. Then the PSFs are detected using a second order wavelet filtering [55] associated to an intensity lower threshold. PSFs closer than 2 µ are discarded to avoid mislocalisations due to imperfect single molecule regime (see section 3.3 for an evaluation of the influence of the density of active molecules per frame in astigmatism and in SAF). Each PSF is localised thanks to a centroid calculation to assess its lateral position (x,y) and an elliptical Gaussian fitting to retrieve its widths (w_x,w_y). To find the correspondence between the spot pairs, for each detected UAF PSF, the EPI PSF is searched in a 2 µm × 2 µm square area centred on the UAF detection, and taken as the nearest neighbour if several EPI PSFs are detected in the area.

The UAF and SAF numbers of photons are extracted thanks to a photon integration on a 2-µm wide square region centred on the centre of mass of the PSF performed on the filtered frame (i.e. after removing the temporal median of the last 10 frames), and the corrected SAF ratio is calculated according to the formula given in equation (3.3). Finally, the SAF axial position can be calculated:

$$z^{\mathrm{SAF}} = 0.24 \lambda_{\mathrm{fluo}} \ln\left(\frac{0.85}{\rho^{\mathrm{SAF}}}\right) \tag{A.5}$$

The astigmatism information calculation relies on the PSF widths previously measured through the Gaussian fitting. The correspondence is found with the calibration table, which is established using the 15 µm diameter microspheres coated with fluorophores. For that purpose, we use a least squares minimisation using an error function defined as the square of the width differences, as described in equation (3.6).

Before the two axial information sources can be merged, the axial astigmatic positions must be corrected using the SAF reference in order to account for axial detection biases such as drift, chromatic aberration and sample tilt. This is achieved by performing a spatially and temporally resolved cross-correlation between $z^{\mathrm{astigmatic}}$ and z^{SAF}. This correction algorithm is explained in section 3.2.

The merged DAISY axial position is obtained thanks to a linear combination of $z^{\mathrm{astigmatic}}$ (after the correction) and z^{SAF} weighted according to their theoretical uncertainties, according to the formula displayed in equation (3.8). Similarly, the lateral posi-

[2] A notable exception to this pre-processing step exists for non-blinking sources, especially fluorescent beads. In that case, this step is replaced with a simple subtraction of the global median of the frame.

tions detected on the EPI and UAF frames are recombined to improve the lateral localisation precision according to the formulas provided in equations (3.1) and (3.2). Finally, the lateral positions are drift-corrected using a temporal cross-correlation algorithm (see part 1.5), with a 50-nm lateral pixel and a slice size equal to 1000.

At the end of the position computation process, several filtering steps are performed in order to remove false detections. The main criteria are the UAF photon number (typically 500 photons minimum for AF647), the EPI PSF width (110 nm $< \sqrt{w_x^{\mathrm{EPI}} w_y^{\mathrm{EPI}}} <$ 350 nm) and the EPI PSF aspect ratio ($0.67 < w_x^{\mathrm{EPI}}/w_y^{\mathrm{EPI}} < 1.5$).

A.3.3 SESAME software

First, each frame is pre-processed by removing the pixel per pixel temporal median of the previous 10 frames in order to get rid of the slowly varying background without altering the PSFs. The spots are detected using a wavelet filtering. Each PSF is characterised using an anisotropic Gaussian fitting to retrieve the PSF positions and widths w_x and w_y. A photon counting is also performed over a 1 µm × 1 µm square area centred on the PSF to determine the number of photons N.

A filtering step based on photon number ($1000 < N < 10000$), PSF widths (70 nm $< w_x <$ 300 nm and 70 nm $< w_y <$ 300 nm) and PSF anisotropy ($0.67 < w_x/w_y < 1.5$) is then operated to get rid of false positive detections and strongly defocused PSFs. Furthermore, localisations closer than 1 µm are discarded to avoid biases due to the signal from neighbouring PSFs. The lateral drift is corrected thanks to a sample-based cross-correlation algorithm with stacks of 1000 frames and a 50-nm large pixel.

Then, each PSF needs to be assigned to one fluorophore based on its width. This is done using the results of the single-colour calibration acquisitions (see section 4.2.1 and Fig. 4.8). In order to identify the domains corresponding to each fluorophore of interest, we use a k nearest neighbours algorithm. For each pixel in the (w_x,w_y) space, the algorithm finds the 50 nearest neighbours from the calibration localisation lists and uses them to calculate the local density of each species i (with $i \in [\mathrm{AF555}, \mathrm{AF647}]$ for instance). From the densities, a probability $p_i(w_x, w_y)$ of belonging to the species i is calculated. The probabilities verify:

$$\sum_i p_i(w_x, w_y) = 1 \quad \forall (w_x, w_y) \tag{A.6}$$

In particular, for the AF555/AF647 couple, this results in:

$$p_{\mathrm{AF555}}(w_x, w_y) + p_{\mathrm{AF647}}(w_x, w_y) = 1 \quad \forall (w_x, w_y) \tag{A.7}$$

It is then possible to calculate domains for each species. This we achieve by assigning (w_x,w_y) pixel to the fluorophore that has the highest probability, but we also exclude from the domains any (w_x,w_y) pixel where no species has a probability high enough to be

considered unambiguous. For instance, in the particular case of dual-colour acquisitions, probabilities below a certain threshold (between 0.5 and 1) can be discarded in order to optimise the specificity, which comes at the cost of a certain localisation loss proportion (see part 4.2.3 and Fig. 4.9).

Eventually, the values of w_x and w_y of each PSF recorded during a simultaneous multicolour acquisition are used to distribute the detected molecules in the corresponding categories according to the domains delimited from the calibration results.

All these processing steps use CPU parallelisation to improve the calculation speed.

A.3.4 PHANTOM software

First, each frame is pre-processed by removing the pixel per pixel temporal median of the previous 100 frames. This allows to get rid of the static background locally without altering the signal contained in each PSF. The spots are detected using a second order wavelet filtering associated with a lower threshold. Each PSF is characterised using a Gaussian fitting to retrieve the PSF positions and widths w. For each PSF on the frame i, a photon counting is also performed over a 1 µm × 1 µm square area centred on the PSF in every frame from $i-100$ to $i+100$ to extract the temporal intensity profile. This profile is fitted around the frame i with a modified rectangular function to allow one intermediary position between the background and the top plateau level at the rising edge, and one another at the falling edge (see Fig. 4.16b, frame $i+1$). The values of τ (defined as the full width at half maximum between the two edges) and ϕ (defined as the difference between the top plateau and the background level) can thus be extracted.

A filtering step based on ON times (0 ms $< \tau <$ 500 ms), intensities ($500 < \phi <$ 10000), PSF widths (80 nm $< w <$ 250 nm) and PSF anisotropy ($0.67 < w_x/w_y < 1.5$) is then operated to get rid of false positive detections. Furthermore, localisations closer than 1 µm are discarded to avoid biases due to the signal from neighbouring PSFs. The lateral drift is corrected thanks to a sample-based cross-correlation algorithm with stacks of 5000 frames and a 50-nm large pixel.

A recombination algorithm is used to group all the detections corresponding to one single molecule in one ON cycle (for instance, in Fig. 4.16b, the localisations in the dotted boxed region are grouped for the frames $[\![i+1, i+5]\!]$). This is done by averaging the localisation data (x, y, w_x, w_y, τ, ϕ) calculated for each detection in the ON cycle (which is known from the fitting performed on the temporal profile) within a region of ± 500 nm × 500 nm around the first position of the ON cycle.

Finally, the values of τ and ϕ are used to distribute the detected molecules in the corresponding categories according to the domains delimited from the calibration results. These domains are automatically determined using a k nearest neighbour algorithm to calculate the likelihood of a molecule belonging to either of the species. The domains are generated excluding too unspecific regions (i.e. probabilities too low or too

undecided between the different species). In order to identify the domains corresponding to each molecule, we use a k nearest neighbours algorithm—much like in the SESAME algorithm (see part 4.2.2). For each pixel in the (τ,ϕ) space, the algorithm finds the 50 nearest neighbours from the calibration localisation lists and uses them to calculate the local density of each species i (with $i \in [\mathrm{AF647}, \mathrm{CF680}]$ for instance). From the densities, a probability $p_i(\tau, \phi)$ of belonging to the species i is calculated. The probabilities verify:

$$\sum_i p_i(\tau, \phi) = 1 \quad \forall(\tau, \phi) \tag{A.8}$$

In particular, for the AF647/CF680 couple, this results in:

$$p_{\mathrm{AF647}}(\tau, \phi) + p_{\mathrm{CF680}}(\tau, \phi) = 1 \quad \forall(\tau, \phi) \tag{A.9}$$

It is then possible to calculate domains for each species. This we achieve by assigning (τ,ϕ) pixel to the fluorophore that has the highest probability, but we also exclude from the domains any (τ,ϕ) pixel where no species has a probability high enough to be considered unambiguous. For instance, in the particular case of dual-colour acquisitions, probabilities below a certain threshold (between 0.5 and 1) can be discarded in order to optimise the specificity, which comes at the cost of a certain localisation loss proportion.

Eventually, the values of τ and ϕ of each PSF recorded during a simultaneous multicolour acquisition are used to distribute the detected molecules in the corresponding categories according to the domains delimited from the calibration results.

All these processing steps use CPU parallelisation to improve the calculation speed.

Appendix B

Appendix: sample preparation

B.1 Biological samples

The culture, fixation and labelling protocols are described below. For the COS-7 cells, the culture and fixation protocols are common for all samples presented in this work, but the labelling protocol will be specifically developed for each experiment.

B.1.1 COS-7 cells culture and fixation

COS-7 cells were grown in DMEM with 10% FBS, 1% L-glutamin and 1% penicillin/streptomycin (Life Technologies) at 37°C and 5% CO_2 in a cell culture incubator. Several days later, they could be plated at low confluency on cleaned round 25 mm diameter high resolution 1.5H glass coverslips (Marienfield, VWR). After 24 hours, the cells were washed three times with PHEM 1x solution (60 mM PIPES, 25 mM HEPES, 5 mM EGTA and 2 mM Mg acetate adjusted to pH 6.9 with 1 M KOH) and fixed for 12 min in 4% PFA, 0.2% glutaraldehyde, 0.5% Triton, 50% PHEM 2x solution (120 mM PIPES, 50 mM HEPES, 10 mM EGTA and 4 mM Mg acetate adjusted to pH 6.9 with 1 M KOH); they were then washed 3 times in PBS (Invitrogen, 003000). Up to this fixation step, all chemical reagents were pre-warmed at 37°C. The cells were post-fixed for 10 min with PBS + 0.1% Triton X-100, reduced twice for 10 min with $NaBH_4$, and washed in PBS three times before being blocked for 15 min in PBS + 1% BSA.

B.1.2 COS-7 cells labelling

In the case of actin labelling (Figures 1.9, 2.4, 3.4 and 3.20), the cells were incubated for 20 minutes at room temperature with 3.3 nM phalloidin-AF647 (Thermo Fisher, A22287) in the (d)STORM imaging buffer (Abbelight) before starting the acquisition—without removing the dSTORM buffer containing the phalloidin-AF647. On the contrary, immunolabelling of tubulin and clathrin required more preparation steps.

For AF647 α-tubulin (Figures 1.10, 1.11, 2.8, 3.5, 3.9, 3.13b–c, 3.15a, 4.14, 4.15 and 4.23), the cells were incubated 1 hour at 37°C with 1:400 mouse anti-α-tubulin antibody

(Sigma Aldrich, T6199) in PBS + 1% BSA. This was followed by three washing steps in PBS + 1% BSA, incubation 45 min at 37°C with 1:400 goat anti-mouse AF647 antibody (Life Technologies, A21237) diluted in PBS 1% BSA and three more washes in PBS.

For AF647 β-tubulin and AF555 α-tubulin (Fig. 3.14), the cells were incubated 1 hour at 37°C with 1:400 rabbit anti-β-tubulin antibody (Sigma Aldrich, T5293) in PBS + 1% BSA. This was followed by three washing steps in PBS + 1% BSA, incubation 45 min at 37°C with 1:400 goat anti-rabbit AF555 antibody (Life Technologies, A21430) diluted in PBS + 1% BSA and three more washes in PBS + 1% BSA. Then they were incubated again 1 hour at 37°C with 1:400 mouse anti-α-tubulin antibody (Sigma Aldrich, T6199) in PBS + 1% BSA, washed three times, incubated 45 min at 37°C with 1:4 goat anti-mouse AF647 antibody (Life Technologies, A21237) diluted in PBS + 1% BSA and washed three more washes in PBS.

For AF647 α- and β-tubulin, the cells were incubated 1 hour at 37°C with 1:400 mouse β-tubulin antibody (Sigma Aldrich, T5293) in PBS + 1% BSA. This was followed by three washing steps in PBS + 1% BSA, incubation 1 hour at 37°C with 1:400 mouse α-tubulin antibody (Sigma Aldrich, T6199) diluted in PBS 1% BSA, three more washes in PBS + 1% BSA, incubation 45 min at 37°C with 1:400 goat anti-mouse AF647 antibody (Life Technologies, A21237) diluted in PBS 1% BSA and three more washes in PBS.

For AF647 heavy chain and light chain clathrin and DNA-PAINT α- and β-tubulin (Figures 2.7, 3.25 and 3.26), the cells were incubated 1 hour at 37°C with 1:400 mouse anti-light chain clathrin antibody (Sigma Aldrich, C1985) in PBS + 1% BSA and washed three times with PBS + 1% BSA, incubated again 1 hour at 37°C with 1:400 mouse anti-heavy chain clathrin antibody (Sigma Aldrich, C1860) in PBS + 1% BSA and washed three times with PBS + 1% BSA. Then they were incubated 45 min at 37°C with 1:400 anti-mouse AF647 antibody (Life Technologies, A21237) in PBS + 1% BSA, washed three times with PBS + 1% BSA, and incubated again 1 hour at 37°C with 1:400 mouse β-tubulin antibody (Sigma Aldrich, T5293) in PBS + 1% BSA. This was followed by three washing steps in PBS + 1% BSA, incubation during 1 hour at 37°C with 1:400 mouse α-tubulin antibody (Sigma Aldrich, T6199) diluted in PBS 1% BSA, three more washes in PBS + 1% BSA, incubation during 2 hours at 37°C with 1:100 anti-mouse-D1 Ultivue secondary antibody diluted in antibody dilution buffer (Ultivue) and washed three more washes in PBS.

For phalloidin-AF647 and DNA-PAINT α-tubulin labelling (Fig. 3.21), the cells were incubated 1 hour at 37°C with 1:400 mouse α-tubulin antibody (Sigma Aldrich, T6199) diluted in PBS 1% BSA and washed three times with PBS + 1% BSA. This was followed by a 2-hour long incubation at 37°C with 1:100 anti-mouse-D1 Ultivue secondary antibody diluted in antibody dilution buffer (Ultivue) and three more washes in PBS. Finally, the cells were incubated 20 minutes at room temperature with 3.3 nM phalloidin-AF647 (Thermo Fisher, A22287) in the (d)STORM imaging buffer (Abbelight) before starting the acquisition without removing the buffer.

For AF555 α-tubulin (Figures 1.10, 1.11, 2.8, 3.5, 3.9, 3.13b–c, 3.15a, 4.6, 4.7, 4.8, 4.9, 4.10 and 4.23), the cells were incubated 1 hour at 37°C with 1:400 mouse anti-α-

tubulin antibody (Sigma Aldrich, T6199) in PBS + 1% BSA. This was followed by three washing steps in PBS + 1% BSA, incubation 45 min at 37°C with 1:400 goat anti-mouse AF647 antibody (Life Technologies, A21237) diluted in PBS 1% BSA and three more washes in PBS.

For AF647 heavy chain clathrin (Figures 4.6, 4.7, 4.8, 4.9, 4.10, 4.17, 4.18, 4.19, 4.24, 4.25 and 4.26), the cells were incubated 1 hour at 37°C with 1:400 rabbit anti-heavy chain clathrin antibody (Abcam, ab21679) in PBS + 1% BSA. This was followed by three washing steps in PBS + 1% BSA, incubation 45 min at 37°C with 1:400 goat anti-rabbit AF647 antibody (Invitrogen, A21246) diluted in PBS 1% BSA and three more washes in PBS.

For AF555 α-tubulin (Figures 4.6, 4.7, 4.8, 4.9, and 4.10), the cells were incubated 1 hour at 37°C with 1:400 mouse anti-α-tubulin antibody (Sigma Aldrich, T6199) in PBS + 1% BSA. This was followed by three washing steps in PBS + 1% BSA, incubation 45 min at 37°C with 1:400 goat anti-mouse AF555 antibody (Invitrogen, A21425) diluted in PBS 1% BSA and three more washes in PBS.

For AF647 heavy chain clathrin and AF555 α-tubulin (Figures 4.11 and 4.12), the cells were incubated 1 hour at 37°C with 1:400 rabbit anti-heavy chain clathrin antibody (Abcam, ab21679) and 1:400 mouse anti-α-tubulin antibody (Sigma Aldrich, T6199) in PBS + 1% BSA. This was followed by three washing steps in PBS + 1% BSA, incubation 45 min at 37°C with 1:400 goat anti-rabbit AF647 antibody (Invitrogen, A21246) and 1:400 goat anti-mouse AF555 antibody (Invitrogen, A21425) diluted in PBS 1% BSA and three more washes in PBS.

For CF680 α-tubulin (Figures 4.17, 4.18, 4.19, 4.22, 4.24 and 4.26), the cells were incubated 1 hour at 37°C with 1:400 mouse anti-α-tubulin antibody (Sigma Aldrich, T6199) in PBS + 1% BSA. This was followed by three washing steps in PBS + 1% BSA, incubation 45 min at 37°C with 1:400 goat anti-mouse CF680 antibody (Sigma, 20063) diluted in PBS 1% BSA and three more washes in PBS.

For AF647 heavy chain clathrin and CF680 α-tubulin (Figures 4.16b, 4.20 and 4.21), the cells were incubated 1 hour at 37°C with 1:400 rabbit anti-heavy chain clathrin antibody (Abcam, ab21679) and 1:400 mouse anti-α-tubulin antibody (Sigma Aldrich, T6199) in PBS + 1% BSA. This was followed by three washing steps in PBS + 1% BSA, incubation 45 min at 37°C with 1:400 goat anti-rabbit AF647 antibody (Invitrogen, A21246) and 1:400 goat anti-mouse CF680 antibody (Sigma, 20063) diluted in PBS 1% BSA and three more washes in PBS.

In any case, after the immunolabelling of tubulin and/or clathrin, a post-fixation step was performed using PBS with 3.6% formaldehyde for 15 min. The cells were washed in PBS three times and then reduced for 10 min with 50 mM NH_4Cl (Sigma Aldrich, 254134), followed by three additional washes in PBS.

B.1.3 Neuron samples preparation

To prepare the neuron samples, rat hippocampal neurons from E18 pups were cultured on 18 mm coverslips at a density of 6,000/cm^2 according to previously published protocols [95] and following guidelines established by the European Animal Care and Use Committee (86/609/CEE) and approval of the local ethics committee (agreement D18-055-8). After 16 days in culture, neurons were fixed using 4% PFA in PEM (80 mM Pipes, 5 mM EGTA, and 2 mM $MgCl_2$, pH 6.8) for 10 min. After rinses in 0.1 M phosphate buffer (PB), neurons were blocked for 60 minutes at room temperature in immunocytochemistry buffer (ICC: 0.22% gelatin, 0.1% Triton X-100 in PB). Following this, neurons were incubated with a chicken primary antibody against map2 (Abcam, ab5392) mouse primary antibody against β2-spectrin (BD Bioscience, 612563) and a rabbit primary antibody against adducin (Abcam, ab51130) diluted in ICC overnight at 4°C, then after ICC rinses with AF 488, 555 and 647 conjugated secondary antibodies for 1h at 23°C.

B.1.4 *E. coli* samples preparation

The *E. coli* K12 (MG1655) cells (Figures 3.15b, 3.23 and 3.24) were grown in 2YT medium (Sigma, Tryptone 16.0 g/L, Yeast extract 10.0 g/L, NaCl 5.0 g/L) at 37°C under agitation (180 rpm). Overnight cultures were diluted 100 times in fresh medium (final volume 300 µL) containing Kdo-N_3 (1.0 mM). Bacteria were incubated at 37°C for 9 hours under agitation (180 rpm). Then 200 µL of the obtained suspension were washed 3 times with PBS buffer (200 µL, 12,000 rpm, 1 min, room temperature). The pellet was re-suspended in 200 µL of a solution of DBCO-Sulfo-Biotin (JenaBioscience, CLK-A116) (0.50 mM in PBS buffer) and the suspension was vigorously agitated for 90 min at room temperature. Bacteria were washed 3 times with PBS buffer (200 µL, 12,000 rpm, 1 min, room temperature). The pellet was re-suspended in a solution of Streptavidin-AF647 / Streptavidin-AF555 (20 µg/mL each) (Invitrogen, Thermo Fisher Scientific, S21374 and S32355) in PBS containing BSA (1.0 mg/mL, 200 µL) and the suspension was agitated at room temperature for 90 min in the dark. Bacteria were then washed 3 times with PBS buffer (200 µL, 12,000 rpm, 1 min, room temperature). The pellet was re-suspended in PBS buffer (400 µL) and stored at 4°C until imaging.

B.2 Labelled microspheres samples

The following protocol was used to prepare the samples of 15-µm diameter microspheres decorated with AF647 molecules at their surface (see sections 2.1, 3.1 and Figures 2.2, 2.3 and 2.4).

We used 15.0-µm (± 1.5 µm) diameter latex microspheres coated with biotin (Kisker Biotech, PC-BX-15.0), on which we attached the fluorophores of interest, namely Alexa Fluor (AF) 647 functionalised with streptavidin (Life Technologies, S21374). The sample was elaborated as follows: we prepared a solution containing 500 µL of water, 500 µL of Phosphate-Buffered Saline (PBS), 100 µL of microspheres solution and 0.5 µL of streptavidin-functionalised AF647. This solution was centrifuged 20 minutes

at 13.4 krpm. The liquid was then removed and replaced with 100 µL of PBS. By vortexing the aliquot, the deposit was dissolved. We then took 50 µL of the final solution, delicately laid it on a glass coverslip and waited for 20 minutes after covering it to protect it from light and evaporation. Finally, we gently added 500 µL of imaging dSTORM buffer (dSTORM smart kit, Abbelight).

B.3 Fluorescent beads samples

B.3.1 100-nm diameter tetraspeck beads deposited on the coverslip

To obtain the samples of 100-nm diameter tetraspeck beads, we prepare a dilution of the initial solution (T7279, Thermo Fisher) by a factor 5.10^{-4} in PBS + 5% glucose (to mimic the refractive index of the dSTORM imaging buffer), and we wait 5 minutes before starting the acquisitions.

B.3.2 20-nm diameter beads deposited on the coverslip

The 20-nm diameter dark red fluorescent beads samples are obtained using a 5.10^{-7} dilution of the bead solution (F8783, Thermo Fisher) in PBS + 5% glucose to mimic the refractive index of the dSTORM imaging buffer. After 5 minutes, the acquisitions can be started.

B.3.3 40-nm diameter beads deposited on the coverslip

The 40-nm diameter dark red fluorescent beads samples are obtained using a 5.10^{-7} dilution of the bead solution (10720, Thermo Fisher) in PBS + 5% glucose to mimic the refractive index of the dSTORM imaging buffer. After 5 minutes, the acquisitions can be started.

B.3.4 40-nm diameter beads deposited on fixed cells

The samples of 40-nm fluorescent beads deposited on fixed cells are prepared according to the following protocol. We take unlabelled fixed COS-7 cells coverslips (see section B.1.1) and add 40-nm diameter dark red fluorescent beads (10720, Thermo Fisher) diluted by a factor 5.10^{-7} during 5 minutes. Beads stuck on the upper side of the membrane are thus located at random heights. Then, we remove the solution and replace it with PBS + 5% glucose for imaging to mimic the refractive index of the dSTORM imaging buffer.

Appendix C

Appendix: Fisher information and Cramér-Rao Lower Bounds calculations

To determine the theoretical limits of DAISY, we calculated the Fisher information and the Cramér-Rao Lower Bounds (CRLB) of both the SAF and astigmatic axial detections, as well as that of the lateral detection in order to have access to the theoretical limits of DAISY.

C.1 Fisher information and CRLB for SAF

We used the same approach as Balzarotti *et al.* [96] to calculate the Fisher information for the supercritical angle fluorescence signal and the associated Cramér-Rao Lower Bounds. Considering an emitter at the position $\mathbf{r}$ exposed to K different illuminations, each photon acquired $n_i\,(i \in [0, K-1])$ follows a Poissonian statistics with a mean λ_i that depends on the illumination. The authors demonstrated that the components of the parameter vector with negligible dark count can be expressed as:

$$p_i^{(0)}(\mathbf{r}) = \frac{\lambda_i}{\sum_{j=0}^{K-1} \lambda_j} \text{ with } (i \in [0, K-1]) \tag{C.1}$$

Adding the background signal, this becomes:

$$p_i(\mathbf{r}) = \frac{\lambda_i + \lambda_{bi}}{\sum_{j=0}^{K-1} \left(\lambda_j + \lambda_{bj}\right)} \tag{C.2}$$

This equation can be simplified:

$$\begin{aligned} p_i(\mathbf{r}) &= \frac{\mathrm{SBR}(\mathbf{r})}{\mathrm{SBR}(\mathbf{r})+1}\frac{\lambda_i}{\sum_{j=0}^{K-1}\lambda_j} + \frac{1}{\mathrm{SBR}(\mathbf{r})+1}\frac{\lambda_{bi}}{\sum_{j=0}^{K-1}\lambda_{bj}} \\ &= \frac{\mathrm{SBR}(\mathbf{r})}{\mathrm{SBR}(\mathbf{r})+1}p_i^{(0)} + \frac{1}{\mathrm{SBR}(\mathbf{r})+1}\frac{1}{K} \end{aligned} \tag{C.3}$$

where $\mathrm{SBR}(\mathbf{r}) = \frac{\sum_{j=0}^{K-1}\lambda_j}{\sum_{j=0}^{K-1}\lambda_{bj}}$ represents the signal to background ratio. Balzarotti *et al.* showed that the Fisher matrix can be expressed in a simple form:

$$F_{\mathbf{r}} = N\sum_{i=0}^{K-1}\frac{1}{p_i}\begin{bmatrix} \left(\frac{\partial p_i}{\partial \mathbf{r}_1}\right)^2 & \cdots & \frac{\partial p_i}{\partial \mathbf{r}_1}\frac{\partial p_i}{\partial \mathbf{r}_d} \\ \vdots & \ddots & \vdots \\ \frac{\partial p_i}{\partial \mathbf{r}_d}\frac{\partial p_i}{\partial \mathbf{r}_1} & \cdots & \left(\frac{\partial p_i}{\partial \mathbf{r}_d}\right)^2 \end{bmatrix} \tag{C.4}$$

The Fisher information matrix gives access to a lower bound for the covariance matrix $\Sigma(\mathbf{r})$. The arithmetic mean of the eigenvalues $\widetilde{\sigma}_{\mathrm{CRLB}}$ of the lower bound matrix is interpreted as a performance metric:

$$\Sigma(\mathbf{r}) \geq \Sigma_{\mathrm{CRLB}}(\mathbf{r}) = F_{\mathbf{r}}^{-1} \tag{C.5a}$$

$$\widetilde{\sigma}_{\mathrm{CRLB}} = \sqrt{\frac{1}{d}\mathrm{tr}(\Sigma_{\mathrm{CRLB}}(\mathbf{r}))} \tag{C.5b}$$

where d is the number of dimensions considered and N is the total acquired photon number.

These results can be transposed to our model provided a few modifications. Rather than considering different illuminations, we consider a sampling of the signal in two parts: one (EPI signal, noted $i = 0$) dependent on the z position of the emitter and one (UAF signal, noted $i = 1$) independent of z. In this case, the Fisher matrix takes the form of a scalar:

$$F_z = N\left(\frac{1}{p_0}\left(\frac{\partial p_0}{\partial z}\right)^2 + \frac{1}{p_1}\left(\frac{\partial p_1}{\partial z}\right)^2\right) \tag{C.6}$$

$p_i(z)$ is provided by **Equation** (C.3):

$$p_i(z) = \frac{\mathrm{SBR}(z)}{\mathrm{SBR}(z)+1} p_i^{(0)} + \frac{0.5}{\mathrm{SBR}(z)+1} \tag{C.7}$$

Equation (C.3) can be differentiated:

$$\frac{\partial p_i(z)}{\partial z} = \frac{\partial \mathrm{SBR}(z)}{\partial z} \frac{p_i^{(0)} - 0.5}{(\mathrm{SBR}(z)+1)^2} + \frac{\partial p_i^{(0)}}{\partial z} \frac{\mathrm{SBR}(z)}{\mathrm{SBR}(z)+1} \tag{C.8}$$

First, we use the theoretical dependence of the SAF signal versus the z position by performing simulations based on the work of Wai Teng Tang *et al.* [97]. By fitting the simulation results, we assume that the ratio between the SAF and UAF photon numbers can be approximated as follows for a numerical aperture of 1.49 and an fluorescence wavelength λ_{fluo}:

$$\frac{N_{\mathrm{SAF}}}{N_{\mathrm{UAF}}} = 0.85 \, \exp\left(-\frac{z}{0.24 \, \lambda_{\mathrm{fluo}}}\right) \tag{C.9}$$

The signal of an emitter is divided in two parts so as to separate the UAF from the EPI fluorescence. In this case, the mean of the Poisson distribution for each part can be expressed as:

$$\begin{aligned} \lambda_{\mathrm{EPI}} = \lambda_0 &= \frac{(N_{\mathrm{UAF}} + N_{\mathrm{SAF}})}{2} \\ &= \frac{N_{\mathrm{UAF}}}{2} (1 + 0.85 \exp(-\alpha z)) \end{aligned} \tag{C.10a}$$

$$\lambda_{\mathrm{UAF}} = \lambda_1 = \frac{N_{\mathrm{UAF}}}{2} \tag{C.10b}$$

with $\alpha = \frac{1}{0.24 \, \lambda_{\mathrm{fluo}}}$. These terms can be used in **Equation** (C.1) to obtain the two components of the parameter vector with neglected Gaussian noise:

$$p_0^{(0)}(z) = \frac{1 + 0.85 \exp(-\alpha z)}{2 + 0.85 \exp(-\alpha z)} \tag{C.11a}$$

$$p_1^{(0)}(z) = \frac{1}{2 + 0.85 \exp(-\alpha z)} \tag{C.11b}$$

At this point, a background noise term B has to be introduced in the calculation. B is a photon number associated to an optical signal produced mainly by fluorescent probes

located outside the focal plane and is approximated to 200 photons per channel in our calculations. B represents $\lambda_{bj} = \lambda_b$, considered constant for each channel. We define the SBR(z) as :

$$\mathrm{SBR}(z) = \frac{\sum_{j=0}^{1} \lambda_j}{\sum_{j=0}^{1} \lambda_{bj}} = \frac{N_{\mathrm{UAF}}\,(2 + 0.85\exp(-\alpha z))}{4B} \tag{C.12}$$

Finally, we can extract the expression of the Fisher information and the CRLB:

$$\begin{aligned} F = N\Bigg(& \frac{1}{\frac{\mathrm{SBR}(z)}{\mathrm{SBR}(z)+1} p_0^{(0)} + \frac{0.5}{\mathrm{SBR}(z)+1}} \left(\frac{\partial \mathrm{SBR}(z)}{\partial z} \frac{p_0^{(0)} - 0.5}{(\mathrm{SBR}(z)+1)^2} + \frac{\partial p_0^{(0)}}{\partial z} \frac{\mathrm{SBR}(z)}{\mathrm{SBR}(z)+1} \right)^2 \\ & + \frac{1}{\frac{\mathrm{SBR}(z)}{\mathrm{SBR}(z)+1} p_1^{(0)} + \frac{0.5}{\mathrm{SBR}(z)+1}} \left(\frac{\partial \mathrm{SBR}(z)}{\partial z} \frac{p_1^{(0)} - 0.5}{(\mathrm{SBR}(z)+1)^2} + \frac{\partial p_1^{(0)}}{\partial z} \frac{\mathrm{SBR}(z)}{\mathrm{SBR}(z)+1} \right)^2 \Bigg) \end{aligned} \tag{C.13a}$$

$$\Delta z_{\mathrm{CRLB}}^{\mathrm{SAF}} = \sqrt{\frac{1}{F(z)}} \tag{C.13b}$$

with the different parameters:

$$\frac{\partial p_0^{(0)}}{\partial z} = -\frac{0.85\ \alpha\ \exp(-\alpha z)}{(2 + 0.85\exp(-\alpha z))^2} \tag{C.14a}$$

$$\frac{\partial p_1^{(0)}}{\partial z} = \frac{0.85\ \alpha\ \exp(-\alpha z)}{(2 + 0.85\exp(-\alpha z))^2} \tag{C.14b}$$

$$\frac{\partial \mathrm{SBR}}{\partial z} = -\frac{N_{\mathrm{UAF}}\ 0.85\ \alpha\ \exp(-\alpha z)}{4B} \tag{C.14c}$$

C.2 CRLB for astigmatism

The Cramér-Rao Lower Bound for the astigmatic detection is directly computed from the work of Rieger and Stallinga [72]. We consider that an astigmatic PSF can be approximated by an elliptical Gaussian PSF with different widths in x and y, noted w_x and w_y:

$$H = \frac{N}{2\pi w_x w_y} \exp - \left(\frac{(x-x_0)^2}{2w_x^2} + \frac{(y-y_0)^2}{2w_y^2} \right) \tag{C.15}$$

From **Equation** (C.15), the CRLB for the $w_{x,y}$ parameters can be approximated with the semi-exact formula:

$$\left(\Delta w_{x,y}\right)^2 \approx \frac{w_{x,y}^2}{2N} \left(1 + 8\tau + \sqrt{\frac{9\tau}{1+4\tau}} \right) \tag{C.16}$$

where τ is approximately equal to the ratio between the peak and background intensities (a being pixel size):

$$\tau = \frac{2\pi b(w_x w_y + a^2/12)}{Na^2} \tag{C.17}$$

The authors derive the axial detection position from the focus S curve:

$$f = \frac{w_x^2 - w_y^2}{w_x^2 + w_y^2} = \frac{2lz}{l^2 + d^2 + z^2} \tag{C.18}$$

where d stands for the focal depth and $2l$ is the distance between the focal lines. Usually, these two parameters are obtained by experimental measurements. The CRLB for the axial position is expressed as follows:

$$\left(\Delta z^{\text{astigmatic}}\right)^2 = \frac{\left(l^2 + d^2 + z^2\right)^4}{4l^2\left(l^2 + d^2 - z^2\right)^2} (\Delta f)^2 \tag{C.19a}$$

$$(\Delta f)^2 = \left(1 - f^2\right)\left(\left(\frac{\Delta w_x}{w_x}\right)^2 + \left(\frac{\Delta w_y}{w_y}\right)^2 \right) \tag{C.19b}$$

By combining **Equations** (C.16), (C.18), (C.19a) and (C.19b), the final expression of the CRLB for the axial position of astigmatic method reads:

$$\left(\Delta z^{\text{astigmatic}}\right)^2 = \frac{1}{N} \frac{\left(l^2 + d^2 + z^2\right)^4}{4l^2\left(l^2 + d^2 - z^2\right)^2} \left(1 - \left(\frac{2lz}{l^2 + d^2 + z^2} \right)^2 \right) \left(1 + 8\tau + \sqrt{\frac{9\tau}{1+4\tau}} \right) \tag{C.20}$$

C.3 CRLB for DAISY

In DAISY, the axial positions from SAF and astigmatism are merged according their uncertainties in order to optimise the final precision (see equation(3.8)):

$$\begin{aligned} z^{\text{DAISY}} &= \left(\frac{z^{\text{SAF}}}{\left(\Delta z^{\text{SAF}}\right)^2} + \frac{z^{\text{astigmatic}}}{\left(\Delta z^{\text{astigmatic}}\right)^2} \right) \Bigg/ \left(\frac{1}{\left(\Delta z^{\text{SAF}}\right)^2} + \frac{1}{\left(\Delta z^{\text{astigmatic}}\right)^2} \right) \\ &= \pi^{\text{SAF}} z^{\text{SAF}} + \pi^{\text{astigmatic}} z^{\text{astigmatic}} \end{aligned} \tag{C.21}$$

where π^{SAF} and $\pi^{\text{astigmatic}}$ are the relative weights of the SAF and astigmatic information sources (note that these weights vary with the axial position):

$$\begin{aligned} \pi^{\text{SAF}} &= \frac{1}{\left(\Delta z^{\text{SAF}}\right)^2} \Bigg/ \left(\frac{1}{\left(\Delta z^{\text{SAF}}\right)^2} + \frac{1}{\left(\Delta z^{\text{astigmatic}}\right)^2} \right) \\ \pi^{\text{astigmatic}} &= \frac{1}{\left(\Delta z^{\text{astigmatic}}\right)^2} \Bigg/ \left(\frac{1}{\left(\Delta z^{\text{SAF}}\right)^2} + \frac{1}{\left(\Delta z^{\text{astigmatic}}\right)^2} \right) \end{aligned} \tag{C.22}$$

The CRLB for DAISY then reads:

$$\left(\Delta z^{\text{DAISY}}\right)^2 = \left(\pi^{\text{SAF}}\right)^2 \left(\Delta z^{\text{SAF}}\right)^2 + \left(\pi^{\text{astigmatic}}\right)^2 \left(\Delta z^{\text{astigmatic}}\right)^2 \tag{C.23}$$

C.4 CRLB for the lateral detection

The lateral lower bound was obtained using the same assumptions (PSF shape, photon number, background) than those described for the axial detection. We used the formula provided in [3]:

$$(\Delta x, y)^2 = \frac{w_{x,y}^2 + a^2/12}{N}\left(1 + 4\tau + \sqrt{\frac{2\tau}{1+4\tau}}\right) \tag{C.24}$$

with τ defined as in **Equation** (C.17).

Like the axial position, the lateral position results from the merging of the measured lateral UAF and EPI positions (see equations (3.1) and (3.2)). Thus it can be written as a weighted sum:

$$\begin{aligned} x^{\text{DAISY}} &= \pi_x^{\text{UAF}} x^{\text{UAF}} + \pi_x^{\text{EPI}} x^{\text{EPI}} \\ y^{\text{DAISY}} &= \pi_y^{\text{UAF}} y^{\text{UAF}} + \pi_y^{\text{EPI}} y^{\text{EPI}} \end{aligned} \tag{C.25}$$

where $\pi_{x,y}^{\text{UAF}}$ and $\pi_{x,y}^{\text{EPI}}$ are the relative weights of the UAF and EPI information sources for the x and y positions respectively (note that these weights vary with the axial position):

$$\begin{aligned} \pi_{x,y}^{\text{UAF}} &= \frac{1}{(\Delta(x,y)^{\text{UAF}})^2} \Bigg/ \left(\frac{1}{(\Delta(x,y)^{\text{UAF}})^2} + \frac{1}{(\Delta(x,y)^{\text{EPI}})^2}\right) \\ \pi_{x,y}^{\text{EPI}} &= \frac{1}{(\Delta(x,y)^{\text{EPI}})^2} \Bigg/ \left(\frac{1}{(\Delta(x,y)^{\text{UAF}})^2} + \frac{1}{(\Delta(x,y)^{\text{EPI}})^2}\right) \end{aligned} \tag{C.26}$$

As a result, the CRLB finally reads:

$$\begin{aligned} \left(\Delta x^{\text{DAISY}}\right)^2 &= \left(\pi^{\text{UAF}}\right)^2 \left(\Delta x^{\text{UAF}}\right)^2 + \left(\pi^{\text{EPI}}\right)^2 \left(\Delta x^{\text{EPI}}\right)^2 \\ \left(\Delta y^{\text{DAISY}}\right)^2 &= \left(\pi^{\text{UAF}}\right)^2 \left(\Delta y^{\text{UAF}}\right)^2 + \left(\pi^{\text{EPI}}\right)^2 \left(\Delta y^{\text{EPI}}\right)^2 \end{aligned} \tag{C.27}$$

Bibliography

[1] Nicolas Bourg. *Nanoscopie de fluorescence tri-dimensionnelle pour la biologie*. PhD thesis, Université Paris-Saclay, 2016.

[2] Alex von Diezmann, Yoav Shechtman, and W. E. Moerner. Three-dimensional localization of single molecules for super-resolution imaging and single-particle tracking. *Chemical Reviews*, 117(11):7244–7275, feb 2017.

[3] Sjoerd Stallinga and Bernd Rieger. The effect of background on localization uncertainty in single emitter imaging. In *2012 9th IEEE International Symposium on Biomedical Imaging (ISBI)*, pages 988–991. IEEE, may 2012.

[4] Z. Gan, S. Ram, R. J. Ober, and E. S. Ward. Using multifocal plane microscopy to reveal novel trafficking processes in the recycling pathway. *Journal of Cell Science*, 126(5):1176–1188, jan 2013.

[5] Sebastian van de Linde and Markus Sauer. How to switch a fluorophore: from undesired blinking to controlled photoswitching. *Chemical Society reviews*, 43(4):1076–87, mar 2014.

[6] Dominique Bourgeois. Deciphering structural photophysics of fluorescent proteins by kinetic crystallography. *International Journal of Molecular Sciences*, 18(6):1187, jun 2017.

[7] Russell E Thompson, Daniel R Larson, and Watt W Webb. Precise nanometer localization analysis for individual fluorescent probes. *Biophysical journal*, 82(5):2775–83, may 2002.

[8] Daniel Axelrod. Cell-substrate contacts illuminated by total internal reflection fluorescence. *The Journal of cell biology*, 89(1):141–5, apr 1981.

[9] Jan Huisken, Jim Swoger, Filippo Del Bene, Joachim Wittbrodt, and Ernst H K Stelzer. Optical sectioning deep inside live embryos by selective plane illumination microscopy. *Science (New York, N.Y.)*, 305(5686):1007–1009, 2004.

[10] M a Neil, R Juskaitis, and T Wilson. Method of obtaining optical sectioning by using structured light in a conventional microscope. *Optics letters*, 22(24):1905–1907, 1997.

[11] Yina Wang, Joerg Schnitzbauer, Zhe Hu, Xueming Li, Yifan Cheng, Zhen-Li Huang, and Bo Huang. Localization events-based sample drift correction for localization microscopy with redundant cross-correlation algorithm. *Optics Express*, 22(13):15982, jun 2014.

[12] Matthew D Lew, Mikael P Backlund, and W E Moerner. Rotational mobility of single molecules affects localization accuracy in super-resolution fluorescence microscopy. *Nano Letters*, 13(9):3967–3972, 2013.

[13] Alla Kress, Xiao Wang, Hubert Ranchon, Julien Savatier, Hervé Rigneault, Patrick Ferrand, and Sophie Brasselet. Mapping the local organization of cell membranes using excitation-polarization-resolved confocal fluorescence microscopy. *Biophysical journal*, 105(1):127–36, jul 2013.

[14] Cesar Augusto Valades Cruz, Haitham Ahmed Shaban, Alla Kress, Nicolas Bertaux, Serge Monneret, Manos Mavrakis, Julien Savatier, and Sophie Brasselet. Quantitative nanoscale imaging of orientational order in biological filaments by polarized superresolution microscopy. *Proceedings of the National Academy of Sciences*, page 201516811, 2016.

[15] Daniel Aquino, Andreas Schönle, Claudia Geisler, Claas V Middendorff, Christian a Wurm, Yosuke Okamura, Thorsten Lang, Stefan W Hell, and Alexander Egner. Two-color nanoscopy of three-dimensional volumes by 4Pi detection of stochastically switched fluorophores. *Nature methods*, 8(4):353–359, 2011.

[16] Audrey Dumont, Annie Malleron, Monzer Awwad, Sam Dukan, and Boris Vauzeilles. Click-mediated labeling of bacterial membranes through metabolic modification of the lipopolysaccharide inner core. *Angewandte Chemie International Edition*, 51(13):3143–3146, feb 2012.

[17] Georgyi V. Los, Lance P. Encell, Mark G. McDougall, Danette D. Hartzell, Natasha Karassina, Chad Zimprich, Monika G. Wood, Randy Learish, Rachel Friedman Ohana, Marjeta Urh, Dan Simpson, Jacqui Mendez, Kris Zimmerman, Paul Otto, Gediminas Vidugiris, Ji Zhu, Aldis Darzins, Dieter H. Klaubert, Robert F. Bulleit, and Keith V. Wood. HaloTag: A novel protein labeling technology for cell imaging and protein analysis. *ACS Chemical Biology*, 3(6):373–382, 2008.

[18] Peter J Bosch, Ivan R Corrêa, Michael H Sonntag, Jenny Ibach, Luc Brunsveld, Johannes S Kanger, and Vinod Subramaniam. Evaluation of fluorophores to label SNAP-tag fused proteins for multicolor single-molecule tracking microscopy in live cells. *Biophysical journal*, 107(4):803–14, aug 2014.

[19] Marina Mikhaylova, Bas M. C. Cloin, Kieran Finan, Robert van den Berg, Jalmar Teeuw, Marta M. Kijanka, Mikolaj Sokolowski, Eugene a. Katrukha, Manuel Maidorn, Felipe Opazo, Sandrine Moutel, Marylin Vantard, Frank Perez, Paul M. P. van Bergen en Henegouwen, Casper C. Hoogenraad, Helge Ewers, and Lukas C Kapitein. Resolving bundled microtubules using anti-tubulin nanobodies. *Nature Communications*, 6(May):7933, 2015.

[20] Nils Gustafsson, Siân Culley, George Ashdown, Dylan M. Owen, Pedro Matos Pereira, and Ricardo Henriques. Fast live-cell conventional fluorophore nanoscopy with ImageJ through super-resolution radial fluctuations. *Nature Communications*, 7(1), aug 2016.

[21] T. Dertinger, R. Colyer, G. Iyer, S. Weiss, and J. Enderlein. Fast, background-free, 3d super-resolution optical fluctuation imaging (SOFI). *Proceedings of the National Academy of Sciences*, 106(52):22287–22292, dec 2009.

[22] Stefan Geissbuehler, Claudio Dellagiacoma, and Theo Lasser. Comparison between SOFI and STORM. *Biomedical Optics Express*, 2(3):408, jan 2011.

[23] Christian Franke, Markus Sauer, and Sebastian van de Linde. Photometry unlocks 3d information from 2d localization microscopy data. *Nature Methods*, 14(1):41–44, nov 2016.

[24] Sripad Ram, Prashant Prabhat, Jerry Chao, E. Sally Ward, and Raimund J. Ober. High accuracy 3d quantum dot tracking with multifocal plane microscopy for the study of fast intracellular dynamics in live cells. *Biophysical Journal*, 95(12):6025–6043, dec 2008.

[25] Sripad Ram, Dongyoung Kim, Raimund J. Ober, and E. Sally Ward. 3d single molecule tracking with multifocal plane microscopy reveals rapid intercellular transferrin transport at epithelial cell barriers. *Biophysical Journal*, 103(7):1594–1603, oct 2012.

[26] Sara Abrahamsson, Jiji Chen, Bassam Hajj, Sjoerd Stallinga, Alexander Y Katsov, Jan Wisniewski, Gaku Mizuguchi, Pierre Soule, Florian Mueller, Claire Dugast Darzacq, Xavier Darzacq, Carl Wu, Cornelia I Bargmann, David A Agard, Maxime Dahan, and Mats G L Gustafsson. Fast multicolor 3d imaging using aberration-corrected multifocus microscopy. *Nature Methods*, 10(1):60–63, dec 2012.

[27] Bassam Hajj, Jan Wisniewski, Mohamed El Beheiry, Jiji Chen, Andrey Revyakin, Carl Wu, and Maxime Dahan. Whole-cell, multicolor superresolution imaging using volumetric multifocus microscopy. *Proceedings of the National Academy of Sciences of the United States of America*, 2014.

[28] Sara Abrahamsson, Rob Ilic, Jan Wisniewski, Brian Mehl, Liya Yu, Lei Chen, Marcelo Davanco, Laura Oudjedi, Jean-Bernard Fiche, Bassam Hajj, Xin Jin, Joan Pulupa, Christine Cho, Mustafa Mir, Mohamed El Beheiry, Xavier Darzacq, Marcelo

Nollmann, Maxime Dahan, Carl Wu, Timothée Lionnet, J. Alexander Liddle, and Cornelia I. Bargmann. Multifocus microscopy with precise color multi-phase diffractive optics applied in functional neuronal imaging. *Biomedical Optics Express*, 7(3):855, feb 2016.

[29] Bo Huang, Wenqin Wang, Mark Bates, and Xiaowei Zhuang. Three-Dimensional Super-Resolution Imaging by Stochastic Optical Reconstruction Microscopy. *Science*, 319(5864):810–813, 2008.

[30] S. R. P. Pavani, M. A. Thompson, J. S. Biteen, S. J. Lord, N. Liu, R. J. Twieg, R. Piestun, and W. E. Moerner. Three-dimensional, single-molecule fluorescence imaging beyond the diffraction limit by using a double-helix point spread function. *Proceedings of the National Academy of Sciences*, 106(9):2995–2999, feb 2009.

[31] Matthew D. Lew, Steven F. Lee, Majid Badieirostami, and W. E. Moerner. Corkscrew point spread function for far-field three-dimensional nanoscale localization of pointlike objects. *Optics Letters*, 36(2):202, jan 2011.

[32] David Baddeley, Mark B. Cannell, and Christian Soeller. Three-dimensional sub-100 nm super-resolution imaging of biological samples using a phase ramp in the objective pupil. *Nano Research*, 4(6):589–598, mar 2011.

[33] Shu Jia, Joshua C. Vaughan, and Xiaowei Zhuang. Isotropic three-dimensional super-resolution imaging with a self-bending point spread function. *Nature Photonics*, 8(March):302–306, mar 2014.

[34] Yoav Shechtman, Steffen J. Sahl, Adam S. Backer, and W. E. Moerner. Optimal point spread function design for 3d imaging. *Physical Review Letters*, 113(13), sep 2014.

[35] Yoav Shechtman, Lucien E. Weiss, Adam S. Backer, Steffen J. Sahl, and W. E. Moerner. Precise three-dimensional scan-free multiple-particle tracking over large axial ranges with tetrapod point spread functions. *Nano Letters*, 15(6):4194–4199, jun 2015.

[36] Andrey Aristov, Benoit Lelandais, Elena Rensen, and Christophe Zimmer. ZOLA-3d allows flexible 3d localization microscopy over an adjustable axial range. *Nature Communications*, 9(1), jun 2018.

[37] Daniel Burke, Brian Patton, Fang Huang, Joerg Bewersdorf, and Martin J. Booth. Adaptive optics correction of specimen-induced aberrations in single-molecule switching microscopy. *Optica*, 2(2):177, feb 2015.

[38] G. Shtengel, J. A. Galbraith, C. G. Galbraith, J. Lippincott-Schwartz, J. M. Gillette, S. Manley, R. Sougrat, C. M. Waterman, P. Kanchanawong, M. W. Davidson, R. D. Fetter, and H. F. Hess. Interferometric fluorescent super-resolution microscopy resolves 3d cellular ultrastructure. *Proceedings of the National Academy of Sciences*, 106(9):3125–3130, feb 2009.

[39] Pierre Jouchet, Clément Cabriel, Nicolas Bourg, Marion Bardou, Emmanuel Fort, and Sandrine Lévêque-Fort. Phase encoded single molecule localization microscopy with structured excitation. In *QBI*, 2019. Rennes, France.

[40] Pierre Jouchet, Clément Cabriel, Nicolas Bourg, Marion Bardou, Guillaume Dupuis, Christian Poüs, Emmanuel Fort, and Sandrine Lévêque-Fort. Structured illumination for single molecule localization microscopy at depth. In *FOM*, 2019. London, United Kingdom.

[41] Pierre Jouchet, Clément Cabriel, Nicolas Bourg, Marion Bardou, Christian Poüs, Emmanuel Fort, and Sandrine Lévêque-Fort. Modulated single molecule localization microscopy using homodyne detection. Submitted, 2019.

[42] Pierre Bon, Jeanne Linarès-Loyez, Maxime Feyeux, Kevin Alessandri, Brahim Lounis, Pierre Nassoy, and Laurent Cognet. Self-interference 3d super-resolution microscopy for deep tissue investigations. *Nature Methods*, 15(6):449–454, apr 2018.

[43] Thomas Barroca, Karla Balaa, Julie Delahaye, Sandrine Lévêque-Fort, and Emmanuel Fort. Full-field supercritical angle fluorescence microscopy for live cell imaging. *Optics letters*, 36(16):3051–3, aug 2011.

[44] J. Hell, S. W.;Wichmann. Breaking the diffraction resolution limit by stimulated emission: stimulated-emission-depletion fluorescence microscopy. *Optics letters*, 19(11), 1994.

[45] Siddharth Sivankutty, Iván Coto Hernández, Nicolas Bourg, Guillaume Dupuis, and Sandrine Lévêque-Fort. Supercritical angle fluorescence for enhanced axial sectioning in STED microscopy. *Methods*, apr 2019.

[46] Thomas Barroca, Karla Balaa, Sandrine Lévêque-Fort, and Emmanuel Fort. Full-Field Near-Field Optical Microscope for Cell Imaging. *Physical Review Letters*, 108(21):218101, may 2012.

[47] N. Bourg, C. Mayet, G. Dupuis, T. Barroca, P. Bon, S. Lécart, E. Fort, and S. Lévêque-Fort. Direct optical nanoscopy with axially localized detection. *Nature Photonics*, 9(9):587–593, aug 2015.

[48] Joran Deschamps, Markus Mund, and Jonas Ries. 3D superresolution microscopy by supercritical angle detection. *Optics Express*, 22(23):29081, nov 2014.

[49] Adam S. Backer and W. E. Moerner. Extending single-molecule microscopy using optical fourier processing. *The Journal of Physical Chemistry B*, 118(28):8313–8329, may 2014.

[50] C. J. R. Sheppard and P. Török. Effects of specimen refractive index on confocal imaging. *Journal of Microscopy*, 185(3):366–374, mar 1997.

[51] Alberto Diaspro, Federico Federici, and Mauro Robello. Influence of refractive-index mismatch in high-resolution three-dimensional confocal microscopy. *Applied Optics*, 41(4):685, feb 2002.

[52] Benjamin P. Bratton and Joshua W. Shaevitz. Simple experimental methods for determining the apparent focal shift in a microscope system. *PLOS ONE*, 10(8):e0134616, aug 2015.

[53] Ryan McGorty, Joerg Schnitzbauer, Wei Zhang, and Bo Huang. Correction of depth-dependent aberrations in 3d single-molecule localization and super-resolution microscopy. *Optics Letters*, 39(2):275, jan 2014.

[54] Yi Deng and Joshua W. Shaevitz. Effect of aberration on height calibration in three-dimensional localization-based microscopy and particle tracking. *Applied Optics*, 48(10):1886, mar 2009.

[55] Ignacio Izeddin, Mohamed El Beheiry, Jordi Andilla, Daniel Ciepielewski, Xavier Darzacq, and Maxime Dahan. PSF shaping using adaptive optics for three-dimensional single-molecule super-resolution imaging and tracking. *Optics express*, 20(5):4957–67, feb 2012.

[56] Clément Cabriel, Nicolas Bourg, Guillaume Dupuis, and Sandrine Lévêque-Fort. Aberration-accounting calibration for 3D single-molecule localization microscopy. *Optics Letters*, 43(2):174, jan 2018.

[57] Manuel F Juette, Travis J Gould, Mark D Lessard, Michael J Mlodzianoski, Bhupendra S Nagpure, Brian T Bennett, Samuel T Hess, and Joerg Bewersdorf. Three-dimensional sub–100 nm resolution fluorescence microscopy of thick samples. *Nature Methods*, 5(6):527–529, may 2008.

[58] Sven Proppert, Steve Wolter, Thorge Holm, Teresa Klein, Sebastian van de Linde, and Markus Sauer. Cubic b-spline calibration for 3d super-resolution measurements using astigmatic imaging. *Optics Express*, 22(9):10304, apr 2014.

[59] Alexander Auer, Thomas Schlichthaerle, Johannes B. Woehrstein, Florian Schueder, Maximilian T. Strauss, Heinrich Grabmayr, and Ralf Jungmann. Nanometer-scale multiplexed super-resolution imaging with an economic 3d-DNA-PAINT microscope. *ChemPhysChem*, 19(22):3024–3034, oct 2018.

[60] Raimund J Ober, Sripad Ram, and E Sally Ward. Localization accuracy in single-molecule microscopy. *Biophysical journal*, 86(2):1185–1200, 2004.

[61] Yoav Shechtman, Lucien E. Weiss, Adam S. Backer, Maurice Y. Lee, and W. E. Moerner. Multicolour localization microscopy by point-spread-function engineering. *Nature Photonics*, 10(9):590–594, aug 2016.

[62] Ke Xu, Hazen P Babcock, and Xiaowei Zhuang. Dual-objective STORM reveals three-dimensional filament organization in the actin cytoskeleton. *Nature Methods*, 9(2):185–188, jan 2012.

[63] Jervis Vermal Thevathasan, Maurice Kahnwald, Konstanty Cieśliński, Philipp Hoess, Sudheer Kumar Peneti, Manuel Reitberger, Daniel Heid, Krishna Chaitanya Kasuba, Sarah Janice Hoerner, Yiming Li, Yu-Le Wu, Markus Mund, Ulf Matti, Pedro Matos Pereira, Ricardo Henriques, Bianca Nijmeijer, Moritz Kueblbeck, Vilma Jimenez Sabinina, Jan Ellenberg, and Jonas Ries. Nuclear pores as versatile reference standards for quantitative superresolution microscopy. *biorxiv*, mar 2019.

[64] Christian Niederauer, Philipp Blumhardt, Jonas Mücksch, Michael Heymann, Armin Lambacher, and Petra Schwille. Direct characterization of the evanescent field in objective-type total internal reflection fluorescence microscopy. *Optics Express*, 26(16):20492, jul 2018.

[65] Rym Boudjemaa, Clément Cabriel, Florence Dubois-Brissonnet, Nicolas Bourg, Guillaume Dupuis, Alexandra Gruss, Sandrine Lévêque-Fort, Romain Briandet, Marie-Pierre Fontaine-Aupart, and Karine Steenkeste. Impact of bacterial membrane fatty acid composition on the failure of daptomycin to kill staphylococcus aureus. *Antimicrobial Agents and Chemotherapy*, 62(7), may 2018.

[66] Anaïs Bouissou, Amsha Proag, Nicolas Bourg, Karine Pingris, Clément Cabriel, Stéphanie Balor, Thomas Mangeat, Christophe Thibault, Christophe Vieu, Guillaume Dupuis, Emmanuel Fort, Sandrine Lévêque-Fort, Isabelle Maridonneau-Parini, and Renaud Poincloux. Podosome force generation machinery: A local balance between protrusion at the core and traction at the ring. *ACS Nano*, 11(4):4028–4040, apr 2017.

[67] Pakorn Kanchanawong, Gleb Shtengel, Ana M Pasapera, Ericka B Ramko, W Davidson, Harald F Hess, and Clare M Waterman. Nanoscale architecture of integrin-based cell adhesions Pakorn. *Nature*, 468(7323):580–584, 2011.

[68] Thomas Orré, Zeynep Karatas, Birgit Kastberger, Clément Cabriel, Marina Theodosiou, Sandrine Lévêque-Fort, Jean-Baptiste Sibarita, Reinhard Fässler, Bernhard Wehrle-Haller, Olivier Rossier, and Grégory Giannone. Linking kindlin molecular behaviour and 3D nanoscale localization to integrin activation in focal adhesions. Submitted, 2019.

[69] Ingrid Chamma, Olivier Rossier, Grégory Giannone, Olivier Thoumine, and Matthieu Sainlos. Optimized labeling of membrane proteins for applications to super-resolution imaging in confined cellular environments using monomeric streptavidin. *Nature Protocols*, 12(4):748–763, mar 2017.

[70] Anna-Karin Gustavsson, Petar N. Petrov, Maurice Y. Lee, Yoav Shechtman, and W. E. Moerner. 3d single-molecule super-resolution microscopy with a tilted light sheet. *Nature Communications*, 9(1), jan 2018.

[71] Clément Cabriel, Nicolas Bourg, Pierre Jouchet, Guillaume Dupuis, Christophe Leterrier, Aurélie Baron, Marie-Ange Badet-Denisot, Boris Vauzeilles, Emmanuel Fort, and Sandrine Lévêque-Fort. Combining 3D single molecule localization strategies for reproducible bioimaging. *Nature Communications*, 10(1), apr 2019.

[72] Bernd Rieger and Sjoerd Stallinga. The lateral and axial localization uncertainty in super-resolution light microscopy. *ChemPhysChem*, 15(4):664–670, 2014.

[73] Claas v. Middendorff, Alexander Egner, Claudia Geisler, Stefan W. Hell, and Andreas Schönle. Isotropic 3d nanoscopy based on single emitter switching. *Optics Express*, 16(25):20774, dec 2008.

[74] Alex von Diezmann, Maurice Y. Lee, Matthew D. Lew, and W. E. Moerner. Correcting field-dependent aberrations with nanoscale accuracy in three-dimensional single-molecule localization microscopy. *Optica*, 2(11):985, nov 2015.

[75] Siân Culley, David Albrecht, Caron Jacobs, Pedro Matos Pereira, Christophe Leterrier, Jason Mercer, and Ricardo Henriques. Quantitative mapping and minimization of super-resolution optical imaging artifacts. *Nature Methods*, 15(4):263–266, feb 2018.

[76] Marie-Jeanne Papandréou and Christophe Leterrier. The functional architecture of axonal actin. *Molecular and Cellular Neuroscience*, may 2018.

[77] Ke Xu, Guisheng Zhong, and Xiaowei Zhuang. Actin, spectrin, and associated proteins form a periodic cytoskeletal structure in axons. *Science (New York, N.Y.)*, 339(6118):452–6, jan 2013.

[78] Emilie Fugier, Audrey Dumont, Annie Malleron, Enora Poquet, Jordi Mas Pons, Aurélie Baron, Boris Vauzeilles, and Sam Dukan. Rapid and specific enrichment of culturable gram negative bacteria using non-lethal copper-free click chemistry coupled with magnetic beads separation. *PLOS ONE*, 10(6):e0127700, jun 2015.

[79] Bo Huang, Sara A Jones, Boerries Brandenburg, and Xiaowei Zhuang. Whole-cell 3d STORM reveals interactions between cellular structures with nanometer-scale resolution. *Nature Methods*, 5(12):1047–1052, nov 2008.

[80] F. Goos and H. Hänchen. Ein neuer und fundamentaler versuch zur totalreflexion. *Annalen der Physik*, 436(7-8):333–346, 1947.

[81] Graham T Dempsey, Joshua C Vaughan, Kok Hao Chen, Mark Bates, and Xiaowei Zhuang. Evaluation of fluorophores for optimal performance in localization-based super-resolution imaging. *Nature Methods*, 8(12):1027–1036, nov 2011.

[82] André Lampe, Volker Haucke, Stephan J. Sigrist, Mike Heilemann, and Jan Schmoranzer. Multi-colour direct STORM with red emitting carbocyanines. *Biology of the Cell*, 104(4):229–237, 2012.

[83] Zhengyang Zhang, Samuel J Kenny, Margaret Hauser, Wan Li, and Ke Xu. Ultrahigh-throughput single-molecule spectroscopy and spectrally resolved super-resolution microscopy. *Nature Methods*, 12(10):935–938, aug 2015.

[84] Corey Butler. *Quantitative single molecule imaging deep in biological samples using adaptive optics*. Theses, Université de Bordeaux, July 2017.

[85] Pierre Bon, Nicolas Bourg, Sandrine Lécart, Serge Monneret, Emmanuel Fort, Jérôme Wenger, and Sandrine Lévêque-Fort. Three-dimensional nanometre localization of nanoparticles to enhance super-resolution microscopy. *Nature Communications*, 6(August):7764, 2015.

[86] Martin Lehmann, Gregor Lichtner, Haider Klenz, and Jan Schmoranzer. Novel organic dyes for multicolor localization-based super-resolution microscopy. *Journal of Biophotonics*, 9(1-2):161–170, may 2015.

[87] Eran Hershko, Lucien E. Weiss, Tomer Michaeli, and Yoav Shechtman. Multicolor localization microscopy and point-spread-function engineering by deep learning. *Optics Express*, 27(5):6158, feb 2019.

[88] Pablo A. Gómez-García, Erik T. Garbacik, Jason J. Otterstrom, Maria F. Garcia-Parajo, and Melike Lakadamyali. Excitation-multiplexed multicolor superresolution imaging with fm-STORM and fm-DNA-PAINT. *Proceedings of the National Academy of Sciences*, 115(51):12991–12996, dec 2018.

[89] Orsolya K. Wade, Johannes B. Woehrstein, Philipp C. Nickels, Sebastian Strauss, Florian Stehr, Johannes Stein, Florian Schueder, Maximilian T. Strauss, Mahipal Ganji, Joerg Schnitzbauer, Heinrich Grabmayr, Peng Yin, Petra Schwille, and Ralf Jungmann. 124-color super-resolution imaging by engineering DNA-PAINT blinking kinetics. *Nano Letters*, 19(4):2641–2646, mar 2019.

[90] Jean Comtet, Evgenii Glushkov, Vytautas Navikas, Jiandong Feng, Vitaliy Babenko, Stephan Hofmann, Kenji Watanabe, Takashi Taniguchi, and Aleksandra Radenovic. Wide-field spectral super-resolution mapping of optically active defects in hexagonal boron nitride. *Nano Letters*, 19(4):2516–2523, mar 2019.

[91] Adrien Mau, Nicolas Bourg, and Sandrine Lévêque-Fort. Versatile uniform illumination method for fluorescence and single-molecule localization microscopy. Unpublished, 2019.

[92] Florian Stehr, Johannes Stein, Florian Schueder, Petra Schwille, and Ralf Jungmann. Flat-top TIRF illumination boosts DNA-PAINT imaging and quantification. *Nature Communications*, 10(1), mar 2019.

[93] Sebastian van de Linde, Anna Löschberger, Teresa Klein, Meike Heidbreder, Steve Wolter, Mike Heilemann, and Markus Sauer. Direct stochastic optical reconstruction microscopy with standard fluorescent probes. *Nature protocols*, 6(7):991–1009, jul 2011.

[94] Nicolas Olivier, Debora Keller, Vinoth Sundar Rajan, Pierre Gönczy, and Suliana Manley. Simple buffers for 3D STORM microscopy. *Biomedical optics express*, 4(6):885–99, jun 2013.

[95] Stefanie Kaech and Gary Banker. Culturing hippocampal neurons. *Nature Protocols*, 1(5):2406–2415, dec 2006.

[96] Francisco Balzarotti, Yvan Eilers, Klaus C. Gwosch, Arvid H. Gynnå, Volker Westphal, Fernando D. Stefani, Johan Elf, and Stefan W. Hell. Nanometer resolution imaging and tracking of fluorescent molecules with minimal photon fluxes. *Science*, 355(6325):606–612, dec 2016.

[97] Wai Teng Tang, Euiheon Chung, Yang-Hyo Kim, Peter T C So, and Colin J R Sheppard. Investigation of the point spread function of surface plasmon-coupled emission microscopy. *Optics express*, 15(8):4634–46, apr 2007.

List of Figures

Résumé du manuscrit

Les études en biologie cellulaires reposent sur l'utilisation de méthodes d'imagerie afin d'observer la structure et la dynamique d'échantillons d'intérêt. L'imagerie permet en particulier d'évaluer le rôle d'une ou plusieurs protéines dans des processus complexes, ou encore de quantifier l'effet d'un traitement. La microscopie est l'une des principales modalités d'imagerie disponibles : en raison de son pouvoir de résolution (allant jusqu'à l'échelle nanométrique), elle constitue un outil de choix pour l'observation des protéines. Plusieurs déclinaisons sont disponibles : la microscopie électronique offre les meilleures résolutions spatiales sur des échantillons fixée, tandis que la microscopie de phase est particulièrement adaptée au vivant. La microscopie de fluorescence est relativement peu toxique pour les cellules, mais elle présente surtout un avantage unique en termes de spécificité, dans la mesure où chaque protéine peut être marquée et observée indépendamment des autres.

En raison du phénomène de diffraction, la résolution spatiale en microscopie de fluorescence a longtemps été limitée autour de 200 nm dans la dimension transverse, et de 600 nm dans la dimension axiale (théorie d'Ernst Abbe, 1873). Depuis les années 1990, les avancées en observation de molécules uniques (équipe de William E. Moerner) et en confinement de l'excitation (équipe de Stefan Hell) ont permis de contourner cette limite pour atteindre des résolutions de l'ordre de la dizaine de nanomètres, donnant ainsi naissance à un nouveau domaine de recherche dans le développement de méthodes d'imagerie, mais également dans l'observation d'échantillons à des échelles jusque-là inaccessibles. L'approche de microscopie de localisation de molécules uniques (*Single Molecule Localisation Microscopie*, ou *SMLM*), se révèle particulièrement puissante dans la mesure où elle permet non seulement l'observation spatiale tridimensionnelle d'échantillons allant jusqu'à 5 nm, mais permet également l'obtention d'information complémentaires telles que le spectre de fluorescence, la polarisation ou encore le temps de vie de chaque molécule.

Ceci nécessite le couplage de techniques complémentaires faisant l'objet de développements indépendants menés par différentes équipes. Il en découle un défaut d'uniformisation des montages optiques, des algorithmes de traitement des données, mais également des protocoles de préparation d'échantillons et d'acquisition. Ce manque en-

trave la généralisation des méthodes de super-localisation comme outil d'étude d'échantillons en biologie, mais également en chimie et en physique des matériaux, malgré un potentiel prometteur. Nous proposons dans ce manuscrit d'introduire de nouveaux outils pour pallier ces défauts afin d'améliorer la reproductibilité des acquisitions et la fiabilité des résultats.

Dans un premier temps, nous posons les bases de la microscopie de fluorescence ainsi que la limite de diffraction. Nous introduisons la microscopie de localisation de molécules uniques comme moyen de contourner cette limite, et les protocoles photochimiques permettant sa mise on œuvre. Les écueils spécifiques à la super-localisation sont détaillés, en particulier les questions de dérives, de polarisation, de marquage, et de densité de molécules. Sont ensuite détaillées plus spécifiquement les méthodes de SMLM tri-dimensionnelles : nous exposons les approches par mise en forme de fonction d'étalement de point (*point spread function shaping*, ou *PSF shaping*), par lecture de la phase, et par détection de la fluorescence d'angle super-critique (*supercritical angle fluorescence*, ou *SAF*). Nous détaillons particulièrement l'implémentation de la méthode SAF en SMLM (*direct optical nanoscopy with axially localised detection*, ou *DONALD*), ses spécificités et ses avantages en matière d'insensibilité aux biais de détection axiale.

Le chapitre 2 est consacré aux caractérisations et aux applications en SMLM tridimensionnelle. Tout d'abord, nous introduisons un nouveau protocole de calibration de la détection axiale pour les méthodes 3D qui permet de tenir compte de l'effet de l'aberration sphérique sur les *PSF*. Plus précisément, nous utilisons un échantillon de géométrie connue (microsphères recouvertes de fluorophores) afin de faire reposer l'extraction de l'information axiale sur la seule mesure de la position latérale. L'échantillon est imagé en conditions standard, de sorte que les résultats reflètent fidèlement les données qui seront par la suite obtenues avec des échantillons biologiques. Nous illustrons la différence entre ce protocole et la calibration habituellement rapportée dans la littérature, qui repose sur l'utilisation de billes nanométriques déposées sur une lamelle. Nous mettons en évidence l'existence de biais axiaux efficacement corrigés par le protocole que nous proposont. Ensuite, nous nous intéressons aux questions de mesure de performances, qui déterminent la capacité d'une technique à produire une résolution suffisante pour les études envisagées. Nous comparons différentes approches : le calcul théorique reposant sur un modèle simplifié de l'encodage de l'information dans les *PSF*, la mesure sur des échantillons biologiques de taille connue, et enfin l'utilisation d'échantillons dédiés à la mesure de performances. Nous montrons l'intérêt de ces derniers pour découpler les différents facteurs intervenant dans la performance (sensibilité de la méthode, nombre de photons, taille de l'objet, stabilité du montage, etc.). Pour finir, nous présentons trois applications de *DONALD* à des problématiques de recherche en biologie et en chimie : la permière repose sur la localisation d'antibiotiques dans la paroi de bactéries *Staphylococcus aureus* dans le cadre de l'étude de la résistance bactérienne. Les deux autres visent à imager l'organisation à l'échelle nanoscopique des protéines dans deux structures d'adhérence différentes, les podosomes et les adhérences focales, dans le but d'identifier le rôle de chacune, ce qui s'inscrit dans le cadre de la compréhension

des processus de migration cellulaire et de transport de cellules tumorales. Pour chacune de ces applications, nous développons les protocoles de préparation d'échantillons, d'acquisition ou de traitement des données spécifiquement développés et mettons en évidence l'importance de la référence absolue obtenue en microscopie DONALD pour la reproductibilité des résultats.

Dans le troisième chapitre, nous proposons une méthode d'imagerie SMLM 3D (*Dual-view Astigmatic Imaging with SAF Yield*, ou *DAISY*) permettant de s'affranchir de la plupart des biais de détection axiale auxquelles sont sujettes les méthodes de *PSF shaping*. Cette technique repose sur l'utilisation d'un montage optique à deux voies de détection combinant les modalités de détection de *SAF* et d'astigmatisme. Dans cette configuration, l'information absolue fournie par la détection *SAF* est utilisée comme référence absolue pour corriger les défauts de l'astigmatisme. Ceci est obtenu grâce à un algorithme de correction par intercorrélation : ceci constitue une approche puissante dans laquelle chaque molécule est utilisée comme une référence, sans qu'il soit nécessaire de recourir à l'addition dans l'échantillon de marqueurs fiduciaux. Nous présentons les avantages de ce choix en matière de complémentarité des deux approches et d'optimisation de l'amplitude de l'aberration. Le procédé de traitement et la recombinaison des informations latérales et axiales est détaillé. Après une étape de mesure des précisions de localisation sur l'ensemble de la plage de capture, nous mettons en évidence l'efficacité de l'algorithme d'intercorrélation entre les informations de *SAF* et d'astigmatisme en matière de correction de la dérive axiale, de l'aberration chromatique et de l'inclinaison de l'échantillon. Cette validation des performances nous permet d'en venir aux applications de *DAISY* dans le cadre d'études en biologie et en chimie : nous présentons des résultats de double couleur pour des problématiques de neurobiologie et de marquage de membrane bactérienne par chimie de *click*. Pour finir, nous proposons plusieurs pistes d'amélioration ou d'applications complémentaires pour *DAISY*.

Le quatrième et dernier chapitre est dévolu à la présentation de deux méthodes d'analyse de données en post-traitement pour l'imagerie multicolore simultanée. Dans un premier temps, un état de l'art des méthodes d'imagerie multicolore est dessiné, ce qui nous permet de souligner la complexité des techniques disponibles et le besoin de simplification. Nous introduisons donc une approche basée sur la détection des tailles de *PSF* pour l'extraction d'information spectrale (*Spot width Evaluation for Spectral Assignment in Multicolour Experiments*, ou *SESAME*), et une autre utilisant la détection du comportement photophysique des molécules pour l'identification de la spécificité entre différents fluorophores et l'assignation des molécules (*PHotophysics-based Allocation for Nanoscopy through inTensity and On time Measurement*, ou *PHANTOM*). Le protocole de traitement associé à chaque méthode est détaillé, et nous présentons les résultats d'acquisitions de calibration, que nous utilisons ensuite pour une preuve de principe de séparation de deux espèces imagées simultanément. Suit une étape de caractérisation des performances, où nous évaluons l'influence de différents paramètres sur les performances de *SESAME* et *PHANTOM*. Enfin, nous détaillons des perspectives d'amélioration des résultats, et nous discutons des possibles couplages avec d'autres méthodes en SMLM, en particulier les approches de détection 3D.

Les travaux présentés dans ce manuscrit constituent une démarche visant à rendre la super-localisation plus aisément applicable aux études en biologie, en chimie et en physique des matériaux. Elle s'inscrit autour de trois axes principaux : l'élimination des biais de mesure, l'amélioration de la reproductibilité des expériences, et la simplification des montages expérimentaux et des protocoles de traitement des données. Dans cette optique, nous pensons que ces travaux peuvent contribuer à la généralisation des observations en microscopie de super-résolution.

Lists of publications

Published articles

- Clément Cabriel, Nicolas Bourg, Pierre Jouchet, Guillaume Dupuis, Christophe Leterrier, Aurélie Baron, Marie-Ange Badet-Denisot, Boris Vauzeilles, Emmanuel Fort, and Sandrine Lévêque-Fort, "Combining 3D single molecule localization strategies for reproducible bioimaging", *Nature Communications* **10**, 1980 (2019) [71]

- Clément Cabriel, Nicolas Bourg, Guillaume Dupuis, and Sandrine Lévêque-Fort, "Aberration-accounting calibration for 3D single-molecule localization microscopy", *Optics Letters* **43**, 174-177 (2018) [56]

- Rym Boudjemaa, Clément Cabriel, Florence Dubois-Brissonnet, Nicolas Bourg, Guillaume Dupuis, Alexandra Gruss, Sandrine Lévêque-Fort, Romain Briandet, Marie-Pierre Fontaine-Aupart, Karine Steenkeste, "Impact of Bacterial Membrane Fatty Acid Composition on the Failure of Daptomycin To Kill Staphylococcus aureus", *Antimicrobial Agents and Chemotherapy*, **62** (7) e00023-18 (2018) [65]

- Anaïs Bouissou, Amsha Proag, Nicolas Bourg, Karine Pingris, Clément Cabriel, Stéphanie Balor, Thomas Mangeat, Christophe Thibault, Christophe Vieu, Guillaume Dupuis, Emmanuel Fort, Sandrine Lévêque-Fort, Isabelle Maridonneau-Parini, and Renaud Poincloux, "Podosome Force Generation Machinery: A Local Balance between Protrusion at the Core and Traction at the Ring", *ACS Nano*, **11**, 4, 4028–4040 (2017) [66]

Unpublished articles

- Pierre Jouchet, Clément Cabriel, Nicolas Bourg, Marion Bardou, Christian Poüs, Emmanuel Fort, Sandrine Lévêque-Fort, "Modulated single molecule localization microscopy using homodyne detection", submitted [41]

- Thomas Orré, Zeynep Karatas, Birgit Kastberger, Clément Cabriel, Ralph Boettcher, Sandrine Lévêque-Fort, Jean-Baptiste Sibarita, Reinhard Fässler, Bernhard Wehrle-

Haller, Olivier Rossier, and Gregory Giannone, "Molecular motion and tridimensional nanoscale localization of kindlin control integrin activation in focal adhesions", submitted [68]

Oral presentations in conferences

- Clément Cabriel, Nicolas Bourg, Pierre Jouchet, Guillaume Dupuis, Cyndelia Guillaume, Aurélie Baron, Marie-Ange Badet-Denisot, Boris Vauzeilles, Christophe Leterrier, Emmanuel Fort, **Sandrine Lévêque-Fort**, "Multi-Color 3D Super-Resolution Imaging by Combining Strong Astigmatism and Supercritical Angle Fluorescence", *Focus On Microscopy*, April 2019, London, United Kingdom

- **Pierre Jouchet**, Clément Cabriel, Nicolas Bourg, Marion Bardou, Emmanuel Fort, Sandrine Lévêque-Fort, "Phase Encoded Single Molecule Localization Microscopy with Structured Excitation", *Focus On Microscopy*, April 2019, London, United Kingdom

- **Clément Cabriel**, Pierre Jouchet, Nicolas Bourg, Guillaume Dupuis, Christophe Leterrier, Aurélie Baron, Boris Vauzeilles, Emmanuel Fort, Sandrine Lévêque-Fort, "Wide depth reproducible multicolor bioimaging through a combination of 3D single molecule localization strategies", *QBI*, January 2019, Rennes, France

- **Clément Cabriel**, Pierre Jouchet, "Combining complementary 3D single molecule localization techniques for reliable multicolor bioimaging over extended depth ranges", *Mifobio*, October 2018, Seignosse, France (workshop)

- **Rym Boudjemaa**, Clément Cabriel, Nicolas Bourg, Guillaume Dupuis, Christian Marlière, Romain Briandet, Alexandra Gruss, Florence Dubois-Brissonnet, Sandrine Lévêque-Fort, Marie-Pierre Fontaine-Aupart, Karine Steenkeste, "Daptomycin failure to treat *S. aureus* biofilms: impact of membrane fatty acid composition", *Rafts4Biotech Symposium*, September 2018, Madrid, Spain

- **Clément Cabriel**, Nicolas Bourg, Guillaume Dupuis, Aurélie Baron, Boris Vauzeilles, Emmanuel Fort, Sandrine Lévêque-Fort, "Combining 3D single molecule localization strategies enables reproducible multicolor bioimaging over wide depth ranges", *ELMI* June 2018, Dublin, Ireland

- Clément Cabriel, Nicolas Bourg, Guillaume Dupuis, Aurélie Baron, Boris Vauzeilles, Emmanuel Fort, **Sandrine Lévêque-Fort**, "Highly Reproducible Multi-Color 3D Super-Resolution", *Focus On Microscopy*, March 2018, Singapore

- **Clément Cabriel**, Nicolas Bourg, Guillaume Dupuis, Aurélie Baron, Boris Vauzeilles, Emmanuel Fort, Sandrine Lévêque-Fort, "Combining 3D single molecule localization strategies for reproducible multicolor bioimaging", *ICON*, March 2018, Bielefeld, Germany

- **Clément Cabriel**, Nicolas Bourg, Guillaume Dupuis, Aurélie Baron, Boris Vauzeilles, Rym Boudjemaa, Karine Steenkeste, Marie-Pierre Fontaine-Aupart, Emmanuel Fort, Sandrine Lévêque-Fort, "Combining complementary localization modalities for 3D imaging of biological samples", *PhysChemCell*, November 2017, Orsay, France

- **Clément Cabriel**, Nicolas Bourg, Guillaume Dupuis, Christophe Leterrier, Aurélie Baron, Boris Vauzeilles, Sandrine Lécart, Emmanuel Fort, Sandrine Lévêque-Fort, "Combining Axial Single Molecule Localization Strategies to Enhance 3D Imaging of Biological Samples", *SMLMS*, August 2017, London, United Kingdom

- **Clément Cabriel**, Nicolas Bourg, Guillaume Dupuis, Sandrine Lécart, Emmanuel Fort, Sandrine Lévêque-Fort, "Combining Axial Single Molecule Localization Strategies to Enhance 3D Imaging of Biological Samples", *Focus On Microscopy*, April 2017, Bordeaux, France

- Anaïs Bouissou, Amsha Proag, Clément Cabriel, Stéphanie Balor, Thomas Mangeat, Christophe Thibault, Christophe Vieu, Guillaume Dupuis, Emmanuel Fort, Sandrine Lévêque-Fort, Isabelle Maridonneau-Parini, **Renaud Poincloux**, "Architecture and Mechanics of the Macrophage Podosome", *Focus On Microscopy*, April 2017, Bordeaux, France

- **Clément Cabriel**, Guillaume Dupuis, "Axial localization in fluorescence nanoscopy", *Mifobio*, October 2016, Seignosse, France (workshop)

- **Rym Boudjemaa**, Clément Cabriel, Nicolas Bourg, Guillaume Dupuis, Sandrine Lévêque-Fort, Romain Briandet, Marie-Pierre Fontaine-Aupart, Karine Steenkeste, "Micro to nanometric optical imaging resolution to ascertain antibiotic target localization: why are these antimicrobials not effective?", *Biofilms7*, June 2016, Porto, Portugal

- Nicolas Bourg, Clément Cabriel, Guillaume Dupuis, Emmanuel Fort, **Sandrine Lévêque-Fort**, "Émission de fluorescence supercritique pour la nanoscopie", *Lumières sur la Photochimie et la Photobiologie*, December 2015, Cachan, France

université PARIS-SACLAY
ÉCOLE DOCTORALE
Ondes et Matière (EDOM)

Titre : Approches tri-dimensionnelles et multicolores en microscopie de fluorescence super-résolue pour la biologie

Mots clés : Optique, Microscopie, Fluorescence, Super-résolution, Biologie

Résumé : Pour analyser la structure et la dynamique des échantillons, la biologie cellulaire repose sur l'utilisation d'outils d'imagerie. En particulier, la microscopie de fluorescence offre une grande spécificité et une toxicité réduite. L'émergence récente des méthodes de super-résolution a permis d'outrepasser la limite de diffraction et ouvert de nouvelles perspectives d'études. Les stratégies de molécule unique sont particulièrement adaptées à l'imagerie nanométrique tridimensionnelle, et permettent de nombreux couplages avec des modalités complémentaires ; toutefois, leur manque de reproductibilité entrave leur généralisation.
Nous proposons ici de nouvelles méthodes dans le but de remédier à ces problèmes en facilitant leur application en biologie cellulaire, en chimie et en science des matériaux. Tout d'abord, nous présentons des protocoles et échantillons dédiés aux acquisitions de calibration et de mesure de performances. Nous décrivons également plusieurs exemples d'utilisation de super-localisation tridimensionnelle dans le cadre d'études d'adhésion cellulaire et de résistance bactérienne.
Ensuite, nous nous concentrons sur le développement d'une nouvelle méthode de microscopie de localisation de molécules uniques tri-dimensionnelle permettant l'élimination de biais de détection. Ceci est permis par le couplage entre deux stratégies complémentaires : la mise en forme de fonction d'étalement de point, et la détection de la fluorescence d'angle super-critique. L'intercorrélation et la recombinaison des informations latérales et axiales permet l'obtention d'une résolution quasi-isotrope, avec des précisions jusqu'à 15 nanomètres sur une plage de capture d'un micron. Nous mettons en évidence l'insensibilité de la méthode aux biais d'imagerie comme la dérive axiale, l'aberration chromatique et l'inclinaison de l'échantillon, et nous l'illustrons à travers des applications à la neurobiologie et au marquage de bactéries.
Pour finir, nous présentons deux nouvelles approches pour le découplage d'acquisitions multi-espèces simultanées. Toutes deux basées entièrement sur le post-traitement des données acquises, elles exploitent respectivement la mesure des tailles des taches et le comportement dynamique du clignotement. Après une preuve de principe, nous évaluons l'impact des différents paramètres susceptibles d'influencer les résultats. Nous concluons en proposant des pistes d'amélioration des performances de découplage, et en suggérant de possibles couplages avec des méthodes complémentaires en imagerie de molécules uniques.

Title : Three-dimensional and multicolour approaches in super-resolution fluorescence microscopy for biology

Keywords : Optics, Microscopy, Fluorescence, Super-resolution, Biology

Abstract : Cell biology relies on imaging tools to provide structural and dynamic information about samples. Among them, fluorescence microscopy offers a compromise between high specificity and low toxicity. Recently, super-resolution methods overcame the diffraction barrier to unlock new fields of investigation. Single molecule approaches prove especially useful for three-dimensional nanoscale imaging, and allow couplings between different detection modalities. Still, their use is hindered by the complexity of the methods as well as the lack of reproducibility between experiments.
We propose new methods to render super-localisation microscopy more easily applicable to relevant studies in cell biology, chemistry and material science. First, we introduce dedicated protocols and samples to eliminate sources of error in calibration and performance measurement acquisitions. We also provide examples of uses of three-dimensional super-localisation for state-of-the-art studies in the frameworks of cell adhesion and bacterial resistance to drugs.
Then, we focus on the development of a novel optical method that provides unbiased results in three-dimensional single molecule localisation microscopy. This is achieved through the combination of two complementary axial detection strategies: point spread function shaping on the one hand, and supercritical angle fluorescence detection on the other hand. By cross-correlating and merging the lateral and axial positions provided by the different sources, we achieve quasi-isotropic localisation precisions down to 15 nanometres over a 1-micrometre capture range. We demonstrate the insensibility of the method to imaging non-idealities such as axial drift, chromatic aberration and sample tilt, and we propose applications in neurobiology and bacteria labelling.
Finally, we introduce two new post-processing approaches for the demixing of simultaneous multi-species acquisitions. They are based respectively on the measurement of the spot sizes, and on the assessment of the dynamic blinking behaviour of molecules. After demonstrating a proof of principle, we assess the impact of the different parameters likely to influence the results. Eventually, we discuss leads to improve the demixing performances, and we discuss the coupling possibilities with complementary single molecule localisation techniques.

Université Paris-Saclay
Espace Technologique / Immeuble Discovery
Route de l'Orme aux Merisiers RD 128 / 91190 Saint-Aubin, France